Evaluation of Novel Particle Detection Methods and their Application to Characterize the Process of Protein Aggregation

Thesis

Submitted in the fulfilment of the requirements of degree of

Doctor of Natural Sciences (Dr. rer. nat.)

equivalent to Doctor of Philosophy (Ph.D.)

To

The Faculty of Pharmacy,

University of Marburg.

by

Julia Groß-Rother (M.Sc.)

from Hohenleuben (Gera)

Marburg/Lahn 2021

First Supervisor: **Prof. Dr. Udo, Bakowsky**

Second Supervisor: **Prof. Dr. Patrick Garidel**

Date of Submission: **29.04.2021**

Defense date: **15.06.2021**

Hochschulkennziffer: **1180**

Evaluierung neuer Partikeldetektionsmethoden und ihrer Anwendung für die Charakterisierung von Proteinaggregationsprozesse

Dissertation

zur Erlangung des Doktorgrades

der Naturwissenschaften

(Dr. rer. nat.)

dem

Fachbereich Pharmazie der

Philipps-Universität Marburg

vorgelegt von

Julia Groß-Rother (M.Sc.)

aus Hohenleuben (geb. in Gera)

Marburg/Lahn 2021

Erstgutachter: **Prof. Dr. Udo Bakowsky**

Zweitgutachter: **Prof. Dr. Patrick Garidel**

Eingereicht am **29.04.2021**

Tag der mündlichen Prüfung am **15.06.2021**

Hochschulkennziffer: **1180**

SPERRVERMERK

Diese Doktorarbeit enthält vertrauliche Daten der Boehringer Ingelheim Pharma GmbH & Co. KG. Veröffentlichung oder Vervielfältigung der Arbeit – auch nur auszugsweise – sind ohne ausdrückliche Genehmigung der Boehringer Ingelheim Pharma GmbH & Co. KG nicht gestattet.

EIDESSTATTLICHE ERKLÄRUNG

Ich versichere, dass ich meine Dissertation

„ Evaluation of Novel Particle Detection Methods and their Application to Characterize the Process of Protein Aggregation “

selbständig ohne unerlaubte Hilfe angefertigt und mich dabei keiner anderen als der von mir ausdrücklich bezeichneten Quellen bedient habe. Alle vollständig oder sinngemäß übernommenen Zitate sind als solche gekennzeichnet.

Die Dissertation wurde in der jetzigen oder einer ähnlichen Form noch bei keiner anderen Hochschule eingereicht und hat noch keinen sonstigen Prüfungszwecken gedient.

Biberach (Riss), den..... .....

Julia Groß-Rother

ACKNOWLEDGEMENTS / DANKSAGUNG

Die vorliegende Arbeit ist das Ergebnis einer aufregenden, lehrreichen und spannenden Zeit mit einigen Irrwegen und vielen Aufs und Abs. Ohne die Unterstützung einer Vielzahl von lieben Menschen gäbe es diese Arbeit nicht und an dieser Stelle möchte ich mich nun bei all denjenigen bedanken, die mich während dieser Zeit unterstützt und motiviert haben.

An erster Stelle gilt mein Dank Herrn Prof. Dr. Patrick Garidel und Herrn Prof. Dr. Udo Bakowsky für die Möglichkeit meine Dissertation in einem Kooperationsprojekt zwischen Boehringer Ingelheim und der Universität Marburg anfertigen zu können. Insbesondere bin ich Ihnen dankbar für die wissenschaftliche Unterstützung, die hilfreichen Anregungen und Diskussionen, sowie die Geduld und das jederzeit offene Ohr auch in schwierigen Phasen. Das habe ich nie als selbstverständlich angesehen. Herzlichen Dank dafür.

Des Weiteren möchte ich mich recht herzlich bedanken bei Herrn Prof. Dr. Torsten Steinmetzer und Herrn Prof. Dr. Cornelius Krasel für die freundliche Übernahme der Aufgaben als Mitglieder der Prüfungskommission.

Außerdem gilt mein Dank Frau Dr. Michaela Blech für die zeitweise Betreuung und Unterstützung, sowie die anregenden Diskussionen, die mir immer sehr viel Freude bereitet haben.

Manchmal können es die kleinen organisatorischen Dinge sein, die einem das Leben schwermachen. Ich hatte das Glück mit Frau Petra Janik und Frau Julia Michaelis, sowohl bei Boehringer als auch an der Uni Marburg, immer schnelle und tatkräftige Unterstützung zu bekommen. Dafür ein riesiges Dankeschön, denn auch das ist keine Selbstverständlichkeit!

Ein großer Dank geht an all die Kollegen (insbesondere im G55) bei Boehringer, die mich mit anhaltender Hilfestellung begleitet haben und den Alltag so abwechslungsreich mitgestaltet haben. Für anregende Gespräche, konstruktive Kritik aber auch viel Spaß zusammen möchte ich dem Büro 014 danken, im besonderen Frau Dr. Anne Karow, Frau Dr. Anne Cosse, Frau Dr. Katharina Reiche, Herrn Dr. Kai Baumgartner und Herrn Dr. Sebastian Kube. Namentlich möchte ich an

dieser Stelle auch noch Herrn Dr. Ingo Presser erwähnen, der auch zu später Stunde mit freundlichen Worten, interessanten Diskussionen und viel Schokolade eine große Unterstützung war.

Auch wenn ich nur wenig Zeit in Marburg verbracht habe, habe ich mich hier stets sehr willkommen gefühlt. Die gemütlichen Weihnachtsfeiern oder auch die spannende Zeit mit Herrn Dr. Konrad Engelhard am AFM werde ich nie vergessen. Vielen Dank daher auch an alle Kollegen an der Uni Marburg. An dieser Stelle möchte ich auch noch Herrn Dr. Eduard Preis recht herzlich danken für die Unterstützung und die tolle Zusammenarbeit bei gemeinsamen Veröffentlichungen.

Während meiner Zeit hatte ich auch das Glück tatkräftige Unterstützung bekommen zu haben von Franziska Schandock, Sabrina Sayle, Dominik Kochard und Johanna Kliche, die ich in ihre Praktikanten-/Bacheloranden-/Masterandenzeit betreuen durfte. Vielen Dank euch für eure Motivation, die fleißige und sehr gute Arbeit im Labor und für die tolle Zusammenarbeit.

Mein größter Dank gilt meiner Familie und meinen Freunden. Ich danke jedem einzelnen von euch für eure liebevolle Fürsorge, die unermüdliche Stärkung und Motivierung, sowie für das stets offene Ohr und die lieben Worte. Insbesondere ohne die familiäre Unterstützung seitens meiner Eltern und meines Bruders hätte ich diesen Weg vermutlich nie eingeschlagen. Ihr habt mich früh in all meinen Vorhaben unterstützt. Ihr habt immer fest hinter mir gestanden, auch wenn es zwischendurch einmal schwieriger war. Gleiches gilt für meine geliebte Frau. Denn du warst es, die mir in den harten Zeiten immer und immer wieder gesagt hat, dass es sich zu kämpfen lohnt und dass Aufgeben keine Option ist. Für all das meinen tief empfundenen Dank.

TABLE OF CONTENT

LIST OF FIGURES

LIST OF TABLES

ABBREVIATIONS

A320	transmission/absorbance at 320 nm (turbidity)
a.u.	arbitrary unit
AC	analytical centrifugation
AF4	asymmetric flow field flow fractionation
AFM	atomic force microscopy
APC	Antigen presenting cells
AUC	analytical ultra centrifugation
CCD	charge-coupled device
CDR	complementary defining region
CH (1/2/3)	conserved domain heavy chain
CL	camera level
CQA	critical quality attribute
CT	capture time
DCS	differential centrifugal sedimentation
DLS	dynamic light scattering
DLVO	Derjaguin, Landau, Verwey and Overbeek theory
DSC	differential scanning calorimetry
DSG	disuccinimidyl glutarate
DT	detection threshold
ELE	extended Lumry-Eyring model
EPD	equivalent particle diameter
ETFE	ethylene tetrafluoroethylene
FC	flow cytometry
FMI	flow microscopy imaging
FTIR	Fourier transform infrared (spectroscopy)
HCLF	high concentration liquid formulation
I	intensity
LENP	extended Lumry-Eyring model with Nucleated Polymerization
LO	light obscuration
mAB	monoclonal antibody
MALS	multi angle light scattering
MEMS	micro electromechanical systems
MFI	micro-flow imaging
NCE	novel chemical entities
NIST	National Institute of Standards and Technology
NTA	nanoparticle tracking analysis
NTU	Nephelometric turbidity unit
PDI	poly dispersity index

PS	polystyrene
PSD	particle size distribution
QELS	quasi elastic light scattering
RI	refractive index
RMM	resonant mass measurement
RPS	resistive pulse sensing
RT	room temperature
SD	standard derivation
SEC	size exclusion chromatography
SLS	static light scattering
SMR	suspended microchannel resonators
STEP	space and time resolved extinction profiles
Tagg	aggregation start temperature
TEM	transmission electron microscopy
Tm	melting temperature
Tonset	unfolding start (onset) temperature
TRPS	tunable resistive pulse sensing
VL	variable region/domain light chain
VH	variable region/domain heavy chain
VPM	variable-pressure module

PART I: Introduction

~

1. Biopharmaceuticals and the role of monoclonal antibodies

1.1. Biopharmaceuticals on the pharmaceutical market: current state and future perspective

The term biopharmaceuticals describes pharmaceutical substances "derived from biological sources" and "derived from genetic engineering or hybridoma technology" (Walsh 2013). The first approved biopharmaceutical was recombinant produced insulin in 1982. Since then the interest in biopharmaceutical molecules has grown intensively, in particular over the last decade (Walsh 2014). Reasons that make biopharmaceuticals highly attractive are the high efficacy already at low concentrations and that they show fewer side effects and high safety. On the other side, the complexity and fragility of the molecules lead to operational and technological challenges (Wang, Singh et al. 2007). The shift from the initial biopharmaceutical research to business, additionally, brings the challenges of quality compliance and regulatory scrutiny as well as cost-pressure and competition on the market (Michl and Heinemann 2009). In consequence, there is an ongoing need for obtaining more basic understanding about the nature, stability and dynamics of these biological molecules as well as technological improvements for better investigation. The rapid developments of new technologies in the last years, such as recombinant DNA technology, were one essential step and the production of biopharmaceuticals became more efficient (Manning, Chou et al. 2010). As consequence a change and an evolution of the pharmaceutical market was observed towards biopharmaceuticals (Figure 1- 1, left and center) (GIReseach 2013, Köpf and Frieß 2016, vfa 2016).

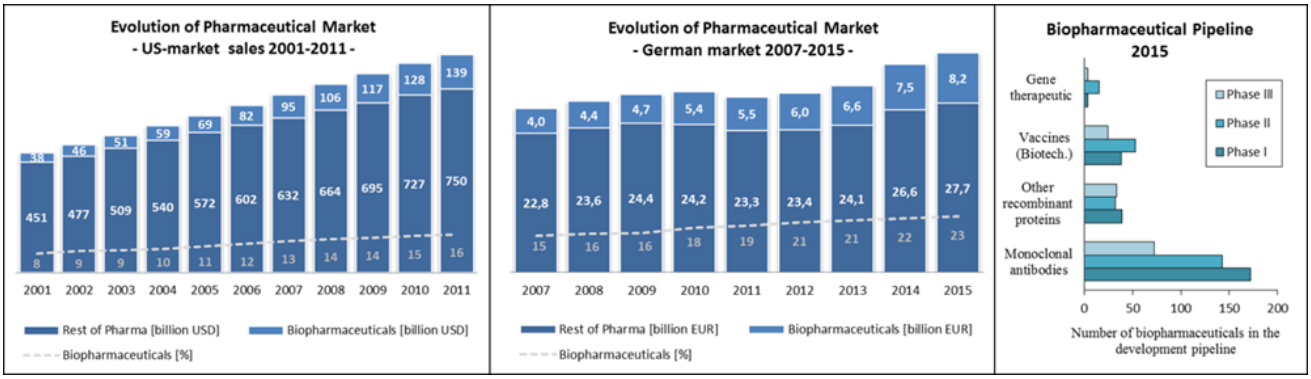

Figure 1- 1: Evolution of the pharmaceutical market.
The sales shares of biopharmaceuticals increased in the last decade over 25 %. The main portion (about ¾) of the biopharmaceuticals in the pipeline belongs to the group of monoclonal antibodies (based on (GIReseach 2013, vfa 2016, vfa 2016)).

About 550 biopharmaceutical approvals are noted since the year 2000 - 56 alone in 2015. Furthermore, the biopharmaceutical pipelines have more than 7000 developments by biopharmaceutical researchers in progress, most likely for the treatment of cancer, neurological diseases, infectious diseases and immunological disorders (Michl and Heinemann 2009). The major portion are antibodies (Figure 1- 1, right) that gained enormously on interest for the biopharmaceutical market and cover up to ¾ in the pipeline and ⅓ of all approvals (Walsh 2014, vfa 2016).

1.2. Monoclonal antibodies (mABs): Nature, function and structure

Antibodies, or immunoglobulins (Ig), are Y-shaped glycoproteins that occur naturally as part of the immune system (Figure 1- 2). They belong to the Ig superfamily and they are produced by B-lymphocytes (Wang, Singh et al. 2007). In contrast to natural antibodies, antigen-specific antibodies identify highly specifically foreign compounds in the body (Zouali 2001). For that reason these antibodies play a key role in immune reactions (Figure 1- 2a), like the antibody-dependent-cell mediated-cytotoxicity (ADCC), immunomodulation, opsonization, virus and toxin neutralization, direct antimicrobial activity or the activation of the complement system (Casadevall, Dadachova et al. 2004, Male, Brostoff et al. 2013, Murphy and Weaver 2016). So far, five different isotypes of human antibodies are identified based on structural differences in the constant regions of the heavy chain: IgM, IgG, IgA, IgE and IgD. For biopharmaceutical applications, especially IgG as major serum isotype is a powerful tool (Wang, Singh et al. 2007). The secondary structure of this molecule consists mainly of ß-sheets (50-70 %) (Peters, 2016, Wang, 2007). These immunoglobulins show a typical structure consisting of two identical heavy (~50 kDa) and two identical light chains (~25 kDa) that are connected via disulfide bonds (Figure 1- 2b). Within these chains, there are highly conserved domains (CH1, CH2, CH3 and CL) as well as variable regions (VL and VH). The variable domains build the complementary defining region (CDR) with the antigen binding site (Wang, Singh et al. 2007). The conserved regions enable additional biological activities, like the macrophage binding side. Besides this structural classification, antibodies consist of two functional parts: the Fc- and the Fab-fragment. While the Fc-fragment is highly conserved and responsible for the binding to effector cells, the Fab-fragments show high variability

and they are responsible for the identification and binding of innumerable antigens (Davies and Metzger 1983, Male, Brostoff et al. 2013).

The first monoclonal antibody product, called OKT-3, was approved in 1986 (Manning, Chou et al. 2010). In 2007, more than 23 antibody drug products have entered the market (Wang, Singh et al. 2007). Today some of the largest selling pharmaceutical products are antibodies, e.g. Humira (Adalimumab), Remicade (Infliximab) or Avastin (Bevacizumab) (Ltd 2014, Ecker, Jones et al. 2015). Reasons for the selection of mABs are the specific actions with less side effects, mABs can be conjugated to other therapeutic entities, mABs can be conjugated to radioisotopes, technology enhancement make complete human abs available – just to name a few (Wang, Singh et al. 2007).

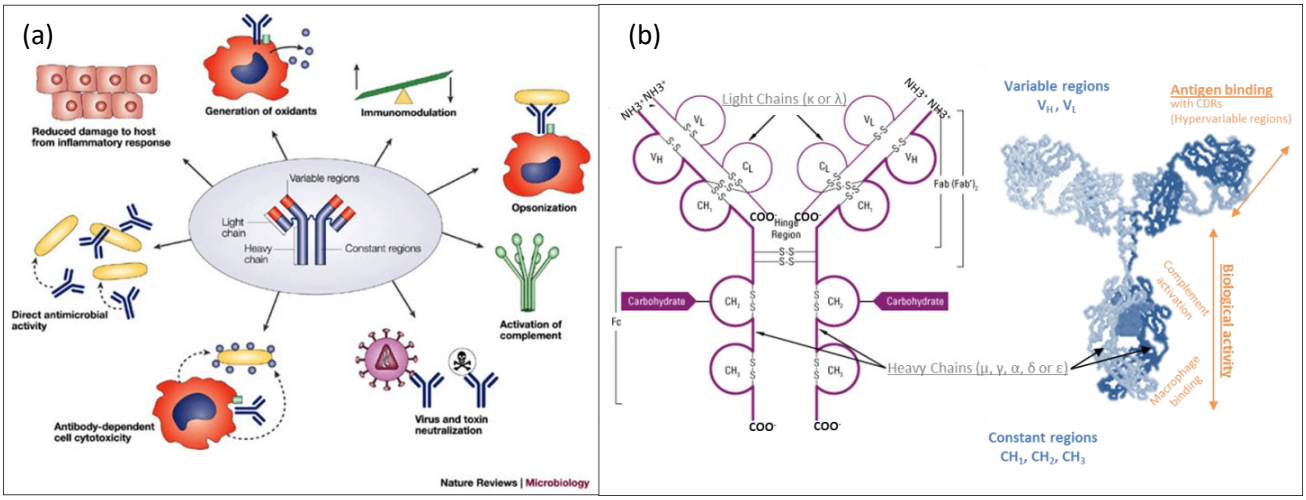

Figure 1- 2: Antibody functions and structure.
(a) Natural antibodies in the human body fulfill various essential functions in the immune system if pathogens like microbes enter the human body. (b) Schematic structure of an IgG with illustrating the heavy and the light chains, the positions of disulfide bridges, common structural domains (VH, variable heavy chain domain; CH, constant heavy chain domain; VL, variable light chain domain; CL, constant light chain domain) as well as functional regions (based on (Casadevall, Dadachova et al. 2004, ThermoFisher 2016)).

2. Protein stability, aggregation and immunogenicity

2.1. Protein stability

Compared to small chemical pharmaceutical molecules (new chemical entities, NCEs), new biological entities (NBEs) such as proteins are highly dynamic, more complex and they are highly sensitive to changes in their (micro-) environment (Jaenicke 1991, Balcão and Vila 2015). Today there is a broad knowledge about structure, function, activity and stability of various proteins available. Due to the fact that each protein behaves in a unique way, protein stability, however, is not completely understood or even predictable. It remains one of the major challenges for biopharmaceutical development as controlling and predicting a protein´s stable, native and functional conformation or the protein behavior in solutions is hardly achievable (Manning, Chou et al. 2010).

Protein stability, in general, can be defined as the balance between stabilizing and destabilizing forces (Jaenicke 1991, Shire, Shahrokh et al. 2004). In consequence, any small change in this balance shifting these forces may lead to changes in the protein molecule, protein instability or even the collapse of the protein solution can occur. Major stress factors to disturb this balance are temperature, pressure, chemical agents, biological agents or the environmental ion strength. Depending on the stress applied and the processes which are responsible for stabilization/destabilization one can discriminate chemical and physical (in-)stability (Wang, Singh et al. 2007). Chemical instability is characterized by processes changing the protein chemistry or the chemical composition, e.g. deamination, oxidation or hydrolysis. In contrast, physical instability is characterized by processes which change the physical state of the protein, e.g. denaturation, aggregation or precipitation and intramolecular or intermolecular forces, like hydrogen bonds, electrostatic or hydrophobic forces, play key roles (Manning, Patel et al. 1989, Manning, Chou et al. 2010).

As proteins are in aqueous suspension, two main stability mechanisms are considered:

The first one is the ***intrinsic conformational stability*** concerning the stability of each single monomer/protein molecule, mainly caused by intramolecular interactions and short-range forces (Figure 1- 3a). A protein molecule in aqueous solution is naturally present in an active and energetic favorable conformation with a specific 3D-structure (native state). In this conformation, about 80 % of the hydrophobic amino acid residues (e.g. Phe, Trp,) are located in the center

stabilized by hydrophobic interactions. Hydrophilic amino acid residues (e.g. Lys, Ser) are situated at the interface with water outside of the protein stabilized by hydrogen bonds or electrostatic interactions (Wang 1999). Perturbations caused by changes of the energy landscape (e.g. temperature or mechanical stress) alter these intramolecular interactions and lead to the loss of the conformational stability. During the unfolding process, the protein may occur in several intermediates with partial unfolded parts. Proteins under extreme conditions, e.g. extreme pH, generally appear in these intermediate states (Jaenicke 1991, Sancho 2013). If the protein reaches an intermediate activated state it might finally end up as denatured, i.e. in an unfolded and inactive state. The free energy difference ΔG between native and denatured state is usually quite small with about 21-85 kJ/mol (Wang 1999). Consequently, conformational stability is highly dynamic and sensitive. For that reason, the general assumption describes that proteins in solution exist in a thermodynamic equilibrium of native, denatured and even intermediate states. After denaturation, however, further processes may follow, such as aggregation as described below.

The second perspective is the protein suspension as colloidal system. ***Colloidal stability*** is mainly caused by intermolecular interactions between protein-protein and protein-solvent (Figure 1- 3b) (Rowe 2001, Nicoud, Owczarz et al. 2015). In this case, intermolecular attractive van der Waals forces or repulsive electric forces are the dominant forces. Charged particles in aqueous suspension, such as protein molecules, form - besides the hydration shell - an electrical double layer around their surface (Figure 1- 3b, left) to enable electro neutrality in the suspension. Close to the particle surface, counterions form a more rigid layer detectable as the Stern potential. Afterwards a more diffuse layer appears which can be described by the measurable zeta potential, a parameter often used for colloidal stability estimations (Verwey and Overbeek 1946, van Oss 2003). These layers, however, depending on the present salt concentration, show an electrostatic shielding effect as they lower the repulsive electrostatic long-range forces critically for colloidal stability. Based on the DLVO theory, colloidal stability is given, if the repulsive forces between two particles dominate and a sufficient intermolecular distance is present (Figure 1- 3b, right) (De Young, Fink et al. 1993, Israelachvili and Wennerstrom 1996). Considering the free energy of the system there is a positive free energy and a high free energy barrier characterizing high colloidal stability. If the shielding effect becomes stronger, the intermolecular distance as well as the free energy and the energy barrier reduce. At the distance of the secondary minimum reversible aggregation may still occur (exemplary about 20 nm in Figure 1- 3b). At the distance of the primary minimum (below 3 nm),

indeed, attractive van-der-Waals forces dominate and lead to irreversible aggregation (De Young, Fink et al. 1993). For proteins, however, such models and estimations only partially apply due to their heterogeneous charge distribution and anisotropic properties. And instead of zeta potential, a more often used parameter, which describes protein-protein interactions and colloidal stability in a non-ideal solution behavior, is the osmotic second virial coefficient (A2 or B22) (Le Brun, Friess et al. 2010). Colloidal instability in all cases leads to either processes of reversible association or mostly irreversible aggregation.

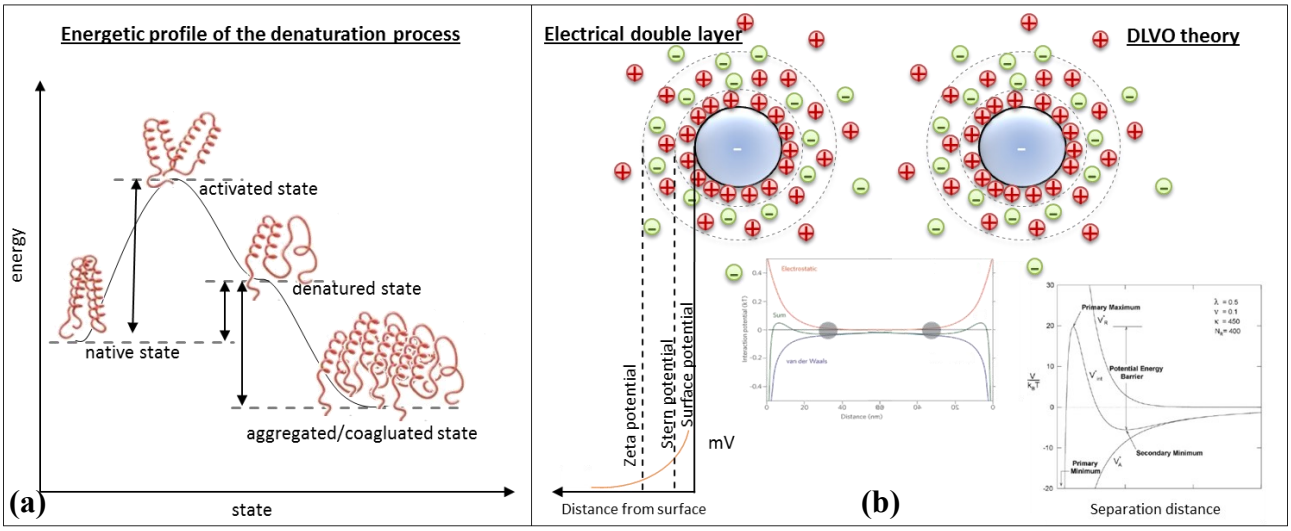

Figure 1- 3: Physical protein stabilities: conformational and colloidal stability.
(a) The energetic profile of protein unfolding, and denaturation describes the initial energy entry necessary to reach the intermediate state and the subsequent conversion to the denatured state with possible aggregation. (b) For the colloidal stability the formation of the electrical double layer around the charged particles by ions and the DLVO theory are illustrated (based on Verwey and Overbeek 1946, Jaenicke 1991, De Young, Fink et al. 1993, Israelachvili and Wennerstrom 1996, Wang 1999, Sancho 2013).

2.2. The analysis of protein stability

While dealing with biological molecules stability is one of the main challenges. For that reason, the investigation of (colloidal and conformational) protein stability and the definition of stability-indicating parameters play a crucial role. In case of pharmaceutical molecules, ICH guidelines "ICH Topic Q 1 A (R2) Stability Testing of new Drug Substances and Products" and "ICH Topic Q 5 C Quality of Biotechnological Products: Stability Testing of Biotechnological/Biological Products" pointing out the importance of stability studies as stability data packages are necessary for registration application of new molecular entities. In fact, the results of stability testing provide

evidence on the stability influencing conditions, the potential degradation pathway and help to determine drug product shelf life and a suitable process control strategy. Due to the nature of proteins a typical stability –indicating profile includes purity and molecular characterization.

For the identification of potential aggregation mechanisms and pathways, the analysis of protein unfolding processes as well as aggregation kinetics are often-used characterization approaches. The analysis of protein unfolding processes (conformational stability) may be performed exemplary by differential scanning calorimetry (DSC) or spectroscopic methods, e.g. infrared spectroscopy, Raman spectroscopy, intrinsic tryptophan fluorescence and extrinsic (thioflavin T) fluorescence measurements (Roberts 2007, Li, Weiss et al. 2009, Morris, Watzky et al. 2009, Brummitt, Nesta et al. 2011). Examples for typical established techniques applied for aggregation kinetics studies are size exclusion chromatography, native polyacrylamide gel electrophoresis, analytical ultracentrifugation or light scattering based techniques, e.g. DLS. In particular, particle detection and characterization technologies as described in chapter 3 are relevant methodologies.

Over the last years of technical developments, new technology approaches appeared in the field of biomolecule analysis. In this thesis, two novel technical approaches have been chosen to evaluate their applicability for protein unfolding and aggregation studies: the Zetasizer Helix instrument and the SwitchSENSE® technology.

Zetasizer Helix. The Zetasizer Helix instrument, manufactured by the company Malvern Instruments, combines dynamic light scattering and Raman spectroscopy – two well-established protein stability analyzing methods – in one instrument (Figure 1- 4).

The method of dynamic light scattering typically used for the determination of the hydrodynamic size (based on the particles diffusion coefficient). In addition, the principle is also used to investigate colloidal stability by the determination of the interaction parameter kD. In principle, the Brownian motion of the particles causes a time-dependent correlation of light intensity. Based on this correlation function a diffusion coefficient is determined and using Stokes-Einstein equation particles hydrodynamic diameter is calculated. The method enables the detection of particle diameters from several nanometers to a few micrometers. There are a tremendous number of publications and studies demonstrating the suitability of the method for aggregation studies. For that reason at this point only a few references are mentioned (Fletcher 1976, Dathe, Gast et al. 1990, Bogdanovic, Colon et al. 2010, Makowski, Berkowitz et al. 2015, Bansal, Gupta et al. 2019).

The method of Raman spectroscopy is typically applied to investigate structural elements of molecules. In case of protein structure, analysis specific markers for secondary and tertiary structure are in the focus. In particular, the analysis of peak positions and ratios considering amide I and amide III peaks as well as characteristic aromatic side chain peaks such as for tyrosine (Tyr) and tryptophan (Trp) is performed. In addition, disulfide bond markers are determined. Consequently, this method is also used to investigate conformational stability. The application of Raman spectroscopy for proteins is well described and reviewed by several authors (Benevides, 2003; Krishna, 2016; Rygula, 2013; Wen 2007). Some typical markers that are analyzed by the provided instrument software are summarized in Table 1.

Table 1: Overview typical protein markers in Raman spectra.

Raman Shift (cm^{-1})	Parameter	Structure element	Structure motif
Secondary structure			
1580-1720	Position + Intensity	Amide I band	1680 β-turn 1670-1680 β-sheet + β-barrel 1650-1655 α-helix 1640 loose β-sheet
1235-1340	Position + Intensity	Amide III band	1300 - 1340 α-helix 1260 disordered 1235 - 1250 β-sheet
930-950	Position + Intensity	Skeletal C-C stretch backbone	α-helix
Tertiary structure (aromatic side chains)			
1360/1340	> 1	Tryptophan Fermi Doublet (W7)	Indole ring in hydrophobic environment or in contact with aliphatic chains
	< 1	Tryptophan Fermi Doublet (W7)	Indole ring in hydrophilic environment or exposed to aqueous medium
1550	Position	Tryptophan dihedral angle (W3)	The angle between the indole ring and the peptide bond plane
870-885	Position	Tryptophan Hydrogen bonding (W17)	883 non H-bonded 877 medium strength 871 strong H-bonded
760		Tryptophan (W18)	Cation-π interaction
850/830	0,25	H-bonding of tyrosine	Donor of strong H-bond
	1,25	H-bonding of tyrosine	Donor and acceptor of strong H-bond; exposed to aqueous environment
	2,5	H-bonding of tyrosine	Acceptor of strong H-bond
	6,7	H-bonding of tyrosine	No H-bond, buried in hydrophobic environment
1000-1004	Position	Phenylalanine ring breathing mode	Used as reference for normalization of the Raman intensity (insensitive to environment changes)
Disulfide bond conformation			
508-512	Position	S-S stretch	GGG conformer
523-528	Position	S-S stretch	GGT conformer
540-545	Position	S-S stretch	TGT conformer

The instrument has been demonstrated in a few studies as versatile tool for protein analysis as well as further applications (Amin, Blake et al. 2014, Kádár, Naue et al. 2014, Lewis, Qi et al. 2014, Zhou, Qi et al. 2015).

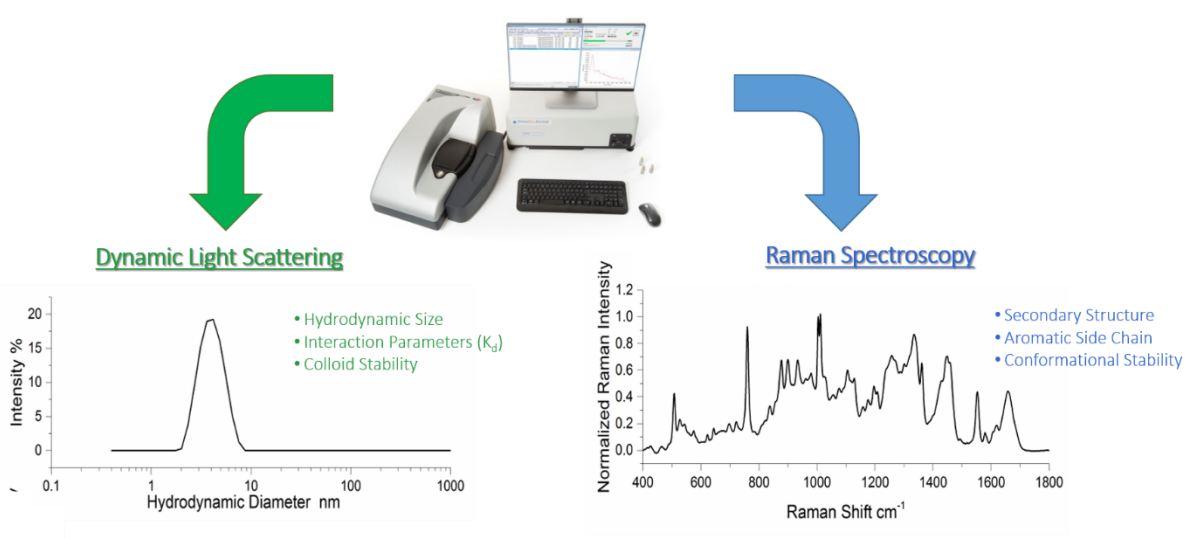

Figure 1- 4: Introduction Zetasizer Helix instrument.
The Zetasizer Helix instrument and the output of dynamic light scattering (DLS) and Raman spectroscopy are illustrated.

SwitchSENSE®. The SwitchSENSE® technology is a chip-based technology developed by the company Dynamic Biosensors in Martinsried (founded 2011). The DNA-based biosurface system was initially developed to investigate molecular interactions, such as binding kinetics and affinities or enzymatic activities. During the last years it was demonstrated that the system is a highly potential and versatile platform for a wide range of further applications. Some examples are the investigation of protein melting processes, thermodynamics, conformational changes and the determination of protein diameters (small proteins) (Kaiser and Rant 2010, Rant 2012, Langer, Hampel et al. 2013, Langer, Kaiser et al. 2014, Langer, Schräml et al. 2015, Lux, Langer et al. 2015).

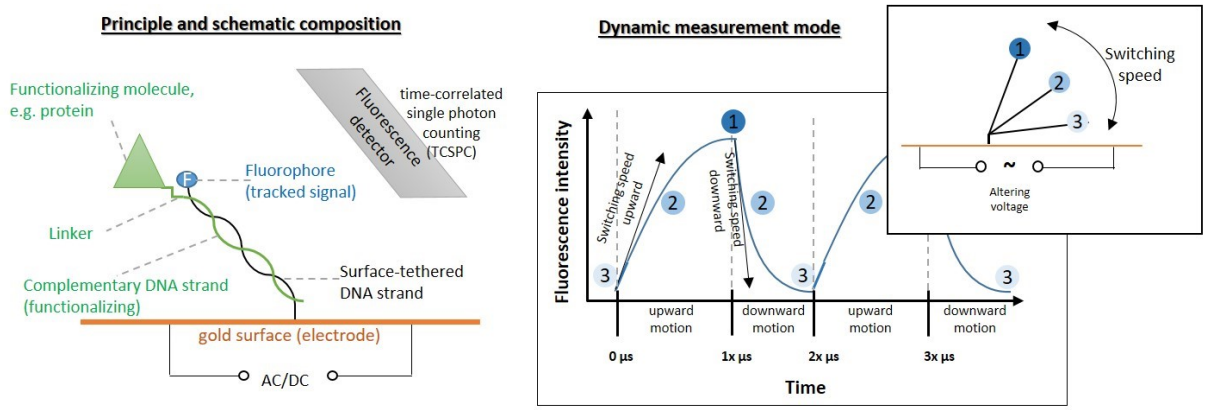

Figure 1- 5: Introduction and schematic overview SwitchSENSE® technology.
Left: Schematic composition of the technology principle illustrating the negatively charged DNA-fluorophore strand (black) tethered to a gold electrode surface conjugated to the complementary functionalized DNA (green) with the signal detection via a fluorescence detector. *Right:* Illustrating the dynamic measurement mode an alternating voltage is applied to the gold electrode causing the "switching" motion of the DNA nanolever (1, 2, 3). The corresponding signal, meaning the fluorescence signal over time, depending on the DNA nanolever position (1, 2, 3) is shown describing the switching speed enabling for example size determinations.

The main functional element of the technology is the specific chip containing four flow cells with six measurement electrodes (gold electrodes). DNA nanolevers are spotted to the gold surface and function as a switchable biosurface. The schematic composition is illustrated in Figure 1- 5 (*left*): A first single strand DNA (black) is tethered to the gold surface and carries the signal molecule, a fluorophore (F). Applying the DNA hybridization principle, a second complementary DNA strand is bound and is used to functionalize and specify the biosensor for the purpose of the assay. Depending on the assay strategy/ set-up, molecules, e.g. proteins, are coupled to the second DNA strand either covalently via thiol or amine groups or non-covalently via specific tags, e.g. His-tag. For the technology, DNA molecules consist of 24 to 96 base pairs and they are negatively charged. Generally, the technology enables two measurement modes: static and dynamic. The static measurement mode uses fluorescence proximity sensing and is only applicable if the analyte quenches the fluorescence signal by binding to the functionalized surface. In this case, the electrode is constantly negatively charged. The evaluation of the assay is only based on the differences in the detected fluorescence intensities. The static set up enables typical binding assays as they are also performed on other systems with orthogonal principles. The unique mode of the technology is the dynamic measurement mode. An alternating voltage at the electrode causes an alternating charge of the gold surface. In consequence, the DNA nanolever is electrically triggered

to oscillate with a certain frequency. During this movement of the nanolever the fluorescence signal of the attached fluorophore changes depending on the distance to the gold surface:

(1) Close to the surface, i.e. smallest angle between nanolever and gold surface, the fluorescence signal is quenched due to energy transfer on the gold surface

(2) In the upward position of the nanolever, i.e. largest angle between nanolever and gold surface, the maximal fluorescence signal is measured.

The evaluation of the assay is based on the differences in the detected fluorescence intensities and the resulting speed of motion. DNA nanolevers without bound molecules or with small bound molecule show a rapid motion and larger bound molecules show a slower motion. The dynamic set up enables exemplary size determinations (Kaiser and Rant 2010, Rant 2012, Langer, Hampel et al. 2013, Langer, Kaiser et al. 2014).

The assay is performed in three steps: In the first step the assay and the biosurface is prepared. On prepared chips the single stranded DNA-fluorophore molecules anchors on the detection spot. For surface functionalization, the next step is the hybridization with the functionalized complementary DNA conjugates resulting in a biosurface of double stranded DNA. In the second step the specific assay is performed as real time analysis. Exemplary for binding studies, first association is analyzed in presence of the analyte and subsequent the dissociation is analyzed, and binding kinetics can be studied. The third step is the regeneration of the chip after the assay by removing the DNA-conjugates.

The SwitchSENSE® technology has been demonstrated to be suitable in many fields, aiming the investigation of a high variety of molecules and biological processes. The usage of the DNA molecule as a versatile molecule allowing a highly potent and flexible system for a high number of possible applications.

2.3. Protein aggregation: Pathways, mechanisms and kinetics

The process of protein aggregation (intrinsic protein aggregation) is a process “by which protein molecules assemble into stable complexes composed of at least two proteins” and the consequence of colloidal instability of the protein suspension (Roberts 2007). It is caused either by chemically or physically alteration of the native monomer or an unfavorable protein environment (ionic strength, pH, etc.) leading to initially reversible but later irreversible agglomerates, so called

protein aggregates. The non-native aggregation process and its mechanisms are still highly debated, and the major challenge is that aggregation can be caused by various factors and happen via many pathways.

A common description of aggregation processes is based on a two-stage mechanism with an initial nucleation stage and a subsequent aggregation growth stage (Wang and Roberts 2010). Roberts described the process more detailed as a multi-stage process containing up to five stages (Figure 1- 6):

(1) ensemble of interconvertible monomer conformations
(2) first reversible association of at least two "reactive" monomers
(3) general nucleation step that creates an irreversible aggregate
(4) first growth stage of monomer addition to the nucleus
(5) further growth/condensation step of aggregate-aggregate association

The first stage describes the occurrence of active monomers. Depending on the mechanism and the pathway "active" monomers are either natively folded, conformational-altered or chemically-altered monomers that result from protein instabilities. In the second stage, first reversible associates are formed leading to prenuclei, such as dimers or low molecular oligomers. These prenuclei undergo further monomer addition and possibly conformational changes and become the irreversible nucleus (stage 3). In the last two growth stages the increase of the nucleus mass is performed by monomer addition (stage 4) and further aggregate-aggregate association (stage 5) (Roberts 2007). In addition to primary aggregation pathways, secondary pathway may happen, e.g. secondary nucleation or growth processes as well as fragmentation, dissociation and degradation (Cohen, Vendruscolo et al. 2012).

The whole aggregation process, however, is specific for every protein and depends highly on the applied stress and the consequent mechanism. In the major part of aggregation processes it is mainly caused by "incorrect folding", structural unfolding and macromolecular crowding as internal factors (i.e. due to high protein concentrations) or perturbation of the native structure due to damaging external factors (Manning, Chou et al. 2010). For these reasons, the competition of unfolding and aggregation plays a crucial role in most aggregation processes determining aggregation rates. Aggregation rates and the identification of the aggregation rate limiting steps is important to better understand the processes and to control such processes. Typical rate-limiting steps are indicated in Figure 1- 6 by *[1]* unfolding step, *[2]* formation of the irreversible nucleus,

[3] addition of monomers and *[4]* the aggregate condensation step. Examples for often-mentioned aggregation mechanisms are reversible association, nucleation controlled mechanism, prion aggregation, amyloid aggregation, subsequent monomer addition or surface and interface-introduced aggregation mechanism (Morris, Watzky et al. 2009, Philo and Arakawa 2009). The resulting aggregate characteristics, e.g. structure or morphology, depend highly on the pathways and mechanisms. In some cases, amorphous precipitates occur, other mechanisms carry out gels or more structure filaments and fibrils. The amyloid formation is one often described process and important to understand some diseases (Cohen, Vendruscolo et al. 2012). In any case, these aggregates show reduced or no activity, lose efficacy and have medical risks such as increased immunogenic potential.

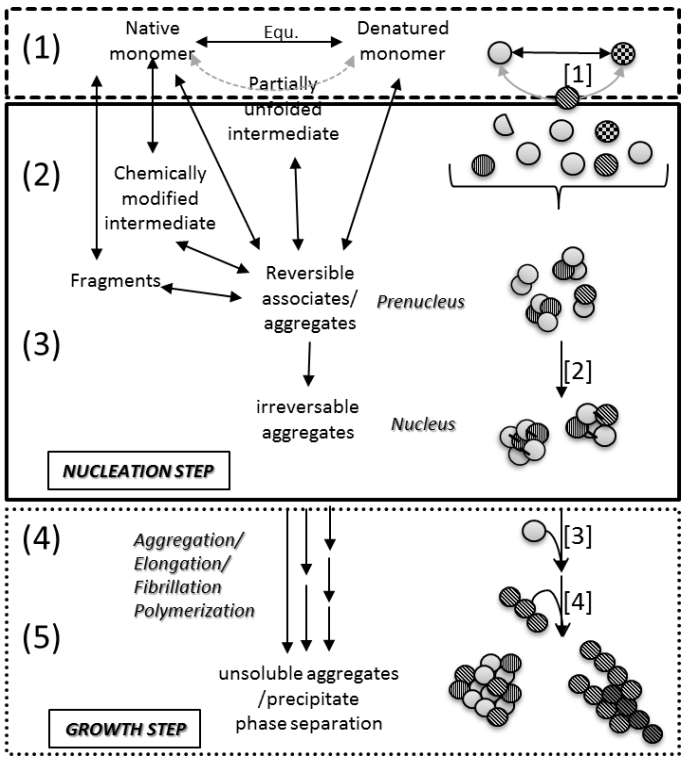

Figure 1- 6: Aggregation pathways and mechanisms.
The multi-stage process of aggregation and its five stages are illustrated. Out of the thermodynamic equilibrium native folded, partially unfolded and denatured monomers are present in the suspension as active monomers. In addition, stress applications may lead to chemically-modified monomers or fragmentation. These native and altered monomers ensemble in stage 2 and form reversible associates that become irreversible nuclei in the nucleation step. In the 4th stage growth of the aggregate occurs by monomer addition and in a possible 5th stage aggregate-aggregate condensation happens. The numbers [1]-[4] indicate potential rate-limiting steps (based on Roberts 2007).

Kinetic profiles of the reaction time course and phenomenological models give no microscopic and molecular mechanism but may give first hints of these mechanisms. For more detailed analysis, mathematic models are used. A great summary of such models is given by Morris et al. (Morris, Watzky et al. 2009). For the description of in-vitro non-native aggregation mechanisms most commonly the Finke-Watzky 2-step model as wells as extensions of the Lumry model are applied (Morris, Watzky et al. 2008, Oliva, Llabres et al. 2015, Singla, Bansal et al. 2016). The Lumry-Eyring model describes a simple 2-step, non-native aggregation mechanism, where the rate-limiting step is reversible conformational transition leading to irreversible conglomeration into aggregates. Two prominent extensions of the model are the Extended Lumry-Eyring (short ELE) - distinguishing between different kinds of aggregated molecules based on the number of monomer chains and intrinsic kinetics of aggregation - and the Extended Lumry-Eyring with Nucleated Polymerization (short LENP) – considering additionally nucleated polymerization processes (Roberts 2003, Andrews and Roberts 2007, Li and Roberts 2009). A model, more reliably used for in-vivo aggregation as involved in Alzheimer disease or Parkinson, was developed by the Knowles Lab (Meisl et al. 2016; Meisl et al 2018). Out of this work Meisl et al. derived a platform (Amylofit) for kinetics mechanism calculations and descriptions (Meisl, Kirkegaard et al. 2016). In consideration of monoclonal antibodies, Oliva et al. demonstrated that the Finke-Watzky 2-step model was suitable to fit Bevacizumab aggregation kinetics after thermal and mechanical stress application (Oliva, Llabres et al. 2015). Singla et al., however, showed that the best and most reproducing fit for a different IgG1 mAB aggregation kinetics was achieved by LENP and ELE-model, while Finke-Watzky 2-step model obtained the worst fitting results.

2.4. Clinical risks of therapeutic protein aggregates

Degradation products of therapeutic proteins in biopharmaceutical formulations, such as protein fragments and aggregates, represent potential medical risks for the patients. Major risks of protein aggregates are vascular occlusion and embolism or adverse immune responses.

Aggregates in the micrometer size range that are directly applied intravenous may function as embolus and cause clogging of blood vessels (embolism) (Figure 1- 7, left). The consequences are blockage of blood flow in veins and arteria infarctions or tissue death. Depending on the location

of the embolism, serious diseases like stroke (brain), heart or pulmonary infarct may appear to name just a few.

The immunogenicity risks of therapeutic proteins and their aggregates have been investigated intensively in the last decade (Hermeling, Crommelin et al. 2004, Fradkin, Carpenter et al. 2009, Filipe, Jiskoot et al. 2012, Jiskoot, Randolph et al. 2012, Johnson and Jiskoot 2012, Joubert, Hokom et al. 2012, Brinks, Weinbuch et al. 2013, Ahmadi, Bryson et al. 2015, Freitag, Shomali et al. 2015, Shomali, Tanriverdi et al. 2015, Jiskoot, Kijanka et al. 2016, Moussa, Panchal et al. 2016). Although antibodies are natural components of the immune system, humanized mABs and mAB aggregates can also function as antigens. While for vaccines immune responses are desired, therapeutic proteins aim to support the immune system rather than induce one. Immunogenicity, however, is still one of the major challenges (Moussa, Panchal et al. 2016). The reason is that therapeutic antibody aggregates show characteristics that foster interactions with the immune system. Most likely, the repetitive nature of aggregates consisting of monomer units (native/modified) mimics pathogen-associated molecular pattern (PAMP) and is recognized by receptors of the immune system, e.g. toll-like receptors. In addition, the Fc parts of the antibodies are recognized by Fc gamma receptors. All these receptor interactions lead to cytokine release and via phagocytosis to the occurrence of antigen-presenting cells (APCs), in particular activated dentritic cells. This was demonstrated by in-vitro experiments (Moussa, Panchal et al. 2016). Consequences of the early stage responses of the innate system are inflammation and the presence of APCs (Figure 1- 7, center). The antigen-specific immune response is induced by the uptake, processing and presentation of the antigen by APCs. Naiv T-cells are activated by the interaction with the APCs and in a T-cell dependent mechanism (TD) B-cells are converted into plasma cells secreting ADAs and memory B-cells for a second application. Studies have also shown that a T-cell independent mechanism (TI) exists. In this process the activation and conversion of B-cells is realized either by crosslinking of several B-cell receptors enabled by the repetitive structure or coactivation of B-cell receptor and toll-like receptor of a B-cell (Figure 1- 7, right). The formation of ADAs and memory cells specifically against the therapeutic antibody disturbs and inhibits a further effective, safe and prompt treatment with the biopharmaceutical.

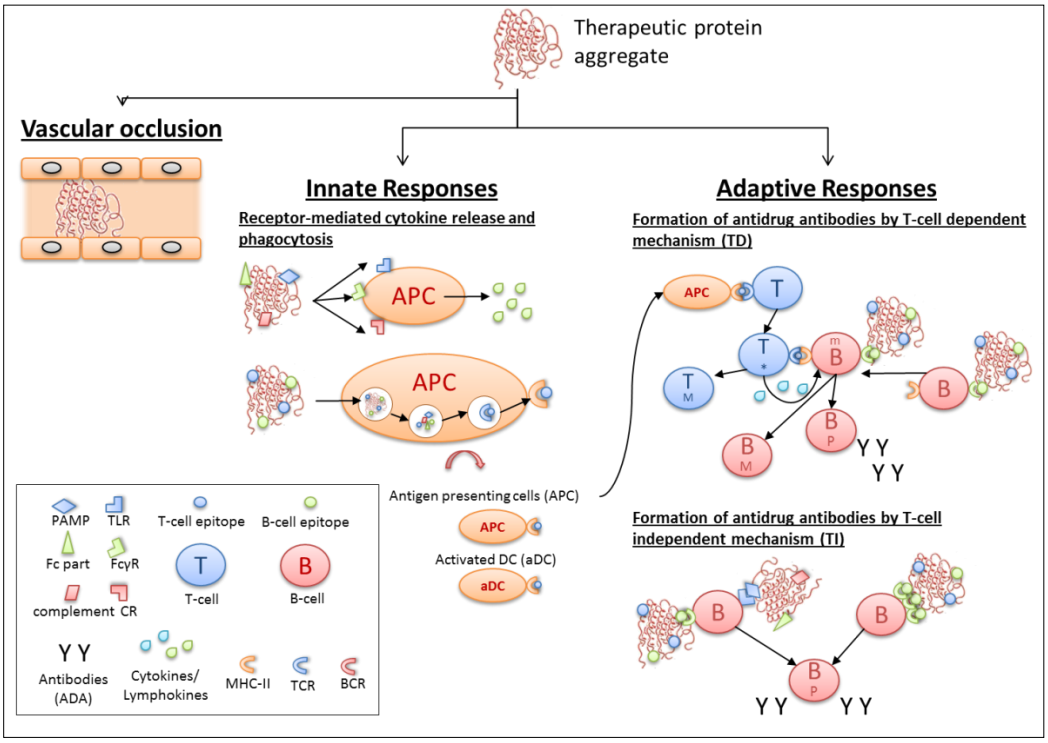

Figure 1- 7: Medical risks of therapeutic protein aggregates.
The major medical risks of therapeutic protein aggregates reaching the patient´s body are vascular occlusion and undesired immunogenic reactions. The aggregates in the body are treated like pathogens due to structural similarities (PAMP).The early stage innate response due to the interaction of aggregates with typical receptors (toll-like receptor TLR, Fc gamma receptor FcγR, complement receptor CR) leads to cytokine release, phagocytosis of the aggregate and the formation of antigen-presenting cells (APC) for the adaptive immune response. For the subsequent formation of antidrug antibodies (ADA) two mechanisms have been defined: The T-cell dependent (TD) and T-cell independent mechanism (TI). In the TD mechanism T-cells get activated and release lymphokines. After B-cell recognition of aggregate B-cell epitope, the released lymphokines initiate the maturation of B-cells to plasma cells secreting antibodies and to memory B-cells. The maturation to ADA secreting plasma B-cells is also achieved during the TI mechanism. For that purpose B-cell receptors (BCR) are cross-linked or coactivation by TLR and BCR is performed (based on Moussa, Panchal et al. 2016).

3. Particle detection and characterization technologies

3.1. Particles and aggregates as critical safety and quality attributes (CQAs) of biopharmaceuticals

Particle detection and characterization play an essential role in diverse applications. In many industrial fields, particles and particular matter have enormous influence and essential effects on product quality and safety. In some applications particle properties have to be defined to achieve desired product properties, e.g. in chocolate production. In other cases, e.g. for biopharmaceuticals, particles have to be detected, identified and in most cases avoided to guarantee patient´s safety and product quality.

As recently discussed by A. Shanley in BioPharm International, aggregation and resulting particles is one of the crucial critical quality attributes (CQAs) for biopharmaceuticals and even found as a top concern, besides glucose concentration and amino acids (Shanley 2019). From the safety perspective particulate matter of any kind in biopharmaceutical formulations, e.g. protein aggregates or residual glass particles, need to be detected and removed (Langille 2013, Shomali, Freitag et al. 2014, Shomali, Tanriverdi et al. 2015). Recent studies showed that undetected particle contaminations reaching patients may contribute to vascular occlusion or induce immunogenic reactions (Shekunov, Chattopadhyay et al. 2007, Langille 2013, Freitag, Shomali et al. 2015). Such adverse reactions occur already by the presence of small amounts of protein particles, but may have strong immunogenic potential (Ahmadi, Bryson et al. 2015). Freitag et al. additionally showed a correlation between immune reactions and the particle/aggregate characteristics (Freitag, Shomali et al. 2015). Identifying and characterizing particles, indeed, enables both assessing their risk to the patient and tracing their origins (Li, Cao et al. 2014). Such studies highlight the need for highly sensitive and accurate detection and characterization techniques to ensure safety and prevent medical risks (Hermeling, Crommelin et al. 2004, Filipe, Jiskoot et al. 2012, Johnson and Jiskoot 2012, Brinks, Weinbuch et al. 2013, Ahmadi, Bryson et al. 2015, Freitag, Shomali et al. 2015, Jiskoot, Kijanka et al. 2016).

Medical/pharmaceutical products underlie strong authority regulations and guidelines for the development, production, characterization and control to address safety, quality and efficacy issues. The regulatory framework is given for example by EMA or FDA guidelines (advices without legal force) and European or US Pharmacopeia (legal force, standardized specifications) (Cavagnaro

2013). In contrast to conventional pharmaceuticals (small chemical molecules, NCE), the biopharmaceutical guidelines follow a more case-by-case approach due to their more complex nature, action and reactions. All regulatory guidelines, however, expect full physicochemical characterization and the identification of purity and impurities. There are generally three impurity types classified: product-related impurities (different variants of the product, e.g. aggregates or fragments), process-related impurities (e.g. cellular components) and contaminants (e.g. microbes). One of the major issues is the presence and characterization of protein aggregates as product-related impurity (Bracewell and Smales 2013, Agency 2016). ICH Topic Q5C "Stability testing of Biotechnological/Biological Products" as well as ICH Topic Q6B "Specifications: Test Procedures and Acceptance Criteria for Biotechnological/Biological Products" illustrated exemplary the need for orthogonal and suitable analytical methods for impurity detection and product characterization. USP<1787> and <1788> describe methods for particle analysis in biopharmaceuticals, embracing methods both new (e.g., flow microscopy imaging) and established (e.g., light obscuration) (USP<1787> 2015). So far regulatory authority specifications in the subvisible particle size range (10 µm and 25 µm) are only given for light obscuration in USP<787> or <788> for parenteral formulations (USP<787> 2014, USP<788> 2014). Both USP chapters set limits for particle sizes and concentrations and define the detection protocol and the instrument based on the current scientific and technical knowledge. To comply with regulations like these, companies have to be prepared and stay up to date considering technical developments.

3.2. Overview about common principles applied for particle analysis, detection, and characterization

Commercially available particle analysis instruments are based on few physical principles (Syvitski 1991, Shekunov, Chattopadhyay et al. 2007, Kathe, Henriksen et al. 2014). Some of them are based on natural phenomena well known for hundreds of years; others, on principles that have emerged over the last decades. The most prominent principles are microscopy as most direct principle, particle-light interactions as basis of variable applications, electric zone sensing and separation-based techniques, e.g. centrifugation. An overview and short description is given in Figure 1- 8 and Figure 1- 9.

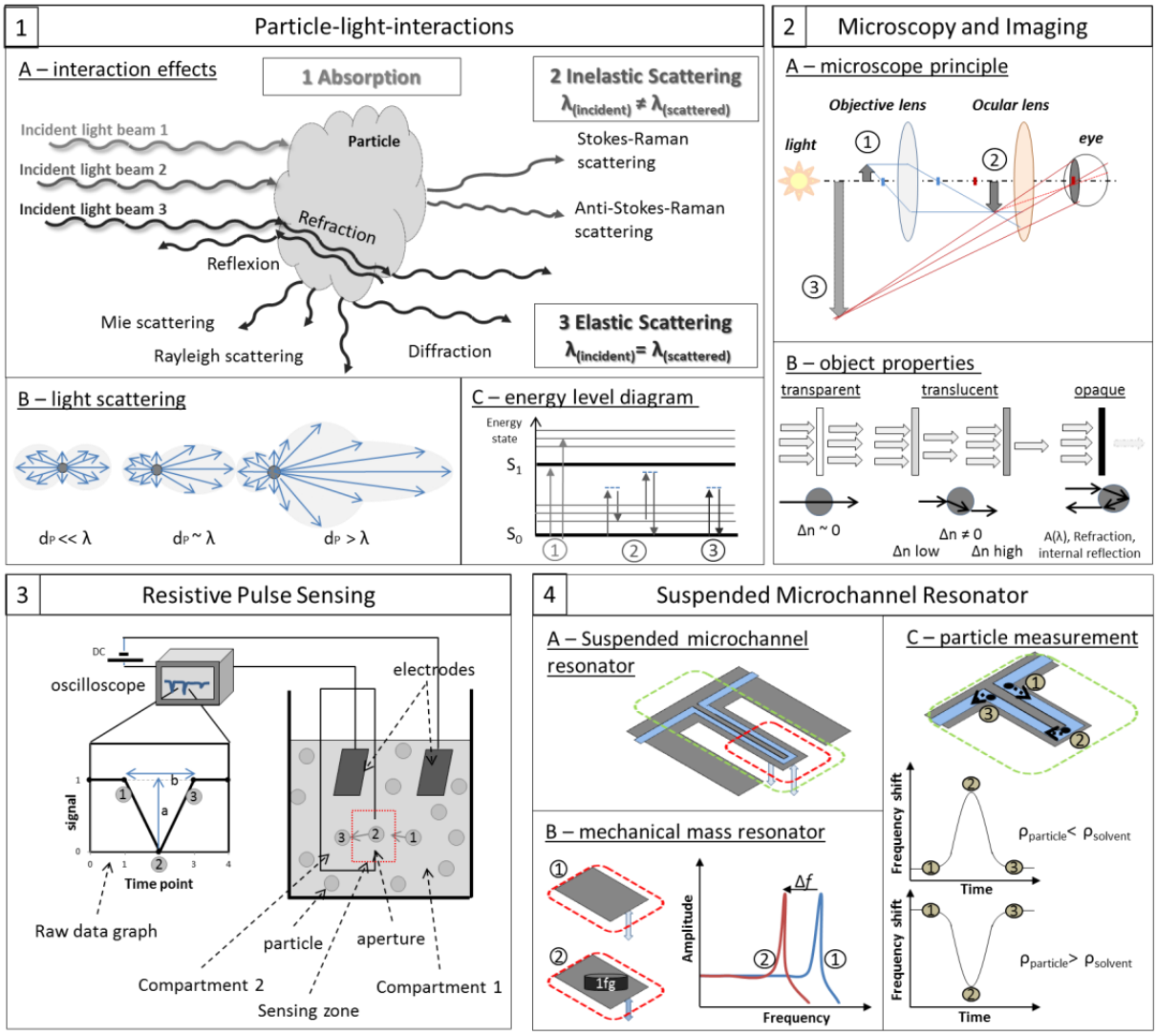

Figure 1- 8: Schematic illustration of important particle detection principles I.
The major principles of particle detection techniques, particle-light interactions (1), microscopy and imaging (2), resistive pulse sensing or Coulter principle (3), suspended microchannel resonators (4), separation principles/approaches (5), sedimentation and centrifugation (6) and further established separation techniques (7) are summarized. (1a) There are different effects of particle-light interaction after an incident light beam encounters a particle. (1b) Based on the Mie theory light scattering intensities in a spatial cross area are characteristic for specific particle sizes (d_P) depending on the wavelengths of the incident light beam. (1c) The final effects are determined by the energetic state the photon causes in the molecule. (2a) Microscopic magnification of tiny objects is based on a complex optical system. A reel image 2 of the object 1 is achieved by the objective lenses. This image is subsequently magnified by the ocular lenses to the virtual image 3. (2b) Depending on the optical properties of particles, e.g. the refractive index and its difference to the surrounding fluid, these particles show different effects and behavior by light interactions: transparent, translucent or opaque. (3) A coulter counter consists of two compartments filled with an electrolyte and connected by a small pore. In each compartment an electrode is present, and a direct current is applied. Adding the particle to one compartment, they pass (1->2->3) the pore inducing a resistive pulse in the applied current. This pulse is monitored and gives information about the size by its amplitude, *a*, and its shape by the blockage duration, *b*. Furthermore, the pulse event frequency is correlated to the particle concentration. (4a) Schematic configuration of a suspended microchannel resonator (SMR). (4b) Already the addition of 1 femtogram causes a frequency shift. (4c) If particle pass the microchannel the frequency changes. Depending on the density difference between particle and fluid peaks appear either positive or negative.

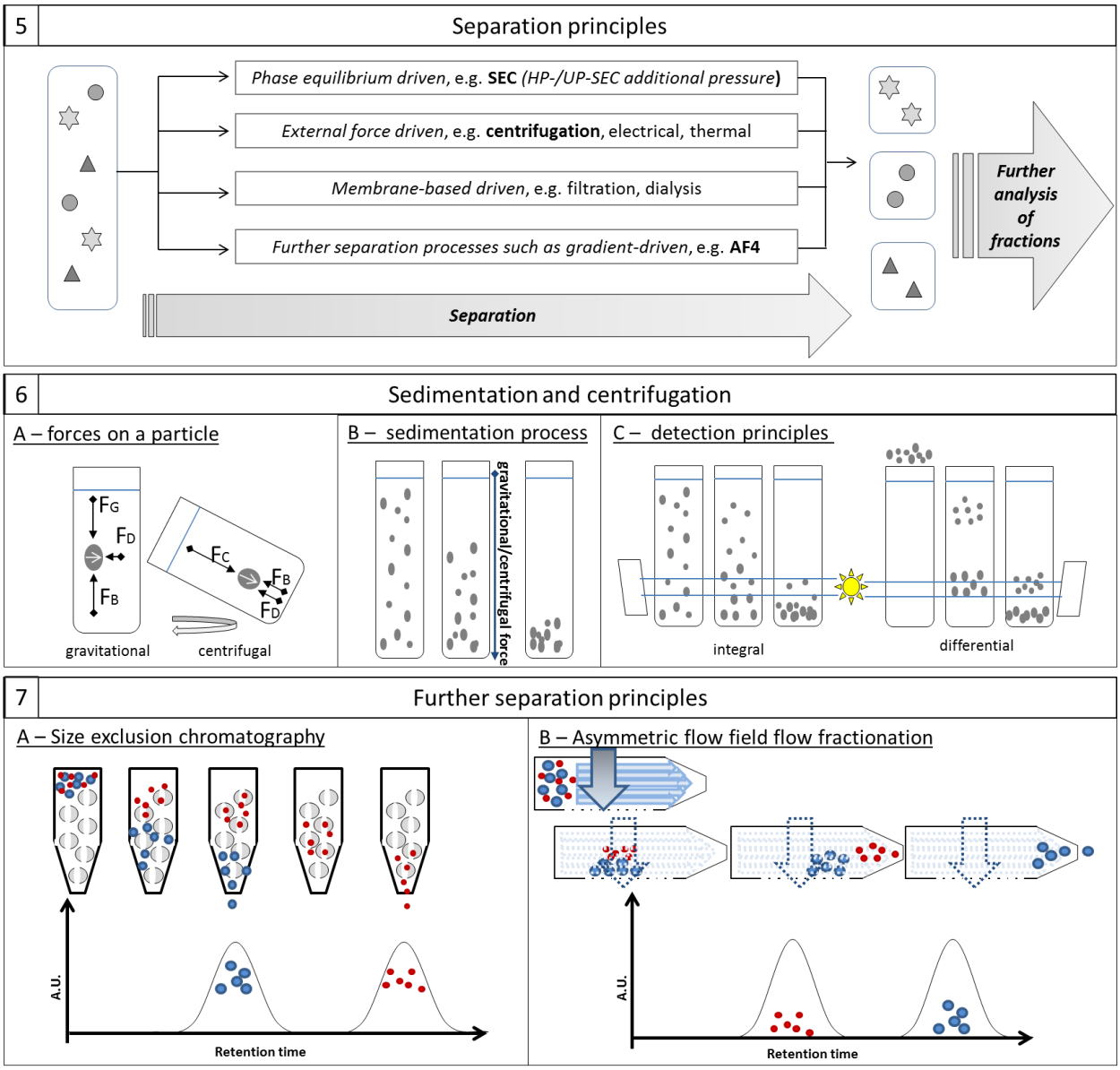

Figure 1- 9: Schematic illustration of important particle detection principles II.
(5) Overview about the general separation process and typical principles and approaches. (6A) The phenomenon of sedimentation/centrifugation is caused by the balance of three forces: F_G gravity force, F_D drag force and F_B buoyancy force. For centrifugal sedimentation the gravity force is replaced by the centrifugal force F_C. (6B) During naturally occurring sedimentation processes, particles in suspension settle down (gravitational or centrifugal) in the direction of the gravitational or centrifugal force with a sedimentation velocity depending on their particle size and density. (6C) The sedimentation can either be detected and analyzed by integral method (left) or by a differential method (right). (7A) The separation principle of size exclusion chromatography based on the molecular size is illustrated. The sample passes a resin containing pores and depending on particle size they either enter this pore leading to a delayed retention compared to larger particles that just flow through without entering. (7B) The separation principle of asymmetric flow-field flow fractionation based on hydrodynamic diffusion behavior is illustrated. The sample passes a channel with pores moving in a vertical flow. The application of a cross flow causes a separation of smaller particles that move faster in the parabolic flow and the larger particles closer to the channel wall.

3.3. Properties and challenges of biopharmaceutical samples and protein particles

Despite the large array of particle techniques available, the detection and characterization of biological particles appear still highly challenging due to their large size range and strong variety in particle concentration. The active molecule forms, e.g. antibody monomers, have a size in the low nanometer range of about 10 nm and show a non-spherical shape (native protein "Y-shaped") and thus reaching the lower limits of common techniques (Wang, Singh et al. 2007). Unfunctional or damaged molecule forms, such as associates or aggregates, caused by protein instabilities, can vary from dimers to extremely large multimeric units with up to over 100 µm diameters reaching the upper limits of common detection techniques (Patel, Lau et al. 2012, Ripple and Dimitrova 2012, Corvari, Narhi et al. 2015, Vasudev, Mathew et al. 2015). The most challenging properties of protein samples can be summarized as following (Figure 1- 10):

(1) A first aspect is the occurrence of *unique single-particle specific properties* that can vary in a broad range, are hard to measure, but often essential for correct size determinations. Examples for such specific properties are refractive index (RI) – essential for most light interaction principles – and density for sedimentation or mass-based processes (Bargieł, Ford et al. 2005, Beekman, Shan et al. 2005, Zolls, Gregoritza et al. 2013, Hu and Ripple 2014, Folzer, Khan et al. 2015). Critical for protein particles is that their RI may be similar to the RI of the surrounding and therefore the particles appear more transparent/translucent, causing low optical contrast and thus challenging optical methods (Zolls, Gregoritza et al. 2013).

(2) A second aspect is that the protein suspension itself is highly heterogeneous and polydisperse, covering size ranges up to six orders of magnitude (Patel, Lau et al. 2012, Ripple and Dimitrova 2012, Corvari, Narhi et al. 2015, Vasudev, Mathew et al. 2015). As the degradation pathway of each particle might differ slightly, each single particle may show individual properties, e.g. structure, size or altered chemical or physical properties. In addition, the composition with a large concentration of small particles (monomers, dimers, oligomers) and small composition of large particles makes light scattering techniques inappropriate due to non-linear increase of the light scattering intensity.

(3) Third, one can state that the protein itself as well as the protein suspension are a highly complex, dynamic and transient systems. The protein suspension is highly sensitive to

(micro-)environmental changes and sample handling and preparation as well as measurement conditions may cause destructive effects and change the actual sample properties (Kim, Randolph et al. 2002, Kim, Randolph et al. 2006, Kueltzo, Wang et al. 2008, Gerhardt, Bonam et al. 2013).

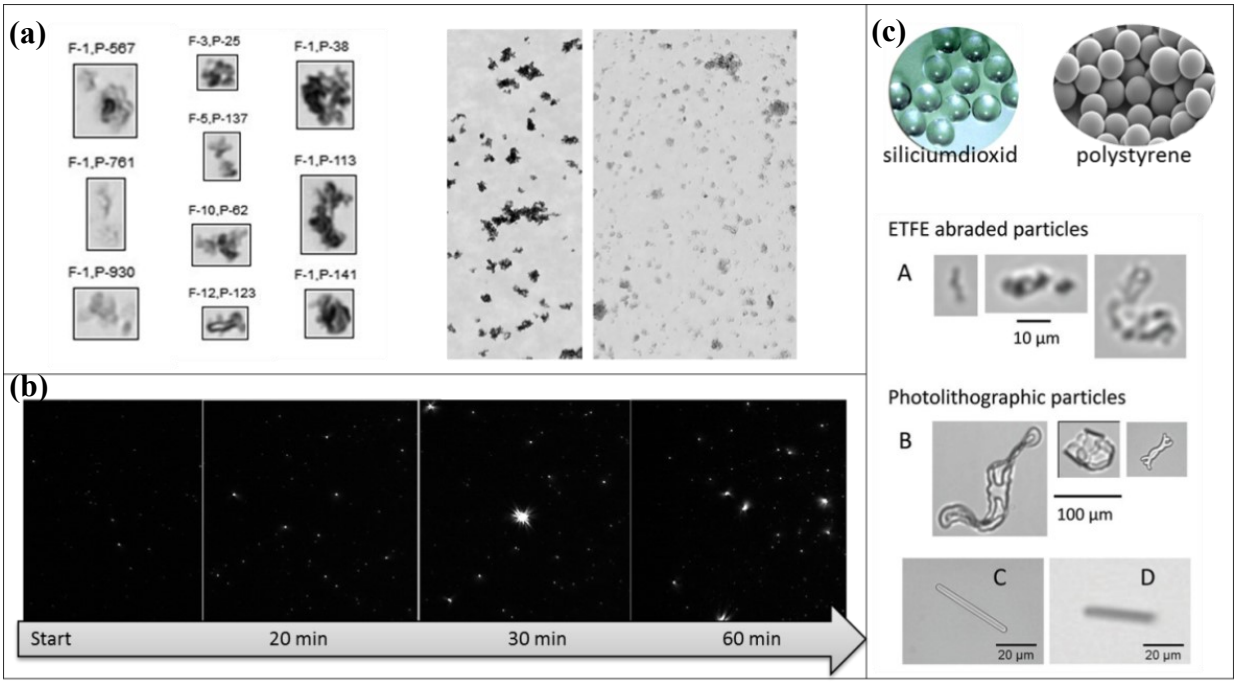

Figure 1- 10: Protein particle properties and calibration standards.
The challenges of protein particles and their highly divers properties are illustrated: (a) The shown protein aggregates of the same therapeutic antibody highlight the great diversity in single particle properties like refractive index, shape or structure. A microscopic image of the complete stressed protein sample illustrates the highly polydisperse composition in the micrometer range. (b) After the application of stress, the aggregation process was monitored by Nanoparticle tracking analysis over 60 minutes illustrating the kinetics and dynamics of protein suspensions. (c) Calibration standards, like siliciumdioxid or polystyrene particles, differ enormously from protein particles in shape and structure as well as refractive index. The National Institute of Standards and Technology (NIST) approaches using abraded ethylene-tetrafluoroethylene (ETFE) and photolithographic particles, in contrast, mimic properties of the protein particle better (based on MFI results, NTA results and Ripple and Dimitrova 2012, Ripple, Wayment et al. 2012, Ripple, Montgomery et al. 2015).

(4) A fourth point is the challenge of investigating highly concentrated liquid formulations. Such samples often have low volumes (below 1 ml), higher viscosities and high basic scattering effects (overlapping) and there is a lack of suitable analytical techniques (Hall and Minton 2003, Ellis and Minton 2006, Alford, Kendrick et al. 2008, Alford, Kendrick et al. 2008, Alford, Kwok et al. 2008, Garidel, Blume et al. 2015, Nicoud, Lattuada et al. 2015, Pindrus, Shire et al. 2015).

(5) A last point mentioned in this consideration is the lack of an appropriate protein standard that mimics the protein properties. The fact, however, that protein particles show a great variety of properties, challenges the search additionally. Efforts have been made by the National Institute of Standards and Technology (NIST) over the last years. Some promising examples are abraded ethylene-tetrafluoroethylene (ETFE) particles and photolithographic particles as shown in Figure 1- 10 (Ripple and Dimitrova 2012, Ripple, Wayment et al. 2012, Ripple, Montgomery et al. 2015).

3.4. Particle detection and characterization techniques established in the biopharmaceutical field

Today a vast number of particle detection and characterization techniques exists for all types of particles aiming the determination of innumerous properties based only on a few principles (see 3.2). For pharmaceutical purposes, especially the properties *particle size* and *particle concentration* determinations are of high importance. Reviewing medicine authority regulations and published studies for biopharmaceuticals confirms these important roles (Haskell 1998, Jin, Heller et al. 2009, Hirn, Semmler-Behnke et al. 2011, USP<787> 2014).

Particle size can be directly correlated to aggregation/agglomeration or suspension instability (Kim, Randolph et al. 2002, Frieden 2007, Morris, Watzky et al. 2009, Philo and Arakawa 2009, Sanchez-Ruiz 2010, Nicoud, Arosio et al. 2014). In addition, particle size affects many aspects of particle behavior (De Jong, Hagens et al. 2008, Koide, Asai et al. 2008, Jin, Heller et al. 2009, Hirn, Semmler-Behnke et al. 2011, Johnson and Jiskoot 2012, Rong, Zhou et al. 2013, Wang, Li et al. 2013, Slutter and Jiskoot 2016). Examples are that a formulation's in vivo performance can be regulated by controlling particle size or the correlation between size and cellular uptake efficiency of nanoparticular matter (Haskell 1998, Jin, Heller et al. 2009, Hirn, Semmler-Behnke et al. 2011). From medical perspective, larger particles increase the incidence of vascular occlusion, and so must be excluded from parenteral preparations (Albrechtsson, Hansson et al. 1977, Bernard, Obermiller et al. 1993, Zheng, Bai et al. 2014). Furthermore, particle sizes are easily detectable by various orthogonal techniques, e.g. dynamic light scattering, coulter counters or analytical centrifuges. Particle concentration determinations remain an option for comparing samples and observing small changes to the system and to overcome the spatial and time limitations preventing

robust real-time detection of every particle at every moment (Haskell 1998). In addition, concentration considerations are essential for estimating viscosity and predicting the behavior of highly concentrated liquid formulations (HCLFs) (den Engelsman, Kebbel et al. 2012, Wagner, Reiche et al. 2013, Karow, Gotzl et al. 2015). Further particle properties of interest include *particle shape*, *surface charge* or *particle structure*. These properties gaining increasing importance in the characterization of particles, e.g. to differentiate particle materials or define the particle origin.

Biopharmaceutical applications and samples, however, have unique and challenging properties limiting the suitable methods and techniques (see 3.3). A selection of some of the most suitable techniques established for biopharmaceuticals is given in Figure 1- 11. These techniques are classified by the size range of the particles for which they are particularly suited and categorized by their measurement type as ensemble (or bulk), single-particle, and separation-based measurement techniques (Haskell 1998, Varenne, Makky et al. 2016). Ensemble (or bulk) measurement techniques, such as dynamic light scattering, static light scattering, turbidity determinations and visual inspection, detect a single overall signal from the particle suspension and result in average properties of the particles (Haskell 1998). This type of measurements is sufficient for homogenous monomodal and low-polydisperse suspensions, but less suitable for more polydisperse suspensions and number-based determinations (concentrations). Single-particle measurements, such as microscopic and imaging techniques (optical, infrared or fluorescence microscopy, transmission electron microscopy, atomic force microscopy), suspended microchannel resonant mass measurement and light obscuration, detect, characterize and report properties particle by particle (Haskell 1998). Particle-by-particle determination enables more reliable number-weighted particle size distributions and more precise extrapolated particle concentrations. Separation-based techniques, such as differential centrifugal sedimentation, analytical ultracentrifugation, size exclusion chromatography or asymmetric flow-field flow fractionation, use various principles to separate particles before or during the analysis. These measurement approaches overcome the drawbacks of ensemble measurement principles and are often combined with the latter.

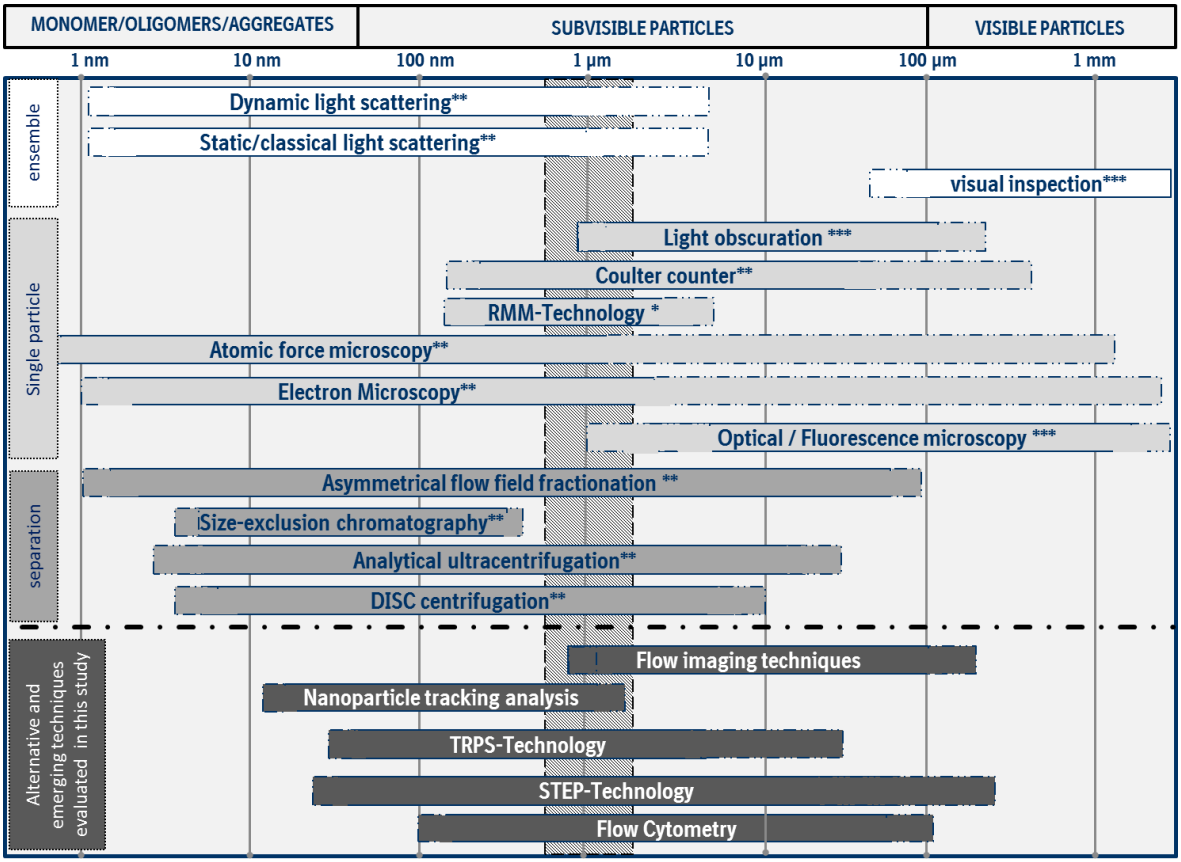

Figure 1- 11: Overview of particle detection techniques used for biopharmaceuticals.
Established (top part) and emerging (lower part) particle detection techniques are summarized according to their size measurement range. Their applicable size range is illustrated by the logarithmic scale at the top and the detection gap around 1 µm is highlighted by a grey bar. Further, the techniques are classified into ensemble, single particle and separation techniques. Stars indicate their current state: * Emerging technique; ** Established and often used techniques for pharmaceutical applications; *** Techniques mentioned in US Pharmacopeia. (Remark: Flow cytometry was excluded from the thesis studies)

Current pharmacopoeia methods include techniques of all categories:

- Light obscuration is a listed pharmacopoeial method measuring subvisible particles in parenterals (see USP<1788>,USP<788>,USP<1787> or USP<787>) (USP<787> 2014, USP<788> 2014),
- Optical microscopy is listed for non-spherical particles greater 1 µm as mentioned in USP<776> or as alternarive method for subvisible particles in parenterals USP<788>
- Visual inspection is prescribed in USP<790> for measuring particles in solution in the visible size ranges (> 80-100 µm) (USP<776> , USP<790>).

Trends in method and technical developments are towards single-particle measurements, like flow-imaging techniques, particle tracking analysis, enhanced coulter counter systems or flow cytometry (illustrated in the lower part of Figure 1- 11). Despite these improvements, there still is no single, universal particle detection method that can fulfill all requirements in all applications. Some of the main challenges are, that none can cover the full range of sizes over the periods of time needed to fully describe protein suspensions and aggregation processes (Roberts, Kozak et al. 2010, Hamrang, Rattray et al. 2013, Nicoud, Arosio et al. 2014, Nicoud, Owczarz et al. 2015, Nicoud, Jagielski et al. 2016). Most concentration determination techniques require dilutions that could change the characteristics of the sample due to narrow detection ranges and that the discrimination among particles of different types, e.g. protein or silicon oil, is only realized by a few techniques (Weinbuch, Zolls et al. 2013). Further technical considerations include the required sample volumes that are most likely large compared to the therapeutic dosage volumes and the need of high-throughput analyses. These and other limitations highlight the need for a more general, more robust approach, a need that will become more acute as process developers continue the trend towards HCLFs or other drug formats.

3.5. Emerging and novel techniques

As already depicted in Figure 1- 11 there is a number of particle detection and characterization techniques, that was already shown to be applicable to analyze particle suspensions, in particular monodisperse standard suspensions (e.g. PS particle suspensions). In this chapter, a short introduction is given to Nanoparticle tracking analysis, the principle of tunable resistive pulse sensing, space- and time resolved extinction profile technology used in a photocentrifuge and flow-imaging technique.

3.5.1. Nanoparticle tracking analysis (NTA)

Nanoparticle tracking analysis (NTA) is a recently commercially available method using microscopic imaging and particle-light interactions, to determine size distributions and concentrations of particles in the nanometer diameter range, based on their Brownian motion. Since the first description of a commercial nanoparticle tracking system (Nanosight Ltd.,

UK/Malvern Panalytics) in 2006, NTA and PTA (particle tracking analysis) systems found applications in many industrial fields; they also have been used in various biopharmaceutical applications (Cromwell, Hilario et al. 2006, Ling, Wang et al. 2006, Dragovic, Gardiner et al. 2011, Kramberger, Ciringer et al. 2012, Hamrang, Rattray et al. 2013, van der Pol, Coumans et al. 2014, Sanchis, Bosch-Orea et al. 2015).

For a measurement, the particle suspension is introduced into the sample cell (Figure 1- 12A). As the particles jitter in Brownian motion, they are illuminated by a laser beam passing obliquely through the cell. A charge-coupled device (CCD) on a microscope above the sample tracks the particles' light-scattering centers, creating a record of each single particle's movement. Software analysis of the path data yields the diffusion coefficient, *D*, calculated via the Stokes-Einstein equation (Equation 1) for each tracked particle. From this, knowing the temperature and viscosity of the suspension, we can calculate each particle's hydrodynamic diameter, *d(H)*, the diameter of a sphere with the same *D*.

$$\boldsymbol{D = \frac{\overline{(x,y)^2}}{4} = \frac{T\kappa_B}{3\pi\eta\, d(H)}} \qquad \textbf{Equation 1}$$

D	diffusion coefficient	η	viscosity
T	absolute temperature	d(H)	spherical-equivalent hydrodynamic diameter
κ_B	Boltzmann´s constant		

Because each scattering center is tracked separately, the resulting estimate of particle size distribution is a direct count, and not an intensity-weighted, z-average distribution (a common limitation of conventional ensemble methods, such as DLS) (Filipe, Hawe et al. 2010, Patois, Capelle et al. 2012, Wright 2012, Malvern Instruments GmbH June 2016). NTA results can be presented as concentration-based particle size distribution (PSD) histograms, or as intensity plots (Figure 1- 12B). Intensity plots help to estimate the polydispersity or even to differentiate between particle with high RI and particle with low RI (Gardiner, Shaw et al. 2014, Van Der Pol, Coumans et al. 2014). Calculations can reveal total particle concentrations in the range of $1x\ 10^7$ to $1x\ 10^9$ particle/ml, mean and mode size, as well as the parameters D10, D50 and D90 which describe the PSD more detailed.

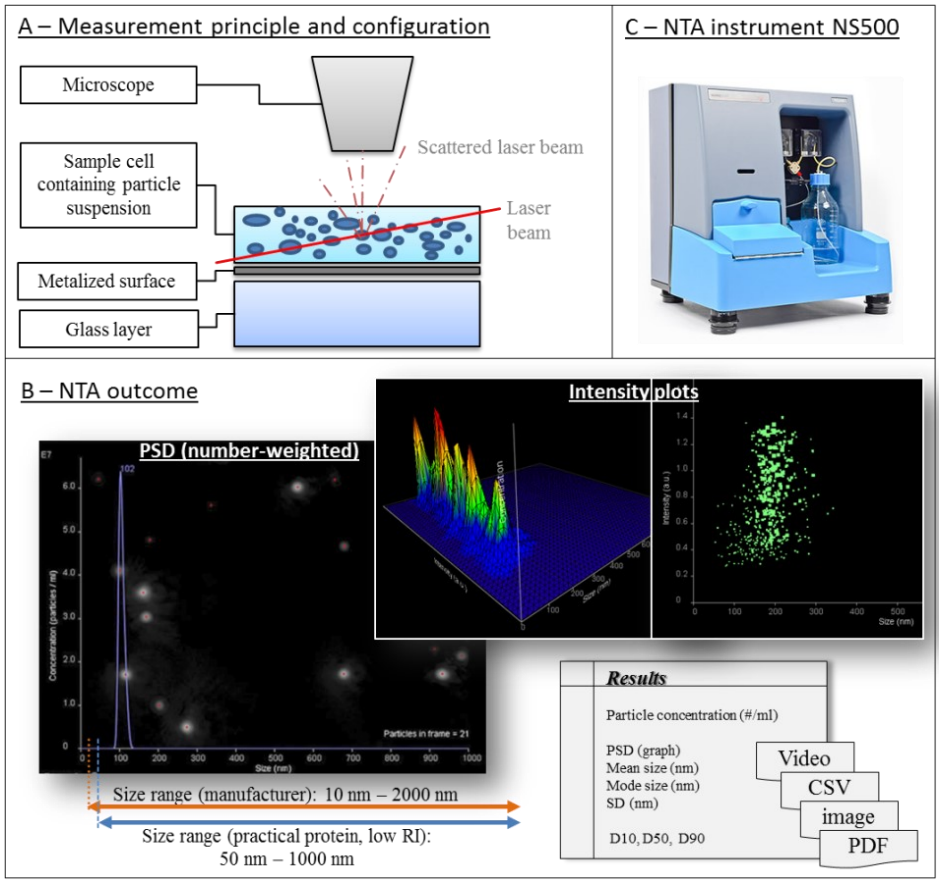

Figure 1- 12: Nanoparticle tracking analysis (NTA): Instrument, measuring principle and final outcome.
(A) Schematic illustration of the measurement principle of the NTA instrument (Nanosight Ltd.). The particle suspension is pumped into the sample cell where the laser beam encounters the particle causing light scattering. The light scattering centers of each particle are recorded and afterwards used to determine the Brownian motion of each particle indirectly by the motion of the scatter center. (B) Example of a measurement result using the provided instrument software. The recorded scattering centers are tracked and finally the number-weighted PSD, 2D and 3D intensity plots and a total particle concentration are achieved. The results are obtained as video file, graph image files, text file (.csv) and PDF-file. (C) NTA instrument NS500 (Nanosight Ltd.).

A few comparative studies highlight where NTA has potential advantages over established methods such as dynamic light scattering, resonant mass measurement, and differential centrifugal sedimentation (Bell, Minelli et al. 2012, Anderson, Kozak et al. 2013, van der Pol, Coumans et al. 2014, Weinbuch, Cheung et al. 2015). In 2010, Filipe, et al. published the first critical evaluation of NTA in a biopharmaceutical application, focusing on the analysis of biologics (Filipe, Hawe et al. 2010). The authors concluded that NTA does offer direct, real-time visualization of particle movement, while simultaneously counting and sizing particles ranging from approx. 30 nm to 1 µm (with some variations in size range limit, depending on the particles' properties). For protein

samples, they set the lower size limit to about 50 nm. According to Filipe et al., NTA provides slightly better resolution than DLS (Filipe, Hawe et al. 2010). Another study by Anderson et al., did not find the NTA resolution superior for the tested samples in comparison with other techniques (Anderson, Kozak et al. 2013). Elsewhere, van der Pol et al. have recently shown that differences in refractive index of different particle populations may help to differentiate single nanoparticle populations by both size and scattering intensity, with the scattering intensity providing information about shape and composition (van der Pol, Hoekstra et al. 2010, Van Der Pol, Coumans et al. 2014). These additional read-outs make NTA a preferred tool for analyzing polydisperse samples. By the same token, however, the flexibility and variability in parameter settings make the final results operator-dependent and thus objective results are questionable. At the same time, methods that depend strongly on operator skills can produce results that vary from user to user, making comparability uncertain. As a practical matter, particles with low refractive indices (RI) - like protein particles (RI protein particle ca. 1.34-1.4, 589 nm at 20 °C) in water (RI of water ca. 1.334, 589 nm at 20 °C) - scatter light only weakly, which makes analysis a challenge. Non-spherical particles with diameters above 500 nm show oscillating scattering centers in NTA measurements. Moreover, highly concentrated suspensions with protein concentrations in the range between 50 mg/ml and 150 mg/ml (Garidel et al. 2017), usually require dilutions that can change the sample composition. The technique of NTA was shown to be a versatile tool, also for biopharmaceutics, but the dependency on the operator parameters may lead to low comparability, i.e. high user-to-user variability.

3.5.2. Tunable resistive pulse sensing (TRPS)

Tunable resistive pulse sensing (TRPS) was developed to address shortcomings in the original Coulter resistive pulse sensing technique. In the literature, TRPS is also called scanning ion occlusion spectroscopy (SIOS), size tunable pore sensing or tunable elastomeric pore sensing (Roberts, Kozak et al. 2010, Vogel, Willmott et al. 2011, Kozak, Anderson et al. 2012). TRPS was first described and patented by Sowerby et al. in 2007 (Sowerby, Broom et al. 2007). Almost three years later, Willmott et al. presented the first commercial nanopore platform, a Coulter-type instrument employing TRPS to determine particle size, concentration, and charge (Willmott and

Moore 2008, Kozak, Anderson et al. 2011). Today, at least one manufacturer (Izon Science, Ltd.) produces TRPS-based instruments for nano- and micro- scale particle analysis.

The measurement principle is a variant of RPS (Coulter principle). TRPS replaces the fixed-diameter pores of RPS with dynamically resizable nanopores for more flexible real-time particle detection, quantitation, and characterization (Willmott, Vogel et al. 2010, Weatherall and Willmott 2015). The system consists of a base unit, the so-called qNano, a fluid cell, and a variable-pressure module (VPM) (Figure 1- 13A, left). The heart of the device is the pore, which is carried on a septum mounted in a cruciform specimen (Figure 1- 13A, right). Tungsten needles of precisely controlled diameters create the pore by punching through a 200 µm-thick elastic polyurethane membrane (Blundell, Mayne et al. 2015, Blundell, Vogel et al. 2016). By varying the needle dimensions and the punctuative process, the manufacturer can produce pores of varying geometries in diameters that range (currently) from 50 nm to 10 µm (2016). Like all Coulter-type counters, the TRPS system includes a fluid cell consisting of two compartments connected through the pore. (Figure 1- 13B) Sample is introduced into the upper chamber, and current is applied across the membrane. As in conventional RPS, a particle passing through the pore changes the resistance and produces a pulse in the current. And, also as in conventional RPS, this pulse record can be interpreted to give information on particle diameters, counts, size distributions, concentrations, shape, and charge. Unlike its predecessor, however, the TRPS system offers three additional controls (Figure 1- 13B, right) (Bell, Minelli et al. 2012, Weatherall and Willmott 2015):

(1) Operators can change the pore's shape. The pore specimen is mounted between inlet and outlet fluid chambers with the limbs of the cross-gripped in teeth that can move inward and outward in the plane of the specimen. This movement stretches the pore, changing its diameter and shape to suit the particles being analyzed. This is finally checked by the baseline and an appropriate standard.

(2) Operators can change the pressure gradient between the two chambers via the variable-pressure module (VPM). This adjusts the fluid flow through the pore independent of the particle charge. An optimal fluid flow is essential for obtaining the right pulse frequency and duration (also see below – optimal assay set-up). The VPM allows the measurement of samples with low particle concentrations down to $1x\ 10^5$ and up to $1x\ 10^{11}$ particles/ml; reverse flow is also possible.

(3) Operators can adjust the voltage. This helps optimize the signal-to-noise ratio and can even induce electrophoretic movement. In particular, the last two mentioned variables need to be controlled and balanced for the optimal assay set-up. Optimal set-up means that each particle that is detected should give a separate "peak" that can be differentiated from the background noise. The optimal voltage guarantees sufficient current for the baseline, i.e. for a stable baseline signal. To separate the peaks the particle velocity through the pore is adjusted by the applied pressure and/or by electrophoretic motion.

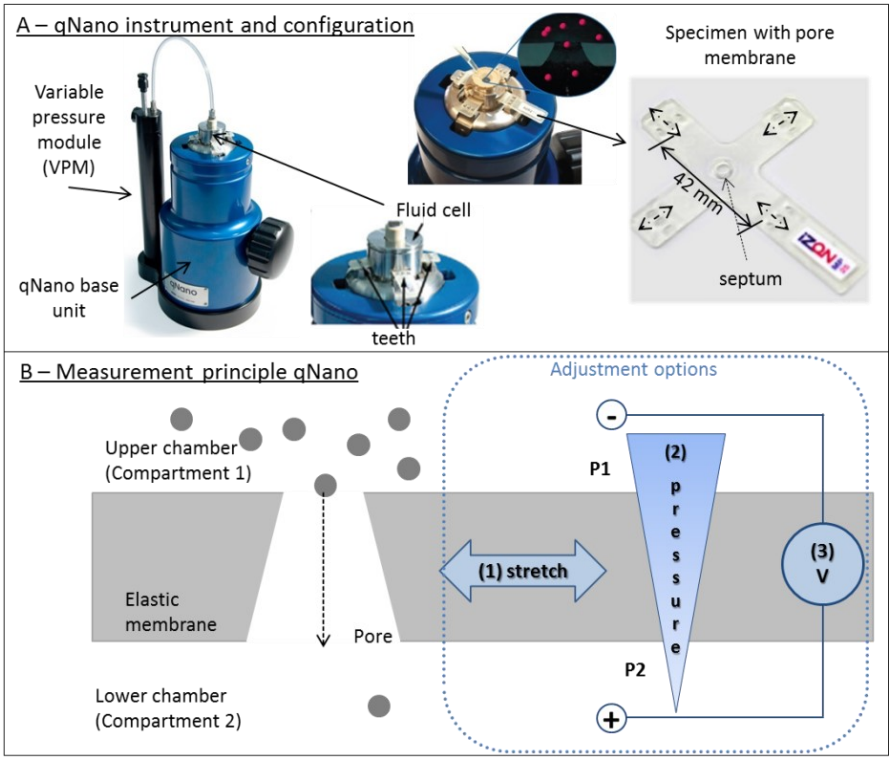

Figure 1- 13: Tunable resistive pulse sensing technology (TRPS): Instrument, specific pores and measurement principle.
(A) Configuration of the qNano instrument using the TRPS technology (Izon Science Ltd.) zooming from the complete device (left) to the specimen with the tunable nanopore (right). The specific cruciform tunable specimen containing a polyurethane membrane (septum) with the nanopore. (B) Schematic illustration of the measurement principle of the qNano instrument. The suspended particles in the upper compartment pass through the pore and cause the resistive pulse. There are three options to adjust the instrument for optimal settings for the specific sample: mechanical pore stretching, pressure difference adjustment and the applied direct current voltage (right).

TRPS has been included in several comparative evaluations of established and emerging particle-analysis techniques (Willmott, Vogel et al. 2010, Bell, Minelli et al. 2012, Roberts, Yu et al. 2012, Anderson, Kozak et al. 2013, Weatherall and Willmott 2015, Blundell, Vogel et al. 2016).

Anderson et al., compared DLS, PTA/NTA, DCS and TRPS (Anderson, Kozak et al. 2013). They assessed populations of polystyrene (PS) spheres with diameters of 220 nm, 330 nm, and 410 nm, first in separate populations and then in multimodal mixtures. All four of the tested techniques could accurately assess same-diameter populations in all three size ranges as long as homogeneous, monomodal samples were investigated. In multimodal mixtures, however, only TRPS could clearly resolve each of the three particle-size populations as a discrete peak (Anderson, Kozak et al. 2013). In a study on the effect of particle concentration, van der Pol et al., found that TRPS measurements matched the TEM reference values better than did flow cytometry or NTA (van der Pol, Coumans et al. 2014).

TRPS may thus be considered a highly accurate and precise method that outperforms other particle analysis techniques in resolving polydisperse or multimodal populations. The technology addresses RPS's principal drawbacks, pore blockage and limited response range for polydisperse suspensions. Increasing pore dimensions increase the upper limit of particle diameters TRPS can handle, of course. Decreasing pore dimensions increase signal to noise ratios for particles at the lower edge of resolvability. Moreover, the ability to determine nanoparticle size, concentration, and charge simultaneously is unique among the methods we reviewed here.

TRPS pores are not immune to clogging, however. Particles that are larger than the pore diameter, or have a high affinity for the pore material, can still block the channel. Membrane coating agents improve data quality by reducing adhesion and chemical reactions between the polyurethane and components of the suspension, especially in biological samples (Homepage iZone, 2016). Moreover, pore elasticity and the ability to reverse the fluid flow make it easier to recover from pore obstructions without interrupting an experimental run.

Despite their wider detection range, it can be challenging to analyze very highly heterogeneous and polydisperse samples. Adding a preceding separation step, such as an SEC column, can help (Boing, van der Pol et al. 2014). Measuring zeta potentials is possible but can be difficult, depending on the material. The mathematical model used to interpret instrument readings may not fully account for the effects of pore geometry, and they fluctuate a bit when particle and pore diameters are nearly the same. Calibration with standard particles is necessary to ensure TRPS comparability from one run to another. This assay protocol includes the calibration with particles of known size to ensure the correct comparability. The whole system is under further development for new applications and approaches. Best to our knowledge no study has been published so far

showing the successful application of the TRPS for biopharmaceuticals, in particular monoclonal antibody suspensions.

3.5.3. Space- and time-resolved extinction profile technology (STEP-technology®)

The space- and time-resolved extinction profile technology (STEP-technology®) was developed by L.U.M. GmbH (Berlin, Germany) and first commercialized in 1998 for use on sedimentation processes. In 2004, the same manufacturer released an optimized centrifuge instrument (LUMiSizer®) for characterizing nanoparticles and analyzing their dispersion stabilities. Instruments using the STEP-technology® are still evolving, with the addition of different light sources and suitable detectors for the wavelength 470 nm or 865 nm enabling multi-wavelength (2012) and X-ray (2015) devices.

The STEP-technology® instrument, an "analytical photocentrifuge" extension of the analytical ultracentrifuge with lower centrifugation speeds of maximum 2300 x g, combines sedimentation separation with real-time optical transmission/absorbance measurements (Figure 1- 14). The specific feature of the LUMiSizer® is the optical setup for detecting real-time sedimentation. Sample cuvettes, with minimal volumes of 0.4 ml or 1 ml, are loaded into slots of a centrifuge rotor. As the sample spins (6-2300 x g), it passes through the light—multiple beams that pass through the sample at many defined points along the cuvette's long axis. Each beam is paired with a CCD sensor. The result is a record of light transmission and absorbance at each height in the cuvette at fixed time intervals over the length of the run (Figure 1- 14A). The incident light wavelength can be chosen to suit the sample: near-infrared, blue light for highly transparent samples, or X-rays for highly concentrated, extremely turbid samples and for gradients within sediments.

In operation, the STEP-technology® instrument functions like "multiple device", combining the fundamentals of sedimentation with a specialized optical detection system for transmission/absorbance measurements. This multi-point data-gathering capacity provides the eponymous space- and time-resolved extinction profiles. The device accelerates particles up to 2300 x *g* and captures extinction coefficient information for every rotation at each level of the cuvette, as described by the Lambert-Beer law.

STEP-technology® produces a set of extinction profiles, a transmission fingerprint, and the software offers a number of options for analyzing the data (Figure 1- 14B): Sedimentation velocity, particle size distribution (from Stokes Equation), using a simple correlation (Equation 2):

$$u = \frac{r_m ln\frac{r_m}{r_0}}{t_m} \qquad \textbf{Equation 2}$$

u	sedimentation velocity	t_m	measurement time
r_m	measurement position	r_0	meniscus position

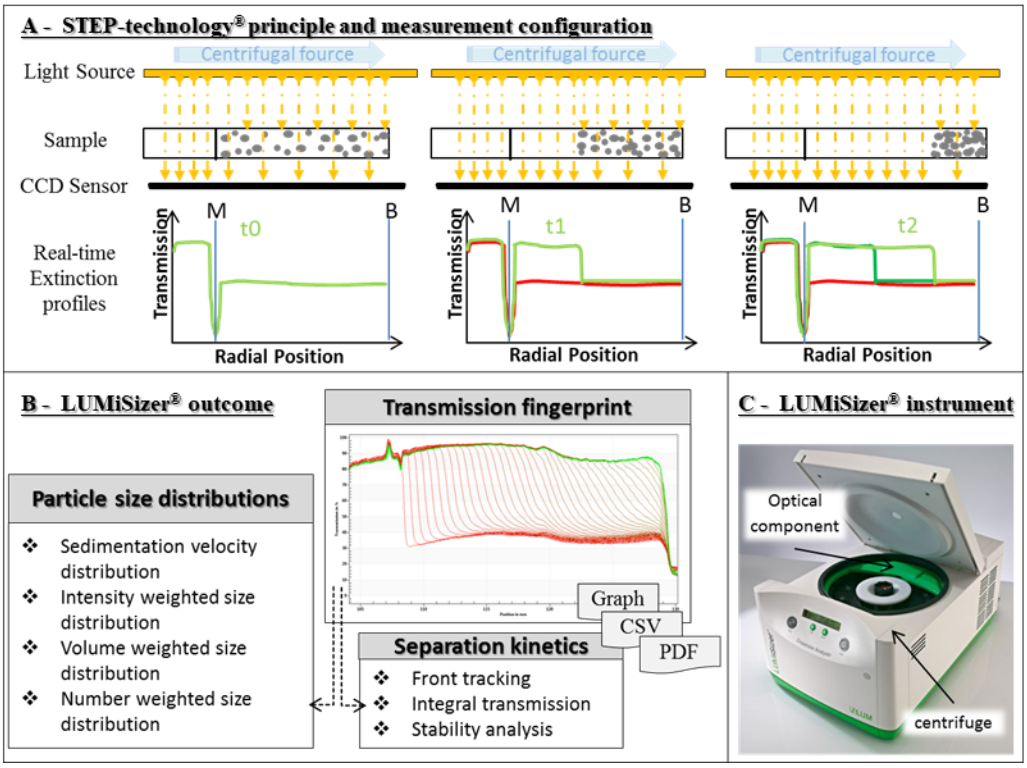

Figure 1- 14: Space- and time-resolved extinction profile technology (STEP-technology®): Instrument, measuring principle and final outcome.
(A) Schematic illustration of the STEP-technology® measurement principle. The particle suspension is homogenously distributed. Light is applied the over the whole sample and the transmission light is detected behind the sample over the whole lengths. The application of a centrifugal force leads to particle movement from the meniscus M to the cuvette bottom B. The clarification over time and a specific sedimentation velocity can be calculated. (B) The direct result achieved is the transmission fingerprint. Based on this various data analysis possibilities are provided by the software. Depending on the information known about the sample particles a wide variety of analysis and data evaluations are possible. The results are obtained as video file, graph image files, text file (.csv) and PDF-file. (C) LUMiSizer® instrument (L.U.M. GmbH).

Centrifugation accommodates a wider range of particle sizes (down to 10 nm and up to 100 µm) than other orthogonal principles and is correspondingly widely used. This type of analytical centrifugation (AC) has, naturally, advantages and disadvantages when compared to the two most used centrifugation techniques, AUC (analytical ultra centrifugation) and disc centrifugation (DISC). The main difference between AC and AUC is rotor speed. AUC uses higher, fixed rotor speeds up to generate higher accelerations and better resolutions, as low as a few nanometers in a reasonable time of 6 to 12 hours. Consequently, AUC is widely considered the most accurate technique. On the other hand, AUC requires excellent operator skills and substantial experimental effort: working with the complex cuvettes/sample cells in the vacuum needed to attain these high speeds and accelerations demands time and care. AUC's fixed rotor speeds limit the technique's dynamic range, and the very high accelerations may damage unstable samples (by contributing to agglomeration and aggregation, for example). Thus, the variable lower rotor speeds of DISC or AC might be beneficial where dynamic range and sample stability are concerns. The major drawbacks of DISC are that a calibration concerning the density zones is necessary and that the density gradient might alter the sample properties.

AC using STEP-technology® is highly suitable where the sample particles' mass and density allow sufficient sedimentation already at low rotor speeds within the experimental setup. Furthermore, three is no calibration necessary; temperatures can be controlled from 4 °C to 60 °C; samples, instrument and software are easy to handle; very turbid samples can be successfully analyzed; and up to 12 samples can be analyzed in a single run. Fast runs are performed for about 2 hours but depending on sample properties measurement times may be up to several days. As Walter et al. demonstrated, AC with STEP-technology® results for particle size and particle size distributions are in excellent agreement with AUC (Walter, Thajudeen et al. 2015, Walter and Peukert 2016). The determination of further particle properties, e.g. density or shape, is another approach supporting the analysis and enables the application in a wider field. However, centrifugation as an ensemble method is no particle-by-particle technique and quantitative evaluations are hard to achieve. In addition, the required material data, like particle density, are hard to determine in particular for aggregated protein samples. Another remaining challenge is the analysis of high concentration samples, e.g. HCLFs with up to 150 mg/ml or particle suspensions up to 90 vol%. If such concentrations of particles are present, hindered settling and multiple scattering occurs. These phenomena can be considered in new hindering functions for evaluation and improved

analysis approaches as shown by Walter et al. (Walter, Lohr et al. 2014, Walter, Thajudeen et al. 2015).

Since the release of the instruments, several studies are published to show AC is a versatile tool for PSD, stability analysis, separation velocity, interactions or structural stability/rheology in various fields: cosmetics, food processing, and material science, as well as biopharmaceuticals. Bharti et al. applied STEP-technology® to investigate interactions among nanoparticles as part of an effort engineering functional structures depending on the used formulation conditions. Further verification as applicable technique in pharmaceutical development was shown for the characterization of vaccines, approaches using nanoparticles and microgels and even for formulation development of various compounds. To date, STEP-technology® does not appear to have been used to develop formulations of proteins (such as therapeutic antibodies) on the nanoparticle scale.

3.5.4. Micro-flow imaging (MFI)

Micro-flow imaging (MFI), first described by Sharma et al. in 2007, is an increasingly popular method that uses dynamic microscopic imaging to determine particle size distributions, concentrations, and shape properties. The first commercial MFI instrument was presented by Brightwell Technologies in 2011 (Sharma, King et al. 2010, http://www.proteinsimple.com/mfi_overview.html June 2016). Today, several manufacturers offer devices based on flow-imaging or closely related principles, and MFI has emerged as one of the techniques with the greatest potential in biopharmaceutical subvisible particle detection by not only quantify but also characterize the detected particles.

In MFI, a simple fluidic system passes the sample through a flow cell (Figure 1- 15A), where it is illuminated by a pulse of bright light. Particle motions / images are recorded using a custom magnification system with well-defined magnification and an extended depth of field. For increased sensitivity, the instrument performs an automated calibration before each sample run, using low-noise electronics to optimize detection thresholds. And as the motion frames are captured, software algorithms are applied to further reduce noise and compensate for variations in spatial and pulse-to-pulse illumination. Image analysis software identifies each particle, tracks it frame to frame, and extracts and records information on size, shape, and contrast. (Raw images are

saved as PDF files, and particle parameters are saved to a database, and can be exported as a spreadsheet.) Post-experiment software analyses of the particle database produce information on counts, concentrations, and characteristic distributions (such as number-weighted PSDs). Image filtering (e.g., for silicon oil) can identify and isolate subpopulations based on particle shapes and grayscale image values. (Figure 1- 15B) The results can be presented as concentration-based PSD showing size distribution, corresponding and particle concentrations - reported, for example, in the particle diameter regions (<10 µm, and <25 µm) generally of interest to regulatory authorities (Sharma, Oma et al. 2010, Wilson and Manning 2013, http://www.proteinsimple.com/mfi_overview.html June 2016).

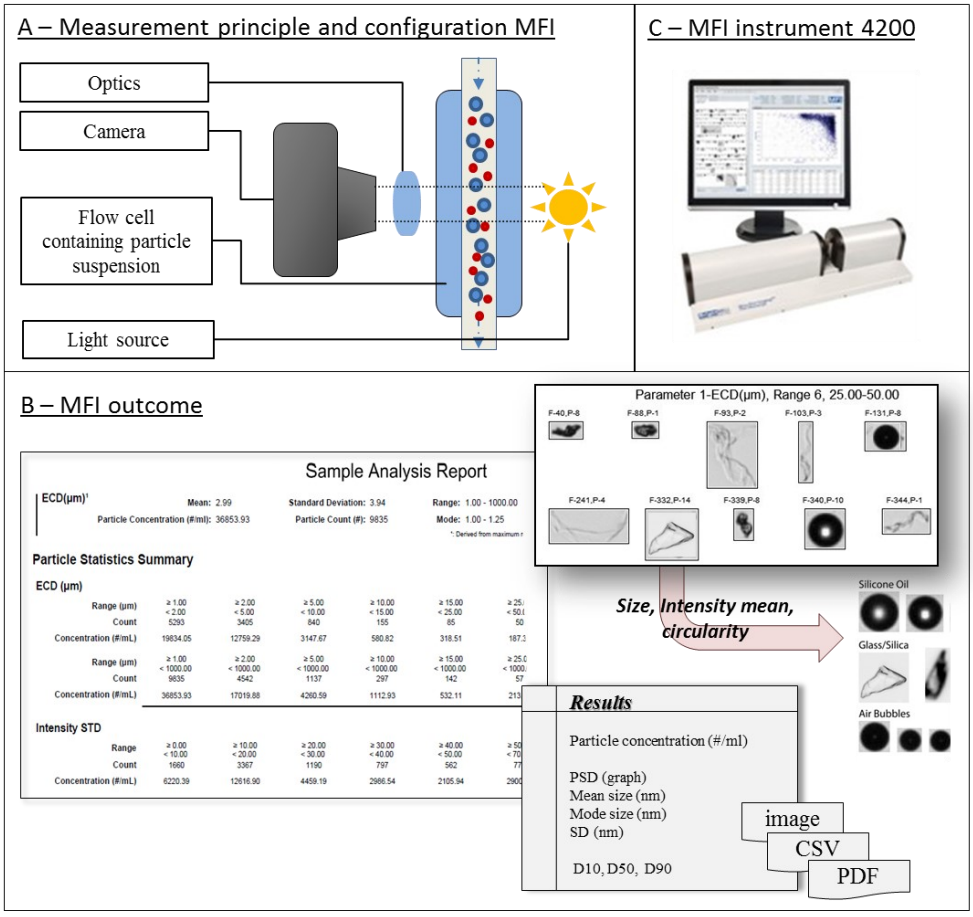

Figure 1- 15: Micro-flow imaging (MFI): Instrument, measuring principle and final result.
(A) Schematic illustration of the measurement principle of the MFI instruments (Protein Simple). The particle suspension is pumped into the flow cell where the camera captures bright field images as raw data. (B) After analyzing the images by an imaging software considering the amount and the greyscale of each pixel a report is generated. This report contents number-weighted PSD as well as example images of single particles. Due to properties like size, intensity mean or circularity, filters can be applied to obtain and analyze particles with specific properties. The results are obtained as particle image files, text file (.csv) and PDF-file. (C) MFI instrument DPA 4200 (Protein Simple).

Numerous studies have applied MFI, e.g. in cytometry or for biopharmaceutical particle detection (Sugimoto, Shiraishi et al. 2010, Wu, Martin et al. 2012, Yang, Liu et al. 2013). Huang et al. compared LO and MFI accuracy in sizing and counting subvisible particulates. Results showed the trends of both methods in high agreement, but concluded that MFI was more sensitive in the analysis of translucent particles, such as proteins and detected about 100 times higher particle concentrations (Huang, Sharma et al. 2009). Sharma et al. further demonstrated the applicability of MFI for protein samples (Sharma, King et al. 2010, Sharma, Oma et al. 2010). MFI's detailed visualization (compared to LO or dynamic light scattering) can be applied to studies of induced aggregation, and to differentiate between protein and other process particles. In polydisperse samples, for example, MFI can, without preparative separation distinguish between protein and silicone oil particles in the range above 10 µm (Weinbuch, Zolls et al. 2013). MFI software allows sorting and grouping particles by specified shape and reflected signal intensity values, and MFI systems can be automated for high throughput, saving time, cost, and labor. A high throughput approach is realized by the provided autosampler system (BOT) as it enables the measurement of 96 samples automatically and saves operator valuable time.

There are also drawbacks, of course. Developing the analytical algorithms is challenging, and the advanced analytical software can produce skewed results if the operator chooses the wrong parameter settings (such as an inappropriate gray-scale threshold). As a particle-by-particle approach, flow imaging microscopy gives detailed results on a relatively small portion of the overall sample, and does not necessarily reflect the properties of the sample as a whole (though careful attention to sampling statistics in specifying appropriate volumes can generate representative results). The instrument may have limits on the number of particles it can detect, count, and file parameters in the database, so suspensions with high particle concentrations might require dilution—which, as noted, can alter key sample properties. Though MFI can discriminate smaller refractive-index differences between particles and media than other techniques can, there is still a limit below which particles become nearly transparent and undetectable (Zolls, Gregoritza et al. 2013). This can be a particular issue in suspensions that combine high protein concentrations with buffers containing a number of excipients (Sharma, King et al. 2011, Pedersen and Persson 2014).

MFI's detection range (particles 2 µm to 100 µm in diameter) is similar to that of light obscuration, but MFI provides more information on shape and material and does a better job characterizing

translucent particles. This makes MFI very promising also for regulatory applications (USP<787> 2014, USP<788> 2014, USP<1787> 2015).

4. Motivation and objectives

Over the last years, the interest on biopharmaceuticals in pharmaceutical industries increased explosively. The appearance of particles in such biopharmaceuticals, indeed, is a critical quality attribute and a serious problem as the presence of particles is one of the main reasons for the recall of parental products and holds serious medical risks for patients.

For that reason, the major challenges and aspects this dissertation focuses on are

(1) the implementation of sensitive particle detection and characterization techniques,

(2) the coverage of the size detection gap

(3) the knowledge/understanding about protein aggregation to avoid particle formation

Aspects (1) and (2): Companies as well as authorities require orthogonal and comparable methods for detecting and characterizing particles in a wide range to ensure product quality and safety. Due to safety concerns, regulatory authorities expect that the number of protein particles is quantified, and that the nature of particles is characterized. This applies both for product in development as well as for routine release and stability testing of market products. Today, only a few established methods for particle detection and characterization in biopharmaceuticals exist. They differ widely in the underlying physical principles and exhibit varying sensitivity for certain particle populations (e.g. size).

In the first part of the dissertation, objectives are

- the assessment of the potential and the limitation of current particle detection methods
- the identification and evaluation of novel/emerging suitable methods for detecting and characterizing protein particles and to close the methodological gap for detection of protein particles 1-10 µm in size (namely Nanoparticle tracking analysis, Tunable resistive pulse sensing, and Space- and time-resolved extinction profile technology)

Aspect (3): Additionally, having a comprehensive technique evaluation at hand enables the investigation of the aggregation kinetic and mechanism. Protein particle formation occurs via various pathways and the mechanisms are not understood so far. Experiments indicate that

particles origin either from protein-protein aggregation due to the exposure of stress (e.g. thermal or ionic stress), via adsorption of proteins to a non-protein particle (e.g. silicon drops, stainless steel shed) or during processing. Consequently, a deeper understanding in the mechanism of protein aggregation and its internal structure and the investigation of factors and conditions may support the avoidance of protein aggregation.

In the second and third part of the dissertation, objectives are

- the evaluation of novel technologies for investigating and characterizing protein unfolding and their role in protein aggregation processes to gain a better understanding of the particle formation mechanism (namely the Zetasizer Helix system and the SwitchSENSE system).
- the analysis of protein aggregation processes of therapeutic antibodies, the analysis of the nature of protein particles as well as the investigation of aggregation kinetic to identify potential conditions to avoid aggregation.

In conclusion, the obtained understanding and knowledge possibly supports the development of early formulation screening and protein characterization tools to better predict manufacturability. By understanding the influencing factors, timelines in order to avoid the presence of protein aggregates may be shortened. This indeed might reduce time and costs in product development processes.

PART II: Material and Methods

~

5. Materials

5.1. Consumables

All consumables used for this thesis are listed in Table 2.

Table 2: Materials: List of used consumables.

Name	Description/Comments	Manufacturer
2R vials	FIOLAX® glass	Schott AG
Amicon® Ultra-4 Ultracell and Ultra-15	30 kDa MWCO, Vol. 15 ml 10 kDa MWCO, Vol 15 ml	Merck Millipore Ltd.
BD Falcon Tubes	15 ml Polystyren (352095) 50 ml Polypropylen (352070)	BD Bioscience
BD Plastipak Syringe	1 ml, 2 ml, 60 ml	Becton Dickinson
BR Mix	HP-SEC standard	BioRad Laboratories GmbH
Disposable cuvettes	Semi-micro 1.5 ml	Brand GmbH & Co. KG
Econofil Syringe Filter	0.45 µm	Thermo Scientific
Eppendorf safe-lock tubes	Reaction vessels, 0.5 ml, 1.5 ml, 2.0 ml	Eppendorf AG
Eppendorf tubes	Reaction vessels, 5.0 ml	Eppendorf AG
Falcon®	15 ml, 50 ml poysytrene conical tube	Corning, Inc
Flow cell (MFI)	100 µm, 1.6 mm, set point 3, silane coating	ProteinSimple
HPLC vials	Fixed insert vials	Thermo Sceintific
iCycler iQ	Optical Tape	Bio-Rad Laboratories
Nalgene™ square PETG media bottles with closure	60 ml, 125 ml, 250 ml	Thermo Fisher Scientific Inc.
Optim 1000 micro cuvettes	Micro cuvette array	Avacta Analytical Ltd.
Precision cells 104.002F-QS and 114F-QS	Cuvettes, Quartz SUPRASIL®	Hellma GmbH & Co. KG
Prometheus NT.48 Capillaries	Standard capillaries High sensitivity capilarries	NanoTemper Technologies GmbH
Rotilab®-syringe filter	PVDF, sterile, pore size: 0.2 µm	Carl Roth GmbH & Co. KG
Single-use UV cuvettes	Half micro (1.5 mL), micro (75 µL)	Plastibrand
Slide-A-Lyzer G2 Dialysis cassettes	20 kDa MWCO, 70 ml Volumen, Nr. 87738	Pierce/ Thermo Scientific
SteritopTM filter units, Steritop-GP 0.22 µm	Disposable, sterile, polyether-sulfone, pore size: 0.22 µm	Merck Millipore Ltd.
Stopper	13 mm, Gusto S2 F451, grey	West Pharmaceutical Services Inc.
TSKgel G3000SWXL	HP-SEC column	Tosoh Bioscience GmbH
UV-cuvette micro	70-850 µl	Brand GmbH & Co. KG
UVette®	50-2000 µl	Eppendorf AG
UV-Star® Microplate	96-well plates, half area	Greiner Bio-one

5.2. Chemicals, reagents and solutions

All chemicals, cleaning solutions and reagents used for this project are listed in Table 3. For the preparation of additional solutions and buffers (listed in Table 4) Millipore milli-Q water (deionized) was used in all cases. All buffers and the deionized water used in all experiments were filtered using 0.22 µm filters prior to usage.

Table 3: Materials: List of used chemicals, cleaning solutions and reagents.

Name	Manufacturer
Acetic acid	Merck KGaA chemicals
Acetonitrile	Sigma Aldrich
Citric acid	Sigma Aldrich
Di Sodium hydrogenphosphate	Merck KGaA chemical/Chemische Fabrik Budenheim KG
Di(N-succinimidyl)-Glutarat (DSG)	Sigma Aldrich
Ethanol	Carl Roth GmbH & Co KG/ Cargill Deutschland GmbH
Hydrochloric acid	Carl Roth GmbH & Co KG
L-Arginin	Kyowa Hakko GmbH
Nitric acid	Merck KGaA chemicals
Sodium chloride	Fluka Analyticals / SigmaAldrich/ AkzoNobel salt
Sodium citrate-dihydrate	Jungbunzlauer Ladenburg GmbH
Sodium hydrogenphosphate	Dr. Paul Lohmann GmbH KG
Sodium hydroxide solution	Carl Roth GmbH & Co KG/ Fluka Analyticals
Sulfuric acid	Merck KGaA chemicals
Trichloroacetic acid	Sigma Aldrich
Tri-Sodium phosphate dodecahydrate	Carl Roth GmbH & Co KG
Decon®90	Decon Laboratories Limited
Hellmanex® II	Hellma GmbH & Co. KG
Küvettol	Hellma GmbH & Co. KG
Electrolyte filling solution, KCl 3 mol/l	Mettler Toledo Inc.
Technical buffer solution, pH 7.00 and 4.01 ± 0.02	Mettler Toledo Inc

Table 4: Materials: List of used buffers and solutions.

Name	Components
Phosphate model buffer	10 mM phosphate buffer containing 10 mM NaCl pH 6.5 ± 0.1
Model buffer pH variations	10 mM phosphate buffers containing 10 mM NaCl pH 4.6 ± 0.1, pH 5.7 ± 0.1, pH 7.6 ± 0.1 and pH 9.3 ± 0.1
Model buffer NaCl variations	10 mM phosphate buffers pH 6.5 ± 0.1 containing 50 mM, 100 mM, 250 mM and 500 mM NaCl
HP-SEC buffer mAB1	50 mM PO_4 ; 0.5 mM NaCl ; pH = 7.0 ± 0.1
HP-SEC buffer mAB2 and mAB3	0.2 M L-Arginine ; 0.1 M PO_4 ; pH = 6.8 ± 0.1
Coupling buffer B22	0.2 M $NaHCO_3$; 0.5. M NaCl ; pH = 7.0 ± 0.1 ; 8.3 ± 0.1
Blocking buffer	0.5 Ethanolamine ; 0.5 NaCl ; pH = 8.3 ± 0.1
Washing solutions	1 mM Hydrochloric acid 0.1 M Tris-HCl ; pH = 8.0 ± 0.1 - 9.0± 0.1 0.1 M Acetate ; 0.5 M NaCl ; pH = 4.0 ± 0.1 - 5.0 ± 0.1

5.3. Polystyrene and silica size standard particles

Nanosphere™ Size Standards (Polystyrene) and Latex Microsphere Suspensions with sizes of 20 nm (Cat No 3020A), 50 nm (Cat No 3050A), 80 nm (Cat No 5008A), 100 nm (Cat No 3100A), 200 nm (Cat No 5020A), 300 nm (Cat No 3300A), 400 nm (Cat No 3400A), 600 nm (Cat No 3600A) and 1000 nm (Cat No 5100A) were purchased from Thermo Scientific (Fremont, USA). In the following denoted as PS-beads. According to manufacturer information, the depicted sizes were determined and verified by Dynamic light scattering (DLS) and Transmission electron microscopy (TEM). The aqueous suspension with a particle concentration of 1 % w/w contains traces of surfactant. Particle density was stated as 1.05 g/cm and the determined refractive index was 1.59 at 589 nm and 25 °C.

In addition to the size standards, a Count-Cal™ Polysterene Particle Count Standard with a size of 5.01 ± 0.035 µm and a depicted concentration of 3000 (± 10 %) particles/ml were purchased from Thermo Fisher Scientific Inc.. The standard was used to evaluate the functionality of the MFI system before a measurement series.

The monomodal distributed silica standard particle suspension (SediTest, Prod.-No. 272-15504) was provided by Dr. Lerche KG (Berlin, Germany). According to the product information sheet, the particles showed a nominal size of 550 nm, a density of 2000 kg/m^3 and a refractive index of 1.46. The measurement concentration was set to 0.11 % w/w.

5.4. Biologicals: Bovine serum albumin (BSA) particle standard suspensions and sample preparation

For the evaluation of the emerging techniques considering protein applicability plain BSA standard particle in aqueous suspensions with sizes of about 177 nm ("BSA1"), 500 nm ("BSA2") and 750 nm ("BSA3") were purchased from micromod Partikeltechnologie GmbH (micromod Partikeltechnologie GmbH, Rostock, Germany). Product size and size distribution was verified by DLS measurements using Zetasizer Nano Series Nano-ZS. The resulting z-averages and PDI values are summarized in Table 5. In general, an increasing polydispersity with increasing depicted standard size was detected. BSA particles were stored at 4 °C in an aqueous solution at a concentration of 5 mg/ml. Based on the obtained PDI values, "BSA1" indicated monodisperse distribution while "BSA2" and "BSA3" indicated polydispersity. These BSA particles were already investigated and characterized in a previous study (Karow, Gotzl et al. 2015, Schaz 2015).

Table 5: Materials: BSA particle standard suspensions: Manufacturer data and DLS analysis results.

	BSA standard 1 ("BSA1")	BSA standard 2 ("BSA2")	BSA standard 3 ("BSA3")
Manufacturer size / nm	177	500	750
z-average /nm	166	394	993
PDI	0.047	0.214	0.232

5.5. Biologicals: Monoclonal antibodies and other used proteins

All used proteins were kindly provided by Boehringer Ingelheim Pharma GmbH & Co.KG. The proteins were produced recombinantly most likely in mammalian cells and were provided after the completed purification downstream process in a pure suspension. All investigated antibodies and antibody format biopharmaceuticals are listed in Table 6.

The molecules mAB4 to mAB6 and AF1 to AF4 were only used in the comparative study with the SwitchSENSE® system. The molecules mAB1, mAB2 and mAB3 have been used as general model molecules and a more detailed information are therefore given in Table 7. The medical application of mAB1 aims the treatment of immunological disorders while mAB2 and mAB3 are considered for cancer therapy. All proteins were stored at 4 °C in the provided formulation buffer. Prior investigation studies and analyses within this thesis, a buffer exchange was performed into

depicted model and assay buffers using either centrifugal filters (Amicon® Ultra-15) or dialysis cassettes with a molecular weight cut-off (MWCO) of 30 kDa.

As unstressed sample, we defined the mAB suspension after buffer exchange, but before the start of analysis and stress application. Depending on the performed study different molecules have been used and treated in specific procedures. For that reason, a more detailed description of the specific sample preparation and stress application procedure is given under 7.2 or in the results.

Table 6: Materials: List of all investigated biologicals (antibodies and antibody formats).

Sample ID	Molecular Weight	Description
mAB1	145 kDa	Therapeutic monoclonal antibody IgG1κ
mAB2	145 kDa	Therapeutic monoclonal antibody IgG1κ
mAB3	147 kDa	Therapeutic monoclonal antibody IgG1κ
mAB4	~ 148 kDa	Artificial monoclonal antibody
mAB5	~ 148 kDa	Artificial monoclonal antibody
mAB6	~ 145 kDa	Therapeutic monoclonal antibody IgG4
AF1	94 kDa	Therapeutic fusion protein containing antibody fragment
AF2	~50 kDa	Therapeutic nanobody
AF3	~ 200 kDa	Therapeutic bispecific antibody format
AF4	~ 200 kDa	Therapeutic bispecific antibody format

Table 7: Materials: Detailed properties of model proteins mAB1, mAB2 and mAB3.

mAB ID	Number amino acids	Extinction coefficient [cm^{-1}]	Expected hydrodynamic radius r [nm]	Expected isolectric point (calculated)	Charge at pH 7.0, (calculated)
1	1324	1.49	~ 5.0	8.4	13.97
2	1328	1.43	~ 5.0	8.4	13.79
3	1334	1.61	~ 5.0	8.1	7.97

6. Experimental approaches

The overall experimental approaches focus on three main tasks: Firstly, the evaluation of particle analysis techniques; secondly the evaluation of novel techniques for unfolding/aggregation studies; thirdly the performance of case studies to better understand the protein aggregation process of biopharmaceuticals. In this chapter, a short introduction is given how these main tasks have been planned and realized.

6.1. Task 1: Evaluation of selected emerging particle detection and characterization techniques for protein particles

The comparative evaluation of the emerging techniques Nanoparticle Tracking Analysis (NTA), LUMiSizer® and qNano isperformed in three steps:

(1) Firstly, well-defined polystyrene standard particles are measured. For internal validation and verification Nanosphere™ Size Standards (Polystyrene) and Latex Microsphere Suspensions with sizes from 20 nm to 5700 nm were purchased from Thermo Scientific (Fremont, USA), in the following called PS-beads. According to manufacturer information, the depicted sizes were determined and verified by Dynamic light scattering (DLS) and Transmission electron microscopy (TEM).

(2) Secondly, plain BSA particle suspensions are measured as a protein-based particle standard covering a subvisible size range (case study I). Some of these BSA particles were already investigated and characterized in a previous study (Karow, Gotzl et al. 2015, Schaz 2015).

(3) The third step is the investigation of unstressed and stressed monoclonal antibody (mAB) solutions (case study II). The antibody solution of 10 mg/ml is investigated before and after the application of various stress conditions. As the focus of this chapter is the applicability of the techniques for proteinous samples, PS bead results are not shown, but experiments of steps (2) and (3) will only be performed, if PS-bead measurement results meet the manufacturer results.

Furthermore, a more detailed evaluation of promising technologies will be performed focusing on specific instrument parameters and their influence on the result, critical sample properties, instrumental limits, the investigation of polydispers/polymodal suspensions and a deeper look in the applicability on routine biopharmaceutical samples, etc.

6.2. Task 2: Evaluation of selected novel technologies for the investigation and characterization of protein unfolding and aggregation processes

The two emerging technologies Zetasizer Helix and SwitchSENSE® are evaluated for the analysis of protein stability and the characterisation of protein aggregation processes.

The Zetasizer Helix evaluation is performed at the BI campus in Biberach in cooperation with the company Malvern Instruments. The three applications provided by the manufacturer are tested, including sample series, thermal ramps and isothermal incubation, with randomly chosen mABs.

The results are compared to results of orthogonal methods. If the results are promising the technique and results will be included in a more detailed characterization of mAB1, mAB2 and mAB3 and their aggregation process (see task 3).

The SwitchSENSE® evaluation is performed in Martinsried in cooperation with the company Dynamic Biosensors. (1) In the first step, potential applications of the system, including size determination, protein-protein interaction analysis and thermal melting analysis, are tested exemplary. (2) In a second step, the application of thermal melting analysis is further evaluated in a comparative study with other orthogonal techniques aiming thermal melting analysis, namely Differential Scanning Calorimetry and Intrinsic tryptophan fluorescence. In the comparative study, five monoclonal antibodies and four emerging biopharmaceutical formats are investigated. If the results are promising the technique and results will be included in a more detailed characterization of mAB1, mAB2 and mAB3 and their aggregation process (see task 3).

6.3. Task 3: Protein aggregation processes: A case study of three therapeutic monoclonal antibodies

In the third part of the thesis, the three monoclonal antibodies mAB1, mAB2 and mAB3 are investigated in a specific defined buffer (=model systems) considering aggregation behaviour and processes using established and novel techniques and technologies.

(1) Initially a biophysical characterization of the model systems is performed considering conformational and colloidal stability as well as particle analysis.

(2) The second aspect of this case studies deal with the characterization of stress-induced aggregation processes: The first stress factor investigated is the temperature. The investigation of aggregation during temperature ramp experiments from 25 °C to 95 °C is performed for mAB1 and mAB2. In addition to temperature ramp experiments, isothermal aggregation studies are performed at various temperatures for all three model systems. In the end the impact of further protein stress factors, such as pH, reducing stress or aggregate addition (seed-induced), is investigated.

In summary, the results of this case study will describe the stability and aggregation process of the three monoclonal antibodies from different perspectives supporting the understanding of the specific aggregation mechanisms. The application of evaluated technologies in this case study outline their suitability for practical stability studies, e.g. in formulation development.

7. Methods and techniques

7.1. Used devices and instruments

All devices and the corresponding methods used for this thesis are listed in Table 8.

Table 8: Methods: List of used devices and the proceeded methods.

Device	Manufacturer	Method description/Application
AX205 Delta Range	Mettler Toledo International Inc.	Scale
Biofuge Primo R	Heraeus Holding GmbH	Centrifuge
Centrifuge 5430	Eppendorf AG	Centrifuge
Conductivity meter	WTW / Mettler Toledo	Meausrement of conductivity
Dry bath FB15103	Thermo Fisher Scientific Inc.	Dry block heater
MilliQ® Advantage A10	Merck Millipore Ltd.	Water purification system
NanoDrop 2000c	Thermo Scientific Inc.	Protein concentration determination (UV/Vis spectrometer)
pH meter pH340 **S20 Seven Easy pH** **Seven Go**	WTW Mettler Toledo Mettler Toledo	Determination pH values
Precision pipettes	Eppendorf AG	
R05 Power IKA	IKA®- Werke GmbH & Co. KG	Magnetic stirring plate with heating
ThermoVac 2 degassing station	MicroCal/GE Healthcare	Degas of solutions/samples
Differential Scanning Calorimeter (VP-DSC)	MicroCal/GE Healthcare	Protein unfolding
DynaPro PlateReader 2	Wyatt Technology	Dynamic light scattering plate reader, particle sizing
Lambda 35	Perkin Elmer Inc.	UV/VIS Spectralphotometer ; Protein concentration and A320 determination
LUMiSizer®	L.U.M. GmbH, Berlin, Germany	Analytical Photocentrifuge; Particle sizing
MFI™ DPA-4200	Brightwell Technologies, Inc./ Protein Simple	Micro-Flow imaging, Particle imaging, sizing and quantification
NTA NS500-HSB	NanoSight Ltd/ Malvern Instruments GmbH	Nanoparticle Tracking analysis; Particle sizing and quantification
Optim 1000	Avacta Analytical Ltd.	Intrinsic Tryptophane Flourescence and Right-angle light scattering
Prometheus NT.48	NanoTemper Technologies GmbH	Nano differential scanning fluorimeter with integrated light scattering detection
qNano™	Izon Science Ltd.	Particle sizing and quantification
SwitchSENSE®	Dynamic Biosensors GmbH	Particle size and unfolding behavior

Device	Manufacturer	Method description/Application
Turbidity meter 2100AN	HACH Lange Company	Turbidity determination in NTU/FNU
Waters Alliance® e2695 **Waters Alliance® e2489**	Waters Cooperation	HPLC system, Separation module HPLC system, UV detector
Zetasizer Helix	Malvern Instruments GmbH	Photonen-Correlation-Spektroscopy and Raman spectroscopy, Particle size and protein structure
Zetasizer NanoZS ZEN3600	Malvern Instruments GmbH	Photonen-Correlation-Spektroscopy; Particle sizing and zeta potential

7.2. Sample Preparation

For each study specific preparations of the polystyrene standard particle suspensions, bovine serum albumin standard suspensions and monoclonal antibody/antibody format samples have been necessary. These preparations are described in more detail in this chapter.

7.2.1. Polystyrene standard particle suspensions

The polystyrene size standard suspensions with estimated particle concentrations up to 1 x10^{15} particle/ml, were diluted in milliQ water prior most analyses. For NTA measurements the monomodal size standard solutions were diluted milliQ water (deionized and filtrated) to obtain optimal particle concentrations between 1 x10^{7} and 1 x10^{9} particle/ml (compare Table 9). The polydisperse/polymodal mixture of 50 nm, 400 nm and 600 nm polystyrene beads was prepared in a number ratio of 9:2:1 to guarantee a comparable particle number and sufficient scatter light intensity. For other analyses, the applied dilutions are mentioned in the depicted result chapter.

Table 9: Dilutions of standard PS-bead suspensions for NTA evaluation.
The Nanosphere™ Size Standards (Polystyrene) and Latex Microsphere Suspensions have been diluted as depicted in below for more detailed NTA evaluation measurements. The start concentration values were calculated based on the depicted particle information properties, like diameter, weight concentrations and particle density.

Particle size / nm	Start concentration / particle/ml	Dilution factor
20	2.27·x 10^{15}	1:1·x 10^{5}
80	3.55·x 10^{14}	1:1·x 10^{6}
200	2.27·x 10^{13}	1:1·x 10^{5}
300	6.74·x 10^{11}	1:1 x 10^{3}
600	8.42·x 10^{10}	1:5 x 10^{2}
1000	1.82·x 10^{11}	1:1·x 10^{3}

7.2.2. Bovine serum albumin standard particle suspensions

Like polystyrene particle suspensions, the BSA particle standard suspension BSA1, BSA2 and BSA3 had to be diluted before measurements, depending on technique specifications:

- For NTA, the BSA standard suspensions were diluted in milliQ water to a final concentration of 0.5 mg/ml to 0.5 µg/ml (approximately 1 x10^8 to 5 x10^7 particle/ml) prior each measurement.
- For TRPS the BSA particle standard solutions were diluted to a final concentration of 5 µg/ml to 0.5 µg/ml (approximately 1 x10^8 to 5 x10^8 particle/ml) in PBS.
- For LUMiSizer® investigations BSA size standard suspensions were measured undiluted with 5 mg/ml and in dilution series down to 0.2 mg/ml.
- For other analyses, the applied dilutions are mentioned in the depicted result chapter.

The BSA standard particle suspensions have been analysed individually as the monomodal suspensions as well as a mixture of two populations in the ratio 1:3. BSA standard particle suspensions have been only analyzed by NTA, TRPS and STEP as stable BSA particle suspensions could so far only be achieved in the submicron size ranges.

7.2.3. Sample preparation of monoclonal antibody suspensions: Comparison of emerging particle size analysis techniques (case study I and II)

For this study monoclonal antibody (mAB) suspensions of mAB1 and mAB2 were investigated. As unstressed sample, the mAB suspensions at the start of the experiment with less than 2 % of aggregates based on HP-SEC data were defined. In addition to the unstressed mAB suspensions, these mAB suspensions were stressed under various conditions to induce aggregation and achieve exemplary protein particles/aggregates. As specific stress conditions lead to specific and characteristic protein particles, we chose following approaches:

(i) Application of stirring stress (= "*mAB-1"*). The mAB suspensions were stirred with 100 rpm for 1h at room temperature as well as at 60 °C.

(ii) Application of temperature stress (= "*mAB-2*"). The mAB suspensions were incubated at 60 °C and 75 °C for 30 min.

(iii) Application of reducing stress (= "*mAB-3*"). The mAB suspensions were reduced due to the presence of 0.024 M DTT for 15 min at 65 °C.

(iv) Application of ionic stress (= "*mAB-4*"). The mAB suspensions were investigated in buffers with increasing NaCl concentrations from 0 mM to 500 mM.

The buffers were chosen considering instrument manufactures requirements with sufficient conductivity, e.g. 20 to 1000 mM for TRPS. The antibody suspensions were measured undiluted to achieve comparable results and to avoid the effect of the dilution on the aggregates. Protein concentrations between 1 mg/ml and 10 mg/ml depending on instrument requirements were investigated. All measurements were performed at room temperature (about 25 °C).

7.2.4. Sample preparation of monoclonal antibody suspensions: NTA evaluation

The investigated monoclonal antibodies mAB1, mAB2 and mAB6 were used for stress-induced aggregation studies. The antibody solutions at the start of the experiment was defined as unstressed samples. These antibody suspensions were subsequently stressed under various conditions (temperature increase or different storage containers, stirring). The shown examples are the result of stirring stress application on the unstressed solution at RT for 30 min and due to different storage conditions, i.e. condition 1 in a 20-L Flexboy® bag and condition 2 in a 2R glass vial at RT. The antibody suspensions were measured undiluted to achieve comparable results and to avoid the effect of the dilution on the aggregates.

7.2.5. Sample preparation of monoclonal antibody suspensions: LUMiSizer® evaluation

The investigated monoclonal antibodies mAB1 and mAB2 have been transferred into a 10 mM sodium phosphate, 10 mM NaCl, pH 6.5 buffer prior analysis. For our experiments, the two physical stress factors of temperature and mechanical stirring have been chosen and kinetic studies were performed. The mAB suspensions were firstly aliquoted (2 ml/vial) into 2R FIOLAX® clear vials (Schott AG, Germany) and closed GUSTO 13 mm butyl hollow stopper. Stirring experiments were performed at different stirring velocities (100 rpm) and temperatures (RT and 60 °C) on an R05 Power IKA stirrer with Surface TEMP Heating Plate (Germany). Samples have been taken after various time points as depicted in the results. Protein density and refractive index were not determined. Literature values indicated protein densities of about 1.41 g/cm^3 and refractive indices around 1.3 to 1.6 (Fischer, Polikarpov et al. 2004, Zolls, Gregoritza et al. 2013).

7.2.6. Sample preparation of protein particles by chemical linkage (DSG-mAB particles).

Prior to preparation, the proteins were transferred into 0.1 M sodium phosphate buffer (pH 8.0) using Amicon Ultra Centrifugal Filter (MWCO 30 kDa, 15 mL) and concentrated up to 44 mg/mL. The preparation of cross-linked protein aggregates using disuccinimidyl glutarate (DSG) has been performed based on Karow et al. (Karow, Gotzl et al. 2015). For the preparation, 10 mg/ml mAB were incubated with 3.4 mM disuccinimidyl glutarate in 150 mM NaCl, 50 mM sodium phosphate, pH 8.0 for 3 h at room temperature. The reaction was stopped by adding Tris/HCl, pH 8.0 (30 mM final concentration) and the cross-linked mAB suspension was stored at 4 °C.

7.2.7. Sample preparation of monoclonal antibody suspensions: Zetasizer-Helix evaluation

For first evaluation, sample series have been performed. For the first sample series, dilution series of mAB2, the concentrated protein suspension with 211 mg/ml in phosphate buffer) was stepwise diluted with buffer to concentrations of 100 mg/ml, 40 mg/ml and 10 mg/ml. The dilution was performed right before the measurements. For the second sample series, samples of mAB1, mAB2 and mAB3 have been analyzed after dialysis process. Stored in the specific formulation buffer, prior analysis a buffer exchange was performed into milli-Q water or respectively the model phosphate buffer using dialysis cassettes with a molecular weight cut-off (MWCO) of 30 kDa. The protein samples were analyzed with a concentration of 10 mg/ml. For further aggregation studies, the investigated monoclonal antibodies mAB1, mAB2 and mAB3 have been transferred into the phosphate model buffer using Amicon Ultra Centrifugal Filter (MWCO 30 kDa, 15 mL). For the aggregation processes caused by extreme pH values and reducing agents the change was applied right before the measurement. All samples have been analyzed in the model system with a concentration of 10 mg/ml.

7.2.8. Sample preparation of monoclonal antibody suspensions: SwitchSENSE® evaluation

The five investigated monoclonal antibodies mAB1-6 and antibody formats AF1-AF4 have been transported and stored in their formulation buffers. For the analysis with the SwitchSENSE® system they had to be coupled on single stranded DNA. For that purpose, the protein was transferred directly into the provided coupling buffer. Further preparation is described under 7.4.2.

7.2.9. Sample preparation of monoclonal antibody suspensions: Protein aggregation case studies

The investigated monoclonal antibodies mAB1, mAB2 and mAB3 have been transferred into the chosen phosphate model buffers and investigated in the concentrations of 5 mg/ml or 10 mg/ml, if not stated differently. If specific preparation was necessary, it was performed as described at the analytical methods below.

7.3. Emerging particle analysis techniques

7.3.1. Nanoparticle tracking analysis (NTA)

Nanoparticle tracking analysis is used to determine particle concentrations and particle size distributions between 50 nm and 1000 nm of hydrodynamic diameter. All NTA measurements were performed using the NS500-HSB particle measuring instrument from NanoSight Ltd (NanoSight, GB) containing a sample chamber of about 0.25 mL, a laser of the category 3B (wavelength of 405 nm), the microscope LM14B and the camera sCMOS. The instrument contains a microfluidic system and inherent pumps to introduce the sample into the measurement cell.
For data capturing and data evaluation, the NTA 2.3 and NTA 3.0 analytical software was used (NanoSight Ltd). The NTA 2.3 software offers two different modes for measuring and capturing of data in the NTA 2.3 software: (1) the general capture mode and (2) the live monitoring mode. In the general capture mode, the capture time is limited by the software to maximal 215 seconds and the camera level settings need to be set prior to the measurement. In the live monitoring mode, in contrast, no time limit is given allowing monitoring real-time stress studies. In addition, capturing an unlimited number of frames lead to improved statistics. During video recording, the camera level can be adjusted anytime. In the more detailed NTA evaluation the measurements of polystyrene standards were performed in the general capturing mode. This mode, however, appeared not suitable for all measurements of protein samples and for that reason both modes were used, as depicted in the experiments. The NTA 3.0 software enables only measurements in the capture mode, but no live monitoring mode. The parameters camera level (CL) - consisting of shutter and gain - as wells as the capturing time (CT) enable the user to set up the perfect conditions for each specific sample depending on the sample properties. For the evaluation of the captured

data video, different detection thresholds (DT) can be adjusted by the operator to distinguish between background and detectable particles. In the analysis the mode size (main peak), mean size and its standard deviation values were obtained.

For each run a total sample volume of 0.80 mL was injected with a sterile 1-ml syringe (BD Discardit) controlled via an external syringe pump with flow rates of 1000 to 1999. The analysis started after a 0.3 mL sample purge in a 250 µl sample cell. The measurements were performed at 20 +/-0.3 °C. The temperature is recorded during the whole capturing process and considered in the evaluation of each measurement. Triplicate measurements were performed for all the polystyrene beads and protein particle samples. As demonstrated by Zhou et al. the total number of valid tracks should be considered as well (Zhou, Krueger et al. 2015). For PS beads only results with at least 100 valid tracks were considered. The suggested required track number for protein samples was stated with 400 valid tracks (Zhou, Krueger et al. 2015). Analysis of protein samples in the capture mode led to valid track numbers of at least 200. The live monitoring mode, in contrast, allowed larger valid tracking numbers of 300 and more due to longer CTs. Prior a set of NTA measurement PS beads with sizes of 200 nm and 600 nm were measured as daily control. The size standard solutions were diluted in deionized and filtrated water to obtain optimal particle concentrations between 1 $x10^7$ and 1 $x10^9$ particles/ml.

Measurements in the comparative evaluation study were performed in the general capture (NTA 3.0) mode and parameters were set with camera levels 3 to 5 and detection threshold 5 to 10. No flow was applied and 5 measurements of at least 60 seconds were performed for each sample. In between every sample measurement the system was flushed with DI-water. Analysis of protein samples in the capture mode led to valid track numbers of at least 200.

Concerning the capturing and evaluation parameters the following settings were used for the more detailed NTA evaluation: All measurements were performed with the auto-adjustment-function (provided by the software developer) for the parameter “Blur”, “Minimum expected particle size” and “Minimal track lengths”. Whenever low particle numbers were expected (e.g. for protein samples) a flow rate of 20 µl/min was employed. The parameters camera level (CL) - consisting of shutter and gain - as wells as the capturing time (CT) were adjusted manually for each experiment. For the evaluation of the captured data video, different detection thresholds (DT) were used to show the impact on the results, as described for each experiment. In order to demonstrate how the parameters CT, CL and DT affect the size distribution and the particle concentration and

with this the overall NTA results, one of the parameters was set as a variable one while all the others were fixed.

The results are expressed as size distribution curve as well as scattering intensity plots over the detected particles sizes by the NTA 3.0 analytical software.

7.3.2. Tunable Resistive Pulse Sensor (TRPS)

The qNano is a bench-top instrument able to measure highly accurate single particle size, particle concentration and particle charge (zetapotential) using particle-by-particle determination. Due to the used principle a sufficient conductivity (20 mM to 1000 mM) is necessary, typically 100 mM salt. The options for measurement set up allow samples with particle concentration between 1 $x10^5$ and 1 $x10^{11}$ particle/ml. It can cover a total size range of 50 nm to 10 µm using various pores. For our measurements mainly the NP100, NP200 and NP300 were used. As the settings are adjusted for each sample to be optimal a calibration of the pulse signal with a polystyrene particle standard of known size supplied by Izon Science Ltd. is necessary before or after a measurement. Measurement control and data analysis is realized with the Control Suite Software, with built in experiment planning and measurement assistants. This data acquisition software allows raw or filtered data to be viewed in real-time.

The buffers were chosen considering manufactures requirements with sufficient conductivity. For each measurement 40 µl of the particle sample was loaded into the top fluid cell and 80 µl of the same buffer were loaded into the bottom fluid cell. The measurements were made with at least 1000 particles being detected and if possible, each sample was run at least in duplicates. From the set of pores three were used to cover the size range from 100 nm to 1000 nm. Depending on the sample the applied stretch to the pore was in the range of 45.01 to 45.03 mm and the applied voltage across the pore in the range from 0.06 V to 0.3 V. The results, a blockage distribution or if a calibration took place a size distribution, are achieved. Blockage magnitudes considerations and calculations of the mean, mode, CV % and percentile values of the number-based PSD were made from the individual particle measurements.

7.3.3. Space and time-resolved extinction profiles technology (STEP-technology®): LUMiSizer®

All experiments were performed with the multi-wavelength analytical photocentrifuge LUMiSizer® (L.U.M. GmbH, Berlin, Germany) using the STEP-technology®. The instrument consists of a rotor with a drive (DC rotor), a light source and a CCD line sensor. The optical detection system enables the use of light sources of 470 nm and 865 nm. Up to 12 different samples can be analyzed simultaneously at constant or variable centrifugal force up to 2300 ×g using the STEP-technology®. Depending on the sample composition, variable centrifugation protocols were used, and they were mentioned in the result sections. For monomodal suspensions fast acceleration and afterwards long-term centrifugation with a constant speed was set. For polymodal and/or polydisperse suspensions, a stepwise acceleration starting with low rotation speeds up to maximal 2300 xg were used. Furthermore, the number of detected profiles, the intervals between these profiles capturing as well as the light factor had to be set. As sedimentation is temperature-depend the temperature was set to 7 °C for all measurements. The manufacturer suggested the use of single-use and reusable rectangular cuvettes with path lengths of 2 mm and 10 mm made of various materials, e.g. polycarbonate or quartz glass. Data analysis was performed with the provided software SEPview resulting in fingerprint, stability kinetics and particle size distributions. The software allowed analysis of the measurements by both, 'Constant Position' and 'Constant Time' methods to determine the PSD. Particle size distribution analysis was realized according to ISO 13318-2. The manufacturer's determined size range was stated with the range from 10 nm to 100 µm. As quality control, silica particles have been measured on irregular base. A sample volume of 1.5 mL suspension was analysed in a rectangular polycarbonate synthetic cuvette with a path length of 10 mm. For all measurements, the 865 nm light was used to measure the more transparent samples. The light factor was set to 0.7 for all protein samples due to the low refractive index. The data was displayed as a function of the radial position, i.e., the distance from the center of rotation. The progression of the transmission profiles contained the information on the kinetics of the separation process and facilitated particle characterization.

7.3.4. Micro-flow imaging (MFI)

Flow imaging was used to determine particle concentrations and to characterize the particle size and morphology between 1 µm and 100 µm of equivalent circular diameter (ECD) based on flow light microscopy. All MFI measurements were performed using the MFI^{TM} DPA-4200 instrument (Brightwell Technologies, Inc.). This instrument enables the measurement of up to 900,000 particle/ml with a size of 2.5 µm and an analysis rate up to 150 µl/min. The manufacturer provides a measurement (MVSS) and analysis software (MVAS). The depicted size range for the instrument is 1 µm to 70 µm of particle diameter. The MVSS software allows, e.g. washing steps, measurements settings and automatically optimized illumination and generates a dataset of different parameters like ECD, particle concentration as well as a range of shape and image contrast parameters about the measured sample. Subsequent, in the MVAS software these parameters can be used, and filters can be created by which a heterogeneous sample solution may be subdivided into its individual particle types. Prior a set of MFI measurements a system suitability test using 1 ml DI-water was performed. To verify the measurement results a 5 µm Count-Cal^{TM} Particle Size Standard was measured before and after every sample set. For each run a total sample volume of 1.0 mL was injected with a filtered pipette tips to avoid contamination. Illumination was optimized before every sample run. The flow cell was purged with 0.2 mL of the sample. About 0.55 mL of the sample were analyzed at a flow rate of 0.17 mL/min. For all measurements the 1-ml standard SOP was used. It must be noted that the system analyzes ~ 80 % of the dispensed volume. In between every sample measurement, the system was purged with about 5 ml DI-water.

The results were expressed as size distribution curve as well as number of particles per milliliter registered at different size ranges based on their ECD. In addition, particle images are provided for each ECD range. A further classification due to filter provided by the MFI View Analysis Suite (MVAS) software was not performed.

7.4. Novel technologies for protein aggregation studies

7.4.1. Zetasizer Helix: combination DLS and Raman measurements

All measurements have been performed using the Zetasizer Helix instrument (Malvern Instruments Ltd., Malvern, UK). It consists of the Zetasizer unit measuring DLS as described by the Zetasizer

Nano-ZS (He-Ne Laser 633 nm, max. 10 mW) and a Raman RxN1 spectrometer manufactured by Kaiser Optical Systems (Diode Laser 785nm, Max 280mW at the sample). For the measurement 50 µl to 110 µl protein suspension were introduced into specific thin quartz cuvettes and the cuvette was sealed by a teflon stopper avoiding evaporation. After an equilibration time of 60s in the general measurement procedure the first step is the DLS measurement for size determination detecting backscattering at 173 °C using an automatically optimized attenuator. The settings are the same as for single DLS measurements with the Zetasizer Nano-ZS. For the second step, the collection of the Raman spectrum typically 15 s accumulation and 10 co-adds were used. In addition to the sample, a Raman spectrum of the buffer was collected. For evaluation this spectrum was subtracted from the protein spectrum. The resulting spectrum was then normalized and specific bands like the amide I band were further investigated (compare Table 1). In case of secondary structure analysis, there are many Raman bands whose intensities and frequencies to consider. For the evaluation, a multivariate analysis is required. The manufacturer provides a proprietary partial-least squares (PLS) numerical model to predict secondary structures of protein samples. Lewis et al. demonstrated the approach as suitable in their study (Lewis, Qi et al. 2014, Zhou, Qi et al. 2015).

In thermal ramp experiments, data was acquired sequentially. After an equilibration time of 60s at each temperature DLS measurement and subsequent Raman measurement was performed before the temperature increased to the next acquisition temperature. The final data evaluation was performed with the Helix software (Lewis, Qi et al. 2014, Zhou, Qi et al. 2015).

7.4.2. SwitchSENSE® technology

All SwitchSENSE® analyses have been performed in Martinsried in cooperation with the Dynamic Biosensor (DBS) team. For the analysis, the protein of interest was coupled to a single strand DNA molecule. For that purpose DBS provided different coupling kits and protocols (Langer, Kaiser et al. 2014). As the most efficient coupling approach for the selected proteins, all mABs were covalently conjugated to cDNA via lysines according to the provided DBS protocol. Firstly, 5′-Thiol modified cDNA was reduced with TCEP for 30 min in 50 mM sodium phosphate buffer (pH 7.2, 150 mM NaCl). Subsequent this cDNA was purified by RP-HPLC and modified by 6-Maleimidohexanoic acid N-hydroxysuccinimide ester using the manufacturer's protocol (Pierce, Germany). The modified DNA was purified from excess linker via Amicon centrifugation filters

and the mAB was mixed with DNA in a ratio of 2:1. In the last step, mAB–DNA conjugates were purified by anion exchange chromatography. This purified conjugate was finally injected to a prepared chip, and after the binding of the conjugate to the chip by hybridizing of the DNA strands analysis was performed (Langer, Hampel et al. 2013).

7.5. Established methods and technologies for particle detection, characterization and aggregation studies

7.5.1. UV/Vis Spectroscopy: Protein concentration and A320 value determination

UV/Vis spectroscopy was used to determine the absorbance of protein suspensions at various wavelengths. For each suspension a spectrum from 260 nm to 350 nm was recorded either by the two-beam UV/Vis spectrometer Lambda 35 or the NanoDrop 2000c (only for samples with low volumes). The protein concentration was determined based on the absorbance at 280 nm and calculated applying Beer-Lambert law. In case of using the NanoDrop 2000c the absorbance at 340 nm automatically was used for a bichromatic normalization by the NanoDrop software. As proteins absorb light only up to about 310 nm, the absorbance value which occurs at longer wave lengths is mainly caused by scattering and depends on particle properties present in the suspension (IUPAC 2006, Lakowicz 2006). For the analysis using Lambda 35 50µl to 100µl of the protein solution and the reference buffer, respectively, were filled into a micro cuvette (Eppendorf AG). An absorbance spectrum from 280 nm to 360 nm was taken with the two-beam UV/Vis spectrometer Lambda 35 (Perkin Elmer Inc.) and the depicted absorbance value at 320 nm was determined (A320). The same buffer was used as blank and reference. The A320 value is often used as turbidity indicator.

7.5.2. Opalescence/Turbidity determination

The turbidity of the suspensions is used as a stability indicating parameter of protein suspensions as the presence of particles can be sensitively detected. It was determined using a turbidity photometer (Hach Lange). For each measurement 1.5 mL of the sample were filled into a clean glass cuvette. In NTU mode, the turbidity value was achieved in NTU (Nephelometric Turbidity Units). Both values, the A320 (described under 7.5.1) as well as the turbidity value in NTU, are not suitable at this point to describe single particle sizes or properties. They, however, describe the

overall sample transmission as highly sensitive method to screen for the presence of particles and an essential property for transmission-based techniques like the LUMiSizer®.

7.5.3. High-Performance Size Exclusion Chromatography (HP-SEC)

Size exclusion chromatography was performed to monitor antibody monomer content as well as soluble low molecular weight aggregates up to 100 µm. For the antibody suspensions a TSK-gel G3000 SWXL column was chosen. Larger particles were removed by prior centrifugation (3000 g, 5 min) and an inline filter to prevent clogging of the column. All antibodies were analyzed at a protein concentration of 1 to 5 mg/mL. For the best resolution two different methods were applied depending on the investigated mAB. For mAB1 20 µl per run have been injected and the flow rate was set to 1.0 mL/min. For mAB2 and mAB3 50 µl sample was injected per run and the flow rate was set to 0.7 mL/min. Separation time was set to 25 min for all mABs. Different separation buffers, however, were chosen to achieve a good separation of the different antibodies: mAB1 with 50 mM sodium phosphate, 500 mM sodium chloride, pH 7.0 and mAB2 with 200 mM L-arginine, 100 mM sodium phosphate, pH 6.8. To evaluate the separation efficiency of the column, a standard (BR-mix, Bio-Rad Laboratories GmbH) was investigated at least at the beginning and the end of each sample set. To detect the separated peaks, the absorbance at 280 nm was monitored by a UV/Vis detector. Monomer and aggregate contents were calculated as a proportion of the total area of all protein peaks in the chromatogram. Total peak areas were also monitored to assess a loss of soluble protein during the stress conditions.

7.5.4. Size determination using Dynamic Light Scattering (DLS): Zetasizer Nano-ZS, ZEN 3600

Dynamic light scattering measurements were chosen to monitor particle hydrodynamic sizes in the size range from a few nanometers up to 1 µm. All protein measurements were performed at a protein concentration of 1 to 5 mg/mL. For a standard size determination, 75 µl of the protein suspension were filled into a disposable micro cuvette (UV-cuvette micro, Brand GmbH & Co. KG). Measurements were performed at 20 °C after an equilibration time of 60 s with 3 measurements à 11 sub runs à 10 s, without delay between measurements. The instrument detects the scattered light at an angle of 173°. The attenuator and the measurement position were set

automatically. Correlator setting: Logarithmic baseline – symmetric, log mode – enabled, fast mode – disabled, linear mode – disabled.

The data were analyzed by the multiple narrow mode model (high resolution) provided by the Zetasizer Software. The cumulant analysis gives two values, a mean value for the size and a width parameter, which is called the PDI. It is important to note that the mean size, which is given by the cumulant analysis, is intensity weighted and known as z-average (Malvern). The z-average gives the average mean hydrodynamic diameter of a particle.

7.5.5. Size determination using Dynamic Light Scattering (DLS): DynaPro PlateReader2

All protein measurements were performed at a protein concentration of 5 mg/mL. Each sample was measured at least in triplicates. For one measurement 150 µl protein suspension were filled into a well of the 96-well plate (UV-Star® Microplate, half area, Greiner Bio-one). After the plate was filled it was sealed with an optical tape (iCycler iQ® Optical tape, BIO-RAD Laboratories Inc.) to avoid evaporation. After an equilibration time of 5 min the measurements were performed at 25 °C with one run à 10 sub runs à 3s without delay between measurements. The data was subsequently evaluated with the Software Dynamics (Version 7.1.7) based on the autocorrelation function and the results are similar to the results of the Zetasizer Nano-ZS.

7.5.6. Zeta potential (ZP) determinations

An electric double layer is formed at the phase boundary between the protein surface and the liquid medium. The zeta potential ζ represents the potential at the shear plane between those two layers and becomes apparent when shearing the diffusive layer. As it cannot be directly measured, the calculation of the zeta potential is based on the electrolyte theory developed by Smoluchowski, Debye und Hückel, which establishes a correlation between the electrophoretic mobility µ and the zeta potential is used for the calculation. The movement of the protein molecules is induced by application of alternating voltage, i.e. the proteins move due to their charge towards the electrodes. The resulting electrophoretic mobility µ can be measured by DLS. The measurement is hence based on the same principle as the kD-measurement. The only difference being that the protein movement is not due to Brownian motion but results from voltage application and protein charge electrophoretic mobility µ.

For the measurement, 3 ml of the different mAB solutions with a concentration of 5 mg/ml were prepared in 5 ml Eppendorf tubes. The zeta potential was determined as triplicates, so that 1 ml of solution was filled for one measurement in a Zetasizer DTS 1060/1061 cuvette using a 1 ml syringe (BD Plastipak^{TM}). The openings of the cuvette were closed by using the provided caps. The measurement was performed on Zetasizer Nano series using the SOP "Vorlage Zeta Antikörper2_modified 90V", fixing thus the driving voltage at 90 V.

7.5.7. Differential Scanning Calorimetry (DSC)

DSC measurements were performed to determine the thermal melting temperature (Tm) of the mABs. Before each measurement, the protein solution was degassed and filled into the sample chamber. Measurements were carried out at a protein concentration of 1 mg/mL. The used measurement settings are a heating rate of 60 K/h, a filter period of 16 s and a temperature ramp of 20 to 90°C. The measured c_p was normalized to the concentration and the thermogram of the assay buffer was subtracted from the sample thermogram to remove buffer effects.

7.5.8. Intrinsic Tryptophan Fluorescence Spectroscopy (ITF) in combination with backlight scattering detection using Prometheus NT.48

For each measurement, a standard capillary was filled with about 10 µl sample and was placed onto the capillary tray. A discovery scan was performed to adjust the initial fluorescence intensity and position of each capillary. The LED (intensity maximum at 285 nm) power was set to 15 % such that the fluorescence emission was between the optimal detection range of 8000 to 18000 counts at 330 nm and 350 nm, respectively. The heating rate was set to 1 K/min and a temperature ramp from 20 °C to 95 °C was chosen. For the evaluation the measured fluorescence values were smoothed by the software and the F_{350}/F_{330} ratio as well as the first derivative of the ratio was calculated and plotted as a function of temperature. The thermal melting temperatures Tm were determined as local maxima of the first derivative. In addition to the melting curve based on the fluorescence signal, a light scattering signal is detected to monitor aggregation events and determine the aggregation start Tagg. All measurements were performed in triplicates.

7.5.9. Intrinsic Tryptophan Fluorescence Spectroscopy (ITF) in combination with right angle light scattering detection using Optim 1000

For each measurement about 9 µl protein sample were filled into micro cuvette arrays and placed into the instrument tray. Using the control software Optim Client 1.5 (Avacta Analytical) experiment settings were selected. In all cases, the method „stepped thermal unfolding and aggregation“ was used. Further settings include exposure time of 1000 ms, center wavelength of 380 nm and slit of 100 µm. The heating rate was set to 1 K/min and a temperature ramp from 20 °C to 95 °C was chosen. For the evaluation the measured fluorescence values were smoothed by the software and the F_{350}/F_{330} ratio as well as the first derivative of the ratio was calculated and plotted as a function of temperature. After the measurement the data was evaluated in the Optim Analysis software (Avacta Analytical). The results include the melting temperature Tm, the unfolding start Tonset and the scattering start temperatures Tagg for the wavelengths 266 nm and 473 nm. All measurements were performed in triplicates.

PART III: Results and Discussion

~

8. Evaluation of selected emerging particle detection and characterization techniques for protein particles

Out of the vast number of emerging techniques for general particle detection and characterization, the three emerging technologies of NTA (Nanosight/Malvern Panalytics), TRPS-technology (Izon Science) and STEP-technology® in a photocentrifuge (LUM GmbH) have been selected to evaluate their applicability for protein particles and routine biopharmaceutical samples. In the first two chapters (chapter 8.1 and 8.2) a comparative study was performed investigating the same samples with all three techniques. Based on the results NTA and LUMiSizer® have been chosen for a more detailed evaluation (chapter 8.3 and 8.4).

8.1. Comparative case study I: Applicability of emerging techniques on a BSA particle standard suspensions (subvisible range)

In the first part of the comparative study BSA particle standard suspensions BSA1, BSA2 and BSA3 with defined size ranges (see Table 5) have been analyzed by each technique.

8.1.1. Nanoparticle tracking analysis (NTA) measurements

Nanoparticle tracking analysis is a technique highly suitable for size determination and quantification in the submicron range and has been evaluated previously for biopharmaceutical applications (Filipe, Hawe et al. 2010, van der Pol, Coumans et al. 2014, Gross, Sayle et al. 2016). For internal control, the following system suitability test (SST) was performed prior to each sample measurement: Analysis of 100 nm, 200 nm and 600 nm standard PS-bead suspensions with concentrations between 1 $x10^5$and 1 $x10^7$ particle/ml. The SST measurements in all cases resulted in expected size and concentrations.

The analysis of all three BSA standard suspensions was performed. All suspensions could be technically measured, but only BSA1 (nominal size: 177 nm) and BSA2 (nominal size: 500 nm) could be analyzed in a reliable manner. BSA3 (nominal size: 750 nm) was also measured, but due to high polydispersity and the presence of particles larger than 1 µm, the parameter setting appeared challenging and results were hard to analyze.

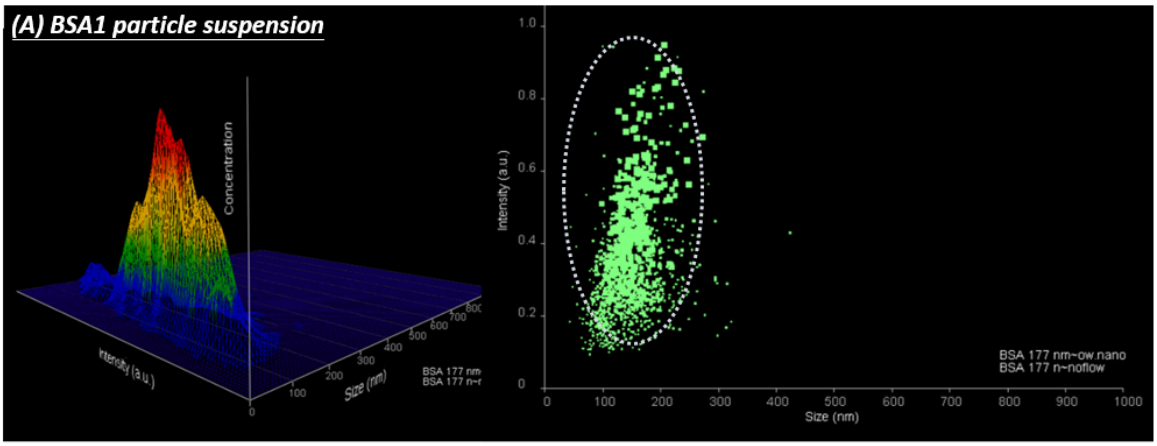

(C) Result Table	BSA1	BSA2
Parameter settings	**CL 5, DT 5**	**CL 3, DT 5**
Particle concentration (#/ml):	1.53 ± 0.2 E08	1.42 ± 0.1 E08
Mean size (nm)	164	452
Mode size (nm)	152	411
D10	126 nm	231 nm
D50	154 nm	422 nm
D90	204 nm	635 nm

Figure 3- 1: Comparative case study I: Nanoparticle tracking analysis BSA1 and BSA2 standard particle suspensions.
Triplicate analysis was performed using BSA standard particles BSA1 and BSA2 with an estimated size of (A) 200 nm and (B) 500 nm (TEM and DLS). The three measurements are merged and results are presented in 2D and 3D intensity plots (A) BSA1 shows one clear population with particle intensities between 0.1 a.u. and 1 a.u. around 200 nm (B) BSA2 shows a broad size and intensity distribution with about three populations at 200 nm, 400 nm, 600 nm. The particle intensities are between 0.2 a.u. and 1.6 a.u. (C) Summary of NTA data for BSA particle.

Exemplary, the NTA results of BSA1 and BSA2 are shown in Figure 3- 1. NTA measurements of BSA1 (Figure 3- 1A) led to a mean size of 164 nm and a mode size of 152 nm, whereas the expected size was 177 nm. The size distribution reaches from 50 nm to 250 nm. Considering the intensity plots scattering intensities of these particles lay between 0.1 a.u. and 1.0 a.u. (ΔI=0.9 a.u.). The major part of the particles scatters with an intensity of 0.5 a.u.. The NTA measurement of

BSA2 led to a mean size of 452 nm and a mode size of 411 nm, whereas the expected size was 500 nm, over a total size distribution from 100 nm to 1 µm. The scattering intensities were between 0.2 a.u. and 1.6 a.u. (ΔI=1.4 a.u.). Both samples, BSA1 and BSA2, show total particle concentrations of about 1 x10^8 particle/ml and were in the advised range. Size and concentration results are in high agreement with the manufacturer and the DLS data (see Table 5).

One additional output of NTA measurements are intensity plots. This plot gives information about the polydispersity. BSA1 occurs with low polydispersity and is comparable to the 200 nm PS sample as the intensity range (ΔI) is similar. The occurrence of various sizes and various intensities indeed appears if the polydispersity increases. This is the case for BSA2 (Figure 3- 1B). In BSA2 results, based on the intensity plots, one could discriminate two populations: one at 400 nm with lower intensity, but higher concentration and one at 600 nm with higher intensity but lower concentration. The intensities can be used to identify additional information or optical properties: The ΔI is also influenced by particle shape as inhomogeneous shape leads to a high distribution in light scattering. Same size and different intensities are the result of either differences in the RI or differences due to shape and surface differences. In contrast to the BSA particles, PS particle of 200 nm (RI = 1.59) show scatter intensities between 0.3 a.u. and 1.4 a.u. (ΔI=1.1 a.u) with the major part around 1 a.u.. Mean and mode size are around 200 nm. This difference in the intensity characterizes the optical properties of the particles, in particular the RI. As protein particles are known to have lower RI (RI =1.3) and appear possibly more translucent. Determination of RI based on NTA measurements have been shown by Gardiner et al. and van der Pol et al. (Gardiner, Shaw et al. 2014, Van Der Pol, Coumans et al. 2014). For direct discrimination of different particles in one sample the difference has to be quite large to overcome the deviations around the intensity maximum. This is the fact, e.g. for gold and latex particles as shown in previous studies. In general, higher scattering intensities are beneficial to eliminate background noise and lower the size detection range.

A general evaluation of NTA based on the experiments with the BSA standard suspensions:

In general, there is no sample preparation necessary, but the narrow measurement range for particle concentrations might require dilutions to obtain the required measurement range. The instrument was initially calibrated based on PS-beads during the installation set-up and further calibration is not necessary. However, control measurements before each measurement series are advisable. The calibration based on PS-beads is also applicable to protein particles as the size measurement

principle is independent of light intensity (optical properties) as the size determination is based on the diffusion coefficient. The difference in the optical properties indeed is further seen in the applied parameter settings, in particular the CL. For PS particles in this size range a CL of 3 is sufficient, while protein particles need CL5 to be detectable. That means more light is needed to obtain sufficient scattering. Instrument settings are highly variable enabling to identify best parameter for each sample but make measurement operator- dependent and less comparable. Furthermore, we demonstrated that the operator may have a significant influence on the result (Gross, Sayle et al. 2016). NTA measurements are hardly to automate, time-intensive and as the operator sets parameters for each sample, general comparability and standard operation procedures are questionable.

NTA in consideration of the five main challenges of particle detection in biopharmaceuticals:

(i) NTA cannot close the complete 1 µm gap but is able to detect particle around 1 µm as its upper size limit.

(ii) NTA shows narrow concentration ranges of 1 $x10^7$ to 1 $x10^9$ particle/ml, but with its submicron size range it is a great complementary method to micrometer range instruments, like MFI.

(iii) NTA as particle-by-particle technique shows higher resolution of polydispers samples, but highly polydispers samples are challenging due to size-intensity correlation.

(iv) NTA is a size determination technique based on Brownian motion and enables particle quantification.

(v) NTA obtains two size results: the mean size, best applicable for describing monomodal and low dispers samples, and the mode size, best applicable for describing polymodal samples containing several size populations.

(vi) NTA is not depending on specific protein particle calibration standards and as useful method for mono- and low disperse samples all particle standards with sufficient scatter intensity can be detected.

The measurement of the BSA standard particle already showed the potential of NTA measurements also for protein-based and protein-like particle. In this case, we had an expected nominal size (Table 5) and settings, like CL or DT, could be adjusted based on these estimations/values. If this is not the case, NTA analysis might be more challenging. Antibody samples with high polydispersity and unknown size distribution are extremely challenging samples.

8.1.2. Tunable resistive pulse sensing technology (TRPS) – qNano measurements

The tunable resistive pulse sensing technology (TRPS) is an enhanced RPS instrument with an elastic pore. The TPRS technology as performed by the qNano instruments (Izon Science Ltd.) has been already evaluated for PS-beads, but best to our knowledge not for protein-based or protein-like particle (Anderson, Kozak et al. 2013, Blundell, Mayne et al. 2015, Weatherall and Willmott 2015). For internal control, prior each measurement a set of standard and calibration particle suspensions provided by Izon Science Ltd. have been analyzed (SST). The SST measurements in all cases resulted in expected size and concentrations. The analysis of all three BSA standard suspensions was performed. In general, all BSA standard particle suspensions were measured and analyzed. The BSA1 and BSA2 samples in particular met the expected results concerning size distributions. Exemplary some results of BSA1, BSA2 and BSA3 are shown in Figure 3- 2.

BSA1 led to a size distribution from 110 nm to 840 nm with a main peak size of 210 nm and smaller peaks at 300 nm and 450 nm. The TRPS measurement of BSA2 led to a size distribution from 440 nm to 1600 nm with main peak size around 500 nm and a smaller peak around 600 nm. The PSD of BSA2 in triplicates is illustrated in Figure 3- 2A. Concentration values have not been obtained as it was not possible to measure sufficient sample volume before pore blockage to allow concentration calculations. The size determination results are in agreement with the manufacturer and the DLS data of 177 nm (BSA1), respectively 500 nm (BSA2). The measurement of BSA3 in duplicates resulted in a size distribution from 75 nm to more than 1500 nm with main peak size of 94 nm and smaller peaks at 150 nm and 303 nm. These results do not meet the expected sizes of about 750 nm from manufacturer or respectively 990 nm from DLS data.

The polydispersity and composition of the sample is based on the counted particles and populations can be weighted by their real portion. BSA2 shows a broad and highly polydisperse composition with more than 95 % of the particles in the submicron range with a distribution range of 1160 nm. The results of the BSA1 sample are shown in Figure 3- 2B illustrated as blockage magnitudes (yellow) and compared to the blockage magnitudes of the 300 nm size standard (magenta) without any prior calibration. BSA1 appears less polydispers with a distribution range of 720 nm and the presence of two clear populations (around 200 nm and 450 nm) covering about 90 % of the whole population. The BSA3 sample is the most polydispers as the distribution range is about 1800 nm. About 80 % of the particles are between 75 nm and 375 nm in size.

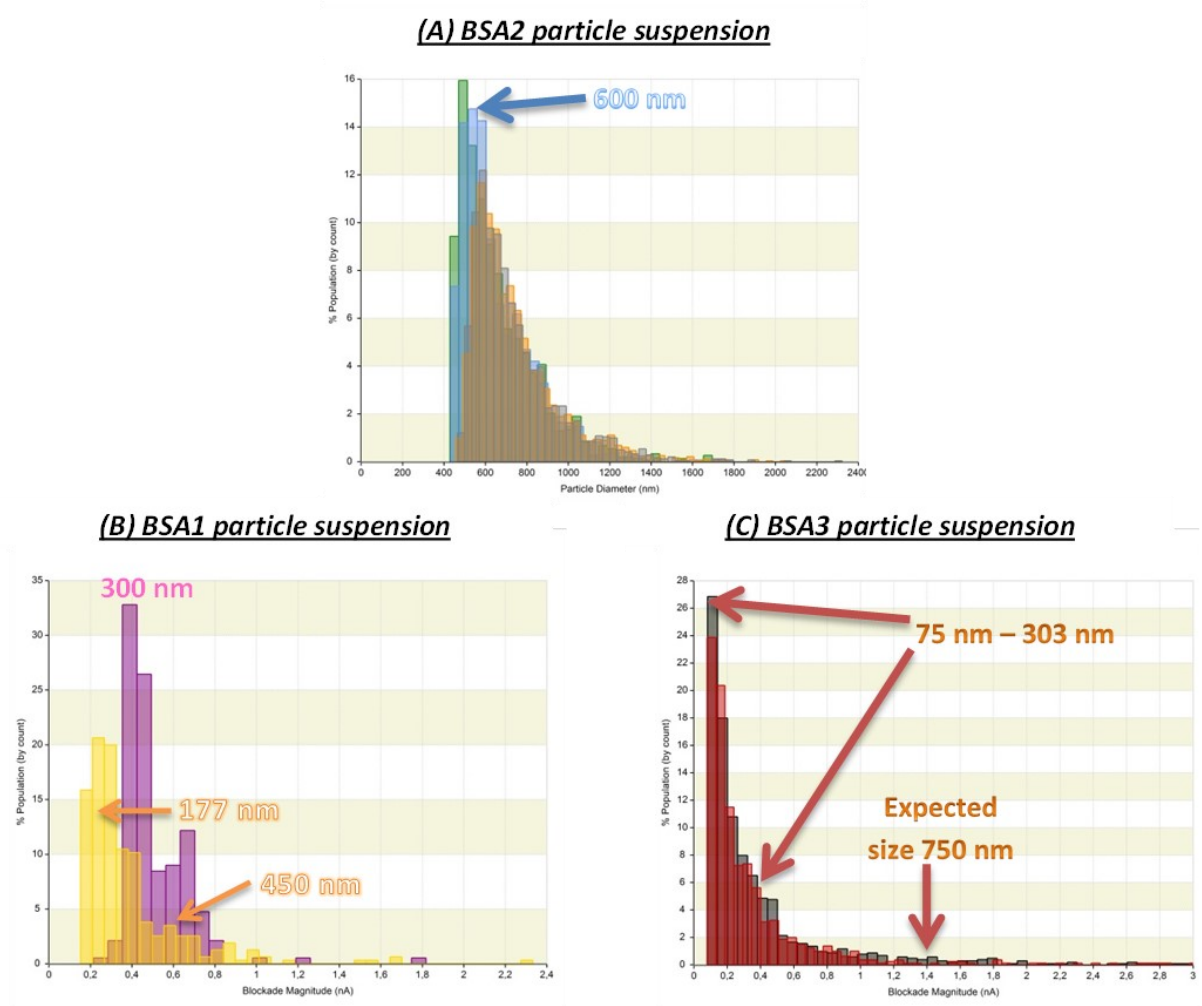

Figure 3- 2: Comparative case study I: TRPS technology measurements: BSA1, BSA2 and BSA3 standard particle suspensions.
(A) Triplicate analysis (green, blue, orange) of BSA2 was performed after calibration and the resulting PSD shows a broad size distribution and a main population at about 500 - 600 nm. (B) Measurement results without calibration of BSA1 (yellow) and the provided calibration standard of 300 nm (magenta). The blockage magnitude ratios correlate to the expected size ratios independent of the particle material. (C) Measurements results of BSA3 (duplicate) were first performed without calibration leading to a particle distribution over the direct blockage magnitude. Size estimations based on later calibration lead to a size range of the main population between 75 nm and 303 nm. Particles with the expected size of 750 nm could only be rarely detected.

A general evaluation of TRPS based on the experiments with the BSA standard suspensions:

In general, there is no specific sample preparation necessary, but due to potential pore blockage at high particle/protein concentrations dilutions might be required. A critical point for RPS as well as TRPS measurements is that specific conductivity ranges (20 to 1000 mM) need to be considered. Before each measurement a stable current and optimal settings (stretching, voltage, pressure) have

to be achieved. Subsequently, calibration is performed and is specific for each setting. In consequence, every change in the settings requires a new calibration measurement. However, measurements are possible without prior calibration and lead to a blockage magnitude distribution (Figure 3- 2B-C). In this case size estimations are possible (Figure 3- 2B), but PSDs cannot be obtained. The difference in the optical properties of PS-beads and protein particles has no direct influence on the result as the size determination, because the measurement principle is based on the volume-based current blockage. For that reason, the properties of the calibration particles are not as essential as for optical measurements.

Best to our knowledge TRPS measurements are not automated so far, but measurements are not as time intensive as e.g. NTA. Furthermore, the operator has in general low influence on the final outcome and general comparability and standard operation procedures seem possible if the same standard for calibration is used. The greatest advantage was demonstrated by Anderson et al. with the best resolution of multimodal systems (Anderson, Kozak et al. 2013).

TRPS in consideration of the five main challenges of particle detection in biopharmaceuticals:

(i) TRPS is an option to close the 1 µm gap even with one single pore.

(ii) TRPS has nominal a wide concentration ranges from $1x10^5$ to $1x10^{11}$ particle/ml and a great total size range from 40 nm to 10 µm, but the complete size range can only be achieved with various pores.

(iii) TRPS as particle-by-particle technique show the highest resolution of polydispers samples, but highly polydispers samples are challenging due to limits of the tunable pore (Anderson, Kozak et al. 2013).

(iv) TRPS is a size determination technique based on resistive pulse sensing and enables particle quantification.

(v) TRPS is not depending on specific protein particle calibration standards. It is a powerful method for mono- and low disperse samples all particle can be detected.

The measurement of the BSA standard particle already showed the potential of TRPS measurements also for protein-based and protein-like particle. In this case we investigated samples with mostly low polydispersity and with sizes below 1 µm. If broader size ranges and higher polydispersity, like in stressed protein solutions are the case challenges may occur due to blockage. The given conductivity of 20 mM to 1000 mM limits the buffer that can be tested.

8.1.3. STEP-technology® - LUMiSizer® measurements

The space and time-resolved extinction profiles technology (STEP-technology®) is a technology used for instance in the analytical photocentrifuge LUMiSizer®. The technique was initially developed for red blood cells, but is nowadays mainly used in chemical approaches like paints, cosmetics or ceramic materials, as well as food industry and all types of dispersions/emulsions (LUM GmbH 2016).

For internal control, prior to the measurement series a silica particle suspension containing 500 nm beads provided by L.U.M GmbH have been analyzed. The measurements resulted in expected nominal size of 550 nm. The SST measurements in all cases resulted in expected size distribution. The analysis of all three BSA standard suspensions was performed. All BSA standard particle suspensions were measurable and have been analyzed without meeting the limitations of the system. The BSA particle standard suspensions were analyzed with a concentration of 1 mg/ml and occurred with start transmissions between 40 % and 60 %. Even in dilutions down to 0.2 mg/ml they appeared as suitable for LUMiSizer® experiments. Exemplary results of BSA1 and BSA2 are shown in Figure 3- 3 and Figure 3- 4.

BSA1 led to a size distribution from 100 nm to 300 nm and 2000 nm to 5000 nm with the main fraction around 200 nm. The measurement of BSA2 led to a size distribution from 300 nm to 1000 nm and 3000 nm to 10000 nm with a main fraction around 600 nm. Concentration values have not been obtained as the principle cannot obtain particle concentrations, but size determination results are in agreement with the manufacturer and the DLS data (Table 5).

In addition to the final PSD determination, the method allows statements about the polydispersity/polymodality, the sedimentation behavior as well as particle interactions. The first result of each sample that was achieved in real-time is the extinction profile fingerprint (Figure 3-3A and Figure 3- 4A). It monitored the space resolved transmission profile over the whole cuvette over time. The start sample transmission should be homogenous and between 30 % and 80 %. During the centrifugation process particle populations moved towards the cuvette bottom and the transmission increased. The transmission maximum of an empty cuvette is about 90 % to 95 %. The progress of clarification and particle movement was monitored by the boundaries and intervals and steepness/shape of these boundaries describe sample properties.

(A) BSA1 transmission profile fingerprint

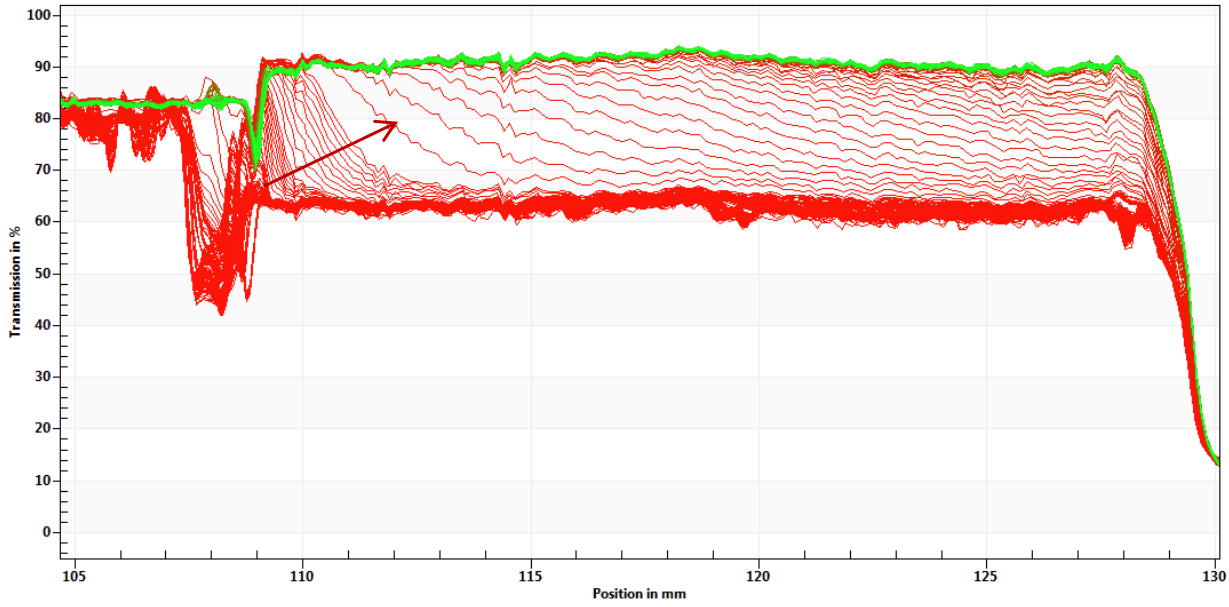

(B) BSA1– sedimentation velocity

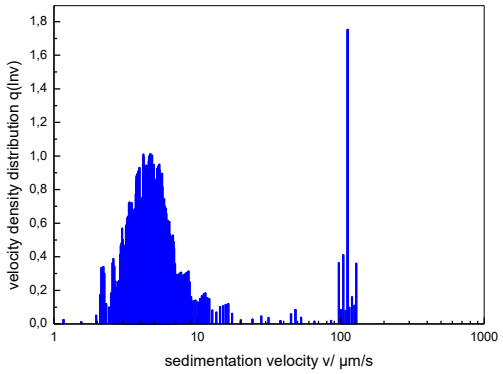

(C) BSA1– particle size distribution

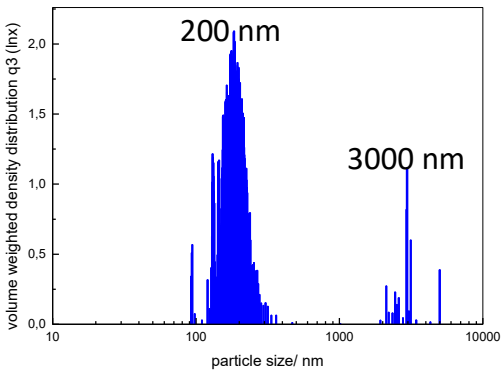

Figure 3- 3: Comparative case study I: STEP-technology® measurement BSA1 standard particle suspension. (A) Transmission fingerprint of the monomodal BSA1 particle suspension. Over the investigated time, integral clarification was detectable. The arrow indicates the progress of the clarification process. Based on this movement the sedimentation velocity distribution (B) and finally the volume weighted PSD (C) have been calculated resulting in a main population around 200 nm.

(A) BSA2 transmission profile fingerprint

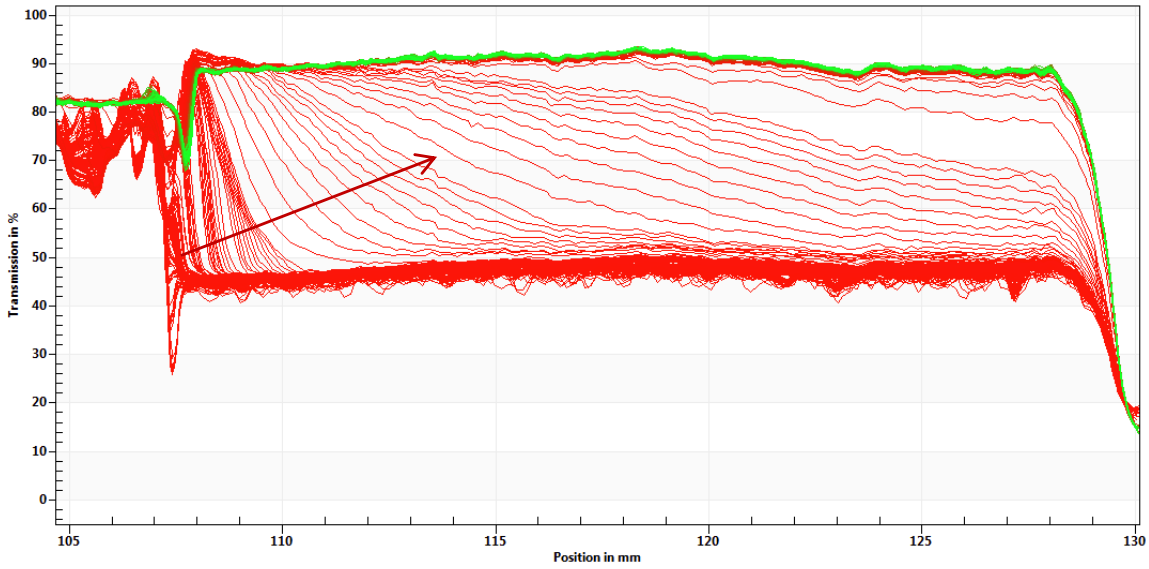

(B) BSA2– sedimentation velocity

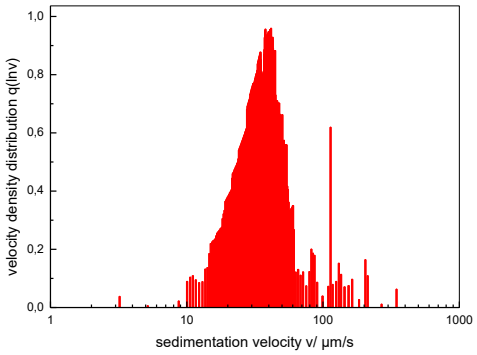

(C) BSA2– particle size distribution

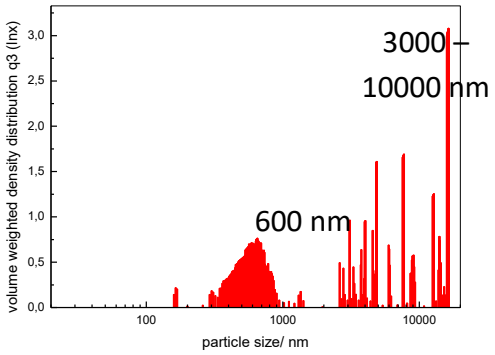

Figure 3- 4: Comparative case study I: STEP-technology® measurement BSA2 standard particle suspension. (A) Transmission fingerprint of the monomodal BSA2 particle suspension. Over the investigated time, integral clarification was detectable. The arrow indicates the progress of the clarification process. Based on this movement the sedimentation velocity distribution (B) and finally the volume weighted PSD (C) have been calculated resulting in a main population around 600 nm.

For BSA1 the start transmission was about 60 % (red profiles). During the centrifugation process the transmission increased stepwise to over 90 % due to particle sedimentation (green profiles). The first boundary movement was observable fast and appeared as clear and sharp lines. It indicated a first population of larger particles with low polydispersity. With the ongoing process, these boundaries changed into a more horizontal and tailing shape and a final horizontal clarification. This indicated a further particle population with higher polydispersity. The intervals

between each profile remained constant in the end and no strong particle interaction was detected. The BSA1 suspension consisted of two populations, whereas the second population was the more dominant fraction. The sample can be dedicated as low polymodal, polydisperse sample. Without any material information, i.e. particle density, only the velocity distribution of the sample is achieved as seen in Figure 3- 3B.

This graph does not give information about the size but converts the information of the fingerprint in a first distribution highlighting the sample composition, polydispersity and modality. For BSA1, a large population was visible with a sedimentation velocity maximum around 5 µm/s (smaller particles) and a smaller second peak with a sedimentation velocity around 100 µm/s (larger particles). In particular, the first peak indicated a high polydispersity as it included particles with a sedimentation velocity range from 2 µm/s to 10 µm/s. Based on this information we can define the sample as bimodal, polydisperse sample. Under the consideration of the density, the calculation of volume weighted particle size distribution (Stokes equation) was realized (Figure 3- 3C). The second and smaller peak with particles in the micrometer range might illustrate aggregates or larger associated due to storage and/or preparation. Due to instrumentation limitations neither NTA and TRPS nor DLS were able to detect this population.

For BSA2, similar centrifugation progress as for BSA1 was observable, but based on the fingerprint profiles BSA2 appeared more polydispers containing at least four populations. These four populations are hardly discriminable in the sedimentation velocity distribution, but in the volume-weighted PSD. In addition, the suspension stability can be evaluated, interesting for sample comparisons, by the integral and stability index.

For an evaluation of an even more complex sample, a bimodal mixture of BSA1 and BSA2 in the ratio 3:1 was analyzed and the results are shown in Figure 3- 5. The start transmission was lower than the start transmissions of the single suspensions with about 58 %. After the centrifugation process, however, the final transmission was similar to the single suspensions. In contrast, the extinction profile fingerprint showed two clear bands highlighted by the arrows 1 and 2 (Figure 3-5A).

Both populations moved in clear lined boundaries with the slight polydisperse tendency (i.e. boundaries change from vertical to horizontal). The first population (arrow 1) might also consist of two populations. The velocity distribution confirmed this suggestion as the result showed three peaks (Figure 3- 5B): The first sedimentation velocity peak with the maximum at 5 µm/s and the

third peak with about 100 µm/s matched with the peak of the 177 nm BSA sample. The second population showed a sedimentation velocity peak of 30 µm/s with a peak width from 20 to 60 µm/s. The corresponding particle size distribution is shown in Figure 3- 5C indicating particle populations of 200 nm and 600 nm. Besides the two main populations, further particles with sizes up to 6000 nm were detected as tailing of the 600 nm peak. The resolution of both BSA standards is possible in a reliable manner.

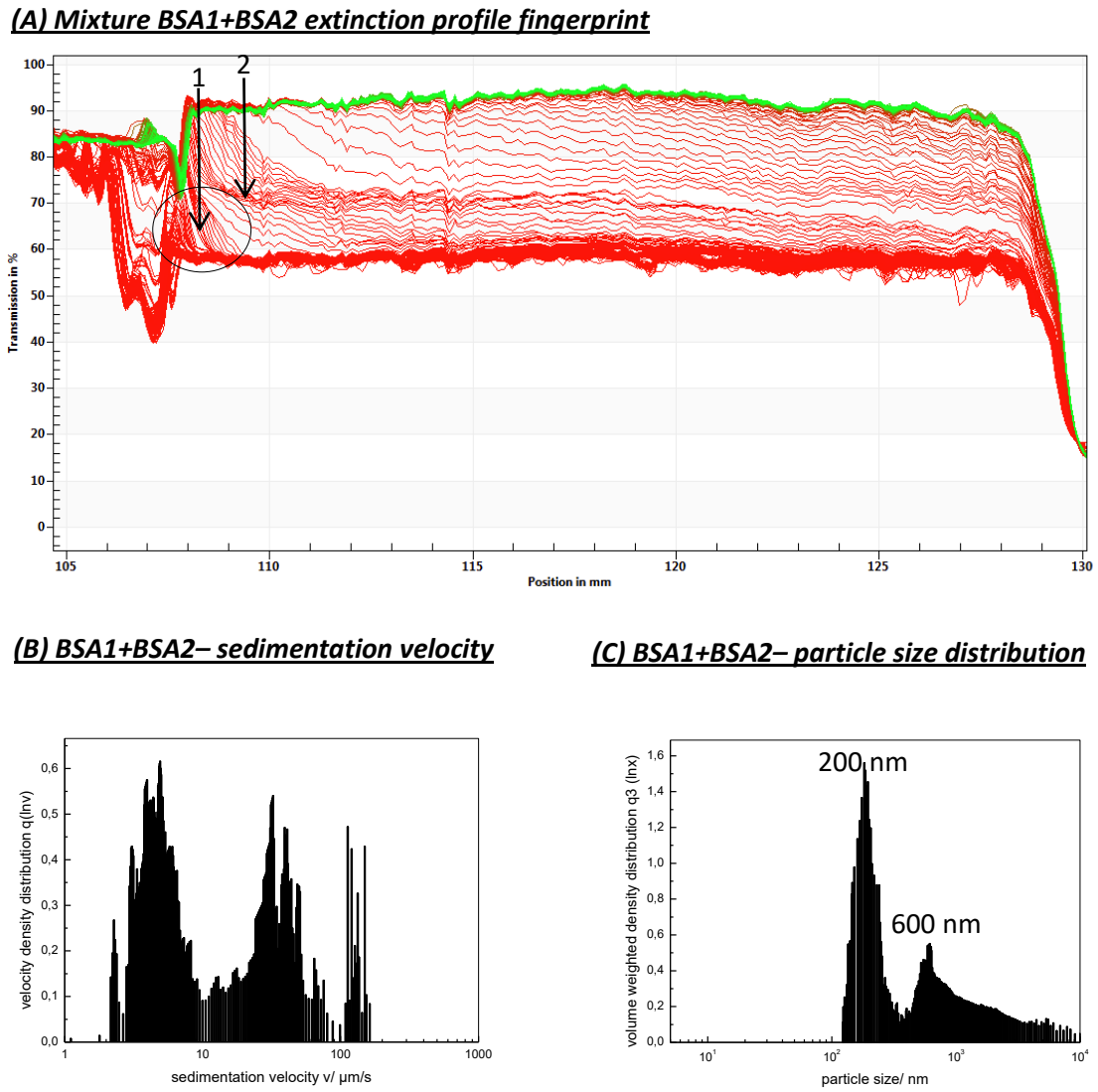

Figure 3- 5: Comparative case study I: STEP-technology® measurement of a bimodal BSA standard particle mixture of BSA1 and BSA2.
(A) Transmission fingerprint of the bimodal mixture of BSA1 and BSA2. Over the investigated time, integral clarification was detectable. The two phases of the clarification are indicated by the arrows and represent two different particle populations. Based on the movement the sedimentation velocity distribution (B) and finally the volume weighted PSD (C) have been calculated resulting in two main population around 200 nm and 600 nm.

A general evaluation of STEP-technology® based on the experiments with the BSA standard suspensions:

In general, there is no sample preparation necessary as the sample is simply filled into the cuvette (non-destructive). An instrument calibration with specific particles is not necessary at all. However, control measurements on a regular base are advisable. One essential challenge is the determination of density and refractive index for final PSD, but as demonstrated already the fingerprint and the sedimentation velocity distribution give insights into sample composition. Crowding effects, indeed, as a general problem of centrifugation processes, might change the final results as crowding might lead to aggregation during the measurement process. A further challenge, but at the same time beneficial for greater resolution of smaller and lager particles is the option for variable centrifugation steps within one experiment. For example, a first period with slower acceleration and centrifugation speed allows the larger particle to separate in an appropriate way and speed. In a later second step the increase of the speed leads to a faster and better resolution of the smaller particles. A critical point for the detection based on transmission is the required turbidity/opalescence. For BSA standards, this was not problematic. Another aspect is the selection of the used cuvettes. Cuvettes are available in different materials with various surface properties. The choice of the material is important to avoid interactions of the particles with the cuvette.

The instrument allows a medium throughput with 12 samples at the time and measurement time from few hours to days depending on the sample. The greatest advantage is seen in its wide size measurement range.

STEP-technology® in consideration of the five main challenges of particle detection in biopharmaceuticals:

(i) STEP-technology® applied in an analytical photocentrifuge is a great option to close the 1 µm gap and

(ii) STEP-technology® shows a size range from 10 nm to 100 µm, but no concentration detection

(iii) STEP-technology®, as separation-based technique, has a great resolution of polydispers samples, but

(iv) STEP-technology® is not applicable for concentration determinations and particle density as well as refractive index are needed for PSD.

(v) STEP-technology® applied in an analytical photocentrifuge is not dependent on a specific protein particle calibration standard.

The analysis of the BSA standard suspensions by the LUMiSizer® was successful and the technique is due to specific ISO certifications and a suitable software a great alternative in industrial settings. However, transmission measurements again rely on optical contrast differences that might be generally challenging for protein particle suspensions containing moderate particle concentrations.

8.1.4. Discussion comparative analysis BSA particle suspensions

On basis of the study results, two aspects are in the focus of the discussion: (1) the evaluation of the BSA size standard suspensions and (2) the performance of the evaluated techniques.

(1) The BSA standard particle suspensions were supposed to mimic typical challenges and characteristics of therapeutic protein samples by defined size and/or particle concentrations. Considering the heterogenic particle structure and particle surface as well as the polydispers composition, BSA particle suspensions occurred similar to stressed therapeutic protein samples. The physical properties density and RI, however, differed significantly from the observed protein particles of therapeutic protein samples. These differences are due to the particle nature, i.e. chemically linked particles show higher density than lose physical aggregates. In consequence, these characteristic leads also to a higher RI. This was confirmed by the bright yellow color of the suspensions. Nevertheless, having a defined particle standard suspension considering size and concentration, with at least partially protein aggregate nature is a valuable tool for technology evaluations. Depending on the applied principle the influence of the differing properties, have to be evaluated before usage.

Out of the three tested standard suspensions, size determinations for the BSA1 and the BSA2 suspension resulted for all selected orthogonal methods in the expected size range and confirmed the manufactures data. The respective achieved size distributions (Figure 3- 6) illustrate that the expected size represented the main particle population. BSA1 (namely 200 nm) contained one single main population around 200 nm and a small population in the micrometer size range. BSA2 (namely 500 nm) contained one broad main population between 400 nm and 600 nm and a small population in the micrometer size range even in the visible range. These broad size distributions represent the sample compositions of stressed mAB suspension but with a defined expected size.

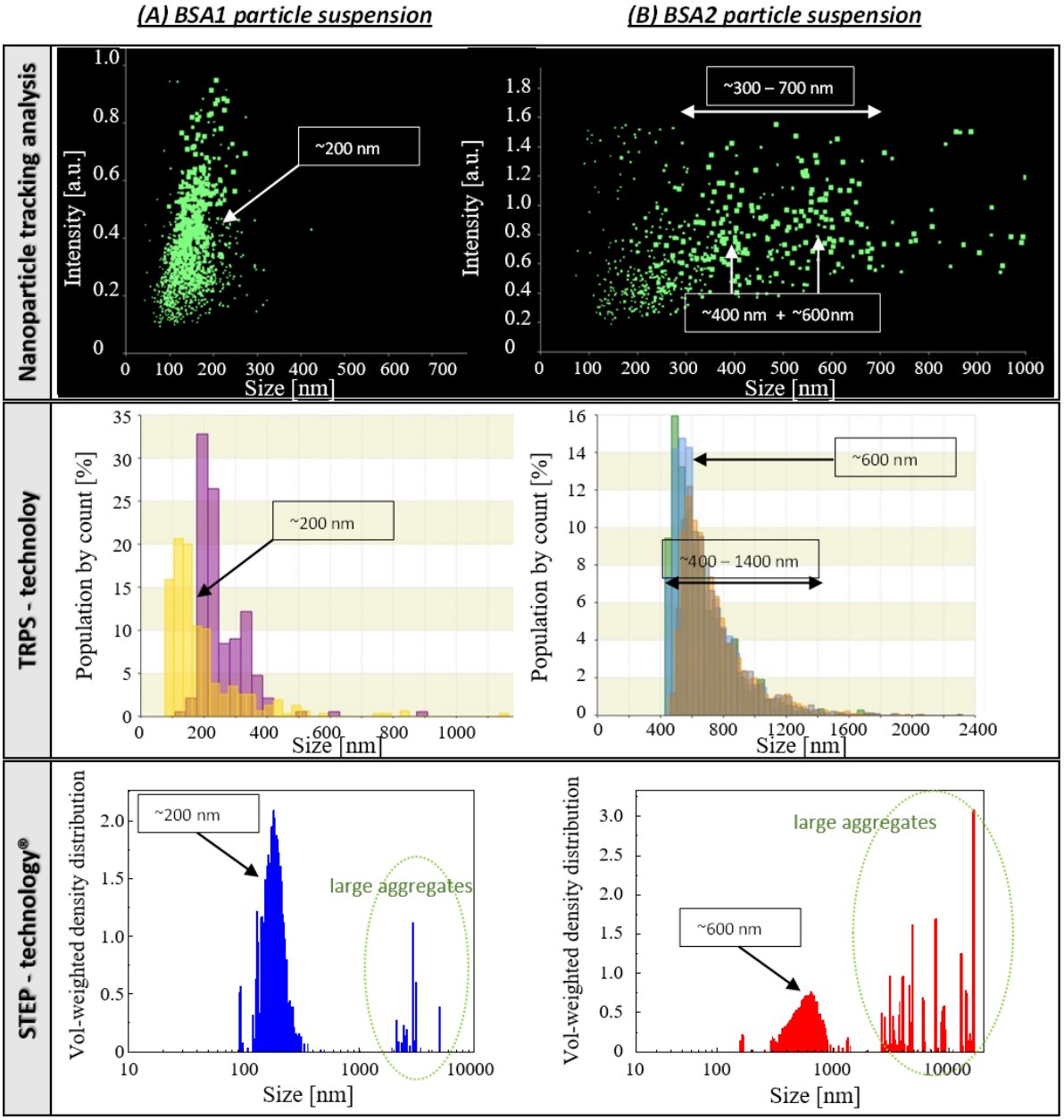

Figure 3- 6: Comparative case study I: Overview BSA particle results of emerging technologies.
The two BSA standard particles suspensions BSA1 (expected size 200 nm) and BSA2 (expected size 500 nm) have been investigated by NTA, TRPS-technology and STEP-technology® and the resulting PSDs are illustrated. The results of BSA1 and BSA2 agree for all three technologies in the nanometer size range (size and polydispersity). Particle populations in the micrometer size range (larger aggregates), in addition, were only detectable by the STEP-technology®.

The detected small populations at higher size ranges have to be discussed more intensive: These particle populations may be real small portions caused by suspension instabilities. The populations, however, may also be present due to technique specific conditions or as unreal artefacts.

Exemplary, the larger size portion in BSA1 was only detected clearly by STEP-technology®. Specific conditions during centrifugation for example or interactions with interfaces during TRPS measurements might cause crowding and aggregation effects. Such method specific artefacts have to be considered, also for particle standard suspensions. The concentration determinations for both suspensions, BSA1 and BSA2, have similar particle concentrations of about 1 $x10^8$ particle/ml. This concentration enables measurements with all techniques without prior preparation like dilution. The BSA3 suspension appeared most unstable before the experiments have been started and was demonstrated as unsuitable standard suspension. All applied analyses resulted in a broad distribution from a few hundred nanometer up to a few millimeter particles in size. The DLS value of 990 nm was only a mean value. The single-particle detection methods indicated still particles in the size around 750 nm, but the largest portion of the particles are either smaller or larger than 750 nm. The initial nominal size of 750 nm, detected by DLS, was not detectable anymore suggesting and, in contrast to BSA1 and BSA2, clear instabilities were detected. In this case, the conformity of the results highlights the quality of the BSA standards and makes the techniques, in general, a suitable set of complementary techniques.

Like other protein suspensions, the BSA standards appeared quite unstable (especially BSA2 and BSA3). Unfortunately, for this reason the manufacturer micromod decided to stop the production. Nowadays, only BSA1 particle suspension with the optimized size of 250 nm is still available on the market. For that reason, new approaches to produce stable size and concertation standards are still required as addressed by NIST. The BSA1 suspension, however, was shown as one suitable option.

(2) The evaluation of the tested techniques resulted in some advantages and disadvantages of each technology and each method has some unique potentials and challenges. These have been summarized in detail in chapters 8.1.1, 8.1.2 and 8.1.3.

The only technology that was able to describe the standard system with expected particle size and a particle concentration was the NTA system. The STEP-technology® was the only technology that detected the expected particle populations and, in addition, larger particles in the micrometer to millimeter range (visible and subvisible). However, the quantification of the particle in particle/ml was not possible. Based on manufacturer specifications, TRPS should be able to detect particle sizes and concentrations from 10 nm to 100 µm. Due to unspecific interactions and resulting fast blockage both benefits were not achievable. The precise size determination, indeed,

was confirmed also with only small volume. The small volume, however, has the drawback, that statistically populations of lower concentrations will not be detected. Further the question arises how these techniques perform analyzing real therapeutic protein samples, such as mABs (see chapter 8.2.5).

8.2. Comparative case study II: Applicability of emerging techniques for monoclonal antibody suspensions

In the second part of the comparative study, stressed and unstressed monoclonal antibody suspensions (mAB) with protein particles of undefined size ranges, broad size distributions and low particle concentrations have been analyzed by each technique.

8.2.1. Visual appearance of the mAB suspensions

The unstressed mAB suspension appeared clear without any visible particles. All types of stress led either to increased turbidity, the presence of particles up to the visible size range or a combination of both indicating a broad particle size distribution. The application of stirring stress (= mAB2, 10 rpm, RT) led to low turbidity, but significant amounts of sedimenting and large subvisible particles as well as visible particles. The application of temperature stress (= mAB2, 100 rpm, 60 °C) resulted in a turbidity of the sample without the observation of visible particles or sediments. After the application of reducing stress (= mAB3) the sample occurred slightly more turbid than mAB1 with a small amount of visible particles. The application of ionic stress (= mAB4) led to a fast turbidity and a highly dynamic system with continuously increase in turbidity and amount of visible particles.

8.2.2. Nanoparticle tracking analysis (NTA) measurements in combination with MFI

The NTA measurement of unstressed mAB samples showed a high background noise due to the large concentration of monomers, but in none of the parameter settings particles with sizes larger than 50 nm could be detected ($c < 10^6$ particle/ml). This agrees with the visual appearance, but dimers or small aggregates/associates cannot be excluded. Further, NTA measurements of stressed mABs 2 to 4 have been performed and analysed. Generally, all samples were measurable. However, due to the appearance of larger particles (micrometer size range), e.g. in mAB2 (100 rpm, RT), or

due to the interaction with the measurements cell caused by the aggregate nature, e.g. in mAB2 (100 rpm, 60 °C), some samples might be more challenging. In these cases, the results depend on the experience of the operator to set suitable parameters to overcome these challenges. One well-measurable sample was the reducing stressed mAB3 suspension. The results of mAB3 are exemplary summarized in Figure 3- 7. After the application of reducing stress the sample occurred slightly turbid with a small amount of visible particles (few product-related particles). From this observation, a particle composition with a large amount of particles in the submicron and micrometer range was expected a priori. For that reason, we decided to follow one promising approach to cover a wide subvisible size range from 50 nm to 75 µm: the combination of flow imaging analysis MFI and NTA to analyze subvisible particles in proteinaceous samples. The combination of both techniques enables a qualitative and quantitative description of the sample in the complete subvisible size range and is a great example for complementary techniques.

NTA results reported particles in the range between 50 nm and 1000 nm in a concentration of $1.14 \pm 0.2 \times 10^9$ particle/ml (Figure 3- 7A). The mean size was 128 nm and the mode size even lower with 70 nm to 90 nm. As confirmed by the D50 value (87 nm) more than half of the detected particles are smaller than 100 nm. Further peaks are seen around 150 nm, 220 nm, 340 nm, 650 nm and 950 nm. There is still bright background due to monomers and particle smaller than 50 nm. The chosen setting (CL5, DT5) is a compromise to cover as much as possible particles. For that reason, the concentration of the smaller particles might be too low as low CLs cannot enable the detection of smaller particles. If the CL is too high the scatter intensity of larger particles outshines the scattered light of the smaller particles. As previously demonstrated it is hardly possible to cover the whole range with only one setting (compare Part III chapter 8.3). The intensity plot indicated a highly polydispers sample, as expected. Intensities are between 0.5 a.u. and 1.5 a.u.. This appeared in the same range as for the BSA standard particles.

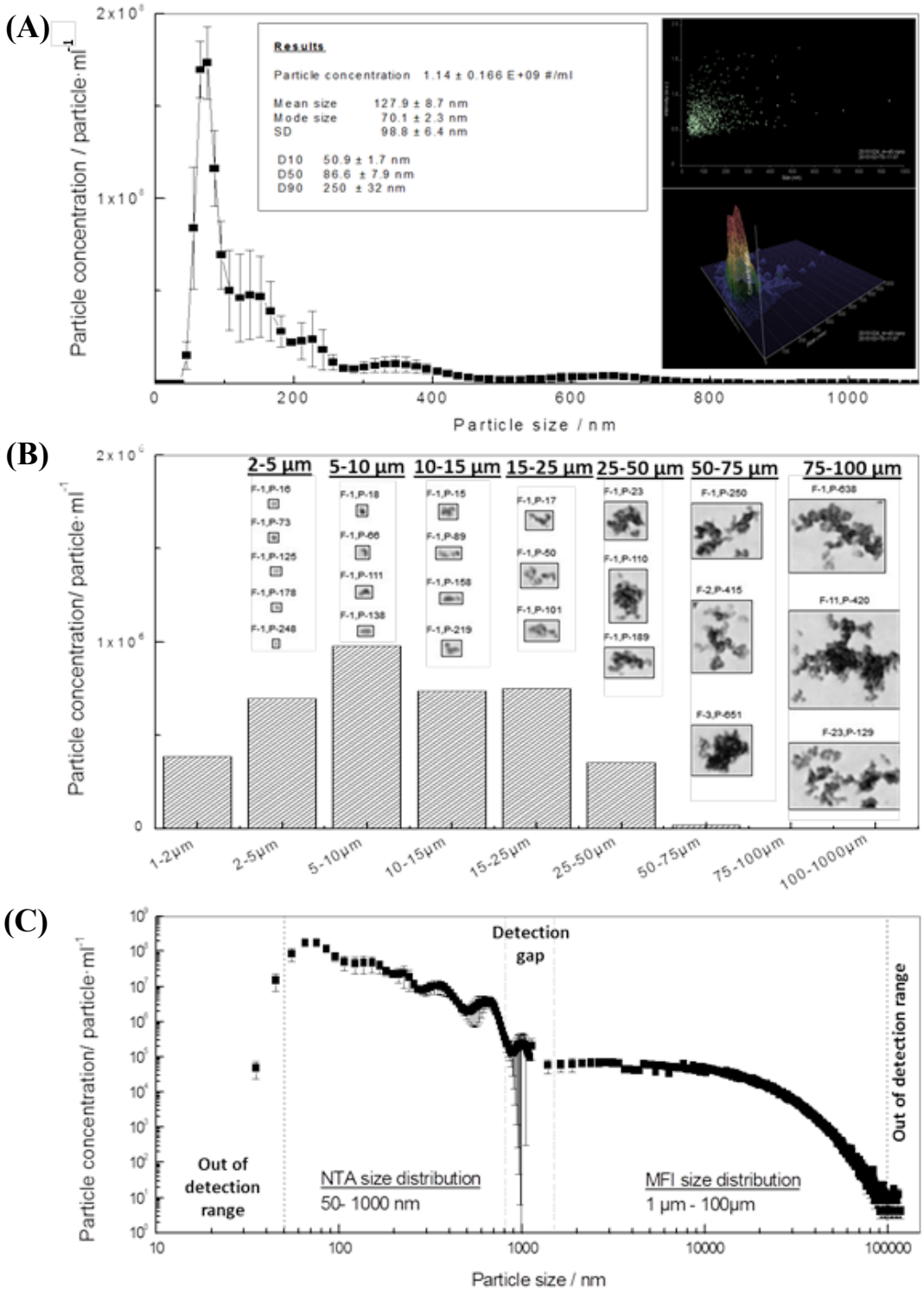

Figure 3- 7: Comparative case study II: Complementary combination of NTA and MFI: Stressed mAB3 suspension.

The stressed mAB3 suspension was analyzed undiluted by NTA and MFI after the application of reducing stress. (A) Summary of NTA results. (B) Summary of MFI results. (C) Number-weighted PSD, the upper and lower detection limits of the technique combination as well as the resulting detection gap around 1 µm are illustrated.

MFI results reported particles in the range between 1 µm and 100 µm in a concentration of 4 x10^6 particle/ml (Figure 3- 7B). Particles lower 2 µm are in the resolution limit and shape descriptions are hardly possible. Like the NTA results the major part of the particles was detected in the lower size range (< 10 µm). Only about 10 % of all MFI detected particles are larger than 25 µm. Particle characteristics typical for air bubbles or silicon oil were not detected. Most of the detected particles were assumed based on their characteristics (intensity and shape) to be protein particles. They appeared mainly in dark grayscales indicating dense particles/aggregates. Even though there are not unique in their grayscale and in some cases translucent parts are present (circles). The challenge of setting the right grayscale threshold was handled by the software. However, the risk of counting two smaller particles instead of one larger particle arises. The detected particles were mainly of non-spherical shape underlying a possible intensity distribution in NTA results due to shape. Fibrils or fiber-like structures were not observable, but unit-like compositions might be stated.

In summary Figure 3- 7C illustrates the results of both techniques for the reducing stressed mAB sample. In total, we detected about 1.1 x10^9 particles/ml. The number-weighted PSD shows that about 99 % appeared with sizes below 1 µm and could be only detected by NTA. In contrast, the concentration detected by MFI represents less than 1 % in the example of mAB3. Based on the MFI observations we assume that the major part consists of protein particles. However, the identification of particles in larger range might support the identification in the lower range, but the scattering intensities have to be considered as well. The resulting sample composition meets the expectations. However, a large amount of smaller particles between 10 nm and 50 nm, i.e. monomers, oligomers or soluble aggregates could not be detected. Same applies for particle in the visible range. Some example methods measuring below this size range are HP-SEC, AF4 or DLS, but none of them is generally used for quantitative particle determination. For quantification of larger sizes microscopic technics are the most suitable methods. There are MFI instruments with extended upper limits that might be an option. The detection gap around 1 µm is practically not covered. A possible approach might be TRPS or SMR devices.

8.2.3. Tunable resistive pulse sensing technology (TRPS) – qNano measurements

TRPS measurements of unstressed mAB suspensions were performed, but in result no significant peaks could be discriminated from the basic current signal even with the smallest pore size tested.

In contrast to NTA measurements, in TRPS measurements the unstressed suspension with high concentrations of monomers did not show any background noise/signal caused by the high concentration of small molecules.

Similar to the NTA experimental set-up, subsequently measurements of stressed mABs 2 to 4 have been performed. During these experiments using the different mAB suspensions as well as various pore sizes, only the stressed mAB4 suspensions could be successfully analysed. The result of the single run is shown in Figure 3- 8. The results of mAB4 showed the main particle population of about 88 % in the submicron range. More than 50 % of the detected particles showed a size around 600 nm. A small portion was also detected between 1 µm and 2 µm. As the aggregation progress appeared fast, only one measurement was achieved.

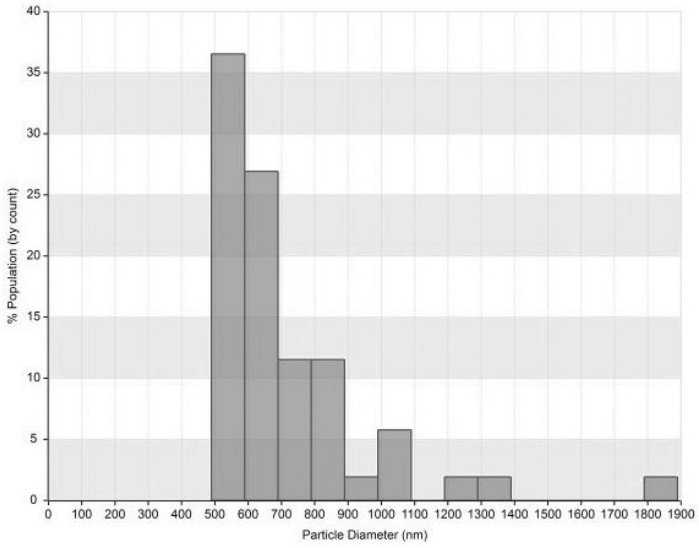

Figure 3- 8: Comparative case study II: TRPS-technology measurement: Stressed mAB4 suspension.
The mAB suspension has been stressed due to increasing salt concentration and subsequently measured by TRPS-technology. Final evaluation indicated the presence of particle between 500 nm and 2000 nm. During sample analysis pore blockage occurred and only low particles amounts of particle were detected. Based on low particle concentrations statistics are not as representative as for the BSA particle standard suspensions and the resulting bin size is larger.

All other samples could not be analyzed as they either caused fast clogging or blockage of the pore or the particles formed a layer on the pore. These might be mainly due to the high polydispersity and the occurrence of larger particles that are not suitable for the used pore. The second major issue is clogging caused by interactions between protein particles and the pores. Considering the different aggregation pathways, the final aggregates may differ tremendously not only in size but also in hydrophobicity or structure. The material of the pores and its properties, in this case the

elastomer polyurethane, need to be carefully considered (charged, hydrophobic, etc.). At that point there may be still some potential to improve the pore for such challenging samples like protein-based particles. Depending on the sample properties, its nature and polydispersity TRPS might still have potential. In our tested cases the stressed mABs appeared as less suitable samples as the samples contained either to many large particles (mAB2) or protein adhered to the pore material (mAB3 and mAB4). Both scenarios led finally to pore blockage. The problematic of measuring complex biologic samples has been discussed before and one approach to lower the polydispersity at the pore is a prior SEC separation step (Boing, van der Pol et al. 2014). Nevertheless, depending on the type and the stress applied for aggregation induction measurements might be possible for other molecules or different stress conditions. The ongoing development of coatings as well as a prior size population separation, e.g. by SEC or AF4 might improve these drawbacks. The technique and the principle in general show a high potential and a great orthogonal method. For applications analyzing particle suspensions with low polydispersity (about the size range one pore can cover) and with low interaction potential with the pore this is a perfect technique for the particle detection toolbox. However, protein samples and especially stressed antibody solutions are highly challenging due to their high polydispersity and their heterogenic surface/nature. Both challenges can be addressed for further optimization. Examples are the avoidance of interactions by a specific material coating or prior particle separation.

8.2.4. STEP-technology® - LUMiSizer® measurements

The analyses of unstressed and stressed mAB2 to 4 have been performed in one run and conditions are equal for all samples. The unstressed mAB showed already a start transmission of about 90 % and no change in the extinction profiles was detectable during the whole centrifugation process (Figure 3- 9A inlet). As the unstressed mAB sample consists mainly of monomers with a size around 10 nm and low refractive index causing a low optical contrast. In that case, the turbidity appears not sufficient (A320 < 1) for an analysis and clarification or boundaries could not be detected.

In contrast, the start transmission of mAB1-3 appeared with at least 60 % and the extinction profiles show significant clarification and boundary movement during the centrifugation process. Exemplary, the results of mAB2 is shown (Figure 3- 9A). In the first profile a sharp boundary is

noticeable (circle) indicating the presence of a larger particle population. To investigate those large particles as well the rotor speed in the beginning has to be adjusted.

In general, the set of the profile interval and the rotor speeds plays a crucial role for a good resolution. Standard operation protocols are given, but adjustment might be necessary for each sample. Nevertheless, mAB2 showed afterwards integral clarification without sharp population boundaries. This phenomenon occurs if highly polydisperse samples are measured. The resulting sedimentation velocity distribution as well as the calculated PSDs are shown in Figure 3- 9C-E. Generally, there is only one highly polydispers population detectable from 2.5 µm/s to 40 µm/s with a modulated mean of 18 µm/s. Respectively, particle sizes from 200 nm to 800 nm with modulated mean values of about 500 nm were achieved. Three slight peaks are seen at 3 µm/s, 10 µm/s and 30 µm/s, respectively 200 nm, 400 nm and 700 nm. Interestingly the smallest particle size detectable in our example is 200 nm. This seems to be the lowest particle size measurable for that kind of particles as SEC results indicate also the presence of smaller particle and monomers.

In that example, the considerations of the integral rate and the instability index lead to a classification (Figure 3- 9B). The unstressed sample without any change in the extinction profiles is stated the most stable with an instability index of 0. The more the change in the sample during the centrifugation process is the more instable is the sample as separation takes place. Consequently, mAB2 at RT is more instable due to the presence of particle that get separated during the centrifugation process. The more particles the greater the change and mAB2 at 60 °C is the most instable sample with the highest amount on particles. That differentiation is already a qualitative valuable statement. The fact that it is a direct and non-invasive technique enables the measurement of exact the same sample and best comparability.

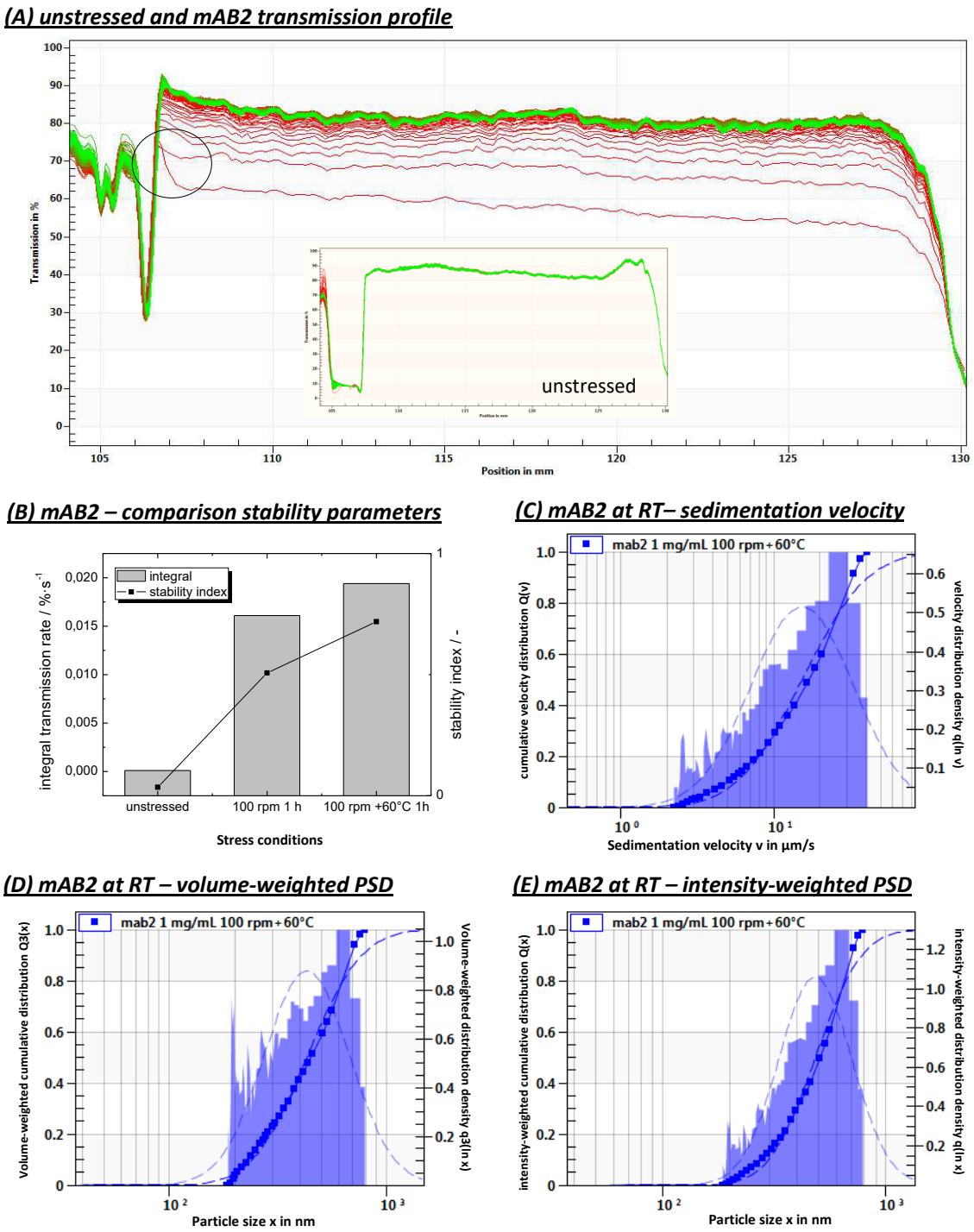

Figure 3- 9: Comparative case study II: STEP-technology®: unstressed mAB2 and stressed mAB2 suspension. (A) Transmission fingerprint of unstressed and stressed mAB2 (at RT and 60 °C) suspension. Over the investigated time no clarification or sedimentation was detectable for the unstressed sample and further evaluation is not possible. The stressed samples were evaluated, and direct comparison is possible by the integral transmission rate and the stability index (B). Further data evaluation lead to the sedimentation velocity distribution (C), volume-weighted PSD (D) and intensity-weighted PSD have been achieved.

8.2.5. Discussion comparative analysis mAB suspensions

The general applicability of the evaluated techniques for protein-based material was demonstrated in the previous chapter. Standard materials, like the chosen BSA standards, indeed, are supposed to show a main population with similar and defined characteristics (e.g. size). Even though there was already a wide range and variability detected, a characterization of this main populations was possible. Therapeutic monoclonal antibody suspensions (stable/ unstressed) should represent a dominant main population as well: the monomer population in the size range of 10 nm with a monomer portion of at least 95 %. This population, however, is not in the working range of the applied techniques and the performed study preferentially aimed to detect smaller portions of particles with larger sizes than the monomer. It reflects two major challenges of unstressed mAB suspensions: detection and characterization of minor populations and potential destruction/influence on the result by the major population of monomers. The size range of unstressed samples, however, is not expected significantly exceeding the lower micrometer size range (no visible particles). Discussing the results summarizing in this context, following evaluation can be stated: The high background noise caused by the monomer population appeared only challenging for NTA measurements. For TRPS and STEP-technology® the dominant monomer portion caused no observable influence. All three technologies were not suitable to detect any particle in the unstressed sample in the nanometer size range. Since particles were detected in the micrometer size range (MFI) it is assumable that particles in the nanometer size range should be present. The sensitivity of the techniques, however, was too low to detect these potential small amounts of particles. Based on the technical features and state of the art of the three technologies the unstressed samples are stated as free of particles and stable mAB suspensions. Technical developments and the application of further orthogonal principles and techniques may increase the sensitivity and prove that statement wrong.

By applying various physical stress factors to unstressed samples an increase in the particle content in the working ranges was aimed exceeding the sensitivity of the technologies. In contrast to the unstressed sample, the expected particle size range occurred from the monomer size of 10 nm up to visible particles above 80 µm. This represents a third challenge, in addition to the two challenges mentioned above. Furthermore, physical stress induced aggregation caused a great variety in resulting particle characteristics depending on the applied stress. This fact makes it additionally challenging not only to describe this particle variety but also to identify technical solutions to

overcome undesired side effects like unspecific interactions or destructive changes of the particles by the measurement principle. The selected three stress factors, temperature and stirring stress, ionic stress and reducing stress led to three significantly different protein particle suspensions. Visual observed phenomena like turbidity, visual sediments and the occurrence of large visual particles illustrated nicely these differences. If measurements and analysis was possible, also the results of the evaluated techniques confirmed this. In consequence, each sample applied its own challenges to the techniques and based on these challenges not all techniques were able to investigate all types of protein particle suspensions: For NTA, besides the challenging background noise, larger particle populations outshine smaller particles and the optimal definition of the measurement setting parameters is hardly achievable. Blockage of inlet or outlet tubes as well as adhering of more hydrophobic particles (partially or complete unfolded protein molecules) to the measurement cell present additional technical challenges. Practically the technique of NTA was able to measure all samples but interpretation of results appeared difficult and further evaluation is necessary (compare 8.3). As already observed for BSA standard particle suspensions, the TRPS technology failed measuring polydispers samples, if the size range of the present particles is not measurable by one pore size. This seemed to be the case for all stressed samples. In addition, extreme interaction between the protein molecules and the pore material appeared. Both aspects led to blockage after a short measurement time and make the technique less suitable for mAB suspension. The STEP-technology® can be evaluated as suitable for protein samples, if the protein sample suspension showed a transmission below 90 % in the start extinction profile, but at further evaluation is necessary (compare 8.4).

8.3. Detailed evaluation of Nanoparticle tracking analysis

In order to monitor parameter-setting effects on NTA results, three experimental approaches were investigated: (1) monodisperse monomodal particle suspensions, (2) polydisperse polymodal PS-bead suspensions and (3) polydisperse protein samples. Polystyrene or latex beads are widely used as calibration standards for size measurements. For that reason, in the first parts of the study these standard particles (20 nm to 1000 nm in diameter) were used. In addition, BSA particles (177 nm in diameter) were used. Finally, a protein stability study (stirring stress and temperature) was performed using 10 mg/ml antibody suspension.

8.3.1. Monodisperse monomodal particle suspensions

The reproducibility and accuracy of the NTA instrument as well as the effects of parameter settings on particle standard suspensions with known size and concentration was investigated. This was realized by analyzing monodisperse, monomodal suspension of 600 nm-PS-beads. Triplicate measurements were performed under the same capturing settings and conditions (Figure 3- 10A). In addition, the evaluation parameter DT was varied and the influence of the flow rate was studied (Figure 3- 10B). As stated by the manufacturer, there is the opportunity to measure during a low sample flow. The software is able to take the flow velocity into account for result calculations. This is an option to improve statistical relevance of particle counts if low particle numbers are expected.

For the used standards, the particle sizes and concentrations were known which allowed adjusting the parameters based on these values. Optimal parameters are defined by the lowest standard derivations and most reproducible results, i.e. where size and concentration matched best with the expected size and calculated concentration values. The determined size mean value of d = 599 +/- 33 nm confirms the expected size according to the product information sheet (Diameter d = 600 +/- 9 nm, sigma = 10 nm, 1.6 % CV) and DLS data (data not shown). The expected particle concentration of 1.68 $x10^8$ particles/ml was calculated based on the depicted concentration of 1 % solid and could be determined by the NTA measurement with 2.02 +/- 0.3 $x10^8$ particle/ml. The variation of DTs in a narrow range did not lead to significant changes in the results as seen in Figure 3- 10B. Nevertheless, the size distributions were different: different DTs had an effect on the main peak position and on the appearance of additional smaller

peaks around 300 nm. As the raw data used for this analysis (CL 6) is the same for all variations of the DT, we show the statistic of three independent measurements of the 600 nm standard particles (Figure 3- 10A to D).

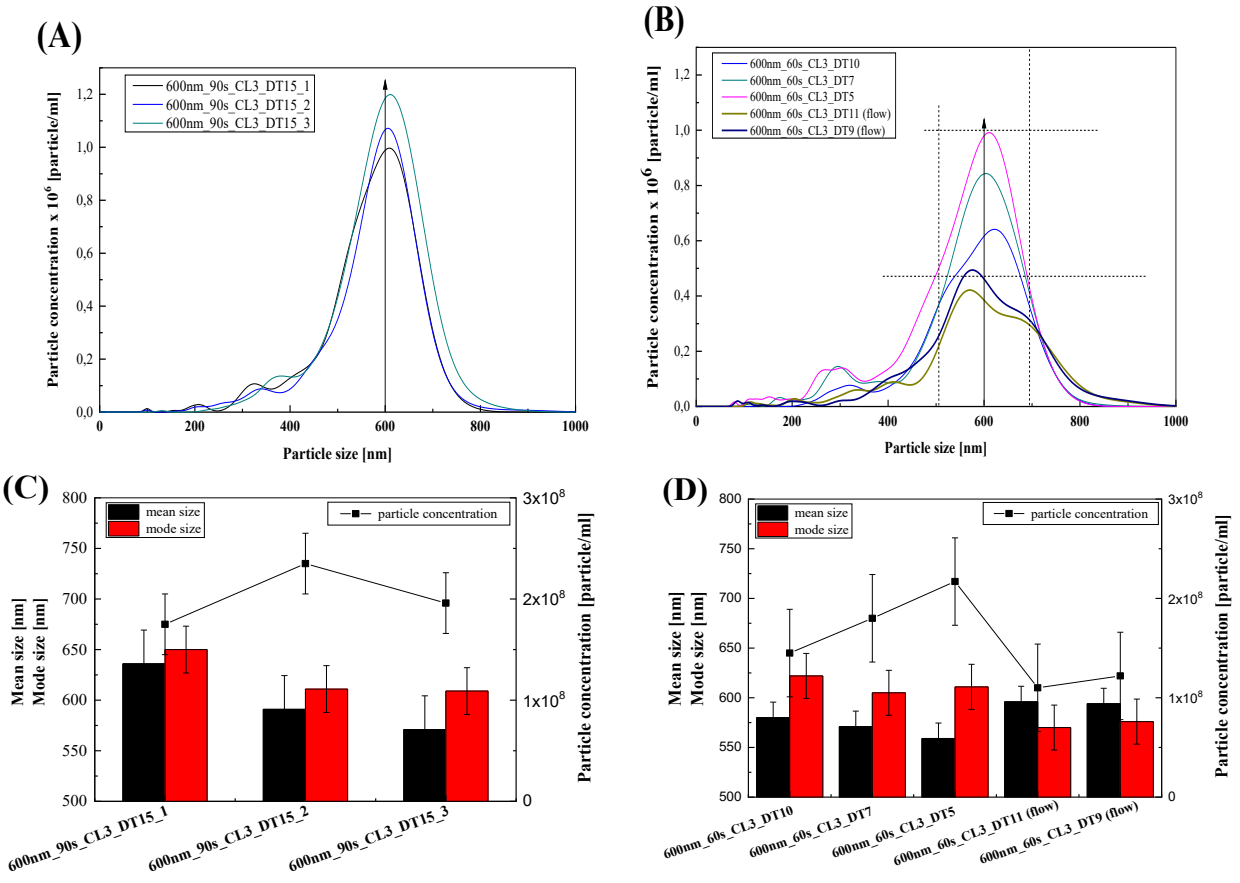

Figure 3- 10: NTA evaluation: Size distribution from NTA measurements of a monodisperse 600 nm polystyrene bead solution.
Based on product information sheet and DLS data (not shown) a single peak around 600 nm is expected. Completed tracks: 250-350. (A+C) Triplicate measurements of the same monodisperse sample were performed using constant optimal experimental and evaluation parameters. (B+D) The same sample was measured and evaluated using slightly different parameters. In addition, the measurements were performed without sample flow or with a sample flow rate of 20 µl/min.

The detected mode sizes at various DT are not significant and appear within the merged standard derivation of +/- 94 nm. The same is the case for the concentration at the main peak (height of the main peak). Even though the influence is larger, all values are within the standard derivation of +/- 0.3 10^6 particle/ml (section pointed out by dashed lines). The experiments with a flow rate of 20 µl/min led to a slight shift of the main peak to lower size distribution and the appearance of a

shoulder at a larger size (Figure 3- 10B). These shoulders appear for larger particles in particular. As already postulated before (Boyd, Pichaimuthu et al. 2011, Vasudev, Mathew et al. 2015) and illustrated in Figure 3- 10A, results of monodisperse monomodal suspensions met the expected size and concentration values reproducibly, if the optimal sample particle concentration is adjusted and the optimal parameters are set. The challenge appears to set these optimal parameters for an unknown sample.

A second experimental setting we set out to investigate the effect of the variable experimental and evaluation parameters capture time (CT), camera level (CL) and detection threshold (DT). A monomodal, monodisperse 600 nm-PS-bead suspension (2.02 +/- 0.5 $x10^8$ particles/ml) and a monomodal BSA particle suspension with a PDI around 0.2 in DLS results (about 1 $x10^8$ particles/ml) were analyzed. Based on the expected concentrations and sizes following parameters were initially chosen: CT of 215 s, a DT of 25 and a CL of 3 for 600 nm PS-beads; CT of 215 s, DT of 25 and a CL of 4 for BSA particles. To study the effect, we varied one of the parameters at a time as depicted in Figure 3- 11. In the tested range variation of CT had the lowest influence on the result independent of particle size and material. Determined sizes and particle concentrations are in the expected ranges without a significant trend for both standard solutions (Figure 3- 11-1 and -2). CL and DT variations showed a significant influence on the concentration determinations, but not on size determinations (Figure 3- 11-3 to -6). Over the tested range of CLs, the particle concentration of PS-beads increased from about 2 $x10^8$ to 6 $x10^8$ particles/ml and there a 12-times increase was observed for the BSA particle concentration. The resulting effects for size determinations were not significant due to high error bars and the data indicated a low reproducibility. For PS-beads a decrease of about 100 nm and for BSA particles a decrease of about 50 nm in size was observed. The optimal settings for PS-beads are CLs of 2 or 3 and for BSA particles CLs of 4 or 5 with respect to the expected values and the calculated standard derivations (Figure 3- 11-3 and -4). The effects of the DTs were larger than the effects of the CLs. Particle concentrations decreased from 5 $x10^8$ to 0.2 $x10^8$ particles/ml for PS-beads and from 1.5 $x10^8$ particles/ml to no detectable particles for BSA particles. The determined particle sizes increased from 595 nm to 660 nm and from 155 nm to 230 nm, for PS beads and BSA particles respectively. Similar to the effects observed by CL results these differences in size determinations were not significant, but cover a size range of 11 % and 30 %, respectively (Figure 3- 11-5 and - 6).

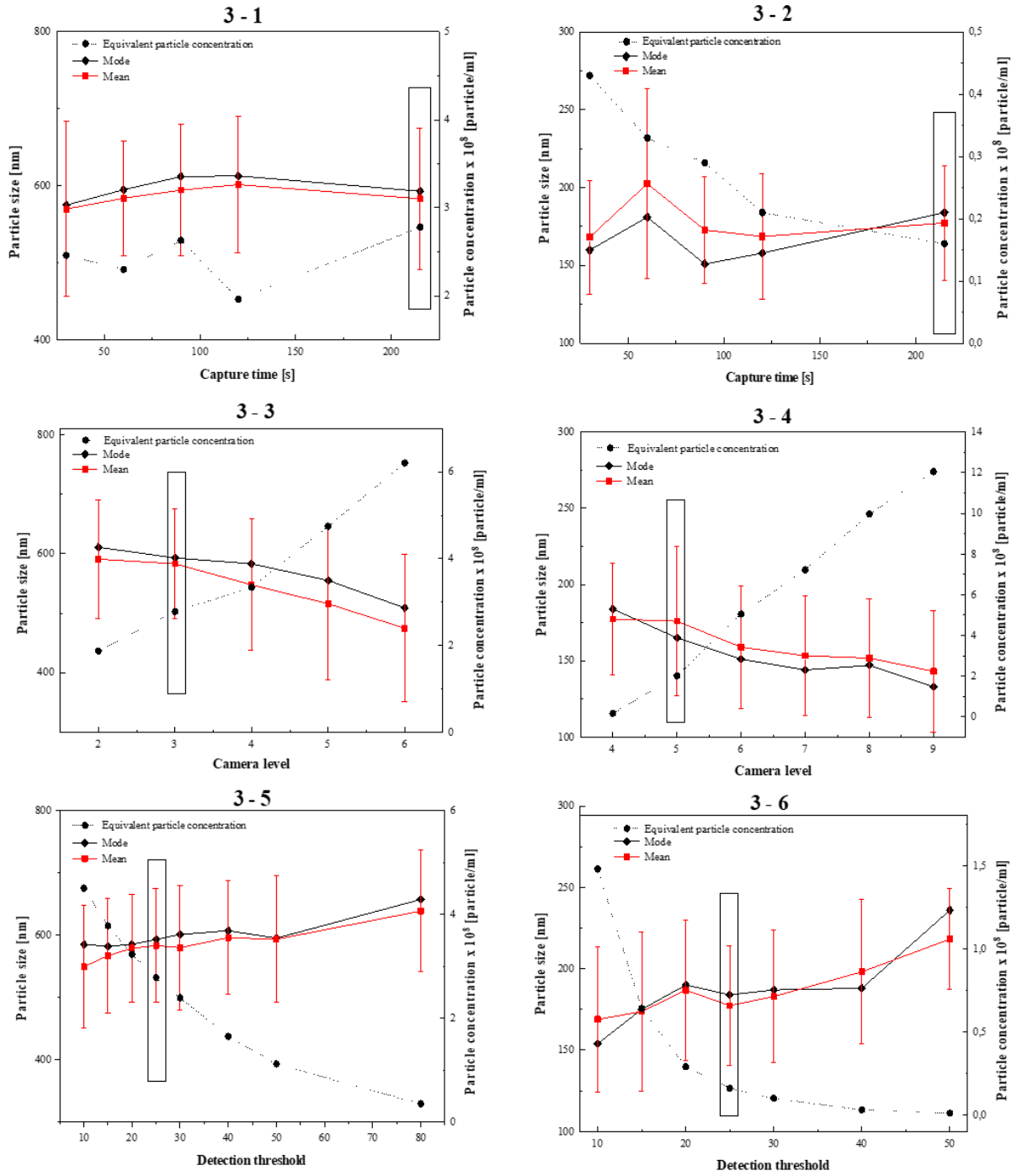

Figure 3- 11: NTA evaluation: Influence of the parameters capture time, camera level and detection threshold of the resulting size main peak (mode), the mean size and particle concentration.
3-1 and 3-2: size and particle concentration as function of capture time, 3-3 and 3-4: size and particle concentration as function of camera level, 3-5 and 3-6 size and particle concentration as function of detection threshold. *Left panel:* Data for a suspension of 600 nm polystyrene beads with an approximate concentration of 1.68 10^8 particle/ml. The black squares point out the parameter with most realistic results. *Right panel:* Data for a suspension of 177 nm BSA particles with a concentration of 5 10^{-4} mg/ml (approximately 1 10^8 particles/ml). The size was also detected by DLS measurement and showed a peak at 159 nm (PDI=0.042).

In a third approach the full CL range from 2 to 16 was tested for various particle sizes to set optimal CL. We analysed monomodal, monodisperse PS-particle suspensions with particle sizes of 20 nm, 50 nm, 100 nm, 200 nm, 300 nm, 600 nm and 1000 nm in a concentration between 1 x10^7 to 1 x10^9 particles/ml. The optimal CLs for each size population, i.e. where size and concentration matched best with the expected and calculated values, are summarized in Figure 3- 12.

Depending on the CL particles of the whole range between 20 nm and 1000 nm can be described, if monomodal and monodisperse suspensions are used. The 1000 nm particle suspension showed an optimal CL of 2. This corresponds to the lower limit of CL. Larger particles are hardly detectable. On the other side, the highest CL (16) is needed for detection of 20 nm particle population. These facts point out the challenge to achieve an optimal setting, especially for highly polydisperse samples in a broad or even the complete size range from 20 nm to 1000 nm. In our experiments the optimal CL (as depicted in Figure 3- 12) plus/minus one CL led to sufficient results with respect to the expected particle concentration, the expected size values and reproducibility of the results.

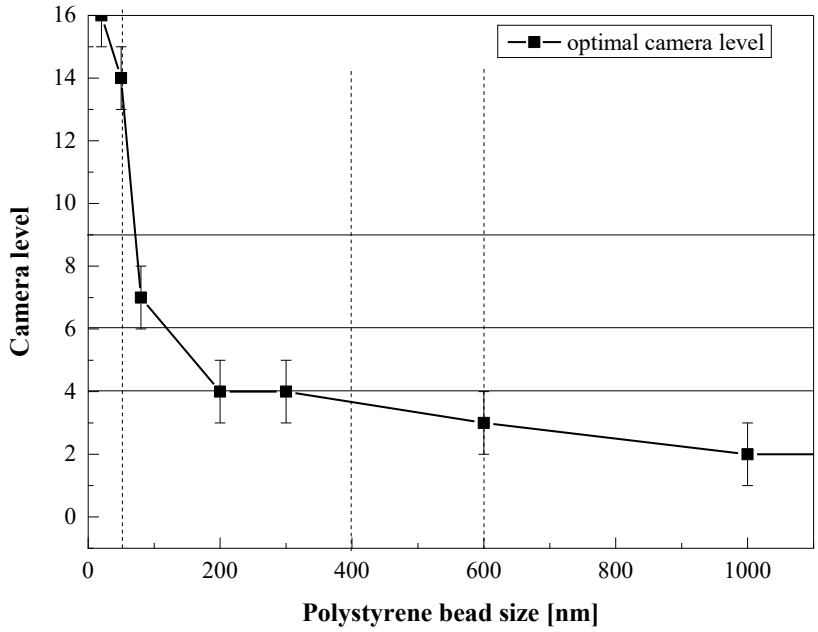

Figure 3- 12: NTA evaluation: Optimal camera levels for different sizes of polystyrene beads (20 nm to 1000 nm).

For each polystyrene bead population (20 nm, 50 nm, 80 nm, 200 nm, 300 nm, 600 nm and 1000 nm) different camera levels were tested and the optimal level is shown leading to the expected size and an appropriate concentration. The concentrations were chosen to be between 1 x10^7 and 1 x10^9 particles/ml. Illustrated by the dotted lines are the three populations of the investigated 50 nm-400 nm-600 nm mixture. The continuous lines indicate the 3 tested camera levels in the mixture experiment.

8.3.2. Polymodal polystyrene particle suspensions

In order to demonstrate the parameter effects on a more complex sample, polymodal suspensions as defined mixtures of the monomodal, monodisperse polystyrene particles were investigated. Such a particle composition is more likely to represent a real protein particle sample.

In a first approach, we used a bimodal mixture containing 200 nm and 600 nm particles in a ratio number of 1:1. Both populations could be detected in two baseline-separated peaks (data not shown). The sample appears more polydisperse as the peaks are broader than the peaks of the single monodisperse samples before. The tested variations of parameters settings caused shifts in the two main peaks in the size distribution profile within the standard deviation (+/- 35 nm) – comparable to the results for the monomodal suspensions. The detected particle concentrations showed significant changes of about 1 $x10^8$ particles/ml.

In a second approach, we investigated a mixture of 50 nm, 400 nm and 600 nm PS-particles. The sizes were chosen to cover the "whole" measuring range, as well as having a particle sample composed of three particle populations that allow the discrimination of three separated particle "peaks". The concentration ratio was chosen to ensure that the different sized particle populations are present in the range of 1 $x10^7$ to 1 $x10^9$ particles/ml. This mimic an "ideal" polymodal, polydisperse system for NTA measurements. To resolve the different particle populations, CLs from 4 to 9 for video capturing and DTs from 4 to 70 for evaluation were tested. The results are shown in Figure 3- 13. Compared to the monomodal, monodisperse samples, the peaks of the ternary particle sample are broadened, and a higher apparent polydispersity is calculated.

The expected total particle concentration (2 $x10^9$ particles/ml) was not detected in all tested cases. There were only two settings (CL6, DT14 and CL4, DT4) enabled us to detect three peaks in the expected size ranges: a small peak around 50 nm, the main peak around 400 nm and a small peak around 619 nm. Interestingly, the 50 nm peak is in all cases very low although the concentration was increased by a factor of 9. All other tested settings or evaluations monitored only two "peaks", or only one particle distribution was observed or even peaks at positions deviating from the expected size distribution. For example, the parameter settings CL4 and DT8 displayed a monomodal monodisperse result with only one significant peak around 400 nm. A bimodal, polydisperse results with peaks around 400 nm and 600 nm were monitored with settings CL4 and DT12. At CL of 6 it was possible to detect the 50 nm and the 400 nm particles with the DT of 14 without a significant peak for the 600 nm particles. In contrast, for the same CL and a DT of 30

the 50 nm particles disappear while 400 nm and 600 nm particles can be detected. The parameter combination CL9 and DT30 presents even a “false” result with the appearance of a single significant peak around 330 nm. Even though the same raw data video (same CL) was evaluated, the peaks around 50 nm and 600 nm disappeared in most cases. The compensation effect and the interplay between CL and DT were not sufficient to achieve the expected result. This illustrates how changing the settings can give misleading results.

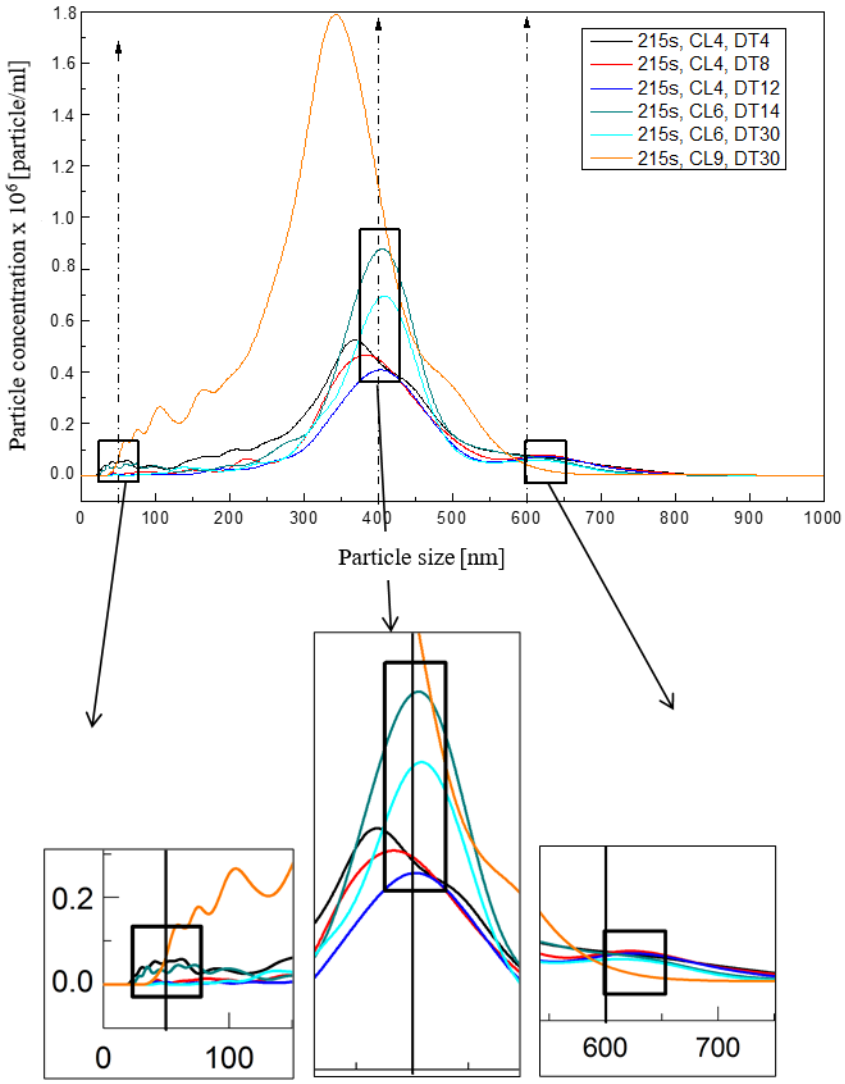

Figure 3- 13: NTA evaluation: Size distribution from NTA measurements of a mixture of polystyrene beads with sizes of 50 nm, 400 nm and 600 nm in a number ratio 9:2:1.
The same sample was measured using the camera levels (CL) 4, 6 and 9 at the maximal capturing time of 215 s. Subsequently, evaluation was performed using different detection thresholds (DT) in the range of 4 to 30. Comparing the evaluation of the same sample depending on different DTs and the set of different CLs the size distribution shows three peaks at the expected sizes, two peaks or only a single peak. The black squares and dashed arrows point out the three peaks which have been expected and could only be seen with CL4, DT4 and CL6, DT15.

The variation of parameters can be seen as an option to gain an approximate description of the sample but can also be misleading as shown in this example. Consequently, a realistic evaluation for samples with unknown composition is challenging and highly depends on the operator and the used settings.

8.3.3. Protein stability study and NTA technique

In addition to the challenges unravelled in the first parts with standards particle suspensions, protein solutions appear as even more complex systems with unknown particle size distributions and concentrations as well as heterogeneous shapes and structures.

For a first analysis of protein samples, we performed experiments in the capture mode, similar to the PS-bead experiments. An IgG antibody solution of 10 mg/ml (unstressed and stressed, stirred, sample to generate the presence of particles) was analysed independently in triplicates. The parameters were kept constant (CL6, DT12 or 17). The statistically required particle number of 1 $x10^7$ particles/ml was achieved in stressed samples, but the size distributions appeared with low reproducibility for both samples. Particle concentrations showed standard deviations of 8.5 $x10^6$ and 7.48 $x10^7$ particle/ml. Due to low particle concentrations the maximum capture time of 215 s did not allow reliable statistical evaluation for unstressed antibody solutions und insufficiently reproducible results for stressed samples. The resulting size distribution curves of the same samples differed from each other in mode and mean size (Figure 3- 14). However, the difference between highly stressed and unstressed protein solutions was detectable. An absolute quantification and determination of "exact" size distributions is hardly achievable. The results are highly operator-depending, no supportive parameter setting is given and optimization of parameter settings is time-consuming and challenging (Figure 3- 15A).

In a second approach, the "Live-monitoring" mode was used. In this case the capture time is not restricted by the software and adjustments of the capturing parameters are still possible during the measurement and supported by the software. This leads to the opportunity to improve statistics and perform real-time optimization for each sample. A further advantage is the process of "auto-adjustment of the light exposure" in the beginning of each measurement based on the background of the sample (Figure 3- 15B). Fine tuning can be done by the operator subsequently.

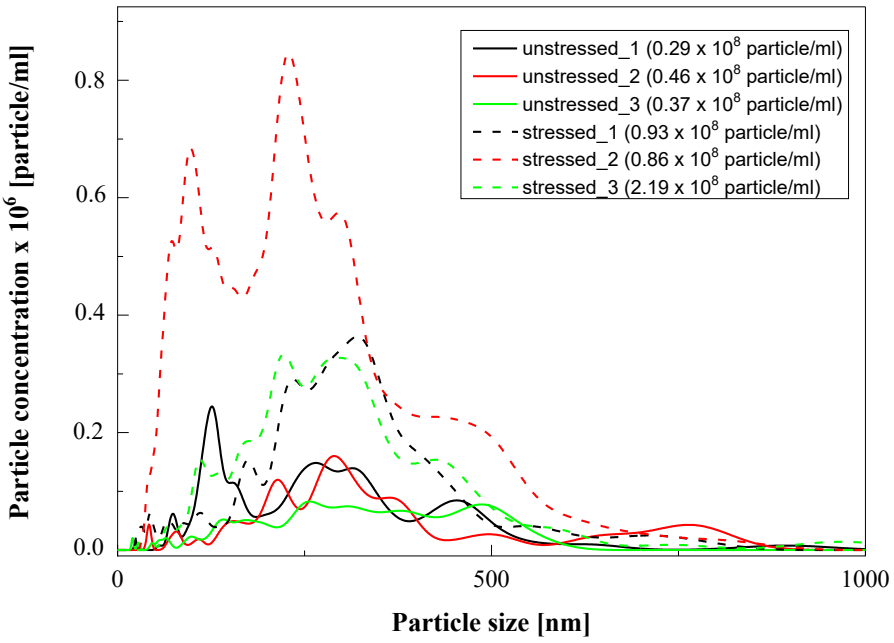

Figure 3- 14: NTA evaluation: Size distribution from NTA measurements Capture Modus of a 10 mg/ml unstressed (continuous black) and stirring stressed (dotted red) protein solution.
The two samples were each measured three times independently and the size distributions as well as the particle concentrations are shown in the graph. The DLS measurements of the samples carried out a z-average of 11.0 nm for the unstressed and a z-average of 11.4 nm. The PDI increased slightly from 0.2 to 0.213.

The resulting size distributions as well as the particle concentrations of differently stored protein samples are shown in Figure 3- 16. The comparison of the two different storage conditions appeared more reproducible. Apparently, storage condition 1 (20-L Flexboy® bag) showed more particles in the range of 50 nm to 200 nm (peak 125 nm) and storage condition 2 (2R glass vials) causes larger particles/aggregates between 125 nm and 500 nm (peak 200 nm). Particle concentrations of about 1 x10^7 particles /ml were detected. Reproducibility for size and particle number detection is improved compared to the capture mode. Consequently, minor differences were detectable - even at particle concentrations below 1 x10^7 particle/ml - which was not possible using the capture mode.

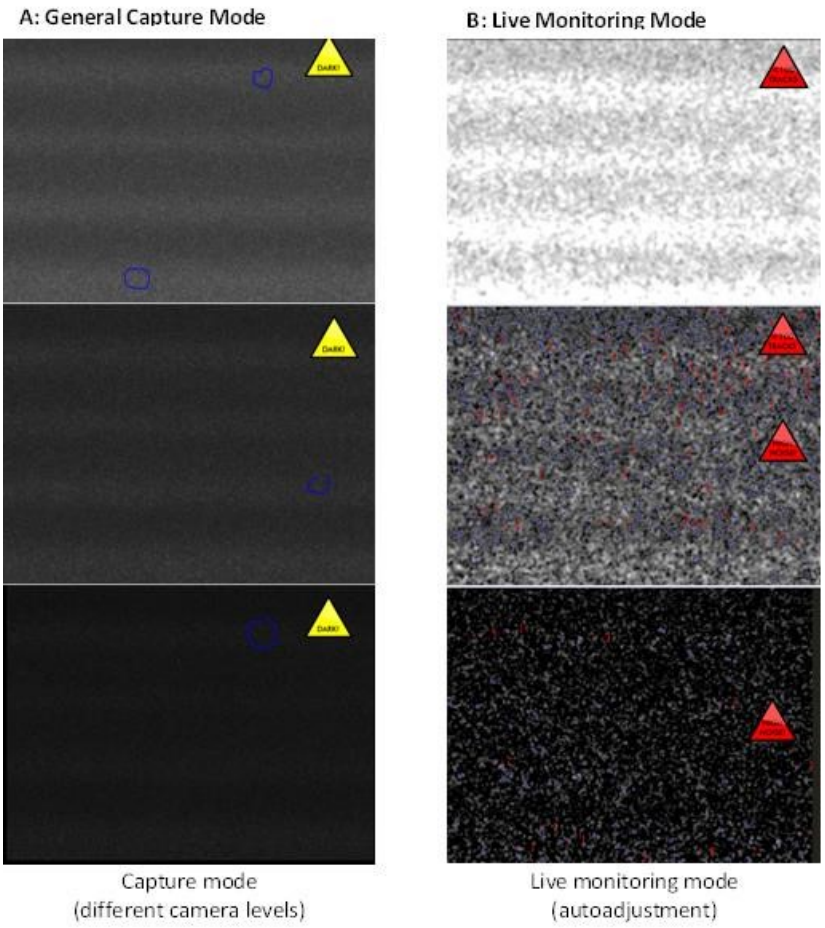

Figure 3- 15: NTA evaluation: Comparison adjustment of measuring settings for a protein solution in the capture and live monitoring mode.
The same protein sample, with a high partition of small monomers and only a few larger particles, was measured in both modes. For the capture mode the CLs of 7 (left upper picture), 6 and 5 were tested. For the live monitoring mode, the CL was set to 7 but the autoadjustment in the beginning of the measurement (right panel) carried out a more suitable setting.

Due to the fact that antibody monomers are too small (hydrodynamic diameter of about 10 nm) for detection (detection start about 50 nm) only background noise was detected (Garidel and Kebbel 2010). The statistics for the detected particles are not sufficient. The choice of the CL and detection threshold was set based to avoid the background noise caused by cooperative monomer scattering due to the huge amount.

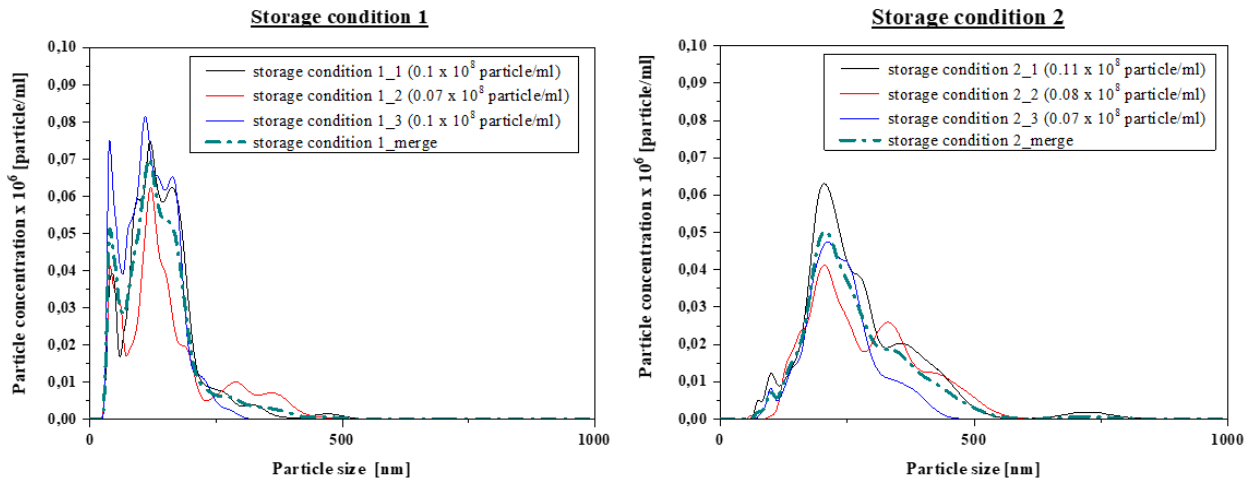

Figure 3- 16: NTA evaluation: Size distribution from NTA measurements Live Monitoring Modus of a 10 mg/ml protein solution stored at different conditions.
The two samples of the same protein were stored in different containers- condition 1 = 20-L Flexboy® bag, condition 2 = 2R vial - and afterwards measured three times independently each. The size distributions as well as the particle concentrations are shown in the graphs.

8.3.4. Discussion detailed NTA evaluation

Consistent with earlier NTA evaluation studies, the results of our study confirmed that the technique has a unique potential as shown in various applications and increasing numbers of publications. Nevertheless, the technique has notable drawbacks, e.g. a relatively narrow particle concentration range limitation (Carpenter, Randolph et al. 2009, Filipe, Hawe et al. 2010, Patois, Capelle et al. 2012).

In fact, we were able to illustrate the consequences of variable settings and risks of misinterpretation or manipulation of the results. In case of NTA, the challenging task for the operator is to identify and set optimal sample composition and the optimal instrument settings, especially for a complex system like a protein suspension. The narrow particle concentration between 1 x10^7 to 1 x10^9 particles/ml, particle properties like shape or refractive index and background noise of the sample are critical requirements on a sample for NTA measurements (Filipe, Hawe et al. 2010, Zolls, Gregoritza et al. 2013, Vasudev, Mathew et al. 2015). Based on these requirements we chose the polystyrene particle system as optimal sample, because such samples are colloidal stable for the time of investigation, a large number of size distributions are available, a few studies were published using these sample and we showed the functionality on this system (Figure 3- 10). However, we are completely aware, that polystyrene particle systems

are not a fully adequate surrogate system to mimic protein particles due to the differences in e.g. morphology, refractive index of the particles.

The parameter capture time (CT) showed the lowest influence or even no influence on the results in the tested range. In general, the increase of CT is an option for samples with low concentrations as increasing capture times increase the total number of detection frames and tracks. Consequently, more reliable statistics and more reproducible results are achieved. This correlation was already shown by Boyd et al. (Boyd, Pichaimuthu et al. 2011) and is used in the live monitoring mode with unlimited CT. During live monitoring measurements of about 30 minutes CT, more than 40000 frames are recorded. For that reason, this mode is highly recommendable for a realistic evaluation, in particular as the capture time does not influence the result of size and concentration determinations significantly, but supports good statistics as seen in our experiments (Figure 3- 11). The importance of statistics and the subsequent reproducibility is highly important for measuring mixtures and protein samples, especially if they contain low concentrations of particles. An option for the analysis of low concentrated suspension is the application of a sample flow up to 50 µl/min (Zhou, Krueger et al. 2015). This, however, can lead to the appearance of a "peak" distortion, i.a. appearance of a shoulder in the peak. For the tested flow rate, we observed the phenomenon in particular for larger particles, e.g. 600 nm PS beads (see Figure 3- 10B). According to Figure 3- 10, the "peak" distortion (shoulder) indicates apparently the presence of a particle population composed of larger particles, which mean slower Brownian motion. An explanation could be that the limit of the mathematical algorithm excluding the influence of the applied flow on the result was reached.

The final result is influenced by the interplay between CL and DT. Increasing CLs lead to increasing particle concentrations because either more background noise (formulation components or protein monomers) or non-desired interferences are detected (false results). On the other hand, increasing CLs enables the detection of smaller particles. The opposite can be seen by decreasing DTs. Concerning size determinations an increase of CL results in a lower size because a larger part of smaller particles is recognized. Depending on the sample the setting of DT plays an important role influencing auto-functions, like minimal track length. Monomodal/monodispers samples with particle concentrations in the optimal range and low background (e.g. PS beads) can be measured in a broad DT range.

In a recent study presented by the group of John Carpenter et al. (Zhou, Krueger et al. 2015), investigating samples at high protein concentrations, they showed that at high protein concentration nanoparticle sizing was not affected, whereas particle concentrations were significantly reduced. Furthermore, they shows that a linear relationship between particle count and dilution factor exist, when a concentrated protein sample was diluted into particle-free solutions at the same protein concentrations, however, not when the concentrated protein solution was diluted into buffer (Zhou, Krueger et al. 2015). This issue, of measuring concentrated protein formulations and impact of dilution was also analyzed by Gruia et al. (Gruia, Parupudi et al. 2015). Based on their results, Gruia et al. come to the conclusions that NTA method performances molecule-specific and may not work as well under all solution conditions, especially when testing opalescent solutions (Gruia, Parupudi et al. 2015). These two studies underline the challenges encountered using NTA for particle analytics.

Stressed antibody suspensions consist of a high amount of monomers that are not detectable in a single-article matter as multiple scattering appears. Nevertheless, they produce a high scattering signal as background noise. The choice of the right DT can cause high variability in the results. One reason is that high DTs help to detect larger particles and reduce background noise but at the same time exclude small particles from evaluation. This is exemplary illustrated by the 50 nm particles in Figure 3- 13. Low DTs would help to detect the smaller particles but at the same time camera noise is detected as particles. This is in particular the case for short minimal track lengths. As we used an auto-function for minimal track length settings the choice of DT by the user determines the particles that should be considered, and the auto-function is based on these settings. In consequence, false results are achieved. The avoidance of high camera noise has already to be considered by the setting of the optimal CL (Figure 3- 12). As these parameters have to be set by the operator, the result is dictated by the operator as well and complementary methods are suggested to support the operator.

Comparing the polystyrene and BSA particle suspensions, we generally observed the same trends when changing the parameters. Apparently, the CL has a higher influence on the size determination of polystyrene particles compared to protein particles but has a lower influence on particle concentration. One explanation could be the difference in refractive index.

As mentioned before, the range of particle sizes than can be characterised by nanoparticle tracking analysis depends on the particle type. The lower size limit of this method is defined by the particle

size and the refractive index of the particles. Particles with a high refractive index, for example colloidal gold particles (Kubo, Diaz et al. 2007), size determination is achievable down to a particle diameter of 10 nm, whereas for particle with lower refractive index, such as protein particles (RI ca. 1.34-1.4) the smallest detectable sizes are above 35 nm. The refractive index of PS-particle (RI ca 1.59-1.6, λ = 589 nm at 20 °C) allows detection of all particles even at low CLs, which might not be the case for protein material (RI ca 1.34-1.4, λ = 589 nm at 20 °C). If the light intensity is higher, the scatter centre appears larger and tracking becomes less precise. On the other hand, the detection threshold (DT) strongly influences the result of protein size determination. This leads to the conclusion that also material specific properties, like refractive index or shape need to be taken into account for choosing optimal parameter settings. One property is the shape which is highly heterogeneous for proteins compared to the spherical particles. Furthermore, the refractive index of protein particles is assumed to be lower with 1.3 to 1.4 (Demeule, Messick et al. 2010, Zolls, Gregoritza et al. 2013) compared to PS-beads with 1.59. This variance leads to difference in the optimal CL. Based on the results with PS-beads (Figure 3- 12) and the known difference in the refractive index, approximations for particles of different materials can be made. For example, protein particle can only be detected if they are at least 35 nm to 50 nm in size and this observation can support the operator to interpret the data. The pronounced difference in particle concentrations of BSA particle suspension compared to PS-beads with increasing CL might also be caused by BSA fragments, which could not be detected before.

The ratio of the mean and the mode size values provides information about the dispersity of the solution (similar to the PDI in DLS measurements). In this case, a ratio value of 1 means the solution is monodisperse.

The difficulty of setting the optimal parameters for polydisperse suspensions in a broad size range is illustrated in Figure 3- 12. The figure precludes the optimization of the parameter settings. Smaller particles below 100 nm can only be detected at high CLs, i.e. high light exposure. Vice versa, it is only possible to detect larger particles at low CLs. Theoretically, a range from 200 nm to 1000 nm can be measured with one CL, but if a small portion of larger particles is present, they might dominate the smaller ones as stated by the light scattering theory. It was already shown that mixtures of particles in a specific ratio can be correctly discriminated (Hamrang, Rattray et al. 2013). In addition, Figure 3- 12 illustrates that a mixture of 50 nm and 600 nm cannot be analysed at the same CL. For a mixture of 50 nm, 400 nm and 600 nm particles it is impossible to find a CL

at which all three populations can be detected, discriminated and quantified. The mean CL, CL9, does not result in realistic size distributions. On the other hand, CL9 results confirm the increasing influence of 50 nm particles with increasing CL, the lowering of the 600 nm peak and the shift of the main peak to lower sizes. The tested CLs 4, 6 and 9 were in the optimal range for particle sizes of 100 nm to 600 nm particles. Unfortunately, measurements of the mixture at optimal CL for 50 nm are not possible due to the high light scatter intensity of the larger particles. Contrary, the optimal CL for 600 nm particles is too low to detect the 50 nm particles. A promising approach is the application of various settings for each sample. However, the question arises if the peak at 50 nm for CL4 and CL6 appeared due to background noise and if the sum of measurements at various CLs lead to a true result as the false results might cause misleading conclusions. Nevertheless, this can lead to false results as well as seen in Figure 3- 13. The fact that the 50 nm peak is in all cases very low even though it was set to a 9 times higher concentration can be explained by two approaches. First, particles with a size of 50 nm are only seen at high camera levels. As illustrated in Figure 3- 13 the optimal CL range for particles of that size is 13-15. At lower CL´s these particles are hardly detectable. Unfortunately, at higher CL´s larger particles appear too bright to do any analysis. Second, due to high interferences and background noise of the larger particles at CL9 the DT had to be set high as well. This causes the loss of 50 nm particles scattering as well. For that reason, we highly suggest complementary methods to support NTA result evaluation and interpretation. Consequently, another issue is the comparability of results. If parameters are adjusted and optimized for each sample, the question arises to which extend results are comparable.

The challenges with protein samples were demonstrated in a protein stability study. In both capturing modes it was possible to identify a change in particle number and size after stressing the protein. At constant settings relative comparisons can be made. The choice of the CL – based on Figure 3- 12 - can be used supporting the operator to set the limits for reliable size evaluation. For the samples a CL of 6 was set which allows reliable size determination in the range of 200 nm to 800 nm for proteins (Figure 3- 12 and RI). The capture mode is suitable for estimations, but the statistical evaluation was not sufficient. The live monitoring mode enables more reproducible results due to longer CTs and the software supported settings.

The importance of protein aggregate and particle detection in therapeutic biologics is tremendous (Gruia, Parupudi et al. 2015, Zhou, Krueger et al. 2015). NTA can be stated as one of the

techniques capable of generating more information and might have some application in trouble shooting exercises (USP<1788>). Nevertheless, in a biopharmaceutical setting it is necessary to understand risks of aggregates, to fulfil the regulations and to guarantee safety for the patients. For that purpose, studies demanding a high sample throughput and requiring that results are comparable, reproducible and confident are important and necessary.

Thus, it is highly important to understand the generated results and strive towards operator-independent, comparable, reliable, transparently and reproducible results. In our opinion, a major drawback is that results strongly depend on the operator and high throughput is currently not realizable. The development of the NTA technique and the software is still ongoing, and from our point of view the mentioned challenges should be considered.

8.4. Detailed evaluation of LUMiSizer® analysis

In this study the application of STEP-technology® used in the analytical photocentrifuge LUMiSizer® was evaluated. The focus of this method evaluation was based on the specific instrument settings (see below) for particle detection and on adequate sample properties for unambiguous detection. Subsequently, based on these results, some potential applications were demonstrated by using BSA protein standard particles and monoclonal antibody suspensions.

8.4.1. General measurement and sample considerations

For the analysis of particle suspensions with the LUMiSizer® system some critical factors, such as the suspension transmission or specific particle properties, were investigated to enable sample measurement as well as final PSD evaluation.

As one critical parameter concerning the particle detection, we identified the transmission value A320 and the turbidity in NTU of the sample. These values are often considered determinants in formulation development and stability studies as they indicate highly sensitively the presence of particles in a suspension. For that reason, we chose these parameters to set sample requirements and detection limits of the instrument. The importance was demonstrated in a dilution series experiment of 100 nm PS standard particle suspensions and the results are summarized in Figure 3- 17 and Table 10.

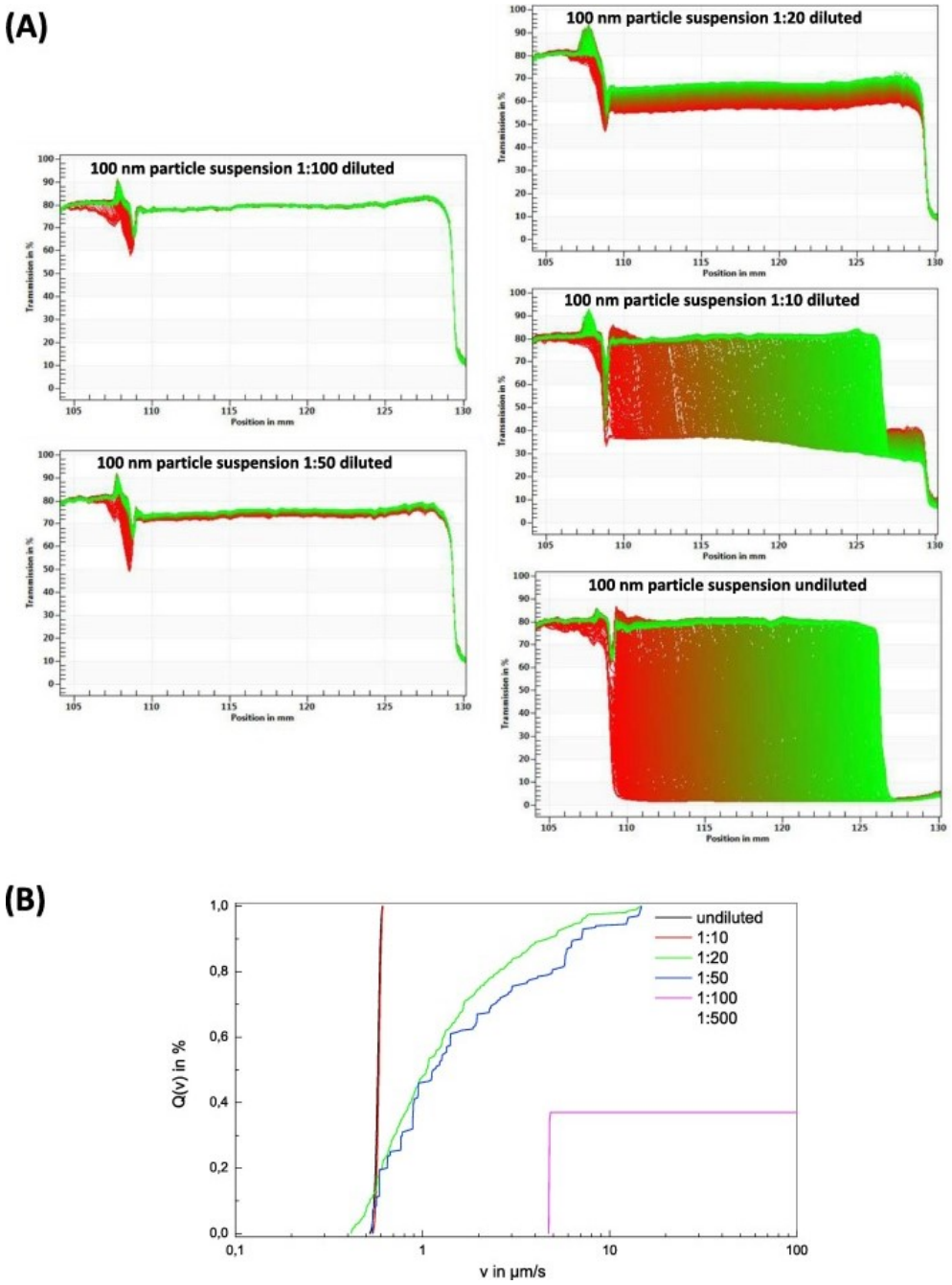

Figure 3- 17: LUMiSizer® evaluation: Influence of the parameter turbidity on the LUMiSizer® analysis outcome: Dilution series experiment of a 100 nm PS-bead suspension.

A dilution series of a PS bead suspension was produced in the depicted ratios and subsequently analyzed by LUMiSizer®. The transmission fingerprints of the dilution series (A) show that with increasing turbidity values, the start transmission values decrease and the bands of the sedimenting populations become clearer and detection is improved. This fact is seen in the subsequent cumulant sedimentation velocity distributions of the dilution series (B). The resulting cumulant sedimentation velocity distributions indicate that 1:500 and 1:100 dilutions cannot be evaluated correctly. Starting with a transmission value A320 of about 1 an appropriate evaluation is possible. These PSD results are summarized in Table 10.

Table 10: Summary of dilution series 100 nm PS-bead suspension (LUMiSizer® results).

100 nm suspension applied dilution	Transmission value A320	Turbidity value in NTU	LUMiSizer® Results (PSD)		
			Median /nm	Harmonic Mean/nm	Standard deviation
1:500	0.21	5.9	n/a	n/a	n/a
1:100	0.86	23.8	447.9	381.7	87.7
1:50	1.32	36.4	97.0	106.9	51.0
1:20	1.93	53.1	92.6	97.2	35.1
1:10	2.38	65.4	99.9	99.7	1.6
undiluted	n/a	n/a	100.1	99.8	2.0

The purchased 100 nm particle suspension was diluted as depicted: 1:10, 1:20, 1:50, 1:100 and 1:500, v:v. The resulting diluted suspensions showed A320 values ranging from 0.2 to 2.4 or respectively turbidity values from 6 NTU to 65 NTU (Table 10). The investigation of these suspensions using the LUMiSizer® resulted in the transmission fingerprints illustrated in Figure **3-17**A. The fingerprints represent a time-resolved motion of the particles during the centrifugation process leading to clearing of the suspension from the top (left) to the bottom (right). The first profiles are shown in "red" and over time the latest profiles are represented in "green". This clarification process is nicely detectable for samples with A320 values over 1 (undiluted, 1:10, 1:20 and 1:50). Suspensions with an A320 value below 1 did not result in sedimentation velocity distribution data that can be evaluated or even allow the calculation of a reliable particle size distribution (PSD) (Figure 3- 17B). Consequently, the calculations of sedimentation velocity distributions as well as the PSDs were unsuccessful or led to false results for the 1:500 dilution (no calculations possible n/a) and for the 1:100 dilution as the calculated median was about 448 nm instead of the expected 100 nm (Figure 3- 17B and Table 10). With increasing A320 value and turbidity, the sedimentation process and the shift of transmission profiles became clearer. Sedimentation velocity distributions of samples with A320 values between 1 and 2 could be analyzed and reproducible data were obtained but showed high standard deviations of over ± 30 nm. Best results were achieved with A320 values larger than 2 for the undiluted and 1:10 diluted suspensions with standard deviations around ± 2 nm.

A general evaluation, based on sedimentation velocity distribution is possible for every sample without knowledge of specific particle properties, if a sufficient start transmission of about 80 %

to 85 % for detection is given. This illustrates already the composition of the sample i.e. if different populations are present. A second critical aspect, however, is the dependency of the final PSD evaluation with the calculation of the particle sizes considering, the particle properties refractive index and density. To demonstrate the influence of these particle properties on the final outcome of size calculations, we investigated a monomodal silica standard particle suspension containing particle with a given size of 500 nm – based on manufacturer data (see materials). The suspension showed an A320 value above 2 (A320 = 2.6) and, thus a sufficient start transmission for LUMiSizer® detection of 20 % (Figure 3- 18A-A). The clarification process was easily detectable and the resulting sedimentation velocity distribution is shown in Figure 3- 18A-B. This distribution indicated the presence of one single population with a sedimentation velocity around 60 µm/s and a peak width of about 30 µm/s. The final calculation of volume weighted PSD and particle sizes based on the manufacturer data set values for particle density ($\rho = 1.85$ g/cm^3) and refractive index (RI = 1.42) of the silica particles – showed a population in the expected range around 500 nm (mean 477 nm). To highlight the deviations caused by false particle properties and to monitor the influence of density and refractive index, we additionally performed the final size evaluation calculation of the achieved silica particle suspension raw data applying different data sets varying these properties. All selected data sets ("Protein1", "Protein3", "Protein4", "Protein6" and "Protein7") including the defined density value and refractive index are summarized in Figure 3-18A-B. The resulting volume weighted PSDs are illustrated in Figure 3- 18A-C. In conclusion, there were no significant changes in the PSD detected by the variation of RI in the range between 1.0 and 1.6. In contrast, density value variations in the range between 1.01 g/cm^3 and 2.0 g/cm^3 led to size difference shifts from 435 nm to 3865 nm mean size. The peak width of about 100 nm as well as the peak shape was constant. The knowledge about the correct density of the particles that are investigated is essential to achieve the correct absolute size values. The refractive index indeed is important to achieve a sufficient transmission for clarification process, but the correct value is not relevant for the size calculation.

(A)

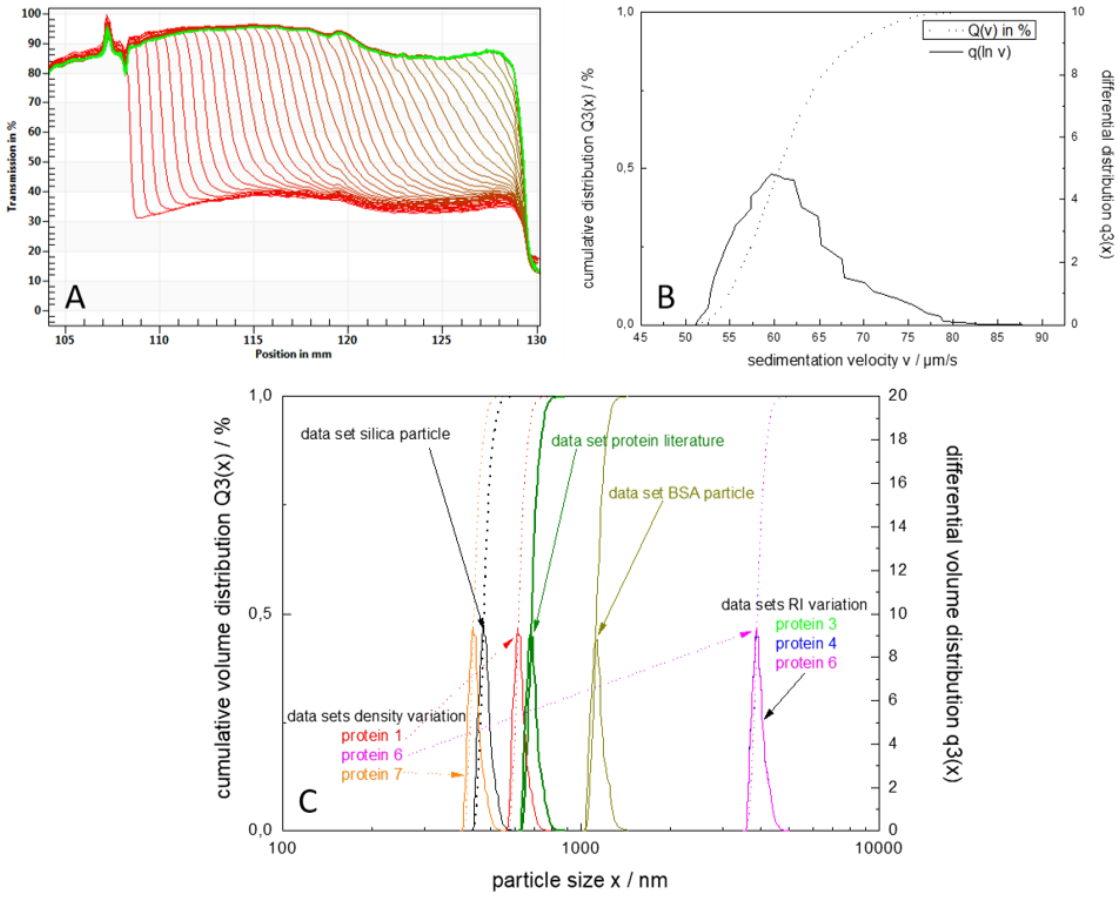

(B)

Dataset name	Data source/variation	Density / kg/m³	Refractive index
Silica particle	Manufacturer data sheet	1850	1.42
Protein literature	Average literature data for proteins	1410	1.40
BSA particle	Average literature BSA	1150	1.34
„Protein1“	Dataset density variation (average density)	1500	1.30
„Protein3“	Dataset RI variation (average RI)	1010	1.30
„Protein7“	Dataset density variation (maximal density)	2000	1.30
„Protein6“	Dataset density variation (minimal density) Dataset RI variation (maximal RI)	1010	1.60
„Protein4“	Dataset RI variation (minimal RI)	1010	1.00

Figure 3- 18: LUMiSizer® evaluation: Influence of the particle density and refractive index on the LUMiSizer® analysis outcome: Example 500 nm silica particle suspension.

A suspension of 500 nm standard silica particles was analyzed by LUMiSizer®. The results are summarized in the upper part of the figure (A). The resulting transmission profile fingerprint shows clear bands and a monodisperse and monomodal composition can be assumed (A)-A. The consequent sedimentation velocity distribution indicates one single population with a sedimentation velocity around 60 µm/s (A)-B. Based on this sedimentation velocity distribution, PSD calculations based have been performed using various datasets differing in RI and density values. The resulting PSDs depicted with the used datasets are seen in (A)-C. An overview of the applied datasets and the defined properties in each data set is given in the lower part of the figure (B). The values provided by the manufacturer are summarized as dataset „Silica particle “.

8.4.2. Characterization of chemically linked protein particle suspensions

The successful characterization and size determination of inorganic standard particles, such as silica and polystyrene particles, has been demonstrated in the previous experiments. In addition, we recently investigated and analyzed commercial protein standard particles (compare PART III chapter 8.1.3). These commercially produced BSA particle suspensions with defined sizes of about 200 nm and 500 nm have been produced by chemical cross-linkage of BSA molecules. The standard particles suspensions showed sufficient turbidity, 60 % respectively 40 % start transmission, even at concentrations down to 0.1 mg/ml and could be nicely characterized by the LUMiSizer®. As an alternative approach in this study, we produced DSG-cross-linked monoclonal antibody particles of two different antibodies, mAB1 and mAB2. Both particle suspensions appeared highly polydisperse (PDI values between 0.3 and 0.4 by DLS) and with high turbidity (mAB1 427 NTU and mAB2 171 NTU). Interestingly, the same cross-linking procedure led to significant different results in PSD for mAB1 and mAB2. Based on DLS results, mAB1 DSG-particles showed a PSD over the whole submicron size range. Two populations were discriminated with mode sizes of 116 nm and 404 nm. In contrast, the resulting mAB2 particle suspension with lower turbidity showed a size range distribution (intensity) from about 20 nm to 400 nm. In this case two populations were likewise discriminated with mode sizes of 42 nm and 171 nm. NTA measurements have been performed, but could hardly be evaluated quantitatively, because the scatter videos (not shown) showed no single scatter centers in any measurement setting but indicated a loose particle network and high background interferences. MFI results showed particles in the lower micron size range in both particle suspensions.

LUMiSizer® results of the two DSG-particle suspensions were summarized in Figure 3- 19. The transmission profile fingerprints indicated not only differences in the composition but also in the sedimentation behavior (Figure 3- 19A and B). The transmission profile fingerprint of the mAB1 DSG-particle suspension (left) showed mainly clear vertical moving phase borderlines indicating separable populations with lower polydispersity and a polymodal sample composition with at least three populations. Furthermore, the solution clarification during separation occurred in different phases over time: In the beginning, the movement of one clear phase border was monitored indicating one single population (***phase I***). Afterwards, the single borderline was split in two separate bands (***phase II***). In each band the varying intervals between the profiles might indicate specific interactions. The final step was an integral clarification indicating a more polydisperse

population of smaller particles (***phase III***). The appropriate sedimentation velocity distribution was calculated and is illustrated in Figure 3- 19B. The sedimentation velocity distribution of exclusively the first phase showed a small population around 0.1 µm/s (labelled with an arrow), a main population around 1 µm/s and one population between 100 µm/s and 1000 µm/s. The evaluation of the total transmission profile fingerprint, indeed, showed sedimentation velocities from 0.15 µm/s to 10 µm/s and one around 1000 µm/s with two significant mode size peaks at 0.9 µm/s and 15 µm/s. A final particle size and volume-weighted PSD calculation was performed based on two different particle property datasets, "BSA2" and "protein literature" (Figure 3- 19C). The defined properties of each set are shown in Figure 3- 19B. The BSA dataset-based evaluation monitored a clear population in the submicron range (34 nm to 200 nm) and one in the micrometer range (10 µm to 100 µm). This micrometer population was not observable by the protein literature dataset. The three peaks in the submicron range are monitored by both settings.

The mAB2 DSG-particle suspension showed an overall integral clarification indicating a highly polydisperse sample composition in the transmission profile. The transmission profile fingerprint in Figure 3- 19A (right) monitored one phase of fast clearing (***phase I***) and a second phase of slower clearing (***phase II***). The resulting sedimentation velocity distribution indicated two populations: One population with a sedimentation velocity from 0.1 µm/s to 10 µm/s and a second population with velocities from 1500 µm/s to 11000 µm/s including two significant mode sizes at 0.9 µm/s and 15 µm/s. Both PSDs showed a submicron population - smaller than the mAB1 particle – and a micrometer population larger than the mAB1 particle. All PSD results were summarized in Figure 3- 19C. In comparison to the results of the applied orthogonal methods (NTA, DLS, MFI), the sedimentation velocity distributions as well as the PSD tendencies correlate partially. However, none of the used material data sets led to similar absolute particle sizes as DLS or MFI.

(A)

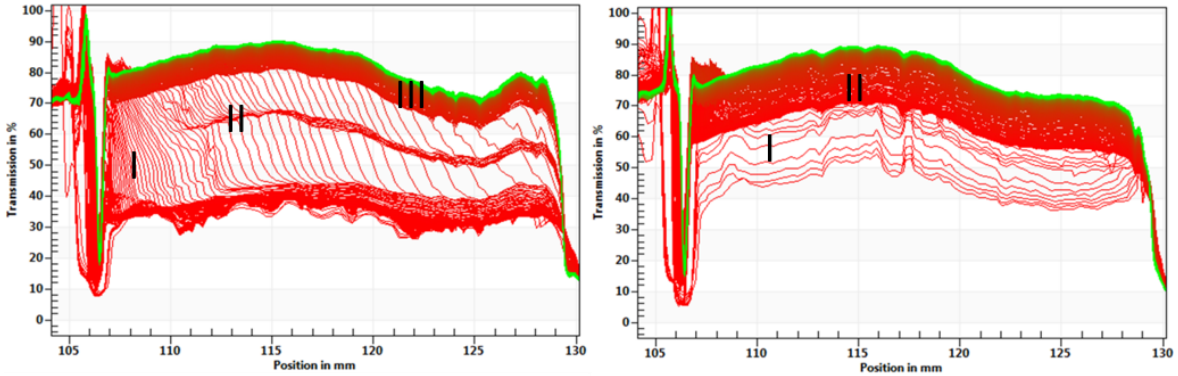

(B)

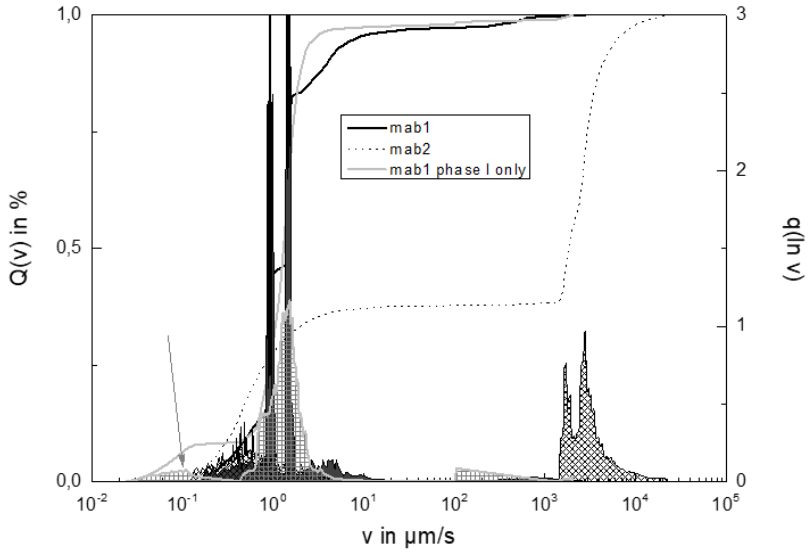

(C)

	Resulting size populations and depicted mode sizes based on protein literature data set	*Resulting size populations and depicted mode sizes based on BSA2 data set*
DSG particle mAB1		
Population 1	20 – 100 nm	34 – 200 nm
Peak1	23 nm	38 nm
Peak2	52 nm	87 nm
Peak3	67 nm	111 nm
Population 2	n/a	10 – 100 µm
DSG particle mAB2		
Population 1	17 – 70 nm	30 – 135 nm
Peak1	18 nm	34 nm
Peak2	21 nm	41 nm
Peak3	37 nm	61 nm
Population 2	28 – 100 µm	46 – 160 µm
Peak1	31 µm	51 µm
Peak2	40 µm	68 µm

Figure 3- 19: LUMiSizer® evaluation: Characterization of chemically cross-linked (DSG) protein particles.
Chemically cross-linked protein particles of mAB1 and mAB2 have been produced and the resulting particle suspension was investigated by LUMiSizer®. The resulting transmission profile fingerprints of mAB1 DSG-particles and mAB2 DSG-Particles (A) as well as the subsequent sedimentation velocity distributions differ significantly (B): mAB1 shows two main populations around 1 µm/s and no larger particles while mAB2 shows one population below 1 µm/s and one with sedimentation velocities larger than 1000 µm/s. The final volume-weighted PSDs have been calculated based on the BSA dataset and the protein literature dataset and results are comparative summarized under (C).

8.4.3. Characterization of unstressed and physically stressed mAB suspensions

Monoclonal antibodies in suspension have been investigated by LUMiSizer®, exemplary for therapeutic proteins. Three aspects were in the focus of this experiment.

(i) The first aspect was the analysis of unstressed mAB suspensions with increasing protein concentrations exemplary for mAB2. The results of the LUMiSizer® analysis of unstressed mAB2 suspensions were summarized in Figure 3- 20A and B. The suspension of mAB2 was investigated at four different concentrations, 0.1 mg/ml, 1 mg/ml, 10 mg/ml and 200 mg/ml. The transmission profiles of mAB2 suspension up to 10 mg/ml showed high start transmissions over 80 %. Consequently, it was not possible to obtain evaluable sedimentation data with the tested settings. The analysis of the mAB2 suspension with about 200 mg/ml, however, monitored an integral clarification up to 120 mm and a transmission decrease from 120 mm to the cuvette bottom. The evaluation between the meniscus and 120 mm indicated particle movement with a sedimentation velocity from 0.1 µm/s to 10 µm/s. Based on literature data (Fischer, Polikarpov et al. 2004) a particle size median was calculated with 98 nm.

(ii) The second aspect was the investigation and characterization of physically stressed mAB suspensions of mAB1 and mAB2. Various physically stressed mAB suspensions were analyzed. The application of stirring stress led to sufficient turbidity in all cases and the particle sedimentation could be captured. Interestingly, mAB incubation at 60 °C without stirring over 12 days was not evaluable as the start transmission was too low (over 90 %). However, the transmission profile fingerprints of mAB1 and mAB2 stirred at room temperature and at 60 °C are shown exemplary in Figure 3- 20C to F. The effects of the depicted stress conditions carried out specific and unique fingerprints depending on the protein and the stress applied. A qualitative comparison of these fingerprints gives valuable information. The stressed mAB1 suspension at RT showed first clear vertical borders, the intervals between the profiles were rather small; the clearing happened slowly, the last transmission profiles show a smooth border at the top and full clearing was not achieved. In comparison, the profiles of mAB1 stressed at 60 °C were more horizontal indicating higher polydispersity, the intervals were larger indicating larger particles and final clearing was achieved at the same protocol.

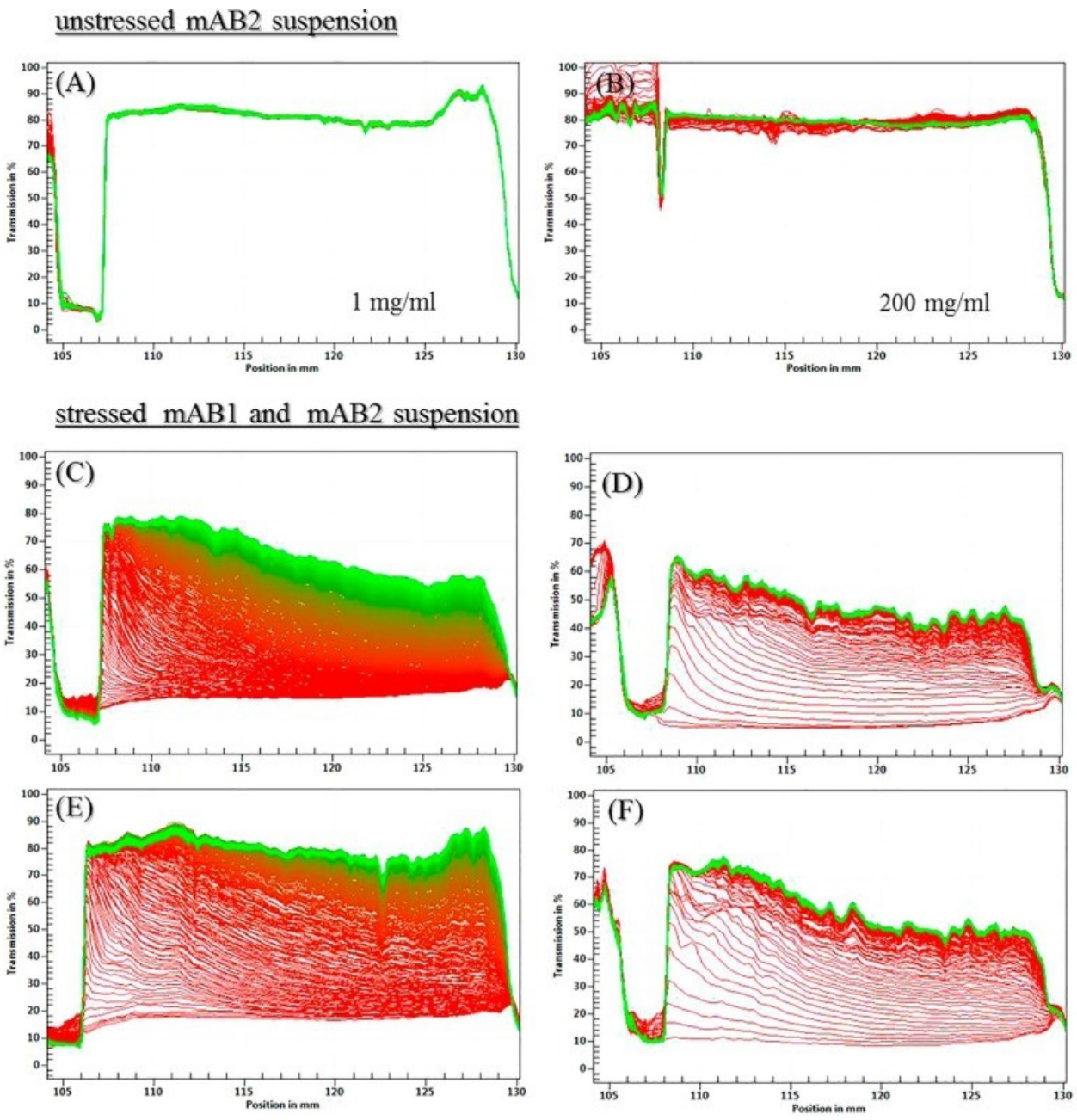

Figure 3- 20: LUMiSizer® evaluation: Characterization of unstressed and physically stressed therapeutic monoclonal antibody suspensions.
Unstressed mAB suspensions of mAB2 in concentrations of 1 mg/ml (A) and 200 mg/ml (B) were analyzed in the same buffer and with the same centrifugation protocol. In both cases, the start transmission appeared with over 80 % and evaluations are hardly achievable. Significant differences during the process of about 10 %, however, are seen in fingerprint (B). In a further step, suspensions of mAB1 (D and F) and mAB2 (C and E) in a concentration of 1 mg/ml have been physically stressed by the application of stirring stress at room temperature (C and D) and stirring at 60 °C (E and F) before investigation and the resulting fingerprints are seen in the lower part of the figure. Stirring stress as well as the combination led to significant changes of the sample and aggregation.

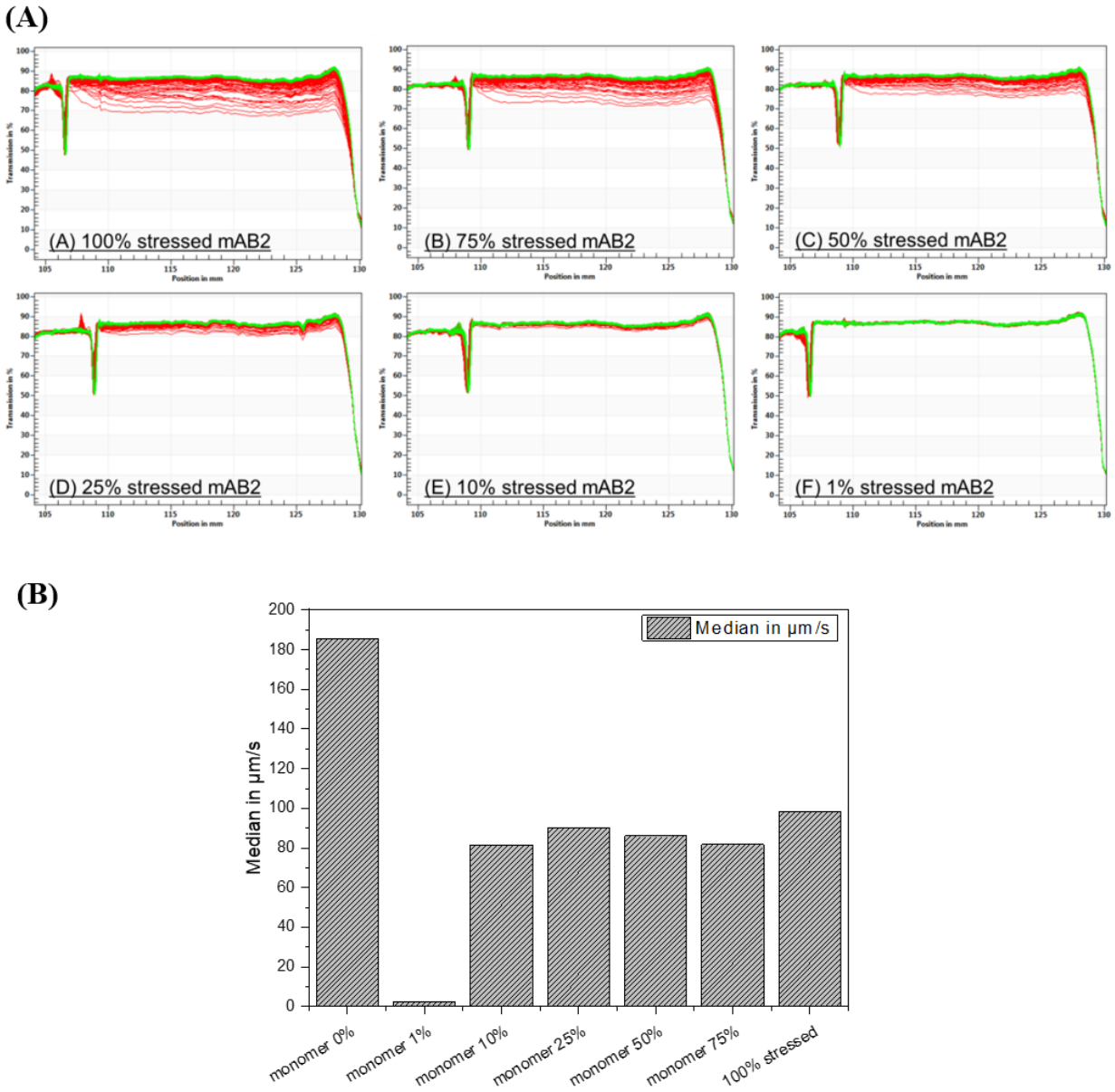

Figure 3- 21: LUMiSizer® evaluation: Detection of minimal portion of stressed mAB present enabling LUMiSizer® analysis (Spiking experiment).
For this experiment an unstressed mAB2 suspension was analyzed after the addition of various portions of physically stressed mAB2 suspension. The spiking suspension was an aliquot of the origin mAB2 suspension but was stirred for 0.5 h at room temperature. The final result of the stressed suspension was set as 100 % physical aggregates (A-A). The depicted portion of stressed mAB2 suspension was subsequently added to aliquotes of the original unstressed mAB2 suspension and analyzed. The transmission fingerprints of sample mixtures with 1 %, 10 %, 25 %, 50 % and 75 % of the stressed suspension are shown (A-B to A-F). The resulting median of sedimentation velocity distributions of each mixture is illustrated under (B). Starting with a portion of 10 % stressed mAB2 suspension the median stayed constant and similar to the 100 % stressed mAB2 suspension.

The mAB2 suspension showed similar effects comparing different stress conditions, but in contrast to mAB1, the last profiles showed a rough surface indicating strong interaction of the particle with the cuvette surface. These interactions gave a better description of the surface properties of the particles.

(iii)A third aspect aimed the identification of the "minimal" requested amount of stressed mAB suspension for a successful evaluation. A stir stressed mAB2 suspension (100 rpm, 30 min, RT) was added to unstressed mAB2 suspension - entitled as spike experiment. The resulting transmission profiles are shown in Figure 3- 21A. A successful detection of the stressed mAB started with a 10 vol% stressed suspension. With increasing potion of the stressed mAB suspension, the start transmission increased, but qualitative evaluation of the fingerprints as well as sedimentation velocity median show similar results (Figure 3- 21B). The highest sedimentation velocity median was detected for the stressed mAB suspension with about 100 µm/s. The 10 vol% to 75 vol% spikes led to a sedimentation velocity median of about 80 µm/s. The results of sedimentation velocity evaluation for 0 vol% and 1 vol% were not reliable based on transmission profile fingerprints. The resulting velocity distributions (data not shown) indicated two clear populations (I: 55 µm/s to 110 µm/s; II: 110 µm/s to 1000 µm/s) in all spike samples. A third population appeared as highly polydisperse and heterogeneous population covering particle with a velocity from 1 µm/s to 55 µm/s. In particular, the 10 % sample showed a high deviation in this population. However, the addition of stressed mAB suspension to unstressed mAB suspensions led to similar results without significant changes in the particle sedimentation velocity.

8.5. Discussion detailed evaluation of LUMiSizer® analysis

The LUMiSizer® system using the STEP-technology® was evaluated for the application for therapeutic protein samples. The two most critical factors, transmission and the particle density on which calculations are based, have been evaluated in more detail.

Particle detection is realized by an optical system and depends highly on the optical properties of the particles and the surrounding medium, i.e. formulation composition. The appearance of a specific transmission (max. 85 %) is essential for the detection of particle movement. This

transmission is realized by a sufficient optical contrast that is based on the difference in the refractive indices between particle and medium as well as particle scattering intensity. If the RI of the particles is similar to the RI of medium (in our case water; RI approx. 1.333), particles cannot be detected. Same applies if the light scattered by the particles shows low intensity. This scatter intensity depends on the particle size and shape as well as the particle concentration. The latter was demonstrated and substantiated by the experiments with a 100 nm particle suspension dilution series. Based on the results of the experiment with 100 nm PS bead suspensions, the following lower limits have been identified: Particle suspension with a turbidity A320 value of at least 1.0 are measurable and calculations showed expected values.

The A320 value is a general parameter and is applied as general criterion for LUMiSizer® suitability as well (A320 < 1: sample not measurable). To demonstrate the applicability, we generated mAB suspensions with a defined ratio of stressed mAB2. In case of mAB2, 10 % of stressed mAB2 suspensions were sufficient for LUMiSizer® analysis. However, depending on the inherent properties (e.g. the translucence) of the protein particles and the aggregation state/aggregate characteristics, this might differ. For the investigated molecule stirring stress application in most cases leads to rather large aggregates that quickly precipitate, while temperature stress causes smaller aggregates that could be hardly detected. In any case, in the performed spike experiments no interactions of the particles with the cuvette wall, i.e. adhering particles at the surface, were observed. Furthermore, monomodal particle suspensions with 100 nm PS-beads (RI = 1.59) should contain at least 2 $x10^{11}$ particle/ml for a successful analysis based on the dilution series illustrated in Figure 3- 17. Based on Mie theory and Rayleigh approximation scattering intensity depends on the sixth power of size. In consequence, the detection of suspensions with larger particles should fulfill the turbidity value already at lower concentration. In contrast to techniques that are only based on light scattering, LUMiSizer® is suitable for the analysis of polymodal and polydisperse mixtures, over a great range due to the separation process during centrifugation.

Protein samples and protein particle suspensions appear most likely on the lower optical detection limits with high transmission. Protein particles with RIs between 1.3 and 1.6 scatter with lower intensity as the difference between particle RI and medium RI is lower. In consequence, a sufficient low transmission (at least about 85 %) is only possible if either high concentration of particles in the nanometer size range or larger particles in the micrometer size range are present.

Considering authority regulations regarding particles in therapeutic protein products, limits are only addressed to the micrometer size ranges (10 µm and 25 µm). As these larger particles scatter in higher intensities, they could be detected already at low concentrations. In contrast, protein particles, e.g. antibody monomers with a hydrodynamic diameter of 10 nm, are hardly to detect even at high concentrations. As shown in Figure 3- 20A and Figure 3- 20B, protein suspensions with the monomer content of about 98 % to 99 % (determined by size exclusion chromatography), i.e. particles with a molecule sizes of about 10 nm, and with content of about 1–2 % of high molecular weight species/aggregates up to a few 100 nm have been investigated in different concentrations. In the first case, monomer scattering was not sufficient at mAB concentrations up to 100 mg/ml and low molecular weight aggregate concentrations were too low. These mAB suspensions with concentrations of 100 mg/ml representing about 4 $x10^{20}$ particles/L – assuming 10 nm monomers with a molecular weight of 150 kDa, N_A=6.022 $x10^{23}$ 1/mol – appeared insufficient. The sample with 200 mg/ml representing about 1 $x10^{21}$ particles/L, indeed, showed sufficient low transmission to detect slight changes during the sedimentation process. At such high concentrations, interpretation of results is challenging, because aggregation/association might appear, and the detected signal can indicate the presence of such aggregated particles as well. A PSD median value of 98 nm might support the presence of aggregates. In addition, the movement of the particle in such concentrations is hindered, due to crowding effects and elevated solution viscosity. In consequence, further investigations are necessary to clarify the sample composition. However, great variations in optical properties of protein particle allow in some cases successful detection of particles in the submicron range. Examples are chemically cross-linked protein standard particles, like the commercial BSA particles or DSG-cross-linked mAB particle, which showed generally high turbidity and could be investigated easily.

The second criterion is the particle density that should be known for final PSD calculation based on Stokes law. Similar challenges as to optical particle properties apply: particle densities reach over a broad range depending on the protein and the aggregate type; protein particles process rather low densities complicating separation and lower the settling process in total; in highly polydisperse and polymodal samples such parameters are hard to achieve/define and could be different for each particle. Density values of proteins have been calculated in literature (Fischer, Polikarpov et al. 2004). Potentially, LUMiSizer® experiments could be used to detect particle densities. However due to the great heterogeneity of our samples, literature data (Fischer, Polikarpov et al. 2004) has

been used for the evaluation and size estimation could be performed. Results are based on estimated densities or literature values but based on aggregation mechanism characteristics and properties of aggregates can extremely differ. These estimations could extremely be different from the real particle sizes. For that reason, the most valuable results as shown in all studies are the transmission profile fingerprints and the sedimentation velocity distributions. In particular, the transmission profiles appeared highly valuable for information about sample composition, sedimentation behavior and interactions.

Cross-validations with light interaction-based techniques were in agreement to the results obtained in case of the purified populations of BSA particles. The provided values of the manufacturer for RI and density showed expected results in PSD calculation that could be confirmed by DLS and NTA. In contrast, the unpurified polydisperse mixture of DSG-crosslinked mAB particle showed variations in the final outcomes. LUMiSizer® PSD with size estimation results did not completely agree with the orthogonal methods. However, light-based methods are generally imprecise for highly polydisperse and turbid samples. In addition, LUMiSizer® is the only technique tested covering the whole size range. An additional orthogonal principle is necessary at this point.

Nevertheless, the evaluation of the transmission profile fingerprints and the sedimentation velocity distributions of the DSG-crosslinked mAB particle suspensions provide valuable information. The same cross-linking procedure was carried out on different particle populations with different sedimentation behavior and sample composition for mAB1 and mAB2. mAB1 moved initially as one dynamic population, eventually a network of particles as seen also in NTA measurements (phase I). At a specific point this network population was split, and the two subpopulations could be separated. This could correlate with the 404 nm DLS peak. In both population particle-particle interactions can be assumed. In a final third phase, integral clearing took place and could illustrate the 116 nm DLS peak. The larger particles are hardly seen in the fingerprint, but nicely seen in the sedimentation distribution. However, the larger particle population seems to be in the submicron range. Without any particle information, a good characterization was possible. Concerning PSDs, the BSA data set seemed to fit best comparing DLS results. One reason might be similar particle properties due to the chemical modification and cross-linkage.

The suspension of cross-linked mAB2 showed only two highly polydisperse phases. The first one indicating large particles could represent the main population in the sample in the micrometer range. The particle sizes calculated are outside the MFI range and at the upper limit of LUMiSizer®

analysis. As MFI results led more to the conclusion that mAB1 would contain larger particles LUMiSizer® might open theses limits and detect particle populations that had been unattended before. Even though only size estimations are possible LUMiSizer® analysis characterized the suspensions in a complementary and unique manner. In conclusion, no technique described the samples completely and one approach is to separate particle populations by size enabling better analysis by light-scatter based techniques.

For that reason, the transmission fingerprints as well as the sedimentation distributions are the most valuable information that can also be used for the description of protein particle suspensions independently of any property information necessary. The examples of stressed mAB suspensions, as shown in Figure 3- 20, underline this statement. Each transmission profile showed sample specific characteristics. The application of stirring stress to mAB1 resulted generally in smaller particles than mAB2. Furthermore, mAB2 particles showed a greater tendency adhering and interacting with the more hydrophobic cuvette surface (visual observation). One explanation that has already been seen in previous thermal unfolding experiments (data not shown) with mAB2 is that mAB2 tends to unfold easily and presents hydrophobic patches already at low temperatures. In addition, self-interactions between the stressed molecules can be assumed based on the transmission profile fingerprint. In contrast, mAB1 showed less interaction with the hydrophobic surface and can be assumed after the applied stress as less hydrophobic particles. As both samples have been treated the same way and the analysis was done under same conditions and in the same run, the assumption of two different aggregation mechanisms can be proposed. The topic of particle-particle interaction has also been addressed at this point. The spike experiment with stressed mAB2, remarkably, could not detect interactions between monomer and the stressed mAB2 molecules after 30 min stirring at room temperature. After 30 min stirring, no significant particle-particle-interactions could be detected as the sedimentation velocity median was constantly around 80 µm/s.

9. Evaluation of selected novel technologies for the investigation and characterization of protein unfolding and aggregation processes

Besides foreign, extrinsic particles, e.g from the manufacturing process, intrinsic/inherent protein particles caused by protein aggregation are one of the main particle sources in biopharmaceuticals. The process of protein aggregation as one of the major challenges of biologicals is highly complex, hardly predictable and are most likely triggered by conformational changes, e.g protein unfolding. Over the last years, novel technologies occurred that enable more sophisticated investigation approaches of these processes from new perspectives to gain more knowledge about these processes. In this thesis, the SwitchSENSE® technology (Dynamic Biosensors GmbH) and the Zetasizer Helix instrument (Malvern Panalytics) as examples of such novel approaches have been selected for more detailed evaluation (chapter 9.2 and 9.1).

9.1. Evaluation of the DLS-Raman combination: Zetasizer Helix system

The combination of DLS measurement and Raman spectroscopy enables the investigation of protein structural changes and simultaneous occurring protein aggregation events. The instrument provided three measurement options: samples series, isothermal incubation and thermal ramp measurements. Within this application portfolio, we decided to evaluate the system for the chosen molecular antibodies. All experiments were performed in the BI laboratories (Biberach/Riss, Germany) in cooperation with colleagues from Malvern Instruments. Similar to measurements with the Zetasizer instrument, specific sample preparation was not necessary, but due to Raman spectroscopy requirements protein concentration was set at least to 10 mg/ml.

9.1.1. Sample series

The mode “Sample series measurements” enables the investigation of a single sample or a series of samples in a study. Exemplary, two sample series studies have been performed: a dilution series of mAB2 and a comparison of the selected mABs (mAB1, mAB2 and mAB3) in phosphate buffer and after dialysis in water. All samples have been measured in triplicates.

(1) The results of the dilution series of mAB2 are summarized in Figure 3- 22. The DLS analysis showed differences in the z-average, PDI and the detected populations within the dilutions. The z-average decreased with decreasing protein concentration. The PDI behaved in a similar manner.

In addition, the high concentrated suspensions with 211 mg/ml and 100 mg/ml showed a second population in the 4 µm size range indicating potential aggregates. The 10 mg/ ml sample showed an exceptional behavior from the z-average trend with an apparent size of about 5 nm, compared to about 3 nm at 40 mg/ml and about 4 nm at 100 mg/ml.

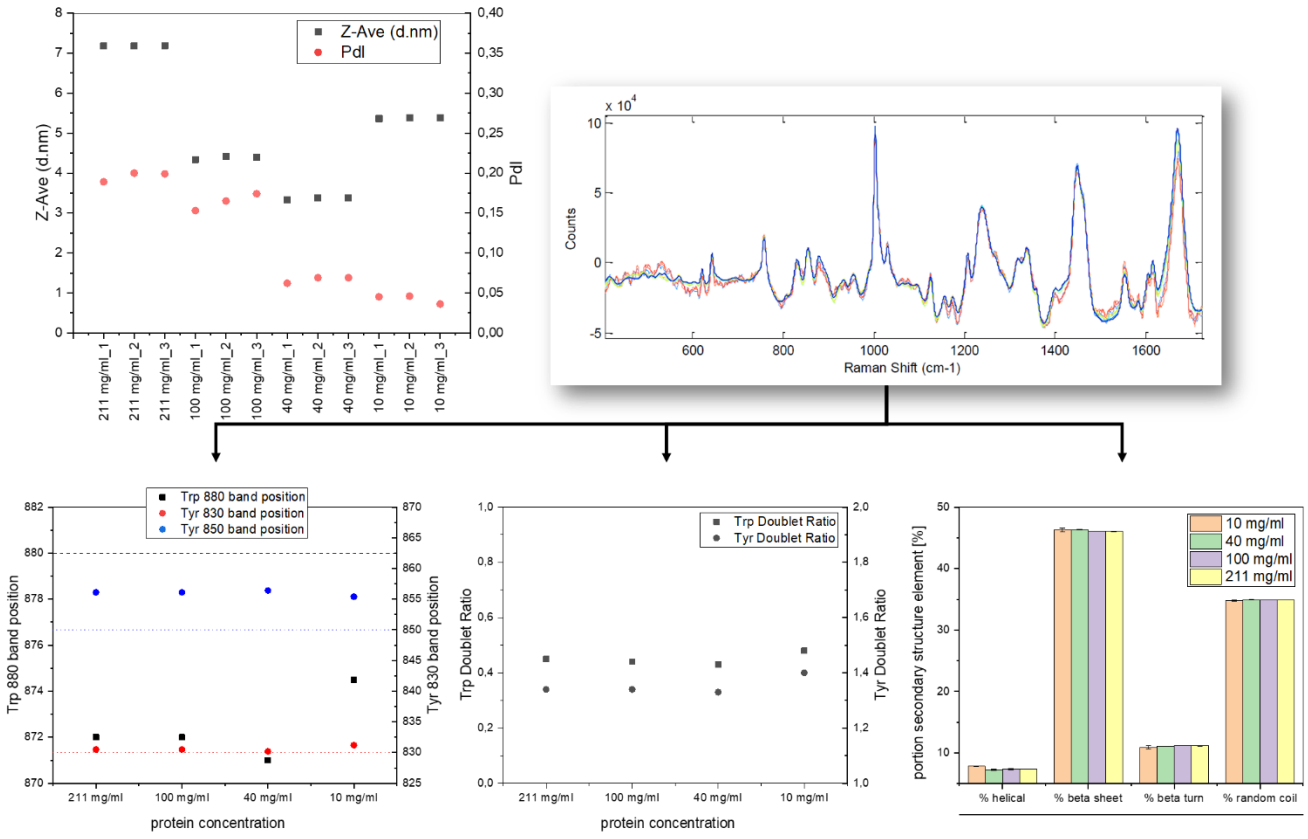

Figure 3- 22: Zetasizer Helix evaluation: Results of dilution series mAB2.
The figure summarizes the Results of DLS measurements (upper left) and illustrates the Raman spectra (upper right) and the resulting specific markers for secondary structure (lower right) and tertiary structure considering tryptophan and tyrosine bands (lower left and center).

In consideration of the Raman spectroscopy results all dilution showed similar secondary structure markers (Figure 3- 22, low right). For mAB2, the main portions detected were beta sheets (~50 %) and random coils (~34 %). The lowest portion was the alpha helices (~7 %). The spectra of the 100 mg/ml and the 211 mg/ml samples lead to similar secondary structure calculations. In comparison, the 40 mg/ml and 10 mg/ml samples showed slightly increased portions of alpha helices and beta sheets and decreased portions of beta turns and random coils. No clear structural changes, however, were detected. Similar to the secondary structure, the tertiary structure markers

for 211 mg/ml and 100 mg/mL showed no differences. A shift was detected in tyrosine and Tryptophan markers from 100 mg/ml to 40 mg/mL and a larger shift from 40 mg/mL to10 mg/mL. It suggested structural changes depending on protein concentration. The differences from higher concentrations to 40 mg/mL, and then to 10 mg/mL, was also detected in shifts in the disulphide region indicating changes in disulphide bond confirmation as concentration changes. In conclusion, both techniques indicated a concentration dependency considering conformational and colloidal stability.

(2) The results of the comparison samples (protein in water vs. protein in buffer) are summarized Figure 3- 23 and Figure 3- 24. The size determinations using DLS resulted in an apparently size (z-average) of about 11 nm for all three mABs in the model buffer (PDI below 0.15). After dialysis into water the measured hydrodynamic diameters decreased and differed for each mAB: mAB1 showed a size decrease to 9 nm and a lower PDI.; mAB2 and mAB3 decreased to an apparent size of about 2.5 nm but increasing PDI. For mAB2 and mAB3, an additional large population above 1 µm occurred indicating potential aggregates.

The resulting Raman spectra indicated no significant differences in the secondary structure but minor differences in the tertiary structure and/or hydration, namely in the tyrosine doublet intensity ratio (I_{850}/I_{830}), tryptophan dihedral angle (1550 cm^{-1}) and tryptophan doublet ratio (1360/1340 cm^{-1}). For mAB1 a major change was detected in tryptophan doublet ratio and a minor change in the tryptophan dihedral angle. In buffer the tryptophan is in a more hydrophobic environment and the angle between main chain and tryptophan side chain increases slightly. Similar phenomenon was observed for mAB2. Major changes in the tryptophan dihedral angle were detected for mAB3, but the angle decreased in the buffer. In addition, mAB2 showed also a change in the tyrosine doublet that indicated an increasing tendency for exposed acceptor of strong H-bonds in water. Concluding, one should consider performing measurements for more than n=3 to overcome and exclude uncertainties and misinterpretation due to noisy spectra.

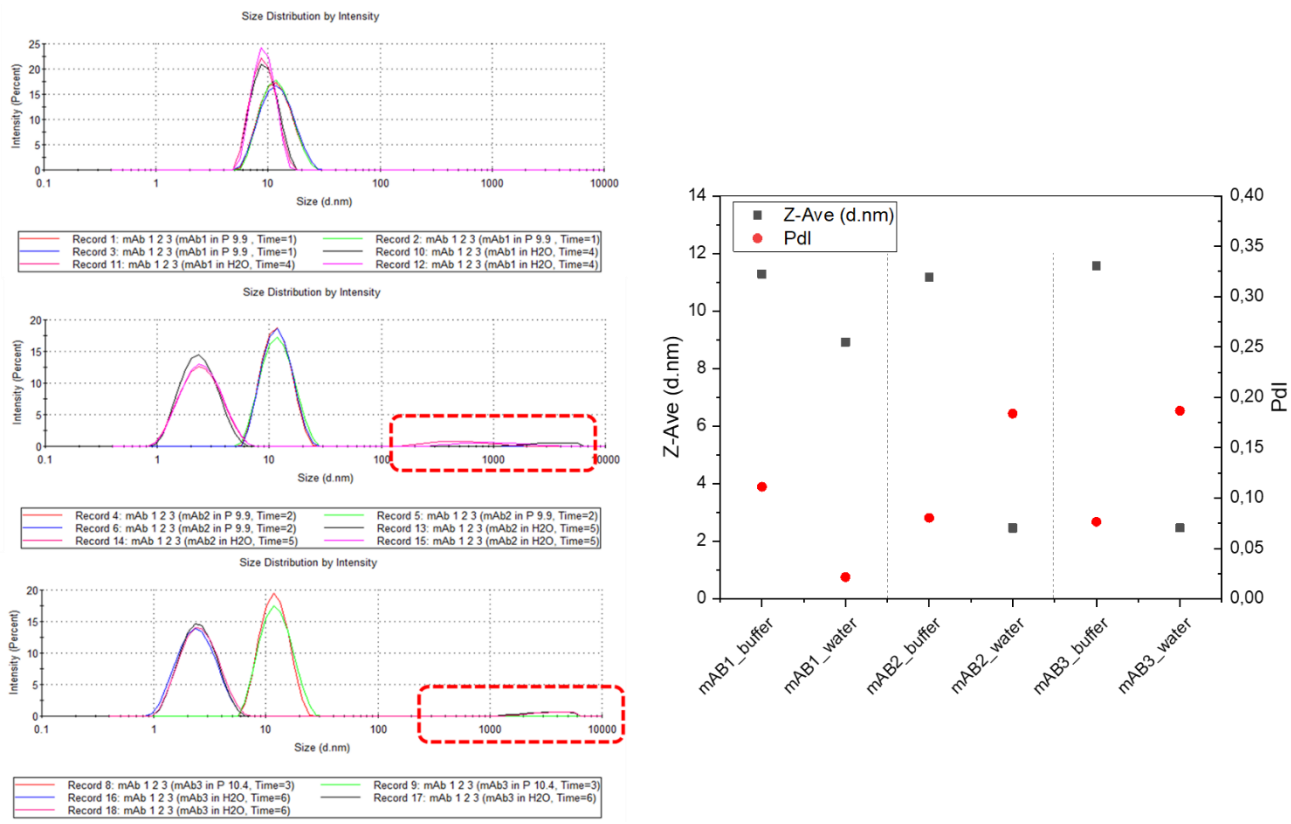

Figure 3- 23: Zetasizer Helix evaluation: DLS results sample series comparison mABs in water and model buffer.

Single sample measurements of mAB1, mAB2 and mAB3 after dialysis in water and phosphate model buffer 10 mM phosphate containing 10 mM NaCl pH 6.5 have been performed. The resulting intensity-based size distributions are shown in the left part: mAB1 upper, mAB2 middle and mAB3 lower. In red dashed boxes the additional population is highlighted that occurred after dialysis in water. On the right part the mean z-average and PDI values are displayed.

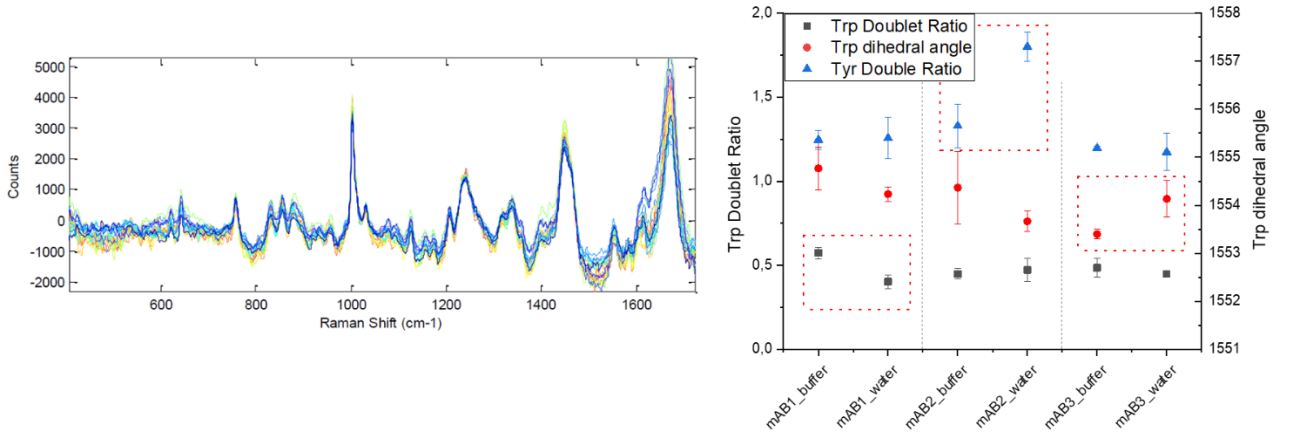

Figure 3- 24: Zetasizer Helix evaluation: Raman spectroscopy results sample series comparison mABs in water and model buffer.

Single sample measurements of mAB1, mAB2 and mAB3 after dialysis in water and phosphate model buffer 10 mM phosphate containing 10 mM NaCl pH 6.5 have been performed. The left part illustrates the resulting Raman spectra and the right part summarizes the three markers for tertiary structure considering tryptophan and tyrosine bands. The red dashed boxes highlight changes.

9.1.2. Isothermal kinetic studies

In the second mode, an isothermal incubation experiment of mAB1 and mAB2 was analyzed using the Zetasizer Helix system. The mAB samples were incubated over 2 hours at 75 °C. The resulting Raman spectra and DLS data are shown in Figure 3- 25, Figure 3- 26 and Figure 3- 27.

(1) For mAB1 changes in size occurred linearly over the time course. The z-average increased constantly from 17 nm up to about 100 nm. The PDI did not exceed 0.24 and indicated only low polydispersity. The changes happened quickly, and it was recommended repeating at lower temperature to slow the process and to collect more data points. The Raman spectra over the time course appeared stable across entire time course and no clear changes in secondary and tertiary structure were detected. Possible minor shifts occurred in tyrosine I850 / I830 ratio: A slight increase in the ratio I850/I830 from 1.25 to 1.55 suggested a tendency to increase the hydrophobicity.

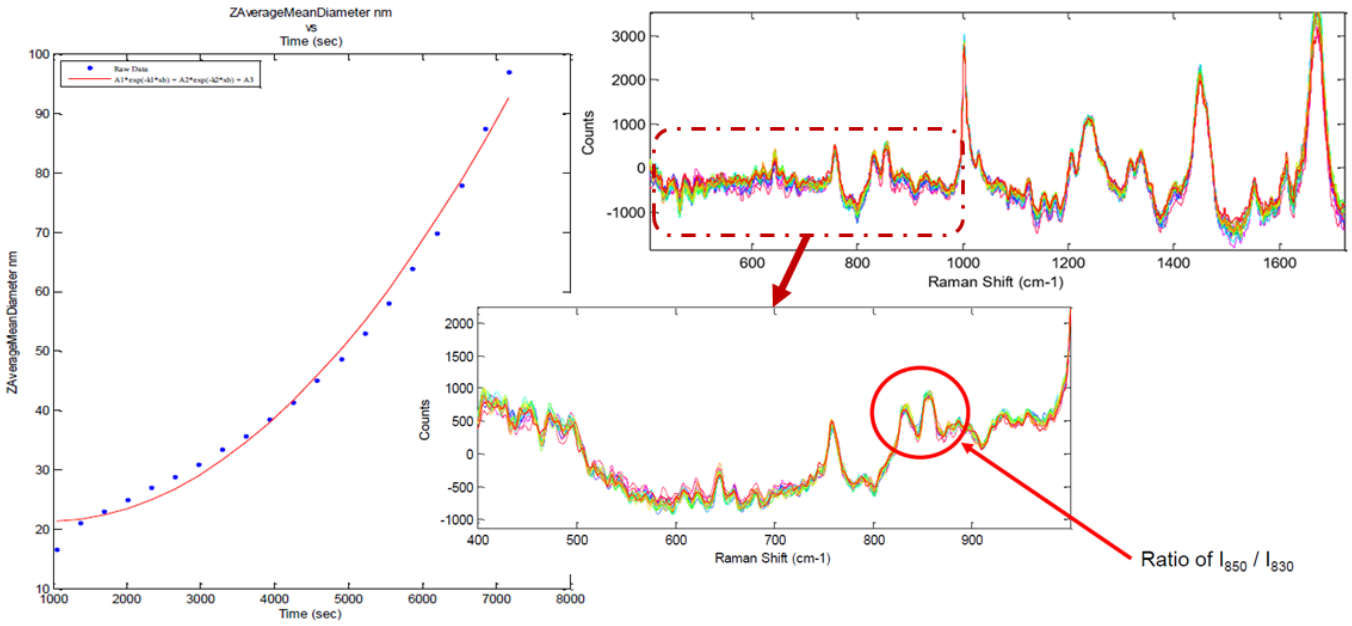

Figure 3- 25: Zetasizer Helix evaluation: Results isothermal incubation of mAB1 at 75 °C for 2 h.
A sample of mAB1 in phosphate model buffer 10 mM phosphate containing 10 mM NaCl pH 6.5 was incubated at 75 °C for 2 hours in the Helix instrument. Every 10 min DLS measurement and Raman spectrum were recorded. The resulting z-average values (*raw data: blue dots, fitting function: red line*) over time are shown in the left graph. All recorded Raman spectra are seen in an overlay in the upper right part of the figure. In the lower right part of the figure, the only section with minor changes (between 400 cm^{-1} and 1000 cm^{-1}) is highlighted. The depicted minor changes in the range of 830 cm^{-1} and 850 cm^{-1} are highlighted in the red circle.

In conclusion, mAB1 was very stable at the tested temperature. Aggregation was detectable, but without detectable changes in the secondary structure.

(2) Similar to mAB1, DLS data of the mAB2 approach changes in size over time. In an initial phase up to 50 min, the z-average increased constantly from 32 nm up to about 100 nm. Afterwards the correlation data and resulting PDI indicated a high polydispersity with further increased z-averages. After about 50 min the correlograms elapsed and DLS analysis was not reliable and applicable anymore. The data is shown in Figure 3- 26 and the red circles highlight the loss of quality data.

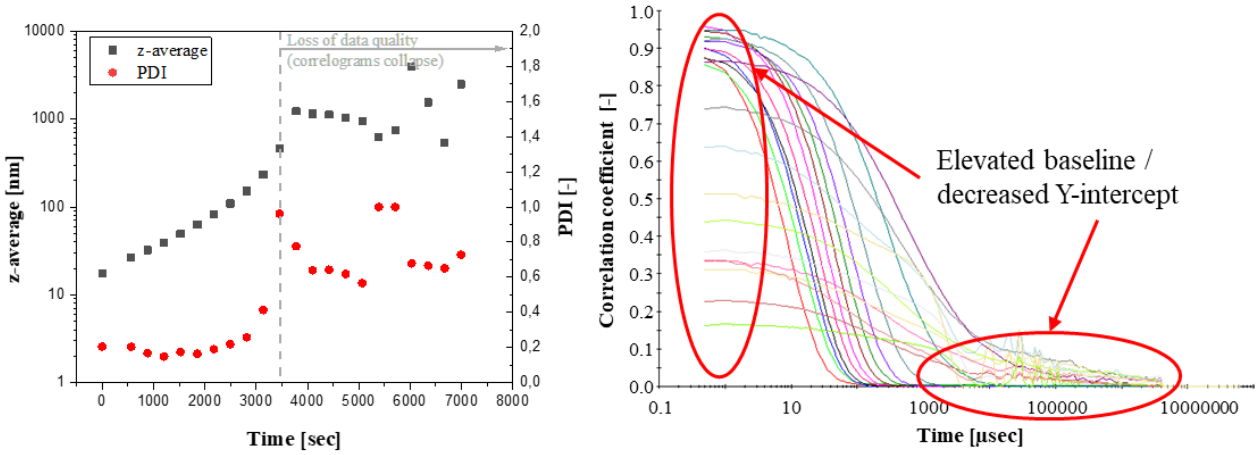

Figure 3- 26: Zetasizer Helix evaluation: DLS results isothermal incubation of mAB2 at 75°C for 2 h.
A sample of mAB2 in phosphate model buffer 10 mM phosphate containing 10 mM NaCl pH 6.5 was incubated at 75 °C for 2 hours in the Helix instrument. Every 10 min DLS measurements were recorded. The resulting z-averages and PDI values are summarized in the left graph. The dashed grey line indicates the point at which the autocorrelation collapsed. An overlay of the autocorrelation functions of all measurements is seen in the right part of the figure. After 9-10 measurements the autocorrelation data changed (red circles) as the baselines elevated and the Y-intercept decreased.

In contrast to mAB1, the evaluation of the Raman spectra showed significant changes in the secondary after about 2350 sec and subsequent in the tertiary structure after about 2760 sec (Figure 3- 27 and Figure 3- 58). Similar to the temperature ramp results, the portion of alpha helices increased from 10 % to 60 % and the portions of beta turns and beta sheets decreased down to 10 %. At the same time, the intensity of the disulfide band increased. The tertiary structure markers showed changes about 500 sec and 750 sec later. This shift suggested that changes in the protein structure may be directly correlated to tertiary structure changes in coincidence with possible aggregation.

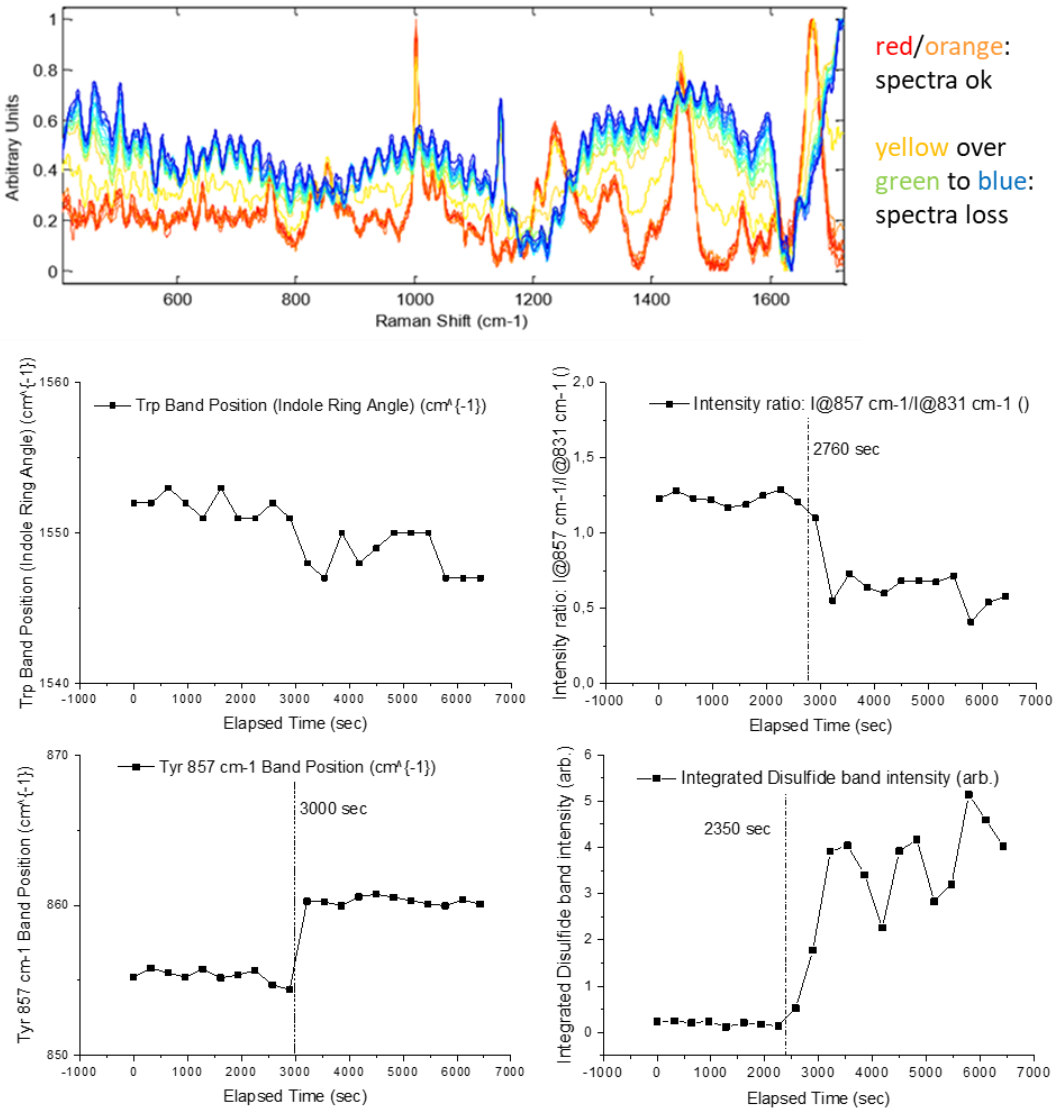

Figure 3- 27: Zetasizer Helix evaluation: Raman spectroscopy results isothermal incubation of mAB2 at 75°C for 2 h.
A sample of mAB2 in phosphate model buffer 10 mM phosphate containing 10 mM NaCl pH 6.5 was incubated at 75°C for 2 hours in the Helix instrument. Every 10 min Raman spectra were recorded. An overlay of the recorded Raman spectra is seen in the upper part of the figure. After the first 9 measurements the spectrum changed significantly suggesting complete structure loss of the protein. The resulting Raman spectra have been evaluated for secondary and tertiary structure markers. The four lower graphs illustrate tertiary structure markers as well as the disulfide band over the 2 h incubation evaluated.

The Raman spectra lost quality after about 50 minutes incubation, likely due to significant aggregation/ precipitation (Figure 3- 27). The first nine spectra (red/orange), however, were evaluable. A selection of marker changes is shown in the graphs. These changes appeared in the secondary and tertiary structure. In the secondary structure the fraction of random coiled portions

increased up to 40% and the more ordered structures of alpha helices (down to 3 %) and beta sheets (down to 43%) decreased. The tryptophan marker (ratio 1360 cm^{-1}/1340 cm^{-1}) decreased down to 0.25, the tryptophan marker (band position 1555 cm^{-1}), decreased down to 1549 cm^{-1} and the tyrosine marker (ratio 857 cm^{-1} /837 cm^{-1}) increased up to 1.9. All three changes may indicate unfolding. However, with only 9 data points it is difficult to draw any conclusions. At this point, it was recommend repeating the experiment at lower temperature to slow down the process and increase data points. Aggregation started to occur immediately at 75 °C and significant aggregation occurred within 50 minutes. In addition to this first evaluation presented in this chapter, results have been included in the in-depth investigation of the isothermal aggregation in chapter 10.2.3.

9.1.3. Thermal ramps

In the third mode, thermal ramp experiments using a temperature ramp from 20 °C to 85 °C with 1 K intervals were performed. Exemplary, the Zetasizer Helix data of the melting curve of mAB2 is shown in Figure 3- 28.

DLS measurements resulted in increasing trends for z-average and PDI starting 66 °C and consequently the aggregation onset Tagg was determined at 66 °C. This result is in good agreement with the detected melting point for tryptophan band position 1550 cm^{-1} and the first melting temperature determined by ITF (Table 11).

The full Raman spectra truncated at 77 °C indicating the loss of ordered structure at this temperature. Up to 76 °C, however, no clear changes in Amide 1 region were observed, indicating little change in secondary structure. Trending of selected Raman markers detected possible changes in the tertiary structure for tryptophan markers (amplitude 760 cm^{-1} and band position 1550 cm^{-1}) with a clear tendency and for tyrosine marker (ratio intensity at 850/830 cm^{-1}) with no clear tendency but indicating changes in the hydrogen binding environment of tyrosine. The tendencies detected for tryptophan markers have been analyzed and transition temperatures at 51 °C (onset at 40 °C) and 65 °C (onset at 50 °C) were calculated.

In addition to this first evaluation presented in this chapter, more detailed results have been included in the in-depth investigation of the thermal ramp aggregation studies in chapter 10.2.1 and 10.2.3.

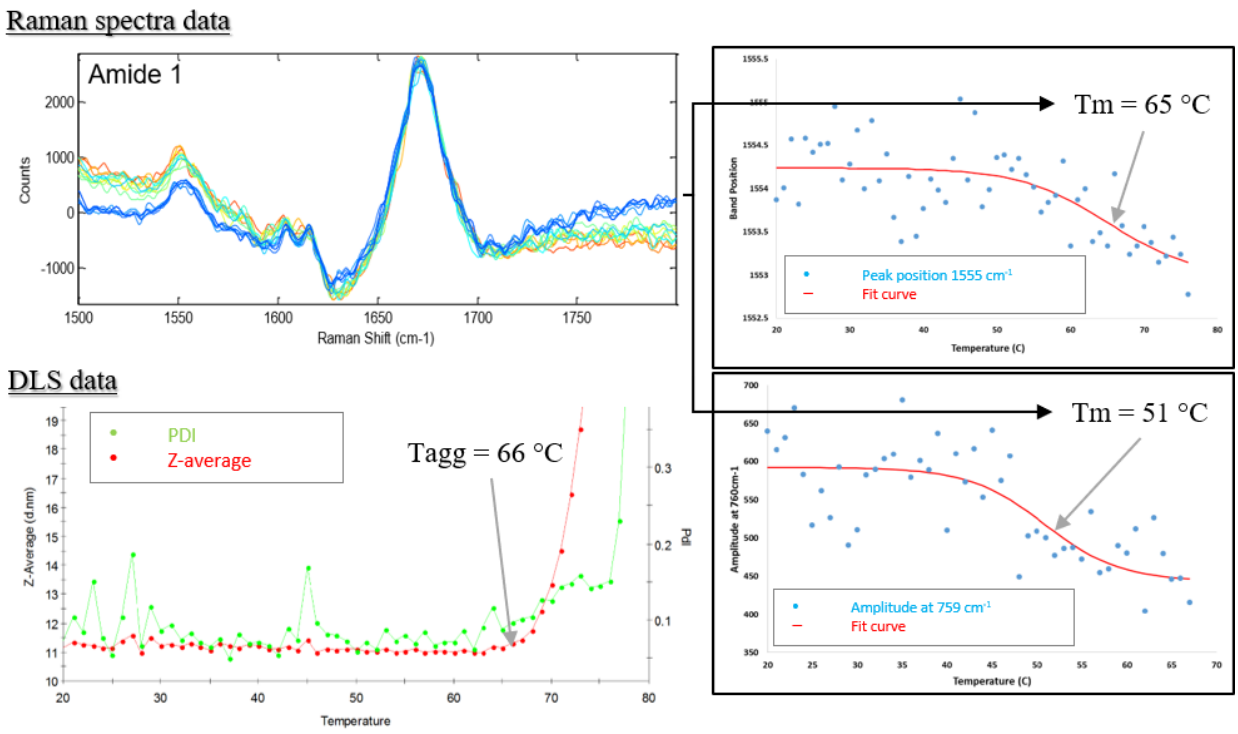

Figure 3- 28: Zetasizer Helix evaluation: Results thermal ramp experiment of mAB2 from 20 °C to 85 °C. A sample of mAB2 in phosphate model buffer 10 mM phosphate containing 10 mM NaCl pH 6.5 was heated up from 20 °C to 85 °C in the Helix instrument. At each temperature step DLS measurement was performed and a Raman spectrum was recorded. All recorded spectra focusing on the amide 1 band are seen in an overlay in the upper left part of the figure. Out of the whole set of spectra the two markers, the tryptophan band position and the amplitude of band 760 cm^{-1}, have been selected. The tendencies considering the two markers during the temperature ramp as well as the estimated melting temperatures are illustrated on the right. In the lower left part, the resulting DLS data (z-average und PDI) are shown indicating aggregation start between 65 °C and 70 °C.

9.1.4. Discussion Zetasizer Helix system for aggregation studies

Based on the results of Zetasizer Helix evaluation the following two aspects are discussed: (1) the potential and applicability for the investigation of protein stability and (2) the obtained results and the meaning for protein aggregation.

(1) The combination of the two established methods has generally a high potential. The Zetasizer Helix system represents an orthogonal method to the established combination of ITF/RALS for the determination of Tagg and structural melting temperatures (Tm) as shown exemplary for mAB2. The time-resolved capturing of size and structural information makes it a great technique for protein aggregation studies.

Advantages of the technique are that the two aspects of conformational and colloidal stability are considered in one measurement experiment (same sample, almost at the same time point). Furthermore, there is no specific/destructive sample preparation necessary. The instrument and the provided software are easy to handle with a short introduction and without in-depth knowledge. In comparison to ITF/RALS, the DLS/Raman combination provided more information: Raman spectra provided more structural markers enabling also secondary structure estimations and the DLS measurements enabled depicted size determinations and even size distributions calculations. As disadvantages, the technique is not suitable for high throughput or fast screening approaches as it aims more for better understanding protein processes and the molecule itself. Thus, the technique potentially enables the achievement of valuable data for the understanding on structural changes in correlation to aggregation processes. Further challenging, however, are the quality of the raw spectra (Raman) that might not be sufficient to identify minor changes. Furthermore, the drawbacks of DLS as ensemble method have to be considered as well. The software allows the operator a first fast evaluation without in-depth knowledge. This, however, can at the same point be misleading or confusing and mathematical calculations have to be checked and well understood. In addition, orthogonal method approaches are advised. A deeper evaluation of the raw data in more specified software might be necessary, especially for the Raman spectra. Both principles are complex and requirements like protein concentration, buffer composition or viscosity need to be taken in account. This was pointed out in some experiments as the spectra occurred highly noisy or DLS correlation function was hard to fit.

All approaches led to evaluable results. In some cases, however, higher protein concentrations may improve data quality for Raman spectra or higher number of data points and/or measurements has a supportive effect on fitting functions. The experimental set-up, e.g. for the performed temperature ramp, has to be improved and more data points should be captured for a more precise description. Especially at lower protein concentrations, at least triplicate measurements are advised. The triplicates were measured out of the same sample. At this point the markers discussed might show significant changes but to certainly draw the right conclusion it is advisable for all performed experiments to increase the number of replicates at least to 10.

(2) For the second aspect, the obtained results in the evaluation experiments are discussed. Based on literature for single native IgG molecules, a hydrodynamic diameter in the expected range of 10 nm was detected (Wang, 2007). Depending on their environment (surrounding ionic strength),

all mABs dialyzed against water showed lower z-average values compared to the mABs in buffer, which was expectable. The achieved secondary structural composition of mainly beta sheets (Raman measurements ~50 %) and only low fractions of alpha helices is also in agreement with literature data (Peters, 2016).

The DLS results of the ***dilution series (sample series)*** indicated decreasing z-averages with decreasing protein concentrations. Viscosity effects may be an explanation for this trend in the z-average results. Increasing viscosity may lead to lower diffusion velocity and leading to apparently higher z-average values. For that reason, especially for HCLFs, the viscosity has to be known for realistic interpretation of the results. The generally lower calculated hydrodynamic sizes in this samples series may be due to the chosen buffer system with low ionic strength. In addition to these considerations, charge or buffer effects may cause the exceptional trend for the 10 mg/ml sample as well as protein-protein repulsion at higher concentrations, e.g. the 100 mg/ ml or the 40 mg/ml samples that result in smaller apparent size. The DLS results of the ***dialysis experiment (sample series)*** followed the expectations. In contrast to the other two mABs, mAB1 did not show a high decrease in apparent size (from 11 nm to 9 nm) after the dialysis. One reason could be that the dialysis process was not sufficient and the amount of counterions is still higher as for the other mABs. As all dialysis processes have been performed in the same way a possible stronger "binding" of the counterions might be suggested. This is caused by the different charges of the mABs and the different counterions around the protein charges. The results for mAB2 and mAB3, in addition, indicated a higher instability as larger particles seemed to be present (based on intensity-based size distributions). The reduction of charges in the molecule surrounding led to colloidal instability.

The Raman spectroscopy results of the ***sample series*** followed the expectations and no great structural changes in the mAB structures were detected. The changed conditions aimed mainly colloidal stability (protein-protein interactions and protein-ion interactions). The secondary structure compositions of all three mABs under all tested conditions was similar and is comparable with literature values for IgGs (Peters, 20216). The small changes in the secondary structure markers in the dilution series might be – similar to DLS discussion – due to protein-protein interactions and the resulting viscosity effects. The protein-protein interaction, however, may indirectly lead to structural changes in the molecules. In contrast to DLS results, the results after dialysis suggested no secondary structure changes. In consequence, the larger size populations are either aggregation without structural changes or the populations are too small to be detected by

this ensemble method. The indicated changes in the tertiary structural markers (tryptophan and tyrosine makers) are supposed to mainly illustrate the changes due hydration changes (lower ionic strength).

The application of the Zetasizer Helix for ***isothermal incubation*** and ***temperature ramp*** experiments led to results allowing a detailed description of the aggregation processes. For that reason, the results were discussed in more detail in chapters 10.2.1 and 10.2.3.

The analysis of ***isothermal kinetics*** with an incubation at 75 °C for 2 h was performed for mAB1 and mAB2. The DLS results showed increasing particle sizes in both cases, which was expected due to thermal stress-induced aggregation processes. Both molecules started – based on DLS data – aggregation within the captured time frame. Only based on DLS data, the aggregation processes of mAB1 and mAB2 occurred similar, whereas mAB2 aggregation occurred faster than the process of mAB1. The addition of structural data monitored a potential difference in the mechanism: mAB1 showed no changes in the secondary structural markers during constant and continuous aggregation; mAB2 showed significant changes in the secondary structure markers. In this case, the option to analysis isothermal kinetic studies from the conformational as well as from the colloidal perspective was valuable. In all studies, additionally, the calculation of intensity-based size distributions was a valuable approach to further identify new populations and achieving a better understanding on aggregate formation. For that reason, the results were discussed in more detail in chapter 10.2.3.

Similar to the isothermal kinetics, the option of ***thermal ramps*** is a further option to link conformational and colloidal parameters for a more precise description of the aggregation mechanism. Based on the DLS data an aggregation start Tagg was detectable. In addition, the Raman spectra marker enabled - similar to ITF measurements – the determination of structural melting temperature, e.g. by using tryptophan markers. Considering the different makers – meaning different melting temperatures – a more detailed description of the melting and unfolding processes is possible. For that reason, the results were discussed in more detail in chapter 10.2.1.

Considering thermal ramps as an important tool to investigate protein stability (aggregation onset; melting temperature) a comparison to results of orthogonal methods are of interest. For the illustrated mAB2 example, the results were summarized at this point in Table 11: In comparison to RALS (266 nm) and SwitchSENSE®, the aggregation onset Tagg was determined in the same temperature range. The deviation might be due to higher protein concentration of 10 mg/ml for

Zetasizer Helix measurements compared to 5 mg/ml for RALS and SwitchSENSE® measurements. The backscattering approach in this case might show lower sensitivity resulting in a higher Tagg.

Table 11: Discussion thermal ramp results Zetasizer Helix: Comparison of orthogonal aggregation onsets (Taggs).

Zetasizer Helix DLS-based Tagg	Optim 100 RALS (266 nm)-based Tagg	SwitchSENSE® Switching speed based Tagg	Prometheus NT Backscattering-based Tagg
66.0°C	70.5°C	about 70°C	78.4°C

In consideration of unfolding describing parameters (unfolding onset and melting temperatures), a direct comparison of the calculate melting temperatures is hardly to achieve as this depends on the evaluated marker. The combination, however, of the structural marker tendencies with the unfolding parameters and thermograms of the orthogonal methods build up a better understanding of the unfolding mechanisms/process. In addition, it can be described how the process of unfolding and further aggregation might be correlated.

9.2. Evaluation of the SwitchSENSE® technology (Dynamic biosensors)

At the time the experimental work for this evaluation was performed, the SwitchSENSE® technology was primary used to investigate binding kinetics, receptor ligand affinities, enzymatic activities or hydrodynamic protein sizes and conformational changes. Within this application portfolio, it was decided to evaluate the system for therapeutic proteins and check its suitability for the investigation of aggregation processes and formulation development. All experiments were performed in the laboratories of Dynamic biosensors (Martinsried, Germany). As described in chapter "Methods" the proteins were first conjugated to a DNA strand. All investigated therapeutic proteins have been successfully conjugated to 24mer or 48mer DNA stands using lysine-coupling procedure. After the isolation of these conjugates and binding of the conjugate on the chip surface the applications of size analysis, protein-protein self-interaction and thermal melting investigations were tested.

9.2.1. Size analysis of monoclonal antibodies

The analysis of protein sizes was performed in the dynamic measurement mode and evaluated based on the model described in Langer et al. (Langer, Hampel et al. 2013). An example of such a size response curve is shown in Figure 3- 29. The "reference" curve represents the response without protein loading and the "signal" curve represents the response of the protein loaded to the chip. In both cases, the same buffer environment in the floe cell was chosen.

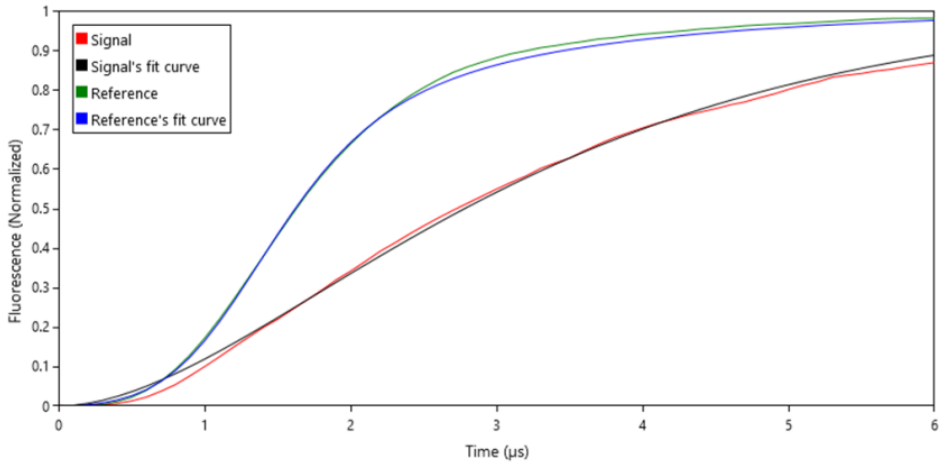

Figure 3- 29: SwitchSENSE® evaluation: Response curve (dynamic measurement mode) of conjugated monoclonal antibody molecule for size determination.
The graph illustrates the shift in the response curve of a DNA chip loaded with a mAB conjugate (red) and an unloaded chip (green). It represents the upward motion of the DNA nanolever as illustrated in Figure 1- 5 showing the normalized fluorescence signal of the fluorophore during the upward motion and defining the motion speed. The signal shift is subsequently used to calculate the hydrodynamic diameter of the molecule based on an existing database. For all tested mABs the maximal hydrodynamic diameter of 14 nm was achieved as all molecules appeared on the upper limit of the database. The fit was performed based on data in (Langer, Hampel et al. 2013).

As described in Langer et al. (Langer, Hampel et al. 2013), the evaluation model was developed based on proteins with diameters in the low nm range. The mAB molecules with a molecular weight of about 150 kDa and an expected hydrodynamic diameter of 10 nm to 13 nm appeared on the upper size limit of the system for absolute size calculations. For that reason, for the investigated mABs a reliable absolute size value calculation was hardly achievable. This limit was caused because these quantitative calculations were based on a database that was at that time not applicable for mAB molecules. Based on the available database, the average maximal diameter was calculated with 14.0 ± 0.2 nm. These calculated size values, however, will not be considered in further studies as for aggregation even higher diameters are expected. The measured signal, however, was sufficient to further investigate the molecules in a relative manner comparing the

signal shifts itself. Today, the development of the experimental setup and the extension of the database are still ongoing and may open the opportunity in future to evaluate the size determination application for mABs and small aggregates again.

9.2.2. Protein-protein self-interaction

One of the major applications of the system is the investigation of (strong) specific binding kinetics/processes exemplary shown in literature (Rant 2012, Lux, Langer et al. 2015). In aggregation processes, less strong protein-protein interactions may appear between the monomer molecules (self-interaction). As the identification of these interactions is a first possibility to predict a potential tendency for aggregation risks (instability) as set up of the system was selected to address this topic.

For that purpose, similar to the sizing experiments, size response curves in the dynamic measurement mode were performed and the dynamic response of the upward motion (dru) was determined (see Figure 3- 30). As described under 9.2.1 no size calculations are possible in that case. The determination, however, of the dru indicating the upward motion speed is a possible approach to investigate and evaluate these experiments in a comparative manner. The same mAB as under 9.2.1 was hybridized to the chip and in the first step the upward motion of the set up was monitored in the pure buffer (absence of free monomer molecules). The detected dru for the protein sample was about 117. The dru of the reference sample without protein was about 155. In further steps the dru was detected in presence of increasing monomer concentrations in the bulk suspension (Figure 3- 30). Between each monomer concentration experiment the chip was washed with buffer. Below the presence of 10 µM mAB in the surrounding the detected signal shift - comparing mAB-conjugate loaded chip and reference chip - was detectable and represented mainly the size difference as obtained in 9.2.1 indicating no influence of the monomers. A clear signal changes in the dru was detected starting in presence of 100 µM mAB in the surrounding (Δdru protein about 18). This decrease, however, was also seen in the in the reference sample (Δdru protein about 45). For that reason, the observed changes might be most likely due to unspecific binding of the monomers on the chip surface and/or increasing viscosity with increasing monomer concentration. As there might be various causes for the observed effect, no clear statement can be given about protein-protein interactions. Concluding, the SwitchSENSE® system in the set-up it

was tested in this study was not suitable for the application aiming the detection of protein-protein self-interactions. Due to the unspecific interactions no experimental setup could be defined to measure only the specific mAB-mAB interaction. Changing buffer components or pH value during measuring might be a possibility to overcome the challenges that appeared in our experiments.

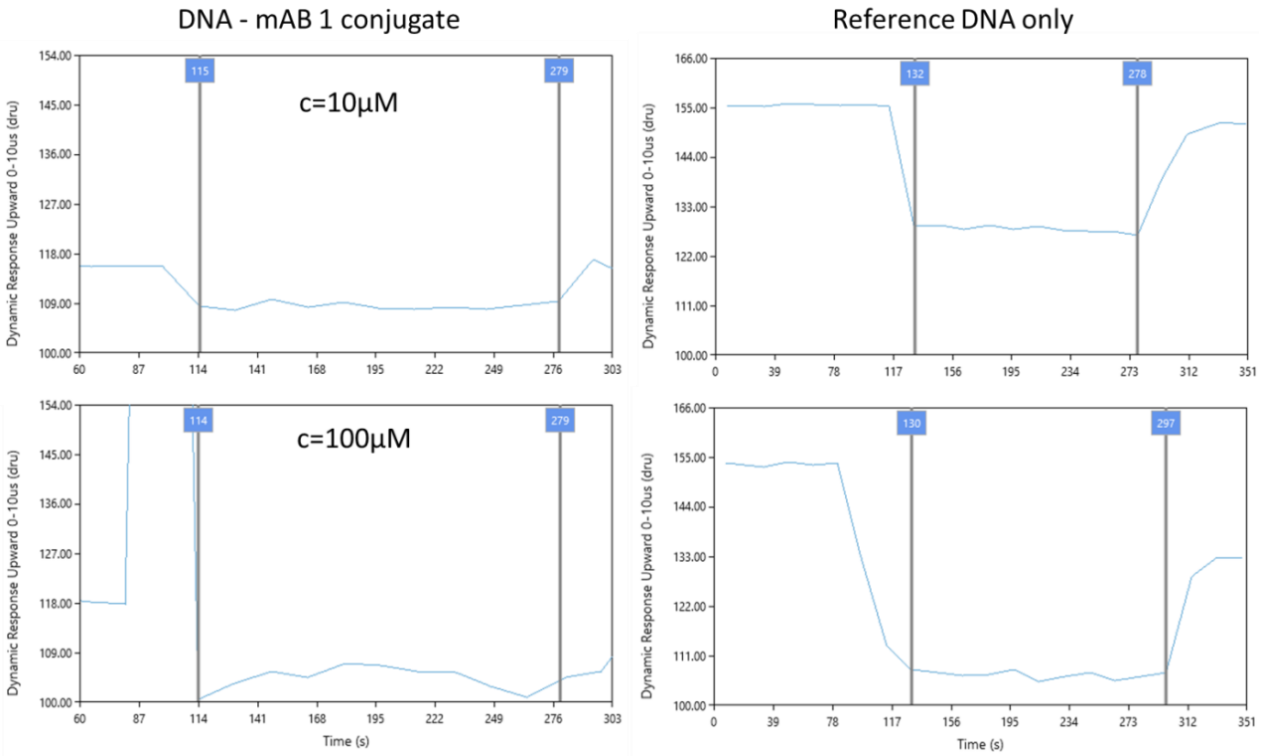

Figure 3- 30: SwitchSENSE® evaluation: Protein-protein interaction experiment.
The graphs illustrate the dynamic response upward (dru) of a chip with DNA-mAB1 conjugate (left) and a reference chip without mAB (right) in presence of 10 µM and 100 µM mAB1 in the bulk surrounding of the chip. In presence of 10 µM the signal shift between conjugate and reference is nicely detectable mainly caused by the conjugated mAB1. With increasing mAB1 concentration in the bulk the upward response decreases significantly in both samples (lower part). As there might be various causes for the effect no clear statement can be given about protein-protein interactions.

9.2.3. Thermal melting, refolding and aggregation experiments

The third application that was addressed to the SwitchSENSE® technology is the investigation of conformational changes during thermal melting processes of proteins.

In a first experiment series after hybridizing the mAB conjugate to the chip, the temperature on the chip was stepwise increased up to 70 °C and response curves have been measured (dynamic measurement mode) to determine the dru (red). For reference, the same experiment was performed with a chip without protein (green). Exemplary, the thermal melting of mAB1 is shown in Figure

3- 31 and Figure 3- 32. The resulting raw data describing the dru at each temperature are shown in Figure 3- 31A. After subtraction of the reference signal, the shape of the response curve gives information about the unfolding process (Figure 3- 31B). Two information were achieved: The first information is given by the behavior of the upward response switching speed. If the switching speed increases the protein may unfold, because the DNA nanolever drags along a smaller fraction of the (partly) unfolded peptide chain compared to a globular conformation. In the opposite case, if switching speed reduces, structural changes may happen that cause a larger resistance apparently a larger size of the protein. The second information is the calculation of the proteins melting temperature(s). For the first experiments, the instrument setup allowed only a heating up to 72 °C. The investigated monoclonal antibody mAB1 started thermal melting/unfolding at about 60 °C. With this set-up, the melting temperature could only be estimated by extrapolation as the upper temperature limit of the technique was too low to melt the protein completely. The resulting melting temperature was calculated with 75.9 ± 14.9 °C.

An instrumental set-up improvement resulted in the "One DRX2400" that was optimized for higher temperatures up to 85 °C. The resulting melting curve of mAB1 for the new set-up is shown in Figure 3- 32. The melting temperature Tm of mAB1 was consequently detected with 75 °C by an experimental measurement time of about 90 min.

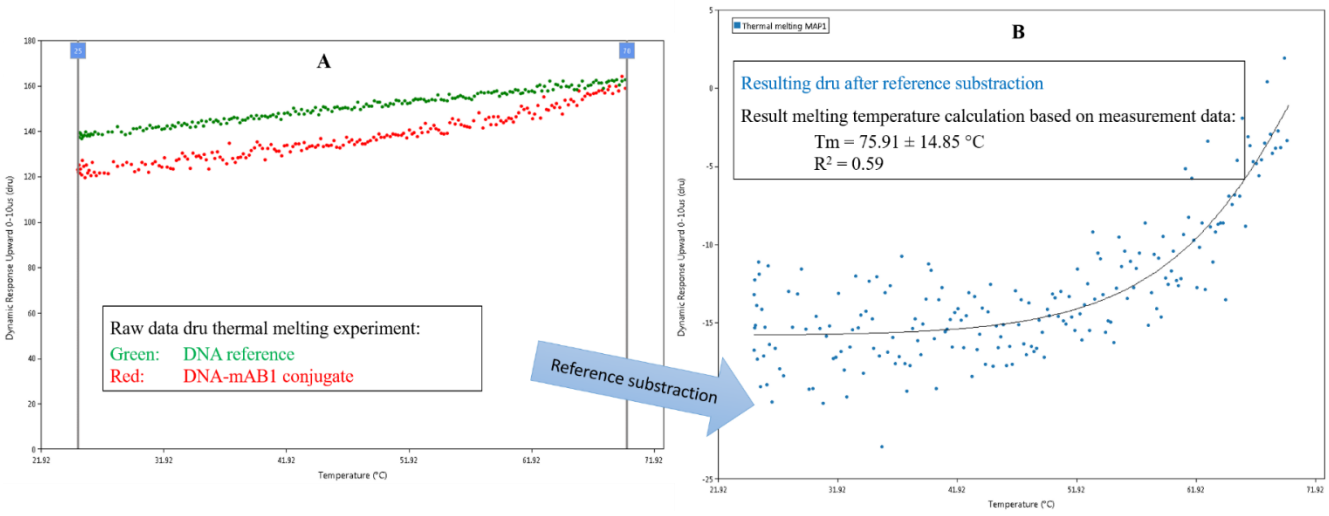

Figure 3- 31: SwitchSENSE® evaluation: Thermal melting experiment of mAB1.
The melting process analysis by SwitchSENSE® is illustrated. A: displays the obtained raw data of the mAB1 sample (red) and the reference (green). After substraction of the reference curve the meltung curve B was achieved for the melting up to 72 °C.

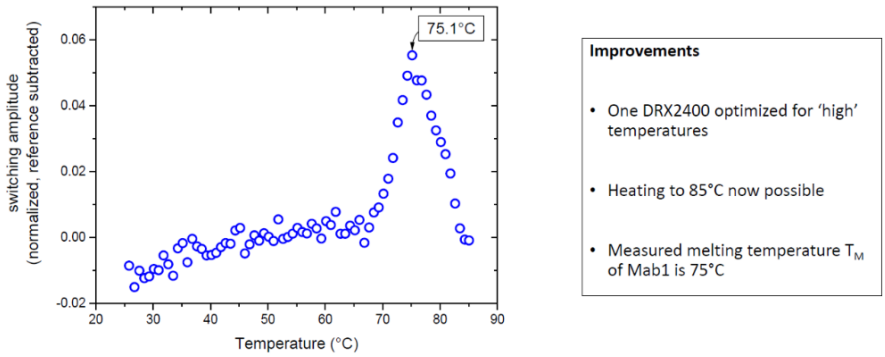

Figure 3- 32: SwitchSENSE® evaluation: Improved thermal melting experiment of mAB1.
The graph shows the melting curve of mAB1 monitored after instrument improvement 2014 enabling the melting process analysis up to 85 °C.

In a second experiment series, a more detailed description of the complete thermal melting process was obtained by the combination of the thermal melting step (as described above) and a previous initial and a final sizing step (dynamic measurement mode to determine dru). In addition, the investigation of reversible refolding was possible. Exemplary, such a thermal melting study was performed for mAB5 to show the potential of this approach (Figure 3- 33). The resulting melting curves (duplicate) and the respective Boltzmann fit are shown in Figure 3- 33A. Both measurements resulted in similar melting temperatures Tm of 74.6 ±0.2 °C and 73.5 ±0.2 °C. Unfolding started at 65 °C. The sizes before the melting (red) and after the melting (green) are shown in Figure 3- 33B and a clear shift of the response curves after the melting towards the reference curve was observed. This observation indicated that the heating step up to 78 °C caused an irreversible and almost complete unfolding of mAB5. After heating up to 78 °C no refolding could be assumed. The investigation of the reversibility of the unfolding process was further performed by stepwise heating and cooling cycles with increasing end temperature (Figure 3- 33C,D): (1) melting up to 62 °C , (2) melting up to 70 °C, (3) melting up to 74 °C and (4) melting up to 78 °C. After each cool down the sizing step was performed at 25 °C. Based on the SwitchSENSE® results, complete refolding is seen after 62 °C. After 70 °C only partial refolding can be assumed. No refolding happened after melting by 74 °C and higher.

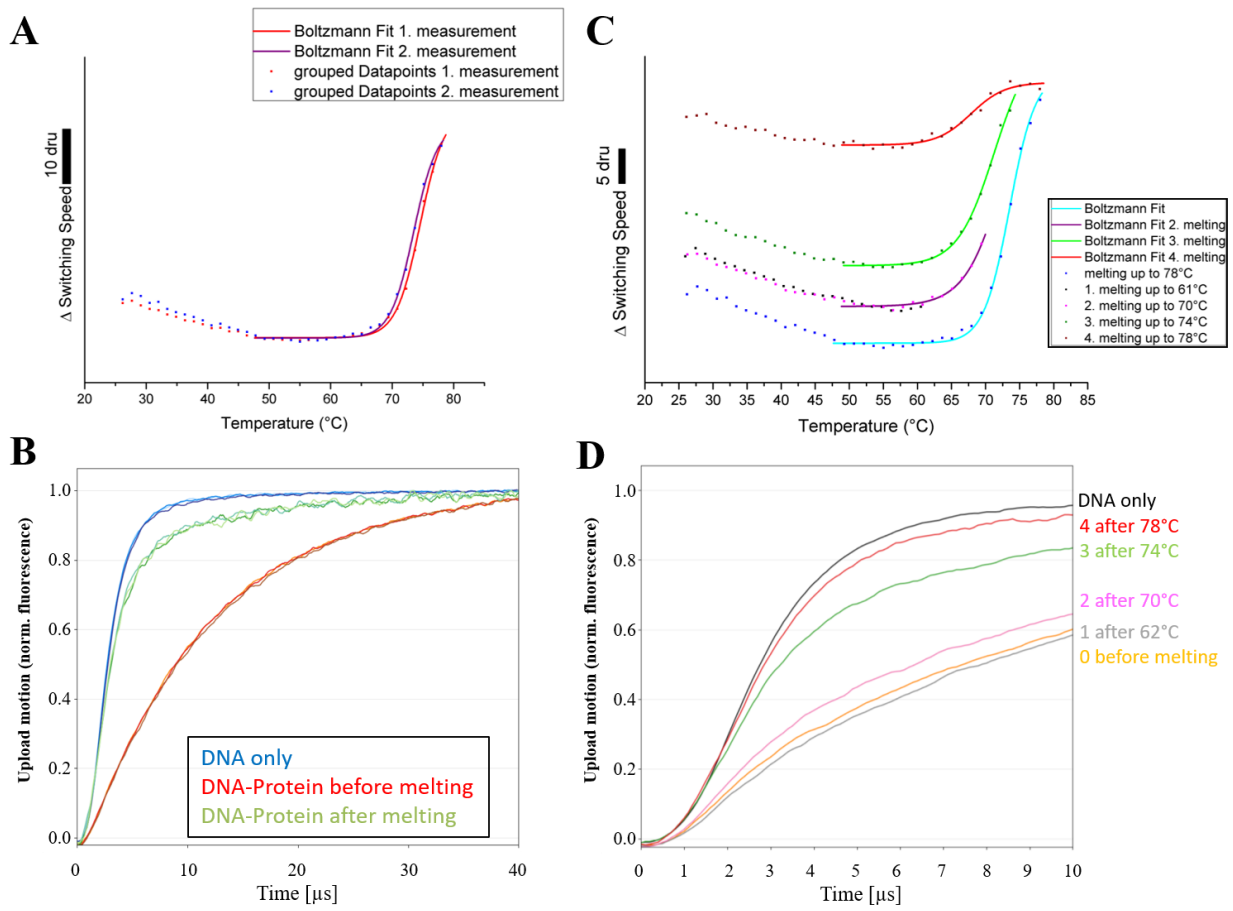

Figure 3- 33: SwitchSENSE® evaluation: Thermal melting study of mAB5.
The studying of unfolding process of mAB5 was performed in two experiments. In the first experiment, mAB5 was heated up to 78 °C in a one-step procedure (A). Before and after the melting step a sizing analysis was performed (B). In the second experiment mAB5 was stepwise heated up to 78°C and performing heating-cooling cycles (C). Before and after each cycle sizing analysis was performed (D).

The described unfolding experiments were performed in model buffer without soluble monomers in the bulk surrounding aiming only the unfolding signal of the coupled mABs. In a third experimental series to further investigate the aggregation behavior, a set up was chosen with soluble monomers of mAB1 in the bulk surrounding. In result, there was a loss of the switch signal detected starting at 70 °C. The conjugated mABs as well as the mABs in the bulk started to aggregate at this temperature and formed a layer over the chip surface inhibiting the motion of the "lollipops" and any further measurement. This point, indeed, can be declared the aggregation onset, estimated at 70 °C. The application of the system to detect the aggregation onset is possible. The chip, however, lost completely its functionality as the aggregated protein layer can hardly be removed after such an experiment and the chip cannot be reused.

9.2.4. Comparative study thermal unfolding of biopharmaceuticals with orthogonal methods DSC and ITF

Concluding the previous three topics addressed to the SwitchSENSE® technology, thermal melting studies were the most potential application. Such studies are highly important to assess the (conformational) stability of therapeutic proteins in early development (e.g. formulation development). Common and established techniques to investigate the conformational stability are differential scanning calorimetry (DSC) and intrinsic tryptophan fluorescence (ITF) assays. To better show the potential and benefits of the SwitchSENSE® technology as an orthogonal technique to investigate conformational stability, a comparative study was performed.

For the comparison, five therapeutic monoclonal antibodies (mAB1- mAB6) and four emerging therapeutic protein formats (AF1 – AF4) have been selected. The unfolding behavior of the proteins have been analyzed from 25 °C to 90 °C, respectively to 78 °C for SwitchSENSE® measurements. The heating rate for all instruments and experiments was set to 1 K/min. The resulting thermograms are illustrated in Figure 3- 34 and Figure 3- 35 and characteristic unfolding onsets and melting temperatures are summarized in Table 12.

The characteristic parameters Tonset and Tm were determined with all methods and for all molecules.

The unfolding processes of the mAB molecules started between 50 °C and 65 °C. All Tonsets were detected within the reliable range of the SwitchSENSE®. For four out of the five tested mABs (mAB1, mAB2, mAB6 and mAB4) changes in the structure/unfolding was first detected in SwitchSENSE® thermograms followed by DSC thermograms and least in ITF thermograms:

Tonset (SwitchSENSE®) < Tonset (DSC) < Tonset (ITF)

For the artificial mAB5, however, unfolding was first detected in DSC thermograms followed by SwitchSENSE® thermograms and least in ITF thermograms:

Tonset (DSC) < Tonset (SwitchSENSE®) < Tonset (ITF)

The unfolding processes of the AF molecules started between 41 °C and 66 °C. In contrast to the mABs, no general trend in the sensitivity of the three methods was determined. For the smaller molecules of AF1 and AF2 (nanobody and antibody fragment), however, changes in the structure/unfolding was first detected in DSC thermograms followed by SwitchSENSE® thermograms and least in ITF thermograms:

Tonset (DSC) < Tonset (SwitchSENSE®) < Tonset (ITF)

For the larger molecules of AF3 and AF4 (bispecific mABs of 200 kDa), however, changes in the structure/unfolding was first detected in SwitchSENSE® thermograms followed by DSC thermograms and least in ITF thermograms:

Tonset (SwitchSENSE®) < Tonset (DSC) < Tonset (ITF)

Table 12: Comparison of unfolding onset (Tonset) and melting temperatures (Tm) detected by DSC, ITF and SwitchSENSE®.

	DSC		ITF (Prometheus)		SwitchSENSE®	
	Tonset	Tm	Tonset	Tm	Tonset	Tm
mAB 1	*61*	*72.2* *85.3*	*63*	71.9 80.9	52	75.6 ±1.7
mAB 2	*61*	70.0 *82.4*	65	*69.1* *81.1*	60	72.7 ±1.2
mAB 6	58	67.2 71.4 78.6	59	66.3 76.2	55	64.9 ±0.4
mAB 4	58	69.4 73.9 82.7	63	66.5 80.9	52	63.6 ±0.4
mAB 5	50	60.1 69.0 72.5 82.4	60	58.6 67.0 80.8	65	74.1 ±0.1
AF 1	41	56.7 82.6	48	54.7 80.8	45	60.5 ±1.1
AF 2	60	71.5 76.2	66	69.5 76.0	62	69.5 ±0.4
AF 3	51	68.9 82.8	57	62.7 80.6	50	64.7 ±1.0
AF 4	53	58.9 67.2	53	57.3	50	58.9 ±2.8

In the selected molecules up to four melting temperatures per molecule were detected. The most melting temperatures were detectable based on the DSC thermograms. For evaluation of SwitchSENSE® thermograms only one melting temperature was determinable. In some cases (e.g. mAB1, AF1 and AF2) the SwitchSENSE® thermograms suggested a second melting point but the mathematic model in the software could not resolve more than one melting point. Reasons might be that the density of the data points was too low, or a better fit was not possible as full unfolding was not reached due to low-end temperature. The determined Tm for the two therapeutic IgG1 mABs (mAB1 and mAB2) was between the two Tms detected by DSC and ITF. For mAB6

(IgG4) and mAB4 the detected Tm was below the Tms detected by DSC and ITF and for mAB5 the Tm was between the two highest Tms detected by DSC and ITF. The detected Tms for the AF molecules were all either between the lowest Tms detected by ITF and DSC or at the similar temperature as Tm1. In particular, for the Tm determinations, the approach with orthogonal principles led to higher variation in the results as different signals were evaluated. Based on the similar Tm values and Tonset values, however, SwitchSENSE® can be evaluated as a suitable orthogonal method for the investigation and description of the unfolding behavior.

In addition to the characteristic calculated parameters Tonset and Tm, the SwitchSENSE® thermograms shown in Figure 3- 34 and Figure 3- 35 give additional information:

(1) One additional aspect is the description of the first part of the thermogram prior unfolding starts. Exemplary, mAB2 and AF2 show initially a decrease of the switching speed indicating a first structural change in the protein leading to an apparently larger size. This phenomenon was not observable for all proteins.

(2) A second aspect is the tendency of the switching speed after unfolding started. In most molecules (mAB1-mAB6, AF1-AF2) the switching speed decreases as unfolding to less globular structure decreases the apparent size. In contrast, AF3 and AF4 showed the opposite behavior, an expansion behavior during thermal melting.

(3) A third remarkable observation of the study was that a complete refolding was seen for mAB1 and AF2 after heating it up to 78°C and a partially refolding of mAB2 is possible. A fourth observation is that at least for AF1 and AF2 two unfolding phases were recognizable also for SwitchSENSE® results, but clear differentiation between various unfolding processes as seen in DSC or ITF thermograms is not possible in all cases.

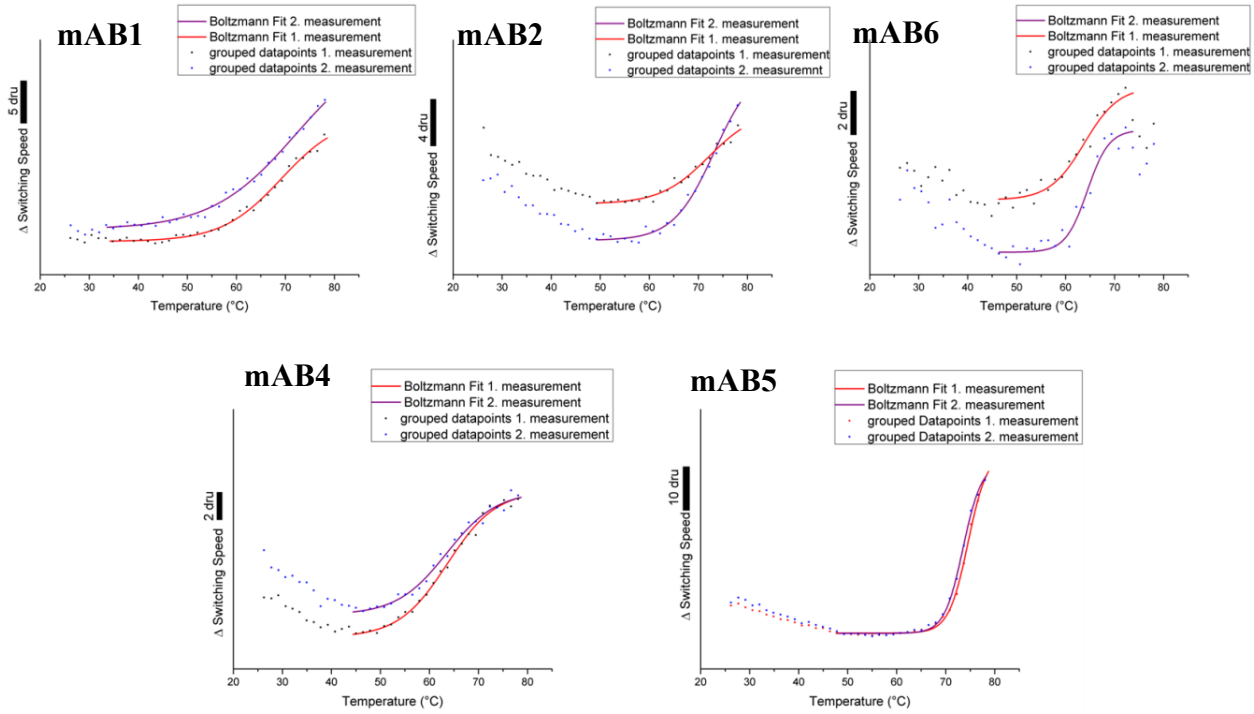

Figure 3- 34: SwitchSENSE® evaluation: Thermograms of the five therapeutic mABs.
The thermograms show the melting profiles of each mAB. For SwitchSENSE® the thermogram is the change in the switching speed of the nanolever over the temperature. The black bar at the y axis is a scale for the quantification of dru.

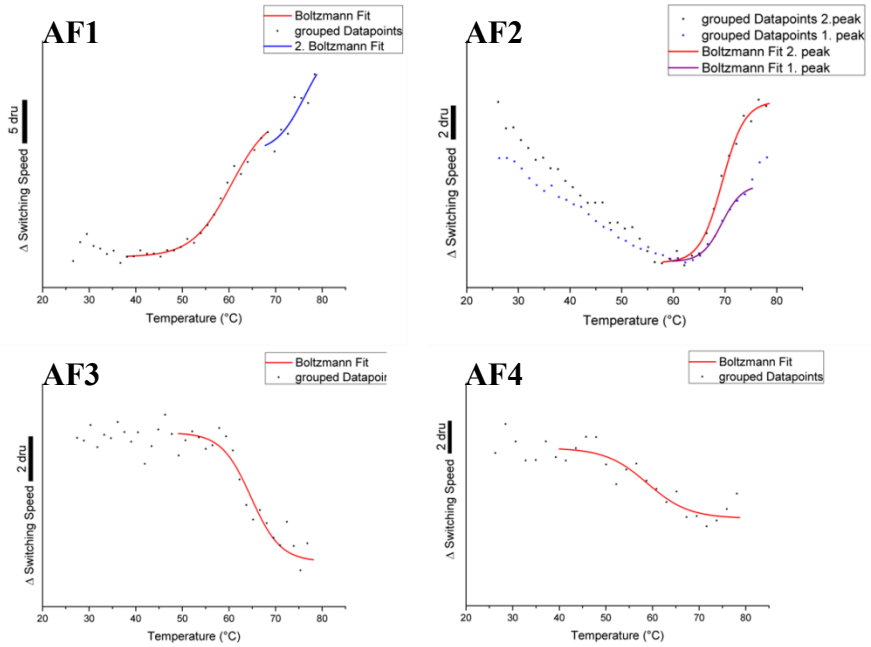

Figure 3- 35: SwitchSENSE® evaluation: Thermograms AFs.
The thermograms show the melting profiles of each mAB. For SwitchSENSE® the thermogram is the change in the switching speed of the nanolever over the temperature. The black bar at the y axis is a scale for the quantification of dru.

9.2.5. Discussion SwitchSENSE® system for protein aggregation studies

The SwitchSENSE® system offers several applications that are interesting for protein instability studies as evaluated in the previous chapters.

For the ***determination of molecular sizes***, represented as hydrodynamic diameter, the SwitchSENSE® system is a potential orthogonal method, e.g. to DLS, by applying a principle independently of light scattering. The system realizes the determination by detecting the dynamic response speed and calculating the hydrodynamic diameter based on a database of measured molecules. At the time the experiments were performed, size determinations even for mAB monomers were not reliable as the database was not configured for molecules larger than 10 nm. Due to ongoing development, the database was extended and updated enabling now the exact calculation of IgG monomers (150 kDa; about 11 nm) (see https://www.dynamic-biosensors.com/project/list-of-protein-hydrodynamic-diameters/).

Single size measurements are possible, but not the main application of the system. A single measurement showed several disadvantages compared to DLS, e.g. destructive, time- and cost-intensive due to the coupling procedure. Based on the achieved results, the higher effort is only a suitable approach for several studies on the monomers. For aggregation studies, however, the size determination application, even of low molecular aggregates of mABs will be also in the future hardly achievable. The largest challenge is the generation of stable DNA linkage molecules resulting in a stable "Lollipop" and consequently a stable dynamic response signal. The changes in the switching speed as raw data signal, however, are a great outcome and further used, e.g. in melting studies. For that reason, the size determination is only applicable in a relative manner for changes of the monomer molecules as it was applied in this study to achieve unfolding information.

The application to ***investigate specific (protein-protein) interactions***, indeed, is a well-established application aiming different types of proteins and other molecules. The investigation of specific interactions by the SwitchSENSE® system has been published in various studies over the last years. The experiments performed within this study aiming mAB-mAB interactions were not successful and at this point no further development was performed. For a better evaluation of the mAB-mAB interaction application a method development has to be performed using a molecule that was shown to tend to self-association. One model system for mAB-mAB interaction studies was described by Westermeier et al. using Avastin (Westermaier, Veurink et al. 2013).

Within the focus of this dissertation on ***molecule unfolding and aggregation investigations***, the monitoring of the switching speed over a temperature ramp was the most promising approach. Thermal melting experiments are a versatile tool to investigate protein stability, e.g. by ITF or DSC. Prior the SwitchSENSE® experiments in this study, the unfolding application was not implemented for the system and the maximum heating temperature limit was 72 °C. As most of the investigated therapeutic molecules have higher melting temperatures between 60 °C and 85 °C, the need for a more stable "lollipop-system" appeared. The experiments of this study have been performed with the low heating system.

In result, the thermogram and the characteristic temperatures Tm and Tonset were evaluated. The Tonsets are most reliable value as in the range of the system. The detection of melting temperatures was not as reliable as the Tonsets for three reasons: (1) the expected melting temperatures are above the range of the SwitchSENSE® system, (2) low density of data points and (3) fitting functions for the calculation of Tm s are hard adjust, if the unfolding process is not complete. The applied Boltzmann fit considers only one melting point. In some cases, e.g. AF1, the SwitchSENSE® thermogram showed already a second transition, but the evaluation software is not able to fit also a second melting point. In consequence, the calculated Tms represent either a mean value as single Tms are not assessable or the detected Tm is only the low Tm and the further Tms were not detected.

The most valuable information – besides the characteristic temperature points- that can be achieved of all three methods are the thermograms. This is exemplary discussed for mAB5. DSC resulted in a low unfolding start temperature at 50 °C. At the same temperature the SwitchSENSE® signal stopped decreasing and continues as a plateau. At 60 °C DSC indicates the first melting temperature, representing the unfolding start of ITF and a slight increase of the SwitchSENSE® signal. Sudden unfolding transition starts at the SwitchSENSE® signal from 65 °C to 70 °C. This represents the second melting point of DSC, respectively the first of ITF. The melting point detected by SwitchSENSE® is in the same range as the third melting point of DSC. Such a comparison of the obtained unfolding and melting points is a useful approach to interpret the unfolding data from different perspectives and bring them together to understand the whole process and illustrates again the need for orthogonal methods.

The refolding set-up is one promising approach to understand the reversibility of the unfolding process and consequently identify the potential state when aggregation may be the dominant process as irreversible aggregation-driving monomer states may be present.

The ***comparative study*** highlighted the potential applying orthogonal methods. Comparing the obtained single melting points to DSC and ITF data there is a high agreement for the unfolding start as well as for the (first) melting temperature.

For the majority of the investigated molecules (6 out of 9) the SwitchSENSE® system was able to detect changes caused by the temperature increase first. For the mABs, except for mAB5, and the larger larger antibody formats (namely AF3 and AF4), SwitchSENSE® detected the first changes in the molecule with increasing temperature. The high sensitivity of the applied principle was already demonstrated in enzymatic assays. The switching speed indicated already tiny conformational changes. The DSC results based on energy changes, are known to be highly sensitive. The changes in structure, however, first structural changes not significant changes in the energy state. The ITF results rely on changes in the environment of the Tryptophan side chains meaning by unfolding the hydrophobic surrounding in the folded structure changes to hydrophilic surrounding in the unfolded state. These changes happened last, resulting in higher Tonsets detected by ITF.

One exception of this tendency is mAB5, an artificial mAB with a highly hydrophobic surface area. In this case, first changes detected are energy changes by DSC followed by changes in the tryptophan environment and last SwitchSENSE®. A hypothesis for this behavior is that the dominating hydrophobic batches on the surface tend to move into the molecule excluding water molecules driven by hydrophobic interactions. Such changes have a high energy impact and are first illustrated as well by ITF. Within this folding processes, structural changes influencing the switching speed are not the case. With higher temperatures, the unfolding process loses the “new” structure und finally has an impact on the switching speed. This hypothesis may be supported by the SwitchSENSE® thermogram of mAB5 in which an initial decrease in switching speed may indicated the first restructure.

The other two exceptions, namely AF1 and AF2, are smaller molecules. In contrast, to the stable, energetic favorable and conserved native structure of mABs, the structure changes of these molecules cause larger energy changes that are first detected by DSC.

The study illustrated that differences between the results of the three orthogonal methods can be explained by the differences in the measurement principles. Further reasons are that DSC and ITF measure the monomers in their surrounding bulk in presence of other monomers. These possible interactions of different monomers are not considered in the SwitchSENSE® system and may have an influence on the unfolding behavior. In addition, monomer and the monomer-DNA conjugate properties may differ. The results, however, were in good agreement with the results of orthogonal systems.

Besides the unfolding studies, further protein stability studies considering protein aggregation are practically possible, as described under 9.2.3, and the Tagg can be determined. The result is a sharp temperature point similar to the onsets determined with orthogonal methods. Compared to orthogonal methods used for the aggregation onset determination, e.g. by light scattering (RALS), the SwitchSENSE® approach is significantly more time- and cost-intensive. Considering the time to set up the specific chip and link the protein to the DNA makes the set up less efficient, especially as the chip cannot be recycled afterwards.

Summarizing the latest publications of SwitchSENSE® systems, the development for applications considering protein stability is not in the focus and most developments consider mRNA –protein interactions (https://www.dynamic-biosensors.com/literature/). Compared to orthogonal methods aiming the investigation of protein size and stability for one sample, the workload for preparation of the chip and the protein-DNA conjugates is much higher. The advantage of the system, however, is that if the chip and the conjugates are prepared the number of various experiments and applications, similar to an investigation platform, is much higher. One highly potential example is the investigation of different buffer systems (variations in pH values, buffer components or excipients) in a fast and high throughput manner. In addition, the development of software and instruments is still ongoing and new applications may be possible in the future.

10. Protein aggregation processes: A case study of three therapeutic monoclonal antibodies

The aggregation of proteins, as highly complex and multi-variant process, is depending on the investigated protein. In this case study, three therapeutic monoclonal IgG1 antibodies (mABs) of medical interest have been selected to investigate their aggregation behavior.

For a comparative study of the aggregation processes, the mABs were investigated in a standardized and defined phosphate buffer system in which all three molecules behaved less stable (compared to the storage buffer). In the following, this system (mAB in the phosphate buffer) is called the "model system". Initially the three model systems have been biophysically characterized focusing on system stability and particle content (***chapter 10.1***). The subsequent chapters focus exemplary on the aggregation processes in the model systems and summarize the results of forced aggregation studies by the application of temperature stress or by the addition of previously stressed protein (***chapter 10.2***). In addition to established methods and technologies, the evaluated emerging and novel techniques from the previous chapters as well as more explorative approaches with established methods were applied.

10.1. Biophysical characterization of mAB1, mAB2 and mAB3

After the mABs have been transferred into the model buffer (containing 10 mM sodium phosphate and 10 mM sodium chloride, pH 6.5), these model systems were characterized considering their colloidal stability and conformational/structural stability, the aggregate and particle content as well as their long-term storage stability (6 months).

10.1.1. Colloidal stability characterization of the model systems

The characterization of colloidal stability was realized by the determination of the interaction parameters A2, B22 and kD value as well as the apparent zetapotential.

The results for A2 and B22 values, describing mainly the protein-protein interactions in two orthogonal approaches, indicated similar stability rankings, trends and tendencies. Relatively, higher B22 and A2 values assume more stabilized systems and lower values assume tendencies in the system for self-association. For the three defined model systems at pH 6.5, mAB1 is the most

colloidal stable system (B22 ~ +1.0 and A2 ~ +0.5) and mAB3 is the least colloidal stable system (B22 ~ -9 and A2 ~ -0.2) (Figure 3- 36).

The resulting kD values, considering the overall suspension stability including ion influence, were not in full agreement with the B22 and A2 tendencies. All kD values were negative values. The model system mAB2 is stated as most stable suspension (kD ~ -6) and mAB1 (kD ~ -9.5) and mAB3 (kD ~ -10.5) as similar unstable suspensions (Figure 3- 36).

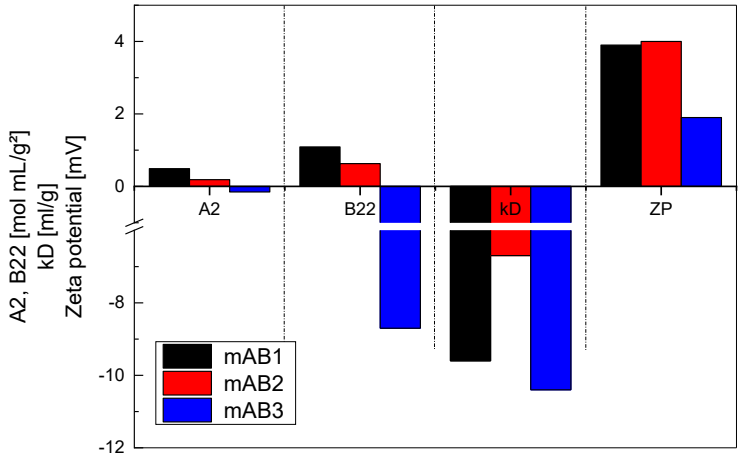

Figure 3- 36: Colloidal stability model mAB systems: B22, A2, kD and the apparent ZP.
The monoclonal antibodies mAB1, mAB2 and mAB3 have been investigated concerning their colloidal stability in the model buffer (10 mM sodium phosphate and 10 mM sodium chloride, pH 6.5). The illustration summarizes the results in a comparative manner of the interaction parameters B22 (determined by SIC), A2 (determined by MALS) and kD (determined by DLS). In addition, the apparent zetapotential (ZP) was determined, supporting charge-based interaction statements.

Furthermore, the apparent zetapotential of the model systems was determined (Figure 3- 36). All mABs showed a positive zetapotential. A similar apparent zetapotential of +4 mV was detected for mAB1 and mAB2. A lower zetapotential of +2 mV was detected for mAB3. Based on pH series of zetapotential measurements, the apparent isoelectric point (pI) was determined for mAB1 at pH 7.6, for mAB2 at pH 8.0 and for mAB3 at 7.0 (Figure 3- 37).

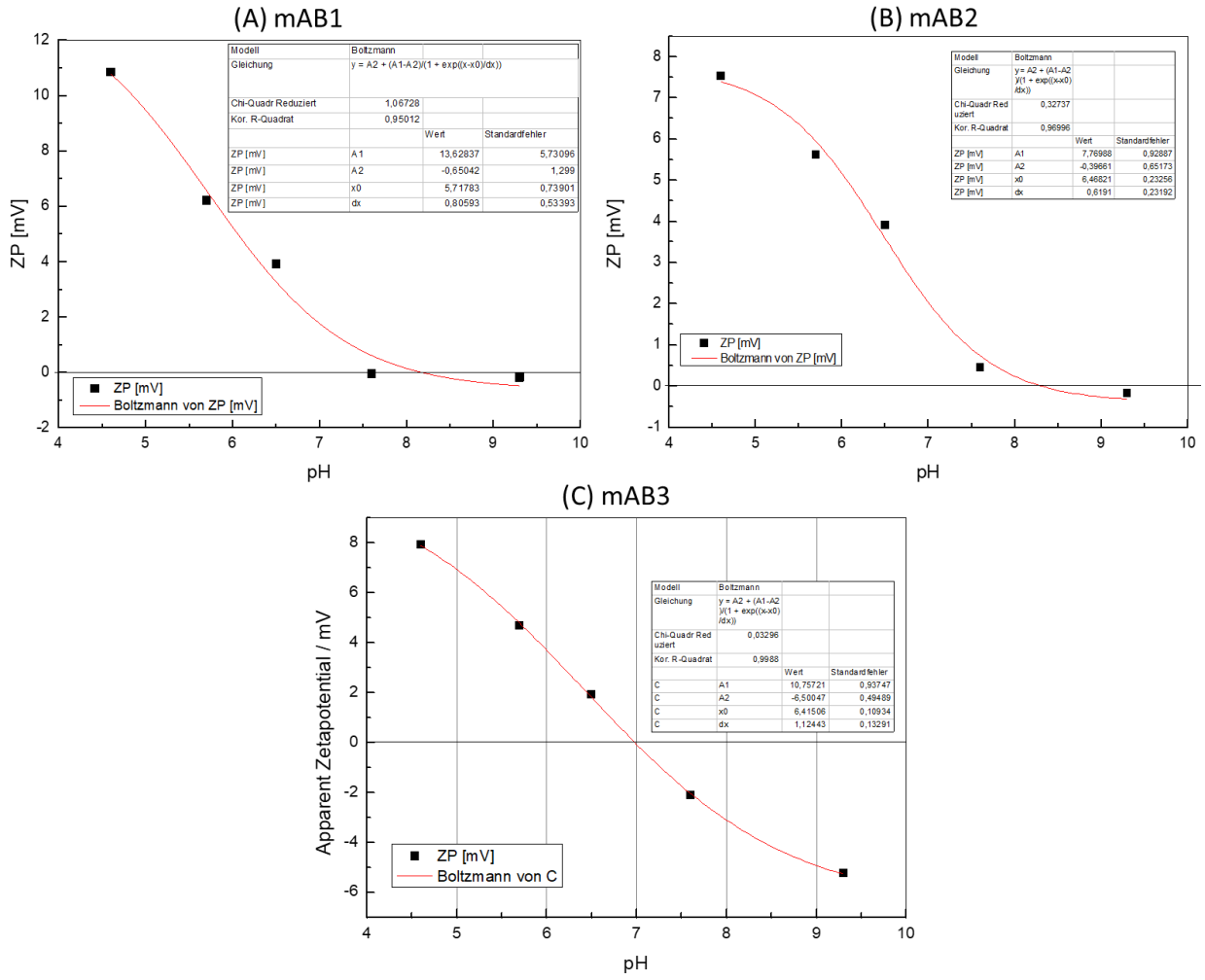

Figure 3- 37: Colloidal stability model mAB systems: Determination of the apparent pI (based on ZP).
All three mABs have been transferred into buffers similar the model buffer but varying the pH value from 4.5 to 9.3. The zetapotential was subsequently determined. By the correlation of the resulting zetapotential values with the adjusted pH, applying of a Boltzmann fit, the apparent pI value of each mAB was estimated at the pH with the zetapotential value of zero.

10.1.2. Structure and conformational stability of the model systems

The structural analysis was performed using the Raman spectroscopy element of the Zetasizer Helix system. The resulting portions of secondary structure elements alpha-helices, beta-sheets and beta-turns are summarized in Table 13. The elements of beta-sheets and beta-turns (above 70%) represented the major portions of all three mABs. Alpha-helices represented the smallest portion. Circular dichroism measurements, as orthogonal method, performed during a student internship confirmed these results especially the results for alpha-helices and beta-sheets (Master thesis S. Sayle).

Table 13: Secondary structural analysis model mABs by Zetasizer Helix system (Raman spectroscopy).

	α-helices	β-sheets	β-turns	others (random coils)
mAB1	~ 9%	~ 43%	~ 30%	~ 18%
mAB2	~ 5%	~ 47%	~ 28%	~ 20%
mAB3	~ 8%	~ 44%	~ 30%	~ 19%

The conformational stability in this case study was evaluated during thermal melting by ITF and DSC measurements and chemical denaturation experiments by ITF measurements.

The melting profiles of all three mABs showed two transitions (two peaks in first derivation) but differed significantly in their unfolding processes as seen in the thermograms (Figure 3- 38). The melting process is further described by the parameters of unfolding start (Tonset), melting temperature 1 (Tm1) and melting temperature 2 (Tm2) (Table 14Table 14).

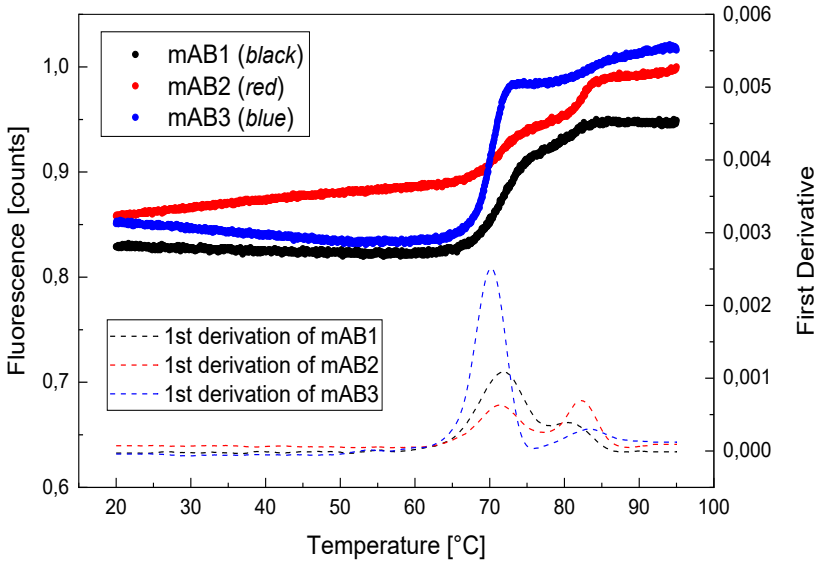

Figure 3- 38: Conformational stability model mAB systems: ITF thermal melting curves.
The antibody suspension of mAB1, mAB2 and mAB3 have been heated up from 20 °C to 95°C with a heating rate of 60 K/h. The fluorescence signal at 350 nm and 320 nm was detected and the ratio 350/320 nm is illustrated over the temperature ramp. To better visualize the melting temperatures (inflection points) the first derivate is shown in the lower part of the graph.

Table 14: Conformational stability: Summary characteristic melting temperatures Tonset, Tm1 and Tm2 (by ITF and DSC)

	Tonset (ITF) /°C	Tm1 (ITF) /°C	Tm2 (ITF) /°C	Tonset (DSC) /°C	Tm1 (DSC) /°C	Tm2 (DSC) /°C
mAB1	66.2	71.9	80.9	62.8	70.7	82.9
mAB2	66.5	71.3	82.3	64.7	69.9	80.1
mAB3	64.9	70.2	83.6	n/a	69.9	81.6

The significant unfolding start was detected between 60 °C and 65 °C. Based on the unfolding start, mAB3 is the least stable and mAB2 the most stable molecule. A first difference in the unfolding processes of all three mABs was already observed before the unfolding start: Based on the ITF signal, the structure of mAB1 stayed constant. In contrast, mAB2 showed a slight ITF signal increase and mAB3 showed an initial ITF signal decrease. After unfolding started mAB1 showed a short, fast first transition and a longer, slower second transition leading finally to a plateau. The two transitions of mAB2 proceeded in a similar lengths and velocity. The mAB3 unfolding profile showed a fast dominant first transition and a slow second transition. Based on the melting temperature Tm1, mAB1 is the most conformational stable mAB, followed by mAB2 and the least stable mAB3. The Tm2 ranking stated mAB3 as the most stable and mAB1 as the least stable molecule. In comparison to the ITF results, DSC (as orthogonal method to ITF) also determined the characteristic parameters. The DSC results are opposed to the ITF results in Table 14.

The results of the chemical denaturation using guanidine hydrochloride (GuHCl) are shown in Figure 3- 39. The $C_{1/2}$ values of mAB1 and mAB2 are similar (about 2.3 M), the $C_{1/2}$ value of mAB3, in contrast, is slightly lower (about 2.1 M) indicating a lower conformational stability.

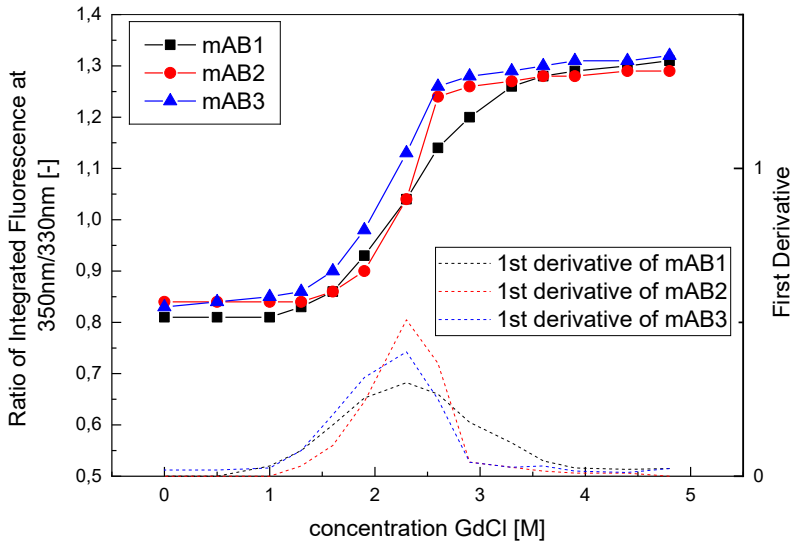

Figure 3- 39: Conformational stability model mAB systems: Chemical denaturation curves using guanidine hydrochloride.
The antibody suspension of mAB1, mAB2 and mAB3 have been incubated with increasing concentrations of guanidine hydrochloride (0 M to 5 M) at RT overnight. Subsequently, the fluorescence signal at 350 nm and 320 nm was detected and the resulting ratio 350/320 nm is illustrated over GdCl concentration. To better visualize the melting temperatures (inflection points) the first derivate is shown in the lower part of the graph.

Table 15: Calculation of Gibbs energy ΔG^0, *m*-value and $C_{1/2}$ for chemical denaturation of mAB1, mAB2 and mAB3 based on a two-state model.

	mAB1	mAB2	mAB3
ΔG^0 / kcal/mol	3.1	4.3	2.7
***m* / kcal/(mol*M)**	1.3	1.8	1.2
$C_{1/2}$ / M	2.41	2.35	2.13

Similar to the thermal unfolding process, all three mABs showed different progresses. The mAB1 unfolding process was observed from 1 M to 4 M (Δ = 3 M) and appeared as slow and continuous process. The mAB2 unfolding process started at a GuHCl concentration of 1.5 M, was completed at 2.9 M (Δ=1.4 M) and appeared with a fast and sharp unfolding event. The unfolding process of mAB3 started already at low concentrations of 1 M and was completely unfolded at a concentration of about 3.4 M (Δ=2.4 M). The characteristics of the first phase correspond to the mAB1 process (initially slow and continuous increase) and the second phase corresponds more likely to the mAB2 process (after $C_{1/2}$ fast unfolding to a plateau at the same concentration as mAB2). Based on the achieved data, a 2-state model was applied and calculation of the Gibbs energy of the protein at zero denaturant concentration ΔG^0, the *m*-value and the $C_{1/2}$ have been calculated as described by Freire et al. (Freire, Schön et al. 2013) and results are summarized in Table 15.

10.1.3. Aggregate and particle analysis of the model systems

The model systems have been analyzed for their particle content from the nanometer range up to higher micrometer size range by size-exclusion chromatography (HP-SEC), dynamic light scattering (DLS), nanoparticle tracking analysis (NTA) and micro-flow imaging (MFI). In addition, static light scattering approaches A320 and aggregation index (AI) were sensitive methods used to detect the presence of particles. The aggregate and particle analysis results are summarized in Table 16. In general, none of the samples showed extreme high particle contents in the model system.

Table 16: Summary particle content and size analysis of the three model systems.

	HP-SEC		Dynamic light scattering		Static light scattering		Nanoparticle tracking analysis 100 – 1000 nm	Micro-flow imaging 1 -100 µm
	monomer	soluble aggregate	z-average	PDI	A320	AI		
mAB1	98.4 ±0.2%	1.5 ±0.1%	10.9	0.14	0.08	2.13	Particle concentrations per ml are below $1x10^7$	1915 p/ml
mAB2	98.1±0.3%	1.9±0.2%	10.9	0.04	0.06	1.74		903 p/ml
mAB3	96.0±0.2%	3.6±0.2%	11.5	0.04	0.06	1.74		13019 p/ml

Based on HP-SEC analysis mAB1 and mAB2 showed similar monomer content of more than 98 % and aggregate content of maximal 2 %. The mAB3 suspension showed a higher portion of soluble aggregates with almost 4 %. DLS data indicated for all three mABs only one population around 11 nm with a PDI value below 0.2. Both light scattering-based analyses, however, indicate a slight higher polydispersity for mAB1 (PDI, A320 and AI). NTA analysis was performed for all three mABs, but as particle content in the NTA size range was below 1x 10^7 particle/ml, concentration was too low for reliable measurements. MFI results showed particle content in the micrometer range of 9x 10^2 to 1.3x 10^4 particle/ ml. The highest particle concentration was achieved in the mAB3 sample, increased particle concentrations of mAB1 occurred compared to mAB2. The images of the MFI analysis showed mainly heterogeneous and polymorph particles without a specific common characteristic. LUMiSizer® analysis was performed as well, but due to a transmission above 80 % no particle distribution was calculated.

10.1.4. Long-term stability study over 6 months

The model systems were investigated over a time course of 24 weeks. The mAB suspensions have been aliquoted to 2R vials (2 ml) and stored at room temperature by exclusion of light. Each month a sample vial of each mAB was pulled and analyzed by the mentioned particle detection methods HP-SEC, NTA, MFI, DLS, turbidity A320 and aggregation index. An overview of the results is illustrated in Figure 3- 40 and Figure 3- 41.

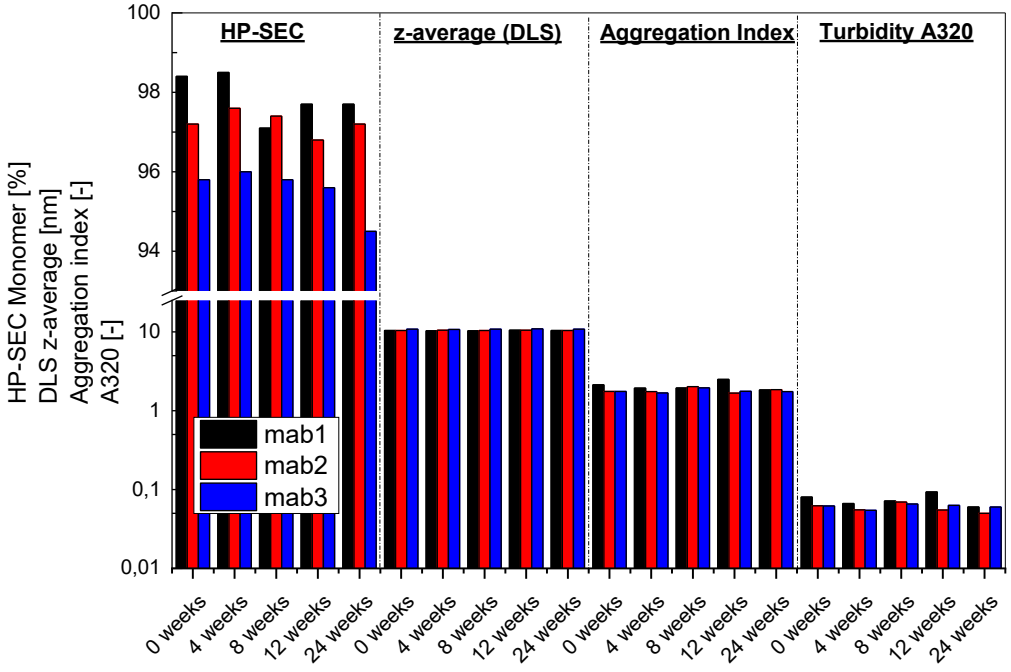

Figure 3- 40: Long-term stability model mAB systems: Monomer content, z-average, aggregation index and turbidity A320.
The results of stability-indicating analyses are monitored over the time course of 24 weeks incubation at room temperature.

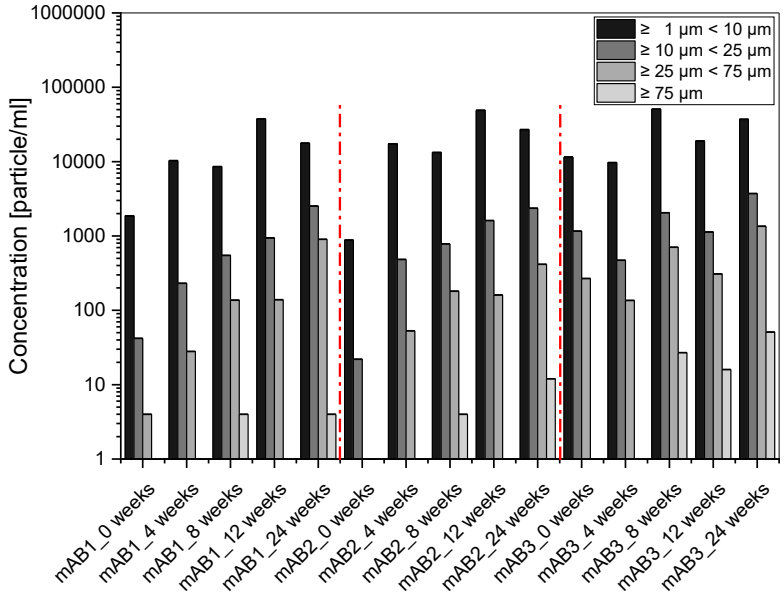

Figure 3- 41: Long-term stability model mAB systems: Particle content micrometer range.
The results of MFI analyses are monitored over the time course of 24 weeks incubation at room temperature. Five size bins are defined within the analyzed size range from 1 µm to 100 µm.

Based on HP-SEC results there was a maximal monomer loss and aggregate content increase of 1 % (mAB1 and mAB3). For mAB2, indeed, was no significant monomer loss for detectable. The particle analysis by DLS did not show any significant changes neither in the z-average nor in the PDI for all three mABs over the complete time course. In addition, the intensity-based calculated size identified only one particle population in the range of the start value. NTA analysis was applied leading to particle concentrations of about 1 $x10^5$ particles/ml constantly at all pull points and all three mABs. For that reason, the standardized three testing settings were not applicable as the concentrations were below the suitable concentration range of 1 $x10^7$ particle/ml. The MFI analysis, however, detected increasing particle concentrations of particles in all binned size ranges in all cases. For mAB3 the particle content was constantly higher than for mAB1 and mAB2. The turbidity as well as the light scattering based aggregation index occurred without tendency and were constant over time. In conclusion, the results of the 24-weeks stability study stated only minor aggregation and instabilities for the three model systems under storage conditions at RT. Without any stress conditions aggregation process studies and kinetics might be hard to perform or have to be performed over a long time.

10.1.5. Discussion biophysical characterization

The biophysical characterization of the model systems is the basis for better understanding further aggregation studies as well as to identify potential aggregation mechanisms. In addition, a stability ranking and critical parameters on the protein stability can be discussed.

For the evaluation of the ***colloidal stability*** the interaction parameters B22, A2 and kD were determined. The values of B22 and A2 describe more the direct protein-protein interactions without high influences due to protein-formulation excipients or excipient-excipient interactions. The kD value, on the other hand, is a description parameter of the total system considering not only protein-protein-interactions but also protein-excipient as well as excipient-excipient interactions. This difference was nicely demonstrated by pH and salt variation experiments: An influence of salt concentration changes was observable on kD values but not on B22 values. Changes in the pH values, indeed, lead to changes of the molecule and therefore have high influence on both values. Several approaches have been published to show a direct correlation between B22 and kD values, e.g. by Menzen et al. or Donev et al.. The correlations highly depend on the tested proteins and for the experiments performed in this study, none of the provided

formulas was able to describe the correlation. A direct correlation based on the data achieved for mAB1, mAB2 and mAB3 could not be identified.

In literature, however, a general interpretation of the parameters is given (Donev et al.): Positive B22 values indicate stabilizing interactions. In a comparative manner, decreasing B22 values indicating higher tendencies to self-associate. For kD values, positive values indicate repulsive intermolecular interactions, and negative values represent attraction. In the model system at a pH of 6.5, the highest tendency to self-association showed the mAB3 (indicated by both, negative B22 and negative kD values). The positive B22 values for mAB1 and mAB2 indicated colloidal stable systems. The negative kD values, however, indicate also a portion of attractive interactions in the system. The difference between B22 and kD ranking are explained by potential differences in the the ratio between the hydrodynamic and other parts of the correlation. From the theoretical perspective, however, the B22 ranking is more reliable and the most colloidal unstable system is mAB3 system.

Based on the DVLO theory, particle charges have influences on the colloidal stability. For that purpose, zetapotential measurements were performed. All samples resulted in positive apparent zetapotential. This was expected as the theoretical isoelectric point as well as the determined isoelectric point are above the pH of 6.5 (see Table 7). All values are lower than 10 mV, the limit given for colloidal stability of spherical homogenous charged particles. From the theoretical perspective the suspensions are colloidal unstable. Antibody molecules, however, have a heterogeneous charge distribution and the zetapotential is only an apparent mean value. For that reason, also suspensions with low apparent zetapotential may be colloidal stable. Based on the amino acid sequence, protein surface models can be calculated, that illustrate such charge distributions in the molecule. For the three mABs, such a modeling was performed by Dr. Michaela Blech and is illustrated in Figure 3- 42. At a pH of 6.5 charge distributions of mAB1 and mAB2 are similar without dominant charge patches. In contrast, mAB3 showed a dominant positive patch in the central molecule area and this may lead to a dipole character of the whole molecule. Due to this character, attractive electrostatic interactions may potentially appear and trigger self-association. Differences between mAB1 and mAB2 are seen over a pH value range. The charge distributions of mAB2 appear more balanced over the whole pH range. This fact explains the observation that mAB2 is more stable in the basic range than mAB1. In a similar manner, one

could explain the increasing stability for mAB3 as the positive batch gets balanced with increasing pH value.

The practical approach to determine the isoelectric point (pI) using the zetapotential led to lower pIs (7.6 for mAB1, 8.0 for mAB2 and 7.0 for mAB3) compared to the calculated values. These differences may be caused due to glycosylation or the influence of the surrounding excipients. Furthermore, such shifts may also be explained based on the calculated charge distributions. The calculations consider all molecule charges independently of their position (buried in the molecule or presented on the surface). The apparent zetapotential measured only surface charges independently of the charges in the molecule. In addition, dominant patches on the surface may overcome single charges and shift he apparent zetapotential.

These considerations showed the complexity of protein properties. Further, they demonstrate the challenge of predicting molecule behavior.

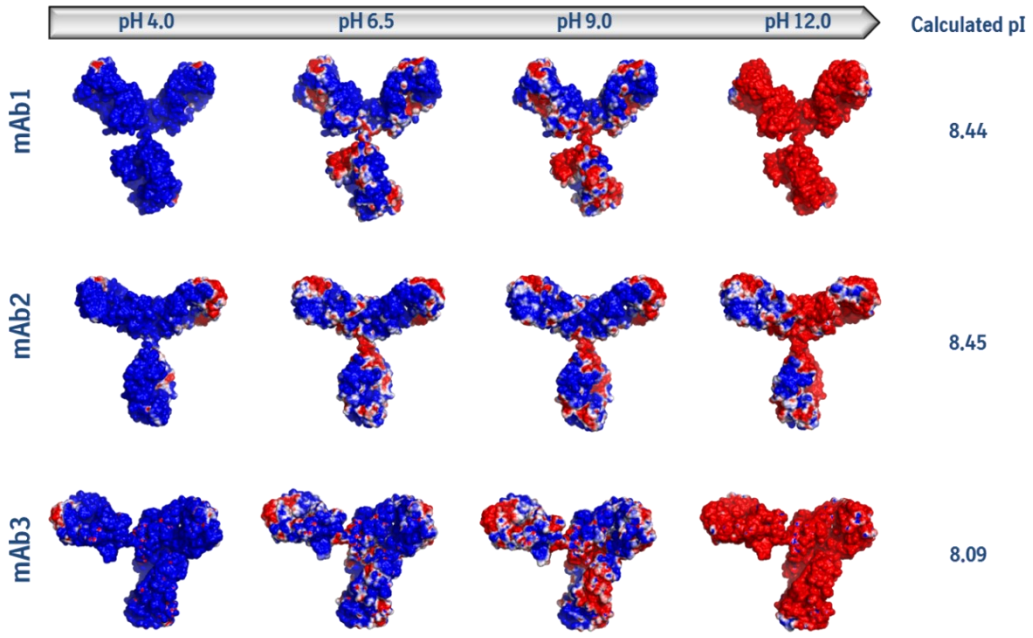

Figure 3- 42: Modulated characteristics model mAB systems: Electrostatic potentials under different pH and constant ionic strength conditions (0.02 M).
Color code: blue surface areas: positive patch; red surface areas: negative patch. Modulations have been performed and provided by Dr. Michaela Blech.

The ***structural analysis*** performed by the Zetasizer Helix system indicated the typical beta sheet dominated secondary structure of monoclonal antibodies using the signal at the characteristic

Amide I band (Wen 2007). A beta sheet fraction of 40 to 60 %, also detected for all three mABs of this case study, builds the structural framework of the molecule. As well described by Morea et al., anti-parallel beta sheets connected by loops form a stable structural unit (Morea, Lesk et al. 2000). This fact and the typical presence of loops in the variable regions explain the high fraction of turns and others as well. For the alpha helical structure, fractions below 10% are quite common. Comparing the three model antibodies, mAB1 and mAB3 are most similar. The beta sheet fraction of mAB2 seemed slightly higher. One assumption could be a slightly more stable beta framework. Nevertheless, all three mABs show a similar secondary structure composition.

The ***conformation stability*** is characterized by parameters like the unfolding start by the application of stress (e.g. temperature or chemicals). Typical parameters in temperature induced unfolding are Tonset or melting temperatures Tm. As discussed under 9.2.5 the values depend also on the applied principle. Due to further experiments, the conformational stability was characterized based on temperature melting and chemical denaturation.

The temperature-induced unfolding process of antibodies is an often-investigated process. For intact antibodies a process with two transitions or in other words with two clear peaks representing two melting temperatures is common model for the unfolding. Based on the ITF thermograms the selected model antibodies of this study meet these expectations. Ionescu et al. correlated the peaks in a DSC thermogram to unfolding of three structural components: CH2, CH3 and Fab fragment (Ionescu, 2008). Transfer their results on the ITF thermograms the first transition represents the unfolding of CH2 and the second one of CH3. The contribution of the Fab fragment, either to the first or to the second transition, cannot be clarified at this point. For that attribution DSC thermograms have been analyzed.

In case of mAB1 and mAB2 the first transition represents CH2 domain unfolding, and the second transition the unfolding of the Fab fragment and the CH3 domain (Ionescu, 2008). A slight shoulder on the second peak may indicate either that CH3 domain unfolded later than Fab fragment or initial aggregation that might also change the enthalpy. In case of mAB3 the DSC thermogram showed only one clear peak and background noise before this peak as well as a potential peak after this peak. Based on the descriptions of Ionescu et al. an attribution is hardly achievable. A possible scenario is a cooperative unfolding of all three structural components considering only the one peak (structural collapse). Another scenario might consider the high background noise as signal for aggregation/self-association that is monitored in DSC measurements, but not in the ITF

thermogram. Same discussion might be applied to the potential second peak. A third scenario would fit to the second model of Ionescu et al.: the Fab fragment is destabilized by the variable sequences and the first dominant peak represents the unfolding of the Fab fragment and the CH2 domain, while the potential second transition represents CH3 domain unfolding (Ionescu, 2008).

The detected Tonsets and Tms were all in the same range. Depending on the parameter three stability rankings may be achieved: Tonset: mAB2 > mAB1 > mAB3; Tm1: mAB1 > mAB2 > mAB3; Tm2: mAB3 > mAB2 > mAB1. The fact, that there is no common tendency for all parameters as well as the thermograms suggest mAB specific processes. For mAB1, prior unfolding start no structural changes were detectable. For mAB2, a signal increase was detectable indicating either continuous slow unfolding or the loss of the hydration shell. For mAB3 signal decrease was observed suggesting self-association/aggregation.

The approach of chemical denaturation is an orthogonal approach to estimate and describe conformational stability. GuHCl is a chaotropic substance and at the same time increases the solubility. In contrast to the thermal unfolding processes, aggregation is mainly excluded due to the solubility increasing character of GuHCl.

Based on the $C_{1/2}$ value, mAB1 showed the highest stability against forced unfolding by guanidine hydrochloride (GuHCl). The characteristic $C_{1/2}$ value estimated from the first derivation were in good agreement with the values calculated based on a two-state model published by Freire et al. (Freire, Schön et al. 2013). The application of the two-state model enabled further the calculation of ΔG^0 and m-value. Increased protein stability is indicated by increased $C_{1/2}$ and ΔG^0 values and increased m-values indicate better solubility of unfolded state und lower tendency to aggregate (more complete unfolding, more cooperative process). The molecules of mAB1 and mAB2 indicated similar structural stability as they showed higher ΔG^0 and $C_{1/2}$ values. The mAB1 is less sensitive to the chaotropic character than mAB2. In contrast, mAB2 showed the highest stability considering protein stability at experimental temperature and solvent conditions except denaturants (ΔG^0). The best solubility of unfolded state is expected for mAB2 with the lowest tendency to aggregate during the uncompleted unfolding process. It represents the most cooperative unfolding process. The molecules of mAB1 and mAB3 showed similar m-values and therefore tend to aggregate already in the unfolding process representing a partially unfolded state. The mAB3 molecule, however, indicated the lowest protein stability.

An overall stability ranking considering colloidal and conformational stability parameters is hardly achievable. In the majority of the parameters mAB3 appeared as least stable and mAB1 and mAB2 showed similar stability. The results of the ***particle analysis*** confirmed that mAB3 is less stable as the fraction of soluble aggregates as well as the particles concentration in the micrometer range is higher than for the other mABs. Similar protein stability of mAB1 and mAB2 is also confirmed by HP-SEC results. DLS results, however, demonstrated a higher polydispersity of mAB1 and MFI detected higher particle concentrations. This supported the evaluation based on chemical denaturation, that mAB2 has a lower tendency to aggregate. The particle contents of all three mABs are relatively low and are comparable to unstressed formulated therapeutic antibodies.
The ***long-term stability*** indicated no significant instabilities. The methods DLS, AI and turbidity, as highly sensitive did not monitor changes over the six months. Considering the stability of monomers, the mAB1and mAB3 monomer fractions decreased confirming the interpretation of chemical denaturation as the tendency to self-associate is higher compared to mAB2. Based on the particle content in the micrometer range, slow aggregation was detectable for all three mABs. A first glance on differences in the aggregation processes is given. The particle content of mAB1 and mAB2 suspensions increased evenly in all size bins. An exception is seen for mAB3, as size bins increase fluctuant.

10.2. Stress-induced protein aggregation studies

The model systems have been stressed by the application of a temperature ramp, isothermal temperature stress at an increased temperature and by the application of further stress conditions (pH, reducing agents, aggregate seeding). The resulting aggregation processes were consequently analyzed by established methods and the emerging methods and technologies that have been evaluated in chapter 8 and chapter 9.

10.2.1. Thermal induced aggregation studies mAB1 and mAB2: temperature ramps

The performance of temperature ramp experiments to investigate protein stability and aggregation is a common approach. For this purpose mAB1 and mAB2 have been analyzed exemplary over a temperature range from 25 °C up to maximal 90 °C by the following devices/technologies:

Optim 1000 (Avacta), Prometheus NT (Nanotemper), SwitchSENSE® (Dynamic Biosensors) and Zetasizer Helix (Malvern Instruments GmbH).

The Optim 1000 and the Prometheus NT used the combination of the intrinsic tryptophan fluorescence and light scattering signal differing in the wavelength and the optical set-up. The detected aggregation start temperatures (Tagg), the calculated unfolded portion at the Tagg and the determined melting temperatures (Tm) were summarized in Table 17. The unfolding thermograms of both methods were similar and they are illustrated in Figure 3- 43 for Optim 1000 and Figure 3- 48 for Prometheus. The Optim 1000 instrument enabled the detection of scattered light at two specific wavelengths: 266 nm and 473 nm. The Prometheus instrument, in contrast, detected only one scatter signal (wavelength not provided by the manufacturer).

Table 17: Temperature ramp models systems: Results of Prometheus NT (*Prom*) and Optim 1000 (*266 nm, 473 nm*) analyses.

	Tagg [°C]			portion unfolded at the Tagg [%]			Unfolding Prometheus NT		unfolding Optim 1000	
	266 nm	*473 nm*	*Prom*	*266 nm*	*473 nm*	*Prom*	Tm1 [°C]	Tm2 [°C]	Tm1 [°C]	Tm2 [°C]
mAB1	70.2	75.2	81.6	23.5	67.1	85.2	71.9	80.9	69	78
mAB2	70.5	72.4	78.4	33.3	45.2	61.6	71.3	82.3	70	75

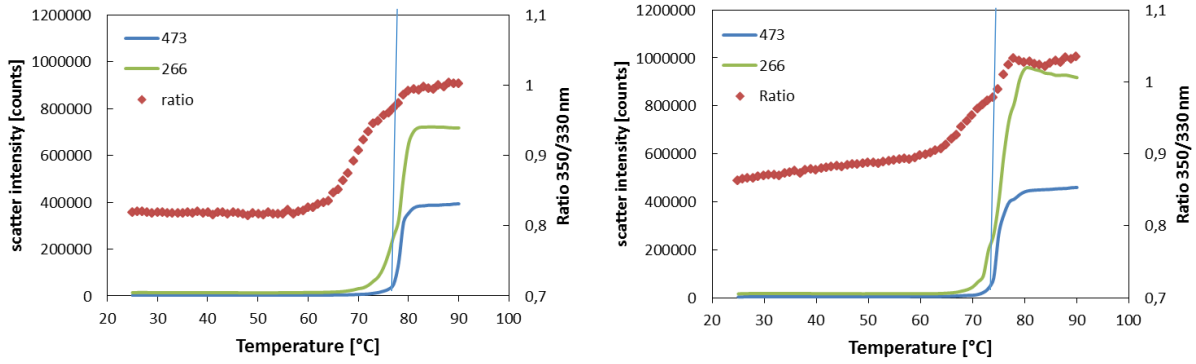

Figure 3- 43: Temperature ramp model mAB systems: Unfolding and aggregation thermograms achieved by Optim 1000 analyses.
The thermograms illustrate the melting process (red dots; ratio 350 nm/330 nm) of mAB1 (upper left) and mAB2 (upper right) as well as the aggregation start detected by light scattering signals at 266 nm (green) and at 473 nm (blue) over the temperature ramp. The blue line highlights the scattering start of the 473 nm scattering signal.

A more detailed description of the unfolding processes was described under 10.1.2 and 10.1.5. In this chapter, the focus is set to the aggregation processes within these unfolding processes. All detected aggregation starts occurred above the determined ITF unfolding start temperature and between the melting temperatures Tm1 and Tm2. The aggregation start values detected by Optim 1000 measurements were in all cases lower as the ones detected by Prometheus measurements. The tendencies of the 473 nm values and the Prometheus values agreed.

For mAB1, the first scattering signal increase was detected for 266 nm at around 70 °C. Based on the unfolding curve, at this temperature a portion of about 24 % was unfolded. The second scattering signal at 473 nm occurred with a portion of about 67 % of the total unfolding process at about 75 °C. The observed shift may indicate several aggregation steps. A similar observation was detected for mAB2 whereas the first step was shorter than for mAB1. The calculated unfolded portions, however, differed as seen in Table 17. Due to the higher sensitivity of the 266 nm value and the possibility to differentiate the scattering signals at two different wavelengths, the Optim 1000 offered more information for the description of the aggregation process.

A further orthogonal technology used to characterize thermal melting and aggregation process was the SwitchSENSE® technology. These experiments with soluble monomer have only been performed with mAB1 as a successful set-up for aggregation studies could not be achieved (compare 9.2.4). The aggregation start for mAB1 was determined at about 70 °C. The resulting melting temperature achieved by the SwitchSENSE® experiment was determined with 70.6 °C. The calculation of portion of unfolding as calculated for ITF was not possible. During the melting process (molecule in buffer), the switching speed increased constantly, indicating continuous loss of structure.

A third orthogonal technology used to characterize thermal melting and aggregation processes was the Zetasizer Helix. Both molecules, mAB1 and mAB2, were analyzed and the results are summarized in Figure 3- 44 to Figure 3- 47, respectively.

For mAB1, DLS results indicated a size increase starting around 69 °C and 70 °C (Figure 3- 44, left). Consequently, this temperature was defined as aggregation start Tagg. Based on the recorded Raman spectra specific temperature points were identified indicating changes in the secondary (amid I band; Figure 3- 44 right) and tertiary structure (tryptophan and tyrosine; Figure 3- 45). The secondary structure markers showed a significant change around 78 °C.

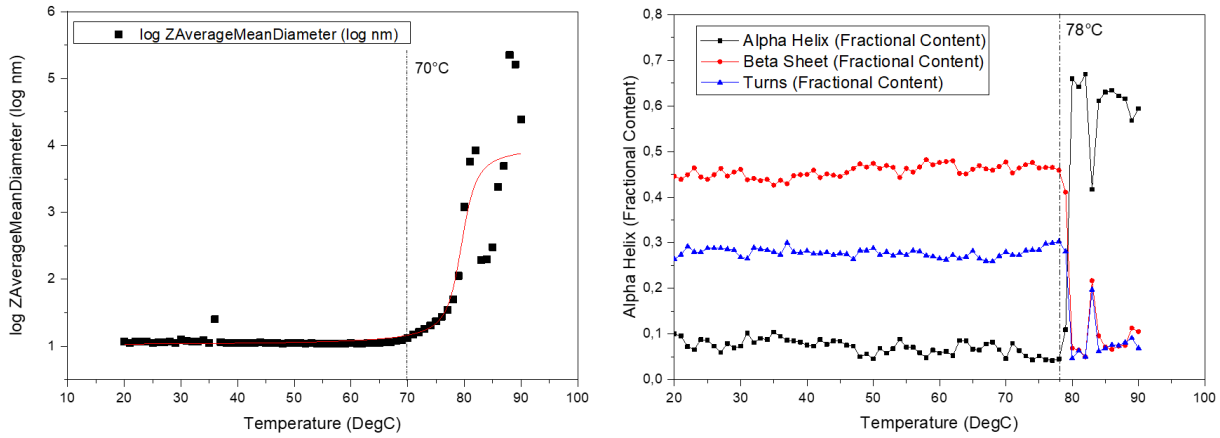

Figure 3- 44: Temperature ramp mAB1: DLS and secondary structure results (based Raman spectra data). The DLS results represented by the logarithm of the z-average over the temperature ramp is shown in the left graph. With increasing temperature, a significant increase of the hydrodynamic radius was observed starting about 70 °C (Tagg). Based on the captured Raman spectra the portion of secondary structure elements was calculated and is monitored over the temperature ramp in the right graph. Significant changes in the secondary structure were detected at 78 °C and above.

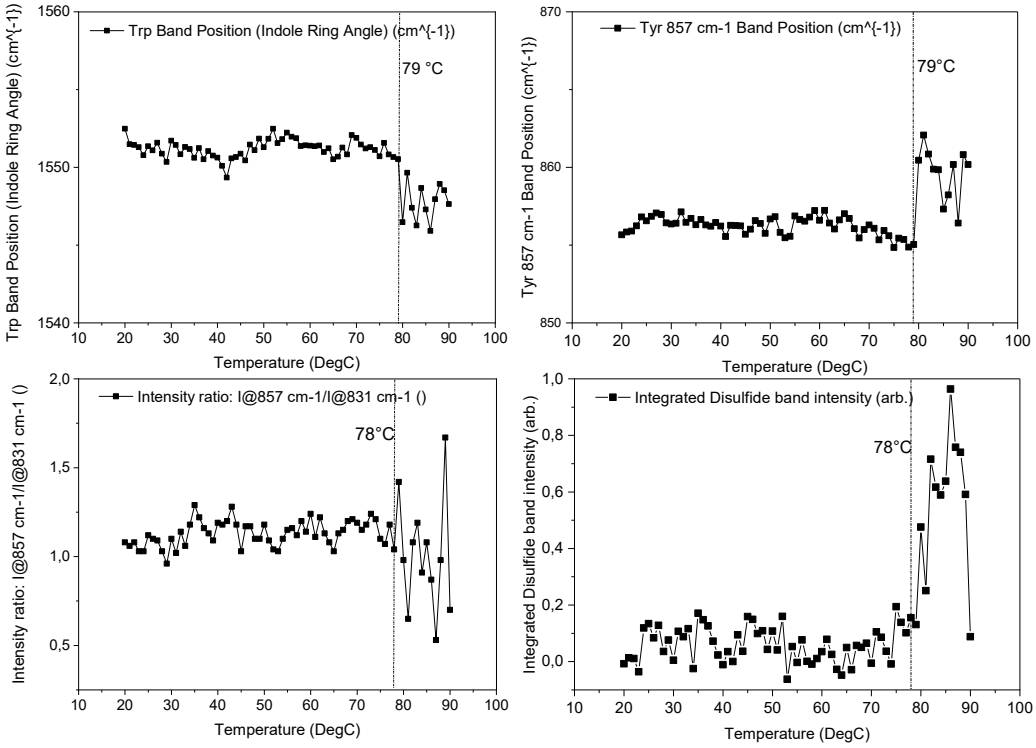

Figure 3- 45: Temperature ramp mAB1: Tertiary structure results (based Raman spectra data). The graphs summarize typical tertiary structure markers over the temperature ramp based on the captured Raman spectra. Changes based on the tryptophan indole ring was detected at 79 °C and above (upper left). Changes in the tyrosine markers were detected at 78 °C and above (upper right and lower left). At the same temperature, the intensity of the disulfide band increased (lower right).

The portion of alpha helices increased suddenly from 10 % up to 60 %. At the same time beta sheets (45 %) and beta turns (30 %) portions decreased down to 10 %. At the same temperature, the intensity of the band considering disulfide bonds increased. The tertiary markers for tryptophan and tyrosine indicated a change slightly later at 79 °C (in the range of Tm2 detected by ITF).

For mAB2, DLS results indicated a size increase starting around 69 °C and 70 °C (Figure 3- 46, left). Consequently, this temperature was defined as aggregation start Tagg. Similar to mAB1, based on the recorded Raman spectra specific temperature points were identified indicating changes in the secondary (amid I band; Figure 3- 46, right) and tertiary structure (tryptophan and tyrosine; Figure 3- 47). In contrast to mAB1, changes in the secondary structure (amide I band), in the disulfide band intensity and the tertiary structure markers appeared at the same temperature at about 76 °C (in the range of Tm2 detected by ITF). The portion of alpha helices increased suddenly from 5 % up to 55 %. At the same time beta sheets (50 %) and beta turns (27 %) portions decreased down to 15 %. At the same temperature, the intensity of the band considering disulfide bonds increased.

Comparing the results of mAB1 and mAB2, the aggregation start appeared in the same temperature range but the structural indicators suggested slight differences in the aggregation processes. Structural changes, beta sheet loss and alpha helices increase, were similar.

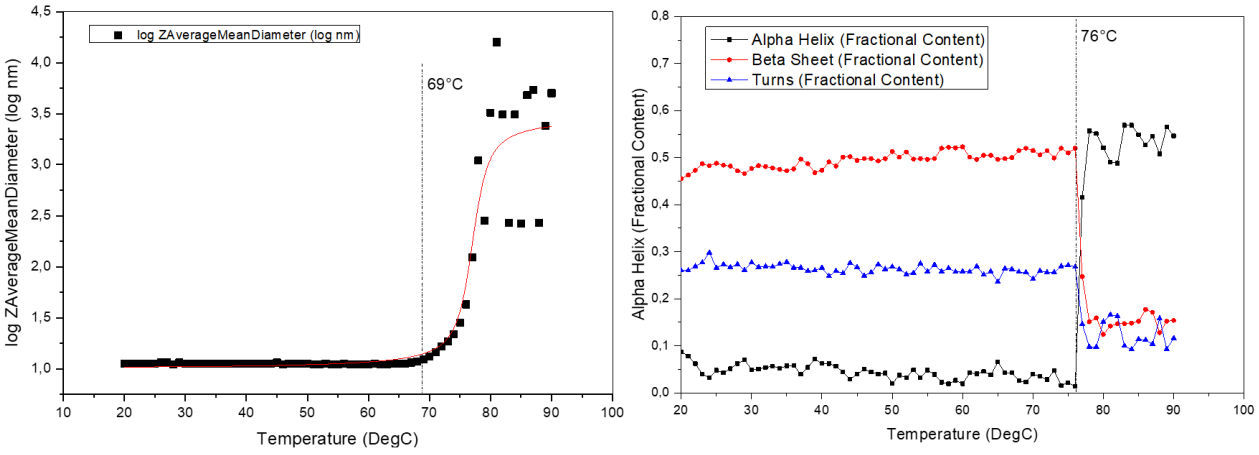

Figure 3- 46: Temperature ramp mAB2: DLS and secondary structure results (based Raman spectra data). The DLS results represented by the logarithm of the z-average over the temperature ramp are shown in the left graph. With increasing temperature, a significant increase of the hydrodynamic radius was observed starting about 69 °C (Tagg). Based on the captured Raman spectra the portion of secondary structure elements was calculated and is monitored over the temperature ramp in the right graph. Significant changes in the secondary structure were detected at 76 °C and above.

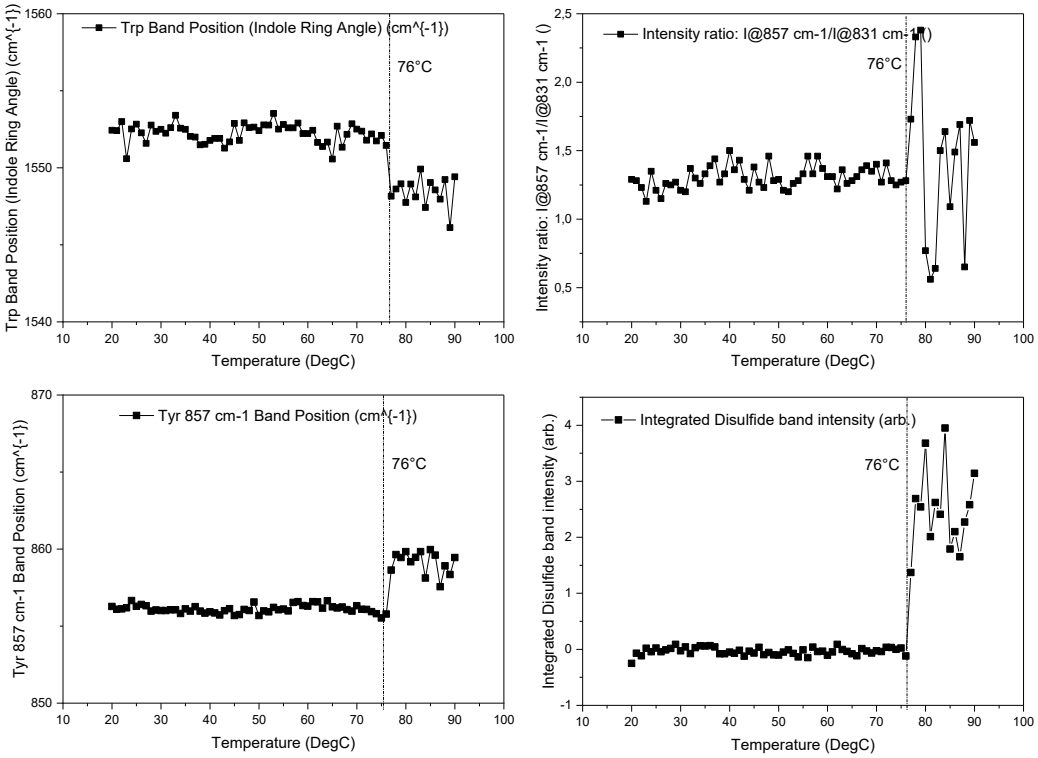

Figure 3- 47: Temperature ramp mAB2: Tertiary structure results (based Raman spectra data).
The graphs summarize typical tertiary structure markers over the temperature ramp based on the captured Raman spectra. Changes based on the tryptophan indole ring was detected at 76 °C and above (upper left). Changes in the tyrosine markers were detected at 76 °C and above (upper right and lower left). At the same temperature, the intensity of the disulfide band increased (lower right).

For all tested approaches, a heating rate of 1 K per min was selected and protein concentrations in the investigated mAB suspensions were set to 5 mg/ml, respectively 10 mg/ml (Zetasizer Helix), allowing the comparison of the results. These results illustrated differences in the aggregation processes of the mABs. In some cases, e.g. the Helix approach, the difference occurred only slightly. For that reason, a further approach was realized by ITF varying the heating rate and the protein concentrations (Figure 3- 48).

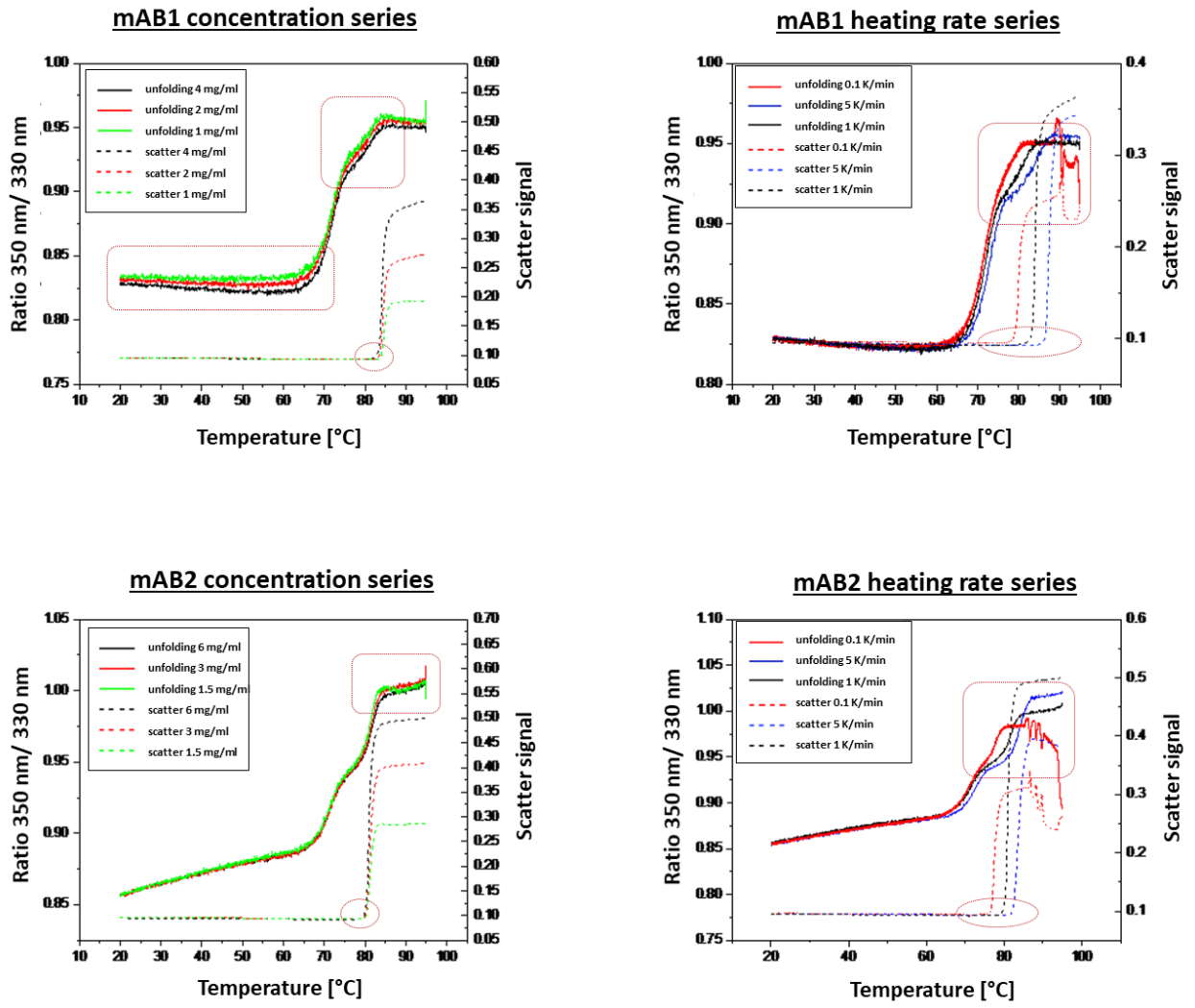

Figure 3- 48: Temperature ramp model mAB systems: Concentration and heating rate variations.
The graphs on the left show the effects of concentration variations on the unfolding curve (ratio 350 nm /330 nm) as well as the scatter signal. The graphs on the right show the effects of heating rate variations on the unfolding curve (ratio 350 nm /330 nm) as well as the scatter signal. The boxes and the circles highlight concentration-influenced, respectively heating rate-influenced, areas. The upper graphs illustrate mAB1 results and the lower graphs illustrate mAB2 results.

In the tested concentration ranges, only minor concentration influences were detected. For mAB1, increasing concentrations led to slightly decreasing Tagg values. Further, the results of mAB1, indicated concentration influences on the unfolding process in the pre-unfolding as well as in the second transition phase. For mAB2, the results did not show significant influences neither in unfolding nor in aggregation start Tagg. Slight influences may be suggested for the unfolding process in the second transition phase.

The variations in the applied heating rates resulted in clear detectable changes within the unfolding and the aggregation processes. With increasing heating rates, the unfolding starts and the aggregation starts (Tagg) increased. Both molecules showed a clear two-step unfolding process whereas the second transition is mainly influenced by the heating rate variation. In addition, clear differences between the mABs occurred: The final unfolding signal (330/350 intensity ratio value) of mAB1 is the same for all three tested heating rates. The aggregation starts of mAB1 were demonstrated by sharp increases of the scattering value in all cases and scattering occurred right before the unfolding curve reached the end value plateau. A correlation between the Tagg and the intensity ratio was investigated. In result, a linear regression was identified with a positive slope of 0.0008. The difference between the Tagg at the lowest heating rate and Tagg at the highest heating rate was 8 K. For mAB2, same as mAB1, most likely the second transition was influenced by the heating rate and sharp aggregation starts could be determined. In contrast to mAB1, the unfolding end values of mAB2 varied for each heating rate. A correlation between the Tagg and the intensity ratio was investigated resulting in a linear regression with a negative slope of -0.0048. The difference between the lowest heating rate Tagg and the highest heating rate Tagg was 4 K.

10.2.2. Discussion aggregation processes during temperature ramp experiments

For the discussion of the temperature ramp experiments, two aspects will be discussed: (1) technical perspective as well as single experimental results and (2) a hypothesis/theory of the specific aggregation process of mAB1 and mAB2 over the temperature ramp.

(1) Technical perspective

During all temperature ramp experiments, protein aggregation was detectable within the selected temperature range from 25 °C to 95 °C and an aggregation start temperature (Tagg) was determined. The resulting Taggs, however, differed depending on the applied measurement principle, the detected property and its sensitivity. For the investigation of the aggregation mechanisms and processes, each applied technique showed advantages and disadvantages.

The light scattering based techniques observed Taggs varying over a temperature range of 20 K. The most sensitive techniques were DLS and RALS at a wavelength of 266 nm. Both techniques detected the aggregation start temperature for mAB1, exemplary, at 70 °C. The Tagg determined by the SwitchSENSE® technology using a light scattering independent principle occurred in the

same temperature range. This agreement implies first aggregation at this temperature. The higher Taggs detected by RALS at a wavelength of 473 nm and with the back-reflection light principle suggested that the detection system is less sensitive for the detection of initial aggregation events. These temperature shifts in the Tagg values - based on the applied method - may be explained by two assumptions: (1) small particles may be present but due to the longer wavelengths (e.g. 473 nm) the frequency of the interaction of these smaller particles (size below used wavelength) is not sufficient to detect these particle; (2) particle concentration was not sufficient to achieve significant light scattering that could be detected.

The reduced sensitivity achieved by back-reflection light measurements has not been expected as the detected wavelengths occurred between 266 nm and 473 nm (information of the manufacturer). It was expected that the Taggs detected with the Prometheus back-reflection principle occurred between the RALS values. The detection principle, however, seemed less sensitive and aggregation was detected later as expected. A possible explanation is that the light passes the sample two times leading potentially reducing the light intensity twice.

The combination of unfolding investigation by ITF and aggregation investigations by light scattering was used in the ***Prometheus NT*** and ***Optim 1000*** (as described under 7.5.8 and 7.5.9). As discussed before, aggregation detected by light scattering depends on the measurement principle. Prometheus uses back-reflection light measurements with a wavelength between 266 nm and 473 nm, which is - compared to right angle light scattering at wavelength of 266 nm and 473 nm - less sensitive. Due to the higher data amount and density, however, the Prometheus NT is more sensitive and robust for unfolding detection. All unfolding thermograms by Optim 1000 and Prometheus suggested a complete unfolding process in the tested temperature range. This allowed the determination of the fluorescence ratio value of the folded and unfolded state and the calculation of the unfolding state/portion at each temperature. The determination of unfolded portion at the aggregation start temperature can give information about the aggregation mechanism. As the examples of mAB1 and mAB2 showed, a sensitive detection is necessary to detect realistically the portion of unfolding at which aggregation appeared. The correlation between the unfolding state and the aggregation start is only reliable for the detected aggregation start by RALS at 266 nm.

If the aggregation process appears continuously, the difference caused by reduced sensitivity by back reflection light might not change the stability order based on aggregation. In some cases, e.g.

if a sudden and fast aggregation takes place, this might not be detected and may change the stability order. To overcome the risk of misinterpretation orthogonal techniques are highly recommended. In the case of the investigated mABs the stability order based on the detected aggregation temperatures did not change and for stability screening both tested techniques are suitable.

The combination of the aggregation start determination by DLS measurements and the monitoring of selected structural markers by Raman spectroscopy over the temperature ramp used in the ***Zetasizer Helix*** gave value information about the aggregation process. Sharp detection of aggregation start in sensitive manner was possible, but the Raman spectra showed high background noise resulting in a high variation in the observed markers values. Small changes for that reason could not been detected but as seen in the examples significant changes have been detected and specific temperatures for these changes can be determined. A correlation between these specific temperatures allowed a better description of the aggregation process. Considering the sample volume of about 1 ml and the measuring time of about 90 minutes the techniques is a highly potential approach to better investigate aggregation processes.

The S***witchSENSE*** technology confirmed aggregation start of mAB1 and offers a light scattering independent orthogonal method. If more experiments than the aggregation start determination are performed with the chip in prior (compare chapter 9.2) the technique can be used as additional Tagg confirmation. If the only experiment is the aggregation start determination, the intense effort and the costs are too high, and this would not be the technique that would be suggested.

The ***variation of protein concentration and heating rates*** in ITF experiments occurred as a successful approach to better understand and differentiate between different aggregation processes. Protein concentration dependencies may highlight phases in which protein–protein interactions play an essential role. In this study, such interactions may play a role for mAB1 already prior and right after unfolding start. Further, an influence is detected in the range, in which aggregation occurs. In this phase, attractive protein-protein interactions are expected as basis for aggregation. Dependencies on the heating rate, on the other hand, may help to identify aggregation driven steps. In this study for mAB1 and mAB2, aggregation starts in the second transition explaining influences in this phase. For mAB3 - data was not shown – a clear influence was already detectable in the first transition indicating aggregation already in the early transition phase. Both approaches take closer look into the factors describing aggregation processes and are valuable. The application of

this approach to the other tested technologies might clarify their results as well und is suggested as next steps.

(2) Hypothetical theory of specific aggregation processes

Summarizing the results of temperature ramp experiments a possible description of the aggregation processes for each mAB is discussed. Based on the three detected aggregation starts (RALS 266 nm, RALS 473 nm and back reflection light detection) the process is described in four phases: the pre-aggregation phase below T (RALS 266 nm), the first aggregation phase from T (RALS 266 nm) to T (RALS 473 nm), the second aggregation phase between T (RALS 473 nm) and T (back reflection) and a last aggregation phase. For this purpose, results have been summarized and illustrated in the defined aggregation phases, shown in Figure 3- 49.

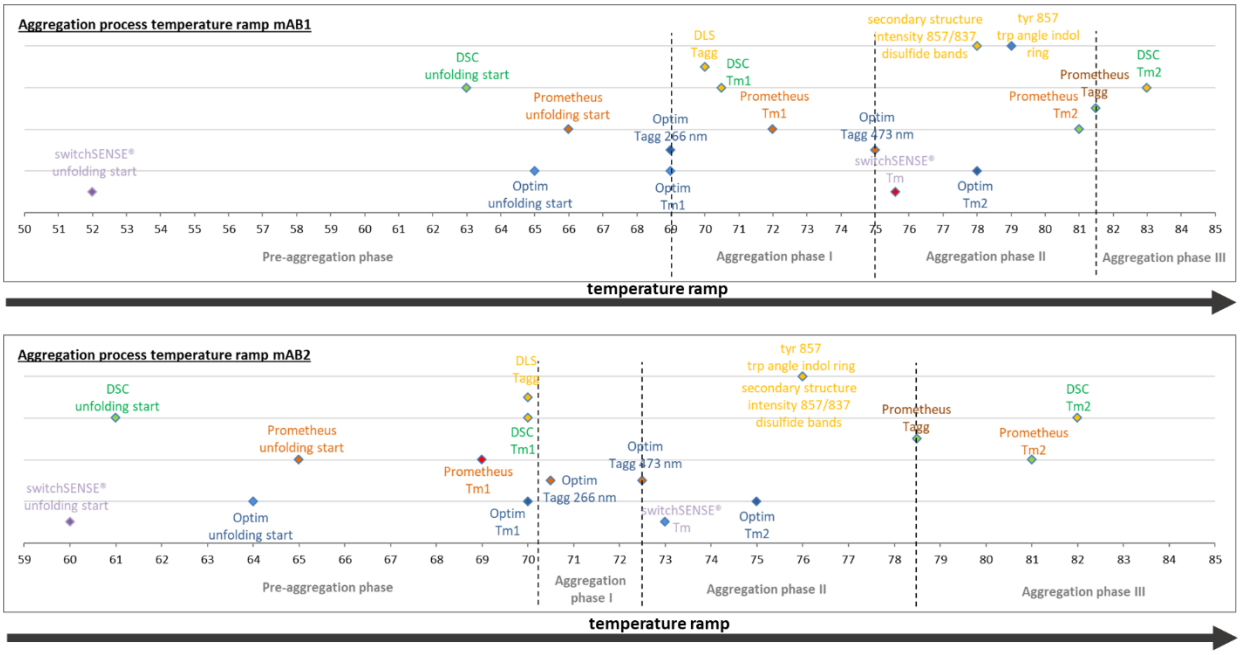

Figure 3- 49: Temperature ramp model mAB systems: Schematic summary of aggregation study results mAB1 and mAB2.
The illustration shows the characteristic parameters of mAB1 (upper) and mAB2 (lower) determined by ITF-RALS (Optim 1000), ITF-backscattering (Prometheus), DLS-Raman spectroscopy (Zetasizer Helix) and DSC.

Discussion of a potential aggregation process of mAB1

a) The pre-aggregation phase for mAB1 is in the range from 25 °C to 70 °C (duration about 45 K). The mAB1 monomers seemed to be conformational stable up to 52 °C. From 52°C, continuous structural changes were detected (switching speed increase) indicating loosening of the structure.

This, however, was only seen by the SwitchSENSE® system. From 63 °C, the monomer molecules unfolding is also detected as an exothermic reaction (DSC), but without changes in the hydrophobic patches (tryptophan environment). In addition, protein-protein interactions (indicated by the concentration dependency) may cause first soluble aggregates, potentially still reversible. Starting from 65 °C, the monomers unfolding process starts to have a measurable influence also on the hydrophobic areas in the molecule. With further increasing temperature up to the first aggregation temperature, the molecule reaches a state of up to 25 % unfolded fractions, but without significant aggregation (changes in intrinsic tryptophan fluorescence). By reaching the first melting temperature at about 70°C, first aggregation was detected. The described unfolding in the pre-aggregation phase happens in the first transition and mainly expected due to changes in CH2 domain. Secondary structure and tertiary structure elements, however, are still stable based on Raman spectra.

b) The first aggregation phase of mAB1 is in the range from 70 °C to 75 °C (duration about 5 K). Until the first aggregation start temperature at around 70 °C, the interactions of the partially unfolded monomers seemed too weak (or reversible) as no aggregation was detectable with the selected methods. Reaching the first melting temperature, indeed, means that half of the molecule underwent first transition and, in this case, mainly half of CH2 domain are unfolded (about 4 K after unfolding start). From this point, these partially unfolded monomers (ongoing unfolding) interact with each other leading to a continuous first aggregation growth phase. The detected initial aggregation signal at a wavelength of 255 nm occurred as the most sensitive signal. Only small aggregates and in low amounts may be present as scattering is only observed with the smaller wavelength (Optim). The further increasing signal may have two reasons depending on the underlying mechanism: (1) increasing amounts of small particles occur and give a signal at the larger wavelengths by reaching a sufficient concentration (enrichment of small particles summing up the scattering signal) leading further to a sudden collapse or (2) continuous growth on few nucleus lead to the signal leading to larger particle. As DLS detects the aggregation start in a similar temperature range, the increasing size from DLS measurements indicate the second scenario/mechanism. This growth led to larger particles that enabled the detection using RALS at a larger wavelength and starting the second aggregation phase (controlled growth). During this first aggregation phase, the first unfolding transition is ongoing and the second unfolding step/transition (CH3 and Fab-fragment) starts. Slowly ongoing unfolding from an unfolded

fraction of about 25 % to an unfolded fraction of about 67 %, can be assumed based on intrinsic tryptophan fluorescence triggering colloidal instability. Even though aggregation and further unfolding was observed in this phase, secondary structure and tertiary structure elements are still stable based on Raman spectra.

c) The second aggregation phase is in the range from 75 °C to 81.5 °C (duration about 6.5 K).
This aggregation phase starts between the two melting temperatures of the molecule (DSC and ITF). At an average unfolding portions of 67 % (based on intrinsic tryptophan fluorescence), the small aggregates/partially unfolded monomers interact with each other in a continuous second growth phase forming larger particles that are detectable with RALS 473 nm. As a **concentration dependency** was detected in the same temperature range, aggregation including single (partially unfolded) monomers is suggested. Based on DSC data the first part of the second unfolding **transition represents the Fab domain and later part the CH3 unfolding**. As the aggregation start is detected in the beginning of the second transition Fab unfolding plays a crucial role for that aggregation phase. Over the complete phase, however, further ongoing unfolding is detected up to 92 % leading finally to a complete collapse of the system. This hypothesis is underlined by SwitchSENSE® results. Close to the Tagg (RALS 473 nm), SwitchSENSE® detected the molecules melting temperature. That means that half of the molecule underwent unfolding (theoretically that means CH2 and partially Fab domain). Further unfolding of the CH3 domain lead finally to the **loss of secondary structure and detectable changes in the tertiary structure** (Zetasizer Helix). Interestingly, secondary structure changes occurred about 1 K before changes in the tertiary structure markers suggesting a direct connection between these changes. A final collapse of the whole structure and the consequent aggregation was detected as Tagg (back-scattering Prometheus) meaning start of the third aggregation phase. A cooperative effect of Fab and CH3 domain is suggested.

d) The third aggregation phase is in the range from 81.5 °C to 95 °C (duration about 13.5 K).
After the structural collapse of the molecule above 79 °C, ongoing aggregation processes are hard to describe. In this phase, a **mixture of structured and random aggregation** might be the case. Such processes are **hardly predictable** by known aggregation mechanism models. At a temperature of 85 °C complete unfolding is detected. The late second melting temperature by DSC describes not only the energetics of unfolding but also of aggregation processes.

For mAB1, a direct connection/correlation between the unfolding and aggregation processes over the complete temperature ramp is highly suggested. It can be assumed that continuous unfolding triggers continuous aggregation. The unfolding process dominates/influences the aggregation process over the whole process. This assumption is supported by the continuously increase of unfolded portions over the increasing aggregation parameters and the unfolded state at the aggregation start: Compared to the other two mABs, mAB1 showed the longest phase of lower scattering intensity (RALS at 266 nm). During this phase, however, fast unfolding appeared with about 9 % per K. The late back reflection aggregation start indicates that the total aggregation process (over 11 K) consisting of two slow aggregation phases showed the lowest kinetics. The fact that the specific determined Tms occurred over a temperature range of 4 K and 8 K, respectively, underlines also a slow unfolding process over the temperature range.

Further properties of the aggregation process may be that

- the final irreversibility is caused by the unfolding of the Fab domain leading to a structural collapse (refolding experiments suggested the hypothesis).
- based on chemical denaturation results and kD value the mAB1 suspension showed a higher tendency to aggregate already in low temperature ranges without detected unfolding.
- Interaction of (partially and native) monomers is describable over the complete temperature range.
- The aggregation process is well describable up to the point of structural collapse as it demonstrates a slow aggregation process
- It is an unfolding-driven aggregation

Summarizing the temperature ramp experiments, the induced aggregation process/kinetics are characterized by a slow unfolding in correlation to slow aggregation. The aggregation-rate determining step may be the unfolding step. In case of mAB1, the temperature ramp is a suitable approach for stability predictions.

Discussion of a potential aggregation process of mAB2:

a) The pre-aggregation phase for mAB2 is in the range from 25 °C to about 70 °C (duration about 45.5 K).

In contrast to mAB1, structural changes of mAB2 are detected by ITF and SwitchSENSE® before the detected unfolding start (from 25 °C up to 60 °C). During this phase, the switching speed

deceased indicating a “growth” of the molecule. At the same time, the ITF ratio 350 nm /330 nm increased caused by changes in the tryptophan surrounding from hydrophobic to hydrophilic (0.6% per Kelvin). Both observations suggest the compact expand of the molecule loosening the dense structure and enable water molecules to reach also hydrophobic areas in the molecule. Possibly a hydration shell is built. Starting at 60 °C, significant unfolding of the monomers is detected by increasing switching speed. This unfolding process is also detected as an exothermic reaction (DSC) in the same temperature range (61°C), but without changes in the hydrophobic patches (tryptophan environment). Unfolding processes caused changes in the hydrophobic areas starting at 65 °C and until aggregation is detectable, the average unfolding portion reached about 30 % (based on ITF). During this pre-aggregation phase, the major part of the first unfolding transition describing mainly changes in the CH2 domain happens. In the end of this phase, more than half of the unfolding in the first transition was performed (the first melting temperatures detected by DSC and ITF). Secondary structure and tertiary structure elements, however, are still stable based on Raman spectra. Until the first aggregation start temperature of 70 °C, the interactions of these partially unfolded monomers are still too weak, and the suspension still appeared colloidal stable and no aggregation could be detected.

b) The first aggregation phase of mAB2 is in the range from 70 °C to 72.5 °C (duration about 2.5 K).

Until the first aggregation start temperature at around 70 °C, the interactions of the partially unfolded monomers seemed too weak as no aggregation was detectable with the selected methods. Aggregation, however, was mainly initiated by reaching the first melting temperature. In contrast to mAB1, the mAB2 molecules aggregate faster and continuous fast aggregation leads to larger particles. Even though fast aggregation was observed, unfolding appeared slow and during the first short aggregation phase the unfolding portion increased only from 33 % up to 45 %. In this case, the aggregation is caused by changes in the CH2 domain. As amplifying factor, a cooperative unfolding effect of CH2 and Fab domain may be suggested. The detected initial aggregation signal at a wavelength of 255 nm and DLS occurred as the most sensitive signal. Only small aggregates and in low amounts may be present as scattering is only observed with the smaller wavelength. The further increasing signal may have two reasons depending on the underlying mechanism: (1) increasing amounts of small particles occur and give a signal at the larger wavelengths by reaching a sufficient concentration (enrichment of small particles summing up the scattering signal) leading

further to a sudden collapse or (2) continuous growth on few nucleus lead to the signal leading to larger particle. Based on the fast process the determination of the underlying mechanism is difficult, but as a fast collapse was observed and low changes in the structure were detected the first hypothesis may apply. Even though aggregation and further unfolding was observed in this phase, secondary structure and tertiary structure elements are still stable based on Raman spectra.

c) The second aggregation phase is in the range from 72.5 °C to 78.5 °C (duration about 6 K).
The second aggregation start (RALS 473 nm) occurred faster as for mAB1. During this phase unfolding proceeds slowly from 45 % to about 62 % (based on intrinsic tryptophan fluorescence). For mAB2, the **loss of secondary structure and detectable changes in the tertiary structure** (Zetasizer Helix) was detectable in this phase, already at low unfolding portions. As a **concentration dependency** was not detected, aggregation is not primary depending on the addition of single (partially unfolded) monomers for continuous growth. The dependency on the heat rate, however, indicated that the aggregation processes control the unfolding process. The collapse of the structure triggered further aggregation and increased aggregation process leading finally to increased light scattering due to larger aggregates at Tagg (back-scattering Prometheus). Structural correlation, such as specific domain dependency is not detectable as the dominant process is the aggregation.

d) The third aggregation phase is in the range from 78.5 °C to 95 °C (duration about 16.5 K).
The ongoing aggregation is hardly predictable. Similar to mAB1, in this phase, **a mixture of structured and random aggregation** might be the case. Such processes are **hardly predictable** by known aggregation mechanism models. The determined melting temperatures in this phase most likely monitor both processes. For that reason, this parameter is not in all cases suitable to evaluate conformational stability.

For mAB2, a direct connection/correlation between the unfolding and aggregation processes is only suggested considering the aggregation start initiation. It can be assumed that an initial unfolding event triggers the aggregation start but afterwards aggregation process dominates with less influence by the unfolding process. This assumption is supported by a slower unfolding rate compared to fast aggregation after aggregation started. The lower changes in the average unfolded portion of 33 % to 61 % at the different aggregation starts underline this assumption. Compared to mAB1, mAB2 showed a shorter phase of lower scattering intensity (RALS at 266 nm). During this

phase the unfolding appeared slower with about 6 % per K. The aggregation kinetics/mechanism, however, leads to a faster formation of particles reaching a sufficient light scattering signal to be detected by RALS at 473 nm. The earlier back reflection aggregation start indicates that the total aggregation process (over 8 K) consisting of two faster aggregation phases. The fact that the specific determined Tms occurred over a temperature range of 3 K and 6 K, respectively, underlines also a slow unfolding process over the temperature range.

Further properties of the aggregation process may be that

- based on chemical denaturation results and kD value the mAB2 suspension showed a lower tendency to aggregate in low temperature ranges
- Interaction of (partially and native) monomers is describable only in the initial aggregation start
- The aggregation process is hard to describe as it demonstrates a fast aggregation process
- it is an aggregation-driven unfolding

Summarizing the temperature ramp experiments the induced aggregation process/kinetics are characterized by a slow unfolding, but a faster aggregation process. The aggregation rate determining step may be the aggregation step. In case of mAB2, the temperature ramp may be not the most suitable approach for stability predictions.

10.2.3. Thermal induced aggregation studies mAB1, mAB2 and mAB3: Isothermal aggregation studies

The investigation of aggregation processes at a fixed temperature, e.g. as a long-time storage stability at 4 °C and 25 °C, helps to understand the underlying aggregation mechanism and to potentially predict the product stability (shelf life). For the three model systems, depicted results of chapter 10.2.1 have been summarized to identify a suitable incubation temperature enabling short-term studies (Table 18).

Table 18: Isothermal incubation of the model systems: Summary of characteristic parameters considering thermal stability.

	mAB1	mAB2	mAB3
Unfolding start (ITF)	66 °C	66 °C	65 °C
Tm 1(ITF)	72 °C	71 °C	70 °C
Tm 2 (ITF)	81 °C	82 °C	84 °C
Aggregation start (back reflecting light / RALS 473)	82 °C / 75 °C	79 °C / 73 °C	67 °C / 62 °C
Unfolding state at 75 °C (ITF)	68 %	54 %	76 %
Unfolding state at 65 °C (ITF)	No unfolding	21 %	No unfolding
Unfolding state at Tagg (ITF)	85 %	61 %	12 %

The models systems of mAB1 and mAB2, showed similar stability characteristics. ITF unfolding started at 65 °C and two melting points have been detected at about 70 °C and 80 °C. The start of aggregation was determined above 78 °C. For that reason, the temperature of 75 °C was chosen for an isothermal stability study. At this temperature, both mABs showed a lower unfolded portion as it was the case at the determined Tagg. Interestingly, the A330/A350 ratio of mAB1 indicates a higher portion of unfolding state compared to mAB2, but mAB1 showed a higher aggregation temperature (based on thermal ramp experiments).

In a first step, isothermal incubation at 75 °C was performed for 120 h. For the characterization of the aggregation process, the analytical set-up included the methods turbidity measurements, HP-SEC, DLS, MFI, LUMiSizer and visual inspection and is illustrated in Figure 3- 50. Samples have been taken for analysis at following time points: 0 h, 1 h, 3 h, 5 h, 7 h, 24 h, 72 h and 120 h.
Based on the technical requirements and limitations an analysis of the samples was not possible at each time point with all techniques. The same set-up was tested for mAB3. At the defined set-up, however, the aggregation process was too fast (about 7 min) for analysis in the second step.

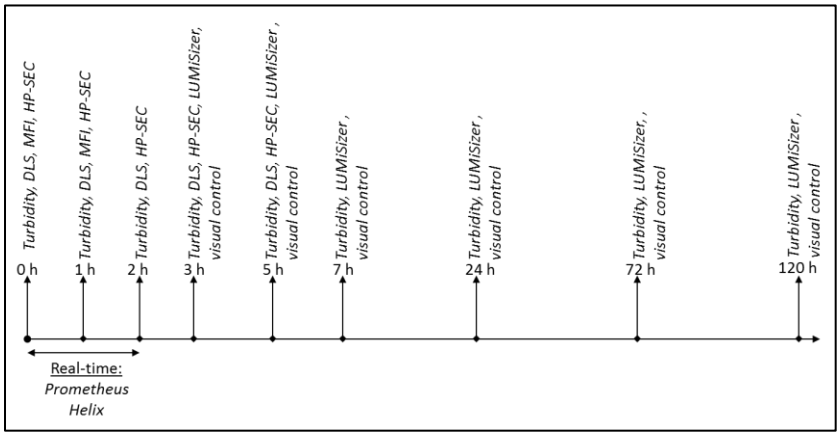

Figure 3- 50: Isothermal incubation model mAB systems: Overview applied techniques for the first approach. In a first approach, the model systems have been incubated at 75 °C for 120 h. At the depicted time points a sample was pulled and analyzed using the mentioned methods. In a further step, a real-time analysis was performed over the first incubation period (2 h to 5 h).

Turbidity measurements demonstrated at a first glance differences between the two mABs. Both mAB suspensions showed low start A320 turbidity values of about 0.1. The turbidity of mAB1 suspension increased fast from 1 h to 3 h incubation up to an A320 value of 1.7 but after 7 h incubation the turbidity decreased again down to 0.2. Subsequently, the turbidity increased continuously up to 1.5 after 24 h and further up to 2.2 after 72 h incubation. After a total incubation of 120 h no further turbidity increase was detectable. The described turbidity behavior of mAB1 was confirmed by triplicate measurements. The turbidity of mAB2 increased continuously over the whole incubation time. Within the first 7 h only low turbidity increase below 1.0 was observed. Between 7 h and 24 h the turbidity increased fast up to 2.6 (Δ~1.6). Within the last 96 h turbidity increased slower up to finally 2.75 (Δ~0.15).

For the mAB1 approach, ***SEC measurements*** monitored the increasing presence of soluble aggregates and the decrease of monomer content and total protein concentration until 3 h. Afterwards, 100 % protein loss was detected at the 5h time point, and SEC measurements could not be performed anymore. For mAB2, no soluble aggregates were detectable, and 100 % protein loss was already detected after 3 h incubation.

DLS results of mAB1 showed an increase in polydispersity and a slight z-average increase after 1h incubation. Subsequent a strong increase up to 4 µm was observed after 3 h and 5 h. Further measurements at later time points were not possible due to multiple scattering and high polydspersity/heterogenicity of the sample (high PDI values; software indicated low quality of the fitting curve). The DLS results of mAB2 showed similar tendencies as mAB1. The final z-average

after 5 h was higher (about 10 µm). Afterwards no reliable measurements were possible due to low data quality.

MFI measurements of undiluted samples were only possible until 1 h due to fast particle content increase and high particle concentrations (reaching particle concentration limit). After 1 h, for mAB1 a particle concentration between 1 µm and 100 µm of 1.6 10^7 particle/ml was detected. For mAB2, a particle concentration of 10^4 particle/ml in the same size range was determined.

The used techniques showed limitations already before the end of the experiment either due to concentration or due to size limits. For that purpose, the visual analysis in combination with the LUMiSizer analysis complemented the previous techniques as the turbidity of the first time points occurred too low, but later time points were analyzed.

LUMiSizer® analysis. The transmission profile fingerprints and the visual evaluation of the mAB1 suspensions before LUMiSizer analysis were summarized in Figure 3- 51. The homogeneous turbid sample after 3 h incubation showed a transmission of 78 % enabling sedimentation velocity evaluation. As seen in the pictures no particles adhered to the cuvette walls. With ongoing incubation, the suspension became clear and contained larger visible white aggregates that tended to adhere to the cuvette walls. This phenomenon is monitored in the rough transmission profiles after 5 h and 7 h. In particular, the particle appearing after 5 h tend to stick to the cuvette wall (hydrophobic surface). For all time points after 7 h, a continuous increase in turbidity was observable visually and the homogenicity of the particle distribution increased. At the same time, the presence of larger particle/ flakes decreased. Starting with the 72h sample the sedimentation profiles became evaluable. The sedimentation velocity distributions as well as the velocity median and the instability index have been determined (Figure 3- 53). The 3 h sample contained the particle with the smallest velocity median, but a similar instability index as the samples after 72 h and 120 h. Except for the 5 h and 7 h sample, the median increased and the larges median velocity showed the particle in the 120 h sample. Remarkably, the sample after 24 h has a lower instability index as the other samples. All velocity distributions monitored a broad range from 1 µm/s to 1000 µm/s. There was a shift observable as the 1 µm/s to 10 µm/s portion became smaller over time and the 100 µm/s to 1000 µm/s became larger.

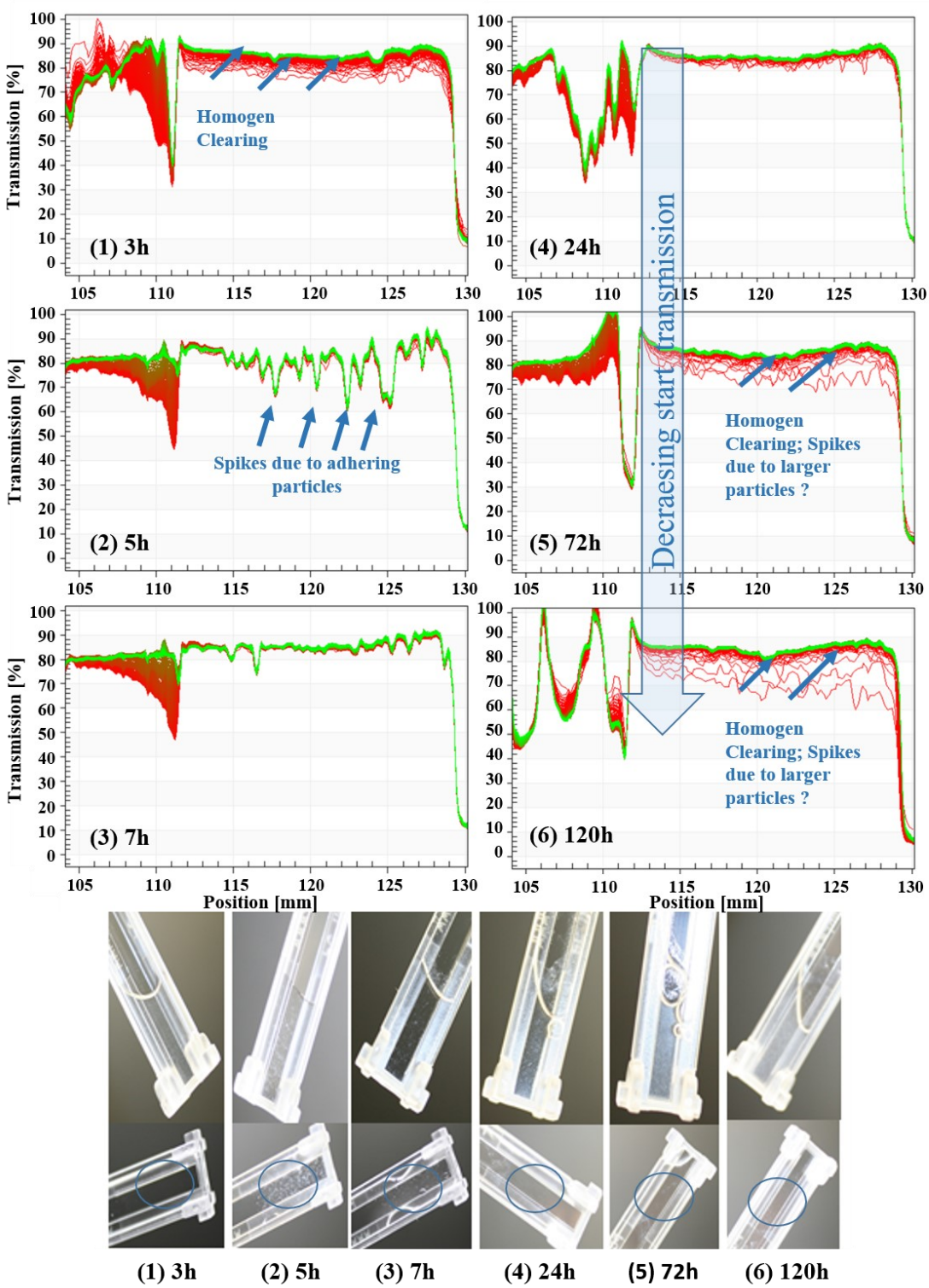

Figure 3- 51: Isothermal incubation mAB1: LUMiSizer® results first approach.
The mAB1 suspension was incubated at 75 °C for 120 h. At the time points 0 h, 0.5 h, 3 h, 5 h, 7 h, 24 h, 72 h and 120 h a sample was analyzed. For LUMiSizer® analysis sufficient turbidity/transmission was reached after 3 h. The fingerprints of each time point are illustrated in the upper part. Blue arrows highlight characteristics. The lower part shows photos of the samples in the rectangular PC cuvettes: upper level shows suspension in upright position, lower level shows cuvette after liquid removal (enable visual detection of adhering particle).

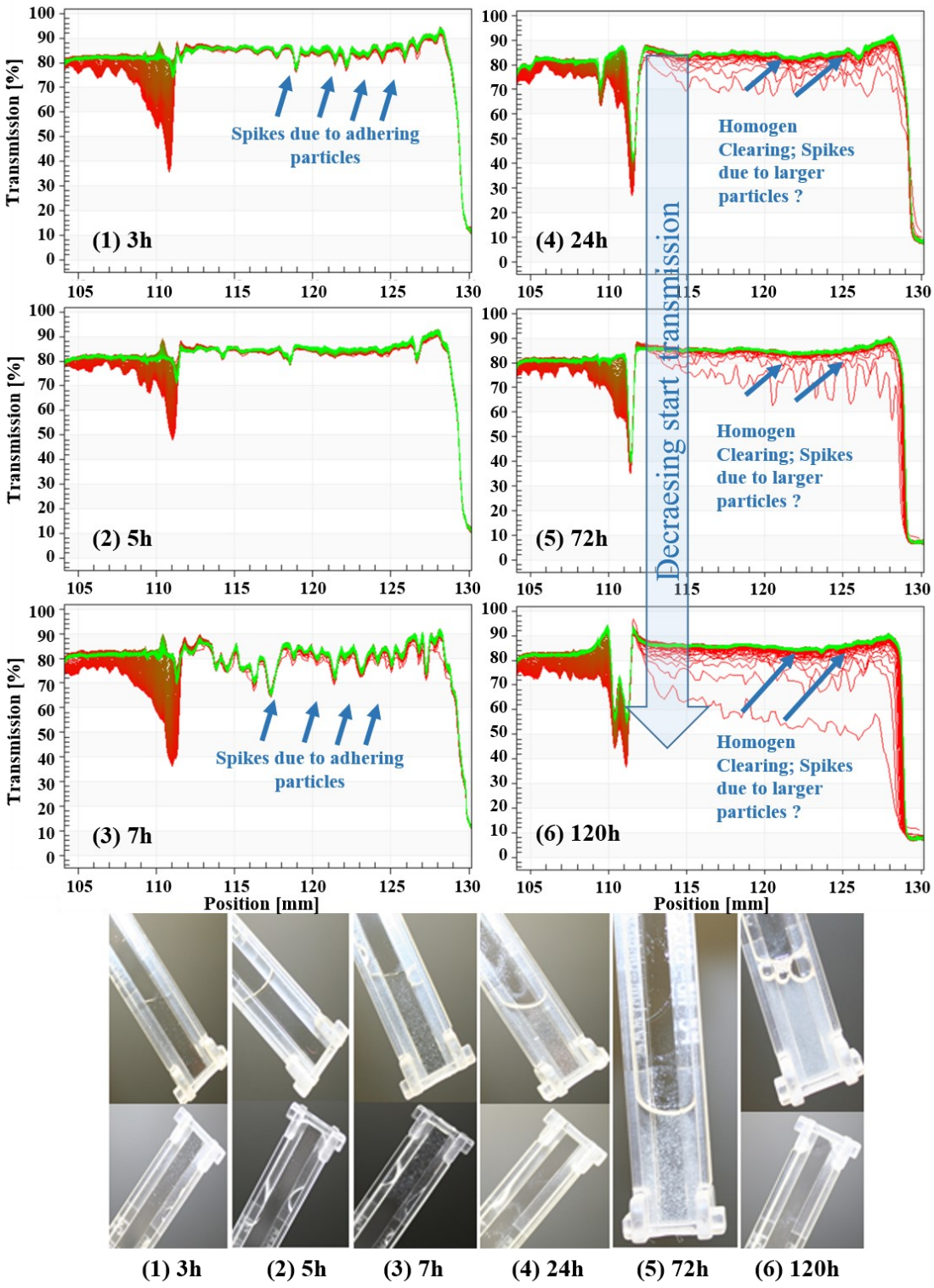

Figure 3- 52: Isothermal incubation mAB2: LUMiSizer® results first approach.
The mAB1 suspension was incubated at 75 °C for 120 h. At the time points 0 h, 0.5 h, 3 h, 5 h, 7 h, 24 h, 72 h and 120 h a sample was analyzed. For LUMiSizer® analysis sufficient turbidity/transmission was reached after 3 h. The fingerprints of each time point are illustrated in the upper part. Blue arrows highlight characteristics. The lower part shows photos of the samples in the rectangular PC cuvettes: upper level shows suspension in upright position, lower level shows cuvette after liquid removal (enable visual detection of adhering particle).

In comparison, the transmission profile fingerprints and the visual evaluation of the mAB2 suspensions before LUMiSizer analysis were summarized in Figure 3- 52. The samples after 3 h and 5 h appeared as clear samples with small amounts of visible particles (spikes?). The transmission profile fingerprints showed slightly rough profiles without a clearing over the centrifugation process. As seen in the photos, no particles adhered to the cuvette walls. In contrast, the sample after 7 h incubation appeared clear, but contained larger visible white aggregates that tended intensively to adhere to the cuvette walls. This was monitored in the rough profiles. Similar to mAB1, at each time point after 7 h a continuous increase in turbidity was observable, but the adhering effect remained. However, the sedimentation profiles were evaluable. The sedimentation velocity distributions as well as the velocity median and the instability index have been determined (Figure 3- 53). The 7 h sample contained the particle with the smallest velocity median that was detected. The velocity median showed lower values than the ones of mAB1 median after the same time.

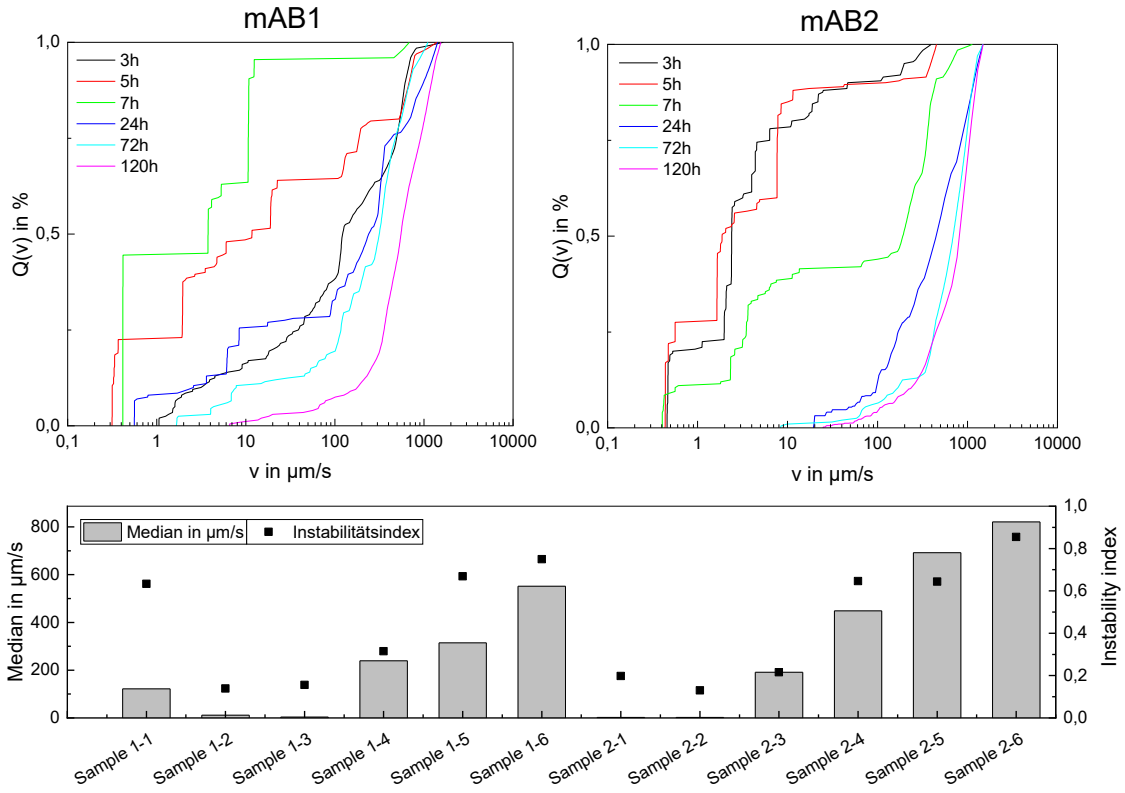

Figure 3- 53: Isothermal incubation model mAB systems: Summary LUMiSizer® results first approach. Sedimentation velocity distributions of the investigated time points after 3h, 5h, 7h, 24h, 72h and 120h incubation at 75°C.

With ongoing incubation time, the median increased faster than the mAB1 suspension and reached a final velocity median of 800 µm/s after 120 h incubation. The suspension instability index stayed constant low until the 7 h sample, were similar for the 24 h and the 72 h samples and the 120 h occurred as the last stable suspension. All velocity distributions showed a broad velocity range. This range was shifted over time to higher velocity ranges.

In the further approach, the initial aggregation phase was analyzed as real-time approach using Prometheus NT and the Zetasizer Helix.

Prometheus measurements. For that purpose, all three mABs were incubated in the Prometheus device at 75 °C for about 3 hours and the unfolding process as well as the scattering signal was reported in real-time (Figure 3- 54).

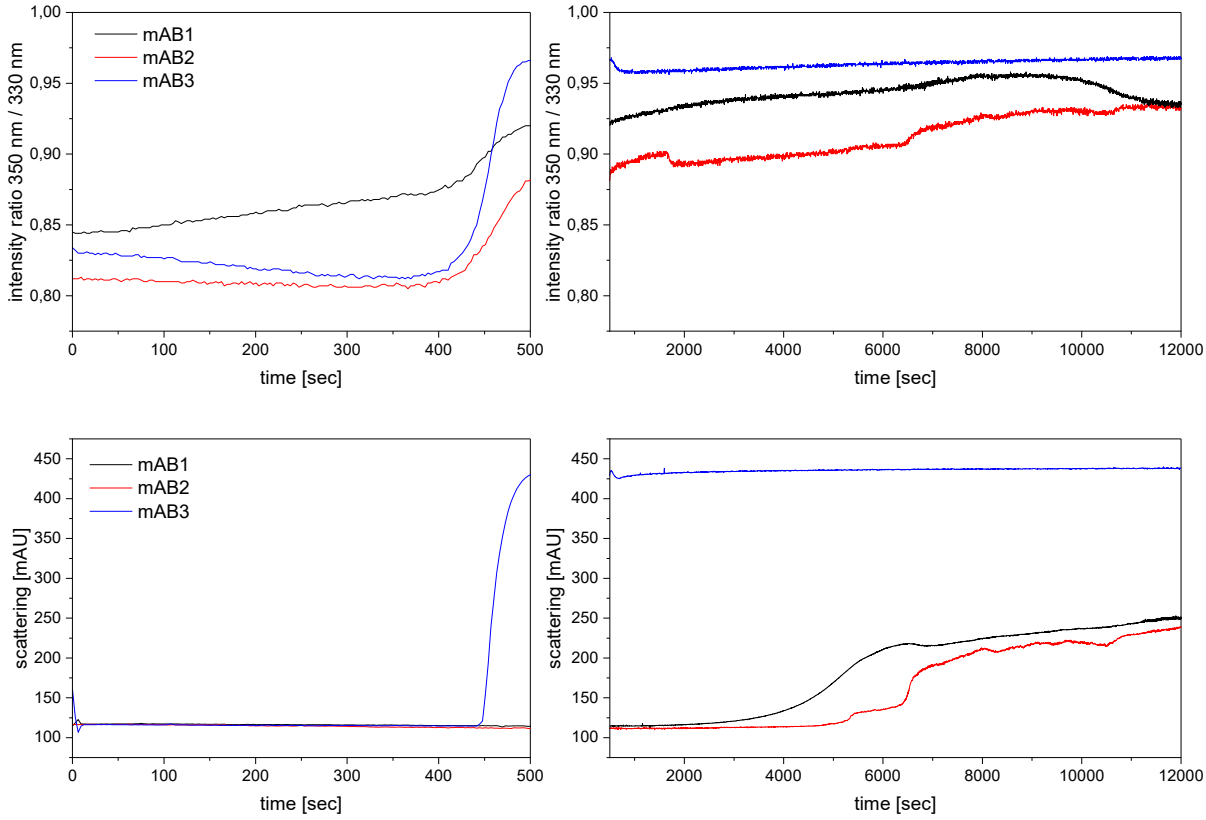

Figure 3- 54: Isothermal incubation model mAB systems: Real-time analysis Prometheus at 75 °C.
The Prometheus NT instrument was used to check the incubation temperature of 75 °C and estimate unfolding and aggregation durations. The upper graph illustrtes the fluorescence intensity ratio 350 nm/330 nm representing the protein unfolding curve. The lower graph is the monitoring of the backscatter signal representing the aggregation-indicating signal.

All three mABs started unfolding within the first 500 sec that represented the heating phase from 25 °C to 75 °C. In this phase, only mAB3 reached the final unfolding value. The unfolding process of mAB1 and mAB2 continued until the end of the experiment. The Tagg of mAB3 was detected in the heating phase below 500 sec (7.5 min). The Tagg of mAB1 and mAB2 were detected after 4000 sec. In result, the initial experimental set-up with 75 °C is therefore suitable for mAB1 and mAB2 but had to be adjusted for mAB3.

In a second experiment series, Prometheus measurements have been performed with adjusted sample preparation enabling isothermal incubation up to 20000 sec. Incubation temperatures of 55 °C, 65 °C, 70 °C, 75 °C, 77 °C and 80 °C have been tested and the results were summarized in Figure 3- 55. The graph illustrates the aggregation start (Tagg), i.e. the time point during the isothermal incubation at which the aggregation started, as function of the incubation time. For mAB3 at all tested temperatures, aggregation starts were detectable. The optimal temperature range for mAB3 to perform isothermal aggregation studies, i.e. with a sufficient duration to enable real-time analysis but not a too long duration to avoid evaporation and air bubbles was determined from 55 °C to 65 °C. In contrast, for mAB1 and mAB2, aggregation was not detected with this set-up before 75 °C to fulfill the mentioned technical requirements.

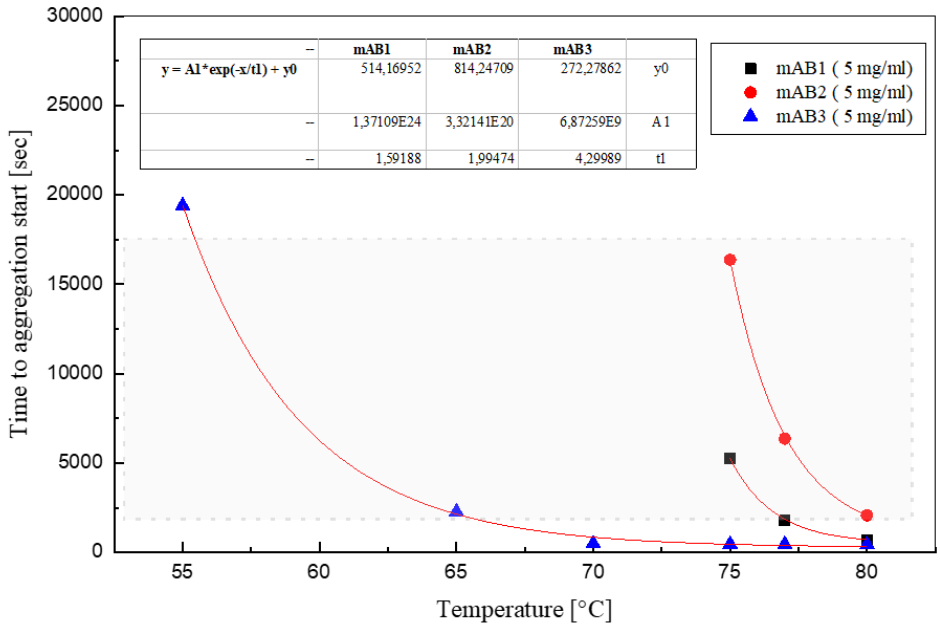

Figure 3- 55: Isothermal incubation model mAB systems: Correlation incubation temperature and aggregation time (Prometheus NT).

Out of isothermal experiments at 55° C, 65 °C, 70 °C, 75 °C and 80 °C using the Prometheus NT aggregation starts were determined for each mAB and a correlation was visualized to estimate suitable aggregation time and respectively experiment running times.

The achieved fitting functions describing the relation between incubation temperature and the aggregation time are shown in the upper table of the graph. These functions confirm that aggregation times of mAB1 (65 °C; ~704 h) and mAB2 (65 °C; ~650 h) are too long for a real-time experimental approach. Based on the aggregation times the most stable mAB was mAB2 and the least stable mAB3. In addition, the curve of mAB3 differs from the other two curves.

Zetasizer Helix measurements. The results of real-time experiments at 75 °C for 2 hours performed by the Zetasizer Helix were summarized in in chapter 9.1.2 (Figure 3- 25, Figure 3- 26 and Figure 3- 27).

For mAB1, the two-hour incubation at 75 °C led to a continuous increase in z-average and PDI values indicating a continuous aggregation process. The Raman spectra, in contrast, did not show significant changes. In addition to the shown results, Figure 3- 56 illustrates the calculated size distributions (intensity- and volume-weighted).

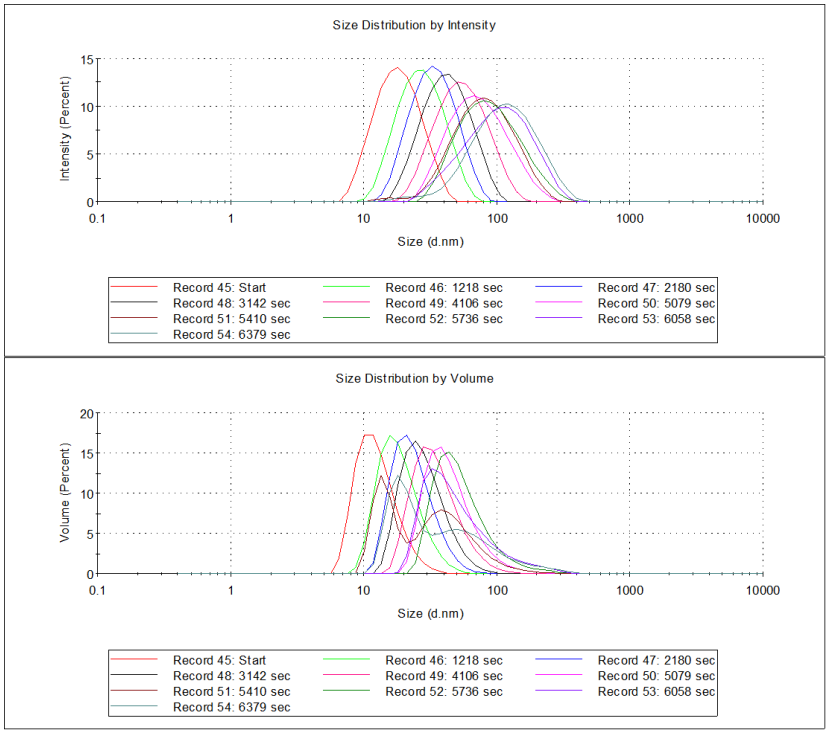

Figure 3- 56: Isothermal incubation mAB1: Zetasizer Helix results at 75 °C.
The mAB1 suspension was incubated for 2 h at 75 °C. The resulting z-average values over time are shown in Figure 3- 25. In this figure an overlay of the resulting DLS data is shown as the intensity-weighted and the volume-weighted size distributions.

The constant increase in size of one particle population up to about 6000 sec. Later on, a second population was resolved, in particular, applying the volume-weighted size distribution model (lower graph). This volume-weighted size distribution indicated one population (increasing) in the range between 10 nm and 20 nm and a second population from 40 nm up to above 100 nm.

For mAB2, the two-hour incubation at 75 °C led to an initial continuous increase in z-average and PDI. After about 50 min the correlogram elapsed and DLS analysis was not reliable and applicable anymore. The evaluation of the Raman spectra showed significant changes in the secondary and the tertiary structure (Figure 3- 27 and Figure 3- 57).

Due to the fast aggregation process at 75°C, that was hard to analyze, additional isothermal incubation experiments at 65 °C were performed over 2 h and overnight to lower aggregation velocity. In contrast to the incubation at 75 °C, the correlogram did not elapse over the tested time periods. The z-averages and the PDI values, however, increased over time indicating ongoing aggregation processes. The Raman spectra indicated only minor changes in secondary and tertiary structure.

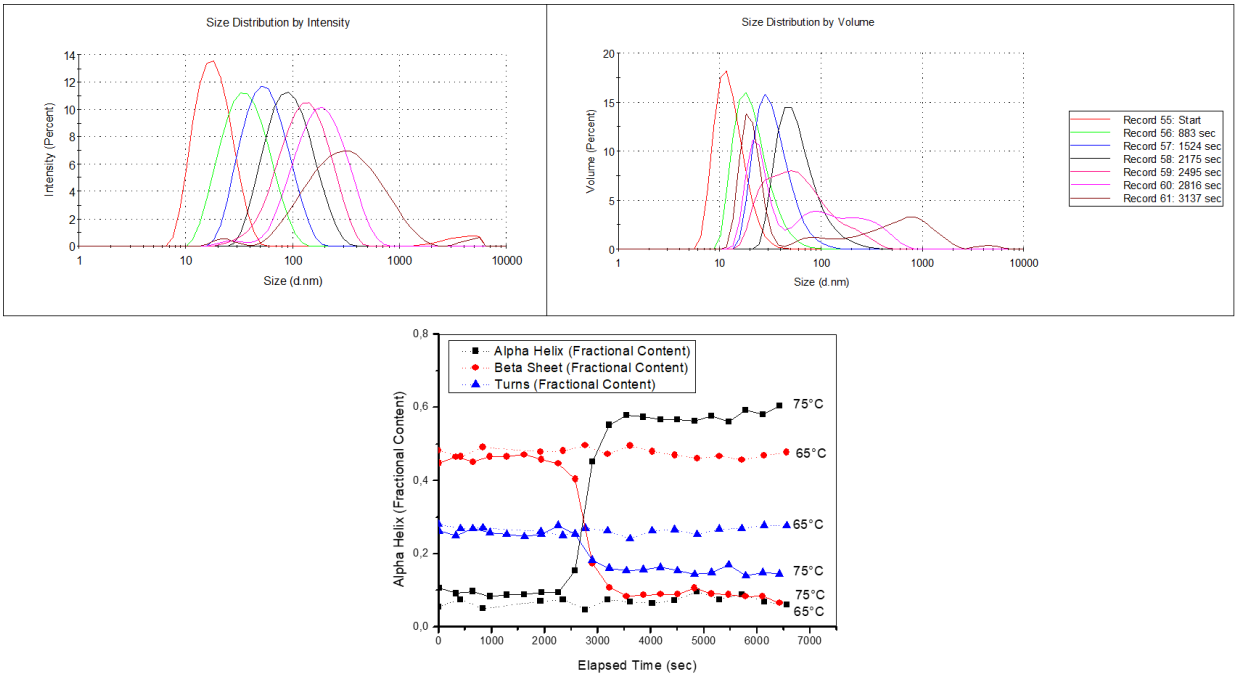

Figure 3- 57: Isothermal incubation mAB2: Zetasizer Helix results of 2 hour incubation at 75 °C and 65 °C. Two isothermal incubation experiments investigating mAB2 have been performed: a) incubation for 2 h at 75 °C and b) incubation for 2 h at 65 °C. In the upper part the intensity-weighted and the volume-weighted size distributions are illustrated for the first 50 min of the 75°C incubation. DLS results of 65°C incubation are not shown. In the lower graph, the resulting Raman spectra have been evaluated for secondary and tertiary structure markers. The upper graph represents the secondary structure elements over the incubation time at the both incubation temperatures. The four lower graphs illustrate tertiary structure markers as well as the disulfide band over the 2 h incubation.

The incubation over 2 h led to minor increases of the z-averages from 11 nm to 15 nm and PDI values from 0.02 to 0.12. Based on the Raman spectra no significant changes were determined in the secondary and the tertiary structure (Figure 3- 57).

The results of the isothermal incubation at 65°C overnight were summarized in Figure 3- 58. The DLS results showed a linear increase in the z-average with a slope (aggregation velocity) of 0.6 nm/h. The PDI values increased non-linear up to 0.2. Secondary structure marker showed only minor changes comparing first and last values of alpha helices (increasing) and beta sheets (decreasing) highlighted by the dashed circles. Out of the tertiary structure markers only minor changes were detected in the tyrosine intensity ratio (857 cm^{-1}/ 831 cm^{-1}). The decrease of the ratio indicated more buried tyrosines over time.

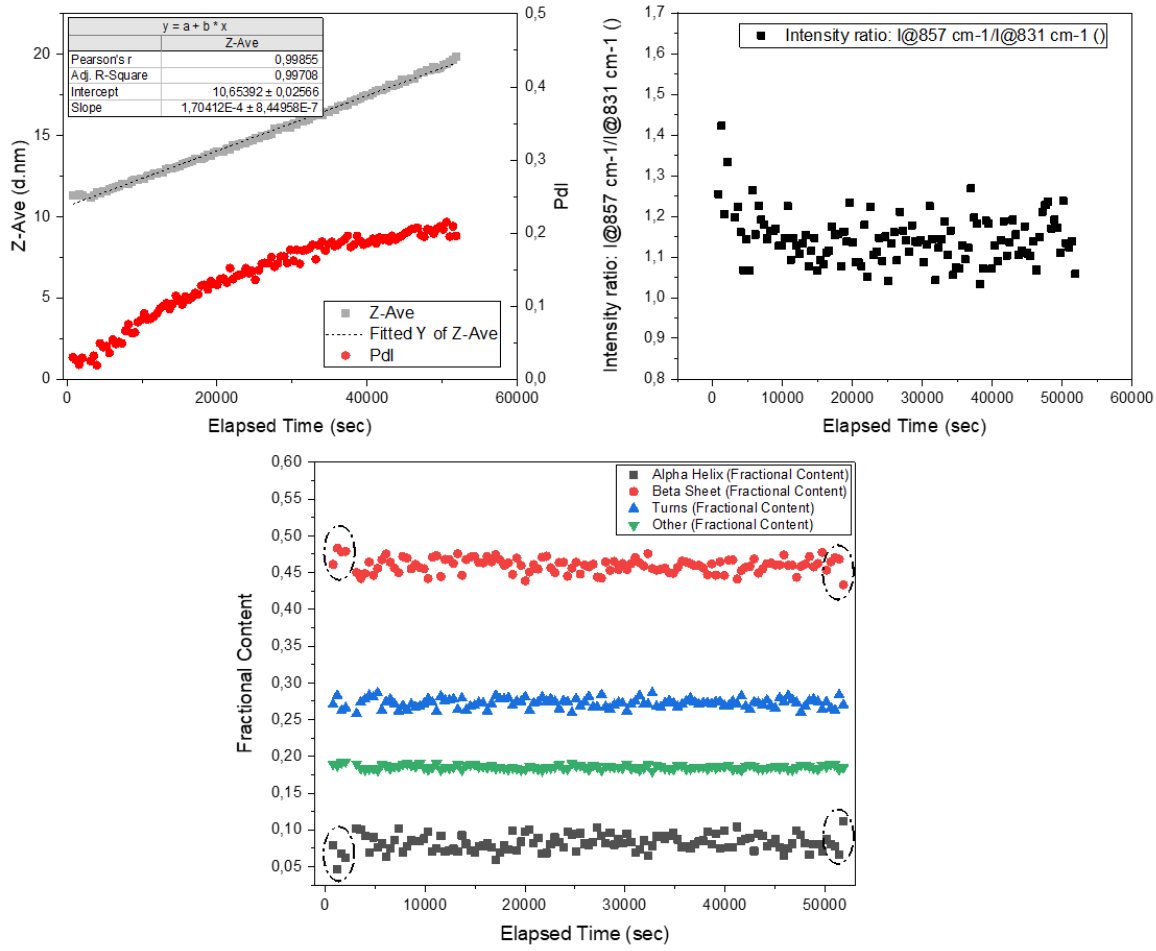

Figure 3- 58: Isothermal incubation mAB2: Zetasizer Helix results of incubation at 65 °C overnight.
The mAB2 suspension was incubated at 65 °C overnight. The resulting z-average and PDI values over time are shown in the upper left graph. For the z-average data a linear fit was performed as indicated in the table. The upper right graph illustrates the progress of the tyrosine marker (857 cm^{-1}/ 831 cm^{-1}) in the Raman spectra over time. In the lower graph the progress of the secondary structure elements over the incubation time are represented.

For the investigation of the mAB3 aggregation process during isothermal incubation, Helix experiments at lower temperatures have been performed: mAB3 suspensions have been incubated at 55 °C, 60 °C and 65 °C overnight (for about 14 h). Based the DLS results, aggregation was detectable as the increase of the z-average (Figure 3- 59). The investigated process showed up to three phases: (1) a first phase of slow size increase up to a z-average of about 20 nm to 30 nm, (2) a second phase in which a sudden strong size increase was observable and (3) a third phase reaching a constant size (plateau). Depending on the incubation temperature, each phase varied in the duration and in the final z-average.

At 55 °C the first phase took about 21000 sec, the second phase about 9000 sec and the third phase about 20000 sec. The final size (z-average) in the third phase was about 800 nm. The investigation of secondary structure markers based on the recorded Raman spectra showed no significant changes during the complete incubation time (Figure 3- 60). The portion of alpha helices and beta sheets was detected with 30 % each, the portion of turns was detected with 15 %. This ratio differed from the composition detected at 25 °C (Table 13).

At 60 °C the first phase took about 9000 sec, the second phase about 7000 sec and the third phase about 35000 sec. The final size (z-average) in the third phase was about 3000 nm. Initially in the first phase (until 10000 sec) the portion of alpha helices was detected with 10 %, the portion of beta sheets was detected with 45 % and the portion of turns was detected with 25 %. The start ratio agreed to the composition detected at 25 °C (Table 13). In the second phase (until 15000 sec) the portion of alpha helices increased while the portions of beta sheets and turns decreased. In the third phase constant values for alpha helices (25 %), beta sheets (40 %) and turns (15 %) appeared. The highest portion was still beta sheets.

At 65 °C the first phase took less than 2000 sec, the second phase about 10000 sec and the third phase about 40000 sec. The final size (z-average) in the third phase was about 4000 nm. Initially in the first phase (until 2000 sec) the portion of alpha helices was detected with 10 %, the portion of beta sheets was detected with 45 % and the portion of turns was detected with 25 %. The start ratio agreed to the composition detected at 25 °C (Table 13). In the second phase (until 12000 sec) the portion of alpha helices increased while the portions of beta sheets and turns decreased. In the third phase constant values for alpha helices (50 %), beta sheets (20 %) and turns (19 %) appeared. The highest portion finally was alpha helices sheets.

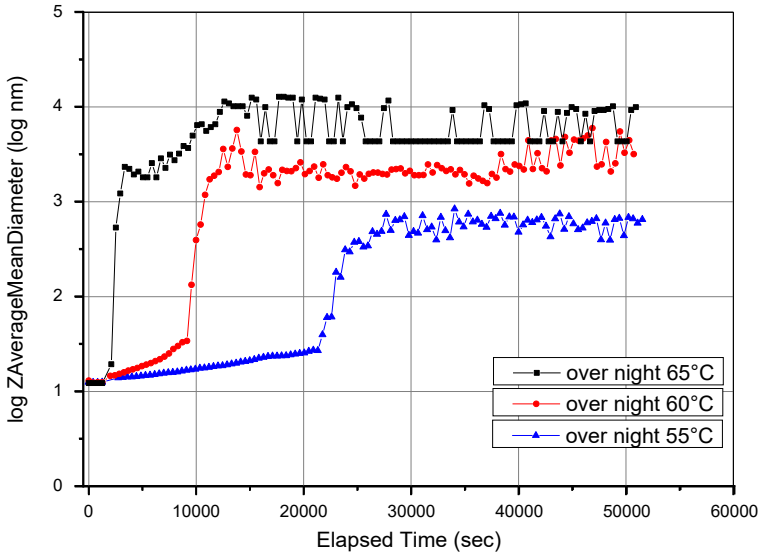

Figure 3- 59: Isothermal incubation mAB3: Zetasizer Helix results DLS.
The mAB3 suspension was incubated over night at 55 °C, 60 °C or 65 °C. The resulting z-average values over time are shown.

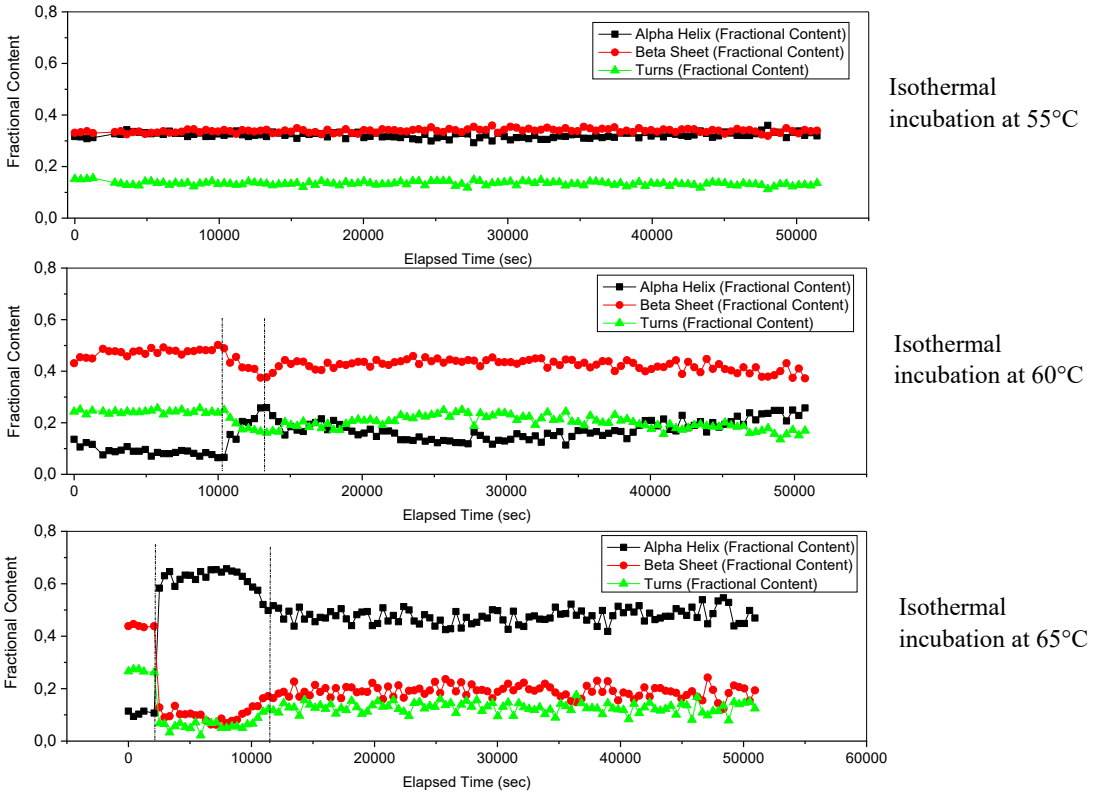

Figure 3- 60: Isothermal incubation mAB3: Zetasizer Helix results secondary structure.
The mAB3 suspension was incubated over night at 55 °C, 60 °C or 65 °C. The resulting Raman spectra have been captured and characteristic marker for secondary structure have been evaluated over time.

10.2.4. Discussion aggregation processes during isothermal incubation

Isothermal aggregation studies for mAB1 and mAB2 have been performed at 75 °C taking a closer look into the differences in the aggregation mechanisms of mAB1 and mAB2. The only method covering the complete incubation time of 120 h was turbidity measurement. SEC, DLS and MFI measurements could only be performed in the first 3 h to 5 h. The LUMiSizer analysis as complementary technique was the only particle detection method applicable after 5 hours due to principle limitations. In addition, a real-time description was performed for the first 3 h, respectively 2 h, by Prometheus and Zetasizer Helix.

For both mABs multi-step non-native aggregation occurs over time, but both proteins seem to differ in their aggregation mechanisms and kinetics. Aggregation mechanisms have been recently summarized and show a great variety (Philo and Arakawa 2009, Wang, Nema et al. 2010, Roberts 2014). In most cases, in particular around a neutral pH, the aggregation mechanism is most likely a combination of nucleation-dominated (ND), chain polymerization (CP) and association polymerization (AP) (Li, Ogunnaike et al. 2010, Barnett, Qi et al. 2015).

Based on the presented results the aggregation of mAB1 and mAB2 may be explained as following: Up to 1 h incubation, the mABs show a similar process for turbidity measurements and particle size by DLS as both values increase slightly. In both suspensions, an increase of small well-distributed particles - low molecular weight aggregates – appear. The SEC results confirm these results but indicate a first difference as the process of mAB2 seems to progress faster (similar to temperature ramp experiments).

Interestingly, mAB1 shows already a significant higher increase in particle concentrations larger than 1 µm from 1x 10^4 to 1x 10^7 particle/ml. Within these first hours ongoing unfolding led to aggregation start and a larger population in the submicron size range. At this point, mAB1 might already undergo significantly CP or AP. In addition, the hydrophobicity of the molecule increase (I850/I830). The present aggregation process is connected to the unfolding process and happens parallel resulting in hydrophobic particles. After 3 h, mAB1 showed an intensive increase in turbidity in an apparently homogeneous suspension. Lumisizer measurements detected a polydispers population containing large particles with a mean sedimentation velocity of 100 µm/s (~440 µm) as result of CP and/or coalescence. After 5 h the aggregates seem to reach a threshold at which coalescence appeared rapidly and phase separation occurred in a colloidal fluctuation manner. However, the fast collapse caused an intensive decrease in turbidity. These large

aggregates showed differed surface properties as they interacted heavily with the cuvette walls. The aggregates consist mainly of partially unfolded monomers. An explanation for the behavior might be that initially turbidity increases as unfolding takes place and hydrophobic patches drive the aggregation to low molecular weight aggregates. At some point, the ratio of hydrophobic surface is large enough to interact with the hydrophobic surface of the cuvette. This effect disappears afterwards, and continuously increasing turbidity starts with increasing mean sedimentation velocities up to 550 µm/s (~1035 µm). It can be assumed that a combination of CP and AP causes this appearance. The particle growth is ongoing slowly and continuously.

For mAB2, a nucleation-dominated (ND) mechanism seems to be prevalent during the first hour. The particle concentration of mAB2 larger than 1 µm, in contrast, stays constantly the same (about $1x\ 10^4$). Within the first hour, complete structure loss leads to sudden aggregation indicated by the apparent decrease of hydrophobicity. In contrast to mAB1, aggregates consist of monomers that are less unfolded. As soon as aggregation started large particle appeared (noisy signal scattering). During further incubation, turbidity seems to increase constantly, which might be mainly due to CP mechanism. Similar to mAB1, a colloid flocculation occurs, but later after 7h. It is assumed that this is due to a parallel progressing AP mechanism. From 24 h on, aggregation growths of mAB1 and mAB2 appeared again similar, but the final mean sedimentation velocity of the mAB2 sample, considering mainly soluble aggregates, is higher and reaches 800 µm/s (~1250 µm).

In conclusion, mAB1 shows initially a ND mechanism with a fast tendency to AP already after 1h. As shown by Kalonia et al. (Kalonia, Toprani et al. 2016) aggregates resulting from AP show less structural changes. During ongoing unfolding at 75°C, surface properties change at a certain point as hydrophobic patches are presented. Over time, these patches are covered by partially unfolded monomers (CP) or aggregate coalescence (AP). In contrast, the mechanism of mAB2 is dominated by ND and CP. Prior works of Barnett et al. and Brummitt et al. demonstrated that ND and/or CP aggregation mechanisms may be dominant in the early-stage steps. If the aggregate concentration is sufficient, the AP mechanism or aggregate-aggregate coalescence is detectable (Brummitt, Nesta et al. 2011, Barnett, Drenski et al. 2016). This is in coincidence with mAB2 aggregation results. The rapid appearance of aggregate-aggregate coalescence as seen for mAB1 is one extreme case which was also described already (Roberts 2014). In any case, the investigation of the early stage steps, but also of the further aggregation process, showed that the characteristics of final aggregates are hard to predict. In most cases, the early stage steps are the rate-limiting steps. In particular, the

rate of coalescence is highly important to determine the net rate of detection for larger aggregates (Barnett, Drenski et al. 2016). Based on temperature-ramped aggregation studies by DLS mAB1 starts to aggregate later around 79 °C. However, at this point we could show that the occurrence of larger aggregates happens much faster und would be more problematical in consideration of parenteral suspensions. Larger particles show higher potential for vascular blockage and/or unwished immunogenic reactions.

From a technical perspective, isothermal studies showed two challenges: if the process is too fast the aggregation process is hard to describe or if the process is too slow technical problems, e.g. evaporation, lead to false results. For that reason, the isothermal studies over a temperature range are highly suggested. For mAB1 and mAB2, aggregation was detected after about 1000 sec. The main aggregation process is detected between 1000 sec and 7000 sec. A 2 h experiment setting was consequently chosen. Further, the set-up was not suitable for mAB3 as aggregation to the maximal scattering signal was already detected in the heating phase. Lower temperatures are necessary for this mAB. Out of these experiments, correlation functions have been achieved for each mAB. Using the determined correlation, the theoretical time before aggregation starts can be calculated at different temperatures. For mAB1 and mAB2, the correlation is not applicable for prediction at lower temperature, e.g. at 25 °C or 4 °C as unrealistic results were achieved. For mAB3, more realistic results have been obtained at 25 °C with about 8 months. Summarizing the biophysical characterization results, the reason for this discrepancy may lay in the aggregation process. The mAB3 monomers tend to aggregate without unfolding events. Therefore, the obtained correlation may fit better to the mAB3 process. For mAB1 and mAB2, unfolding-aggregation connections need to be further investigated to achieve a better formula to predict aggregation times at a specific temperature also for these molecules.

10.2.5.Further protein aggregation studies mAB3

For preparation of seeding experiments, mAB3 suspensions have been set under harsh conditions applying high temperatures, mechanical stress (stirring), reducing agents and extreme pH values. After termination of stress application, the suspensions have been analyzed by HP-SEC, DLS, turbidiy A320, NTA and MFI. In comparison to unstressed mAB3 suspension, the results are summarized in Table 19.

Table 19: Further protein aggregation studies of mAB3: Characteristics of mAB3 seeds.
After application of the listed stress conditions, the stressed mAB3 suspensions were analyzed bevor the seeding experiments. Results of the seed suspensions are summarized in the table. *Definition of Abbreviations: F = fragment fraction, M = monomer fraction, A = aggregation fraction.*

Stress condition	HP-SEC analysis			Hydrodynamic diameter / nm	A320	NTA particles/mL	MFI particles/mL
	F %	M %	A %				
unstressed	0.00	94.85	5.15	11.0 (PDI:0.042)	0.07	< 1.00 x10^6	4.48 x10^4
temperature	0.00	89.42	10.57	60.0 (PDI:> 0.3)	0.64	> 1.00 x10^9	2.84 x10^6
mechanical stirring	0.00	*94.92*	*5.08*	12.2 **(PDI:> 0.3)**	0.19	> 1.00 x10^9	4.42 x10^6
reducing agent	**93.78**	5.92	0.00	**416.8** (PDI:> 0.3)	2.06	9.02 x10^8	n/a
extreme pH (acidic)	0.00	26.37	**73.63**	13.7 (PDI:0.110)	*0.08*	1.26 x10^7	1.33 x10^5

Depending on the applied stress condition, characteristic changes were detected:

Temperature-stressed mAB3 suspension showed decreasing monomer content and at the same time increasing soluble aggregate content (change of about 5 %). The increase in z-average and polydispersity as well as turbidity confirmed the aggregation events. NTA and MFI show particle concentration increase over the whole size range. At the high temperature, the aggregation process is mainly dominated by unfolding. The resulting aggregates are therefore expected to possess hydrophobic patches on the surface. These are potential aggregation inducing factors.

Mechanical stressed mAB3 suspension did not show changes by HP-SEC analysis. Minor changes in DLS results and turbidity confirmed that only small amounts of soluble aggregates were detectable in the suspension. Similar to temperature stress NTA and MFI indicated increased particle concentrations, however, in the higher size range (above 800 nm). At stirring stress conditions, the aggregation is mainly driven by local interface forces. Studies have been shown

that such forces are sufficient to cause protein unfolding. These partially unfolded monomers adhere to the interface and function as nucleus for further local aggregation (nucleation-controlled aggregation mechanism on interfaces).

The incubation of mAB3 suspensions at ***reducing conditions*** led to the destruction of disulfide bonds causing fragmentation of the monomer as illustrated by the results of HP-SEC analysis (major portion fragments). The fragments, however, also caused the formation of large particles and increasing turbidity. MFI measurements were possible, but evaluation failed due to large sticking particles. At reducing conditions, the stabilizing disulfide bonds connecting heavy and light chains as well as the disulfide bonds within the CH3 domain are broken. As consequence, the structure is complete destabilized, and the resulting fragments present their hydrophobic patches leading to colloidal instability and fast uncontrolled aggregation events. The resulting aggregates are highly prone to induce further aggregation.

The incubation of mAB3 suspension at highly acidic conditions (pH of 4) led to the highest portion of soluble aggregates in the HP-SEC analysis. DLS results as well as turbidity values showed only minor changes. An increase of particle concentration was detected, however, over whole size range. At extreme acidic pH conditions, high amount of positive charges are crowded in the molecule leading to structural loosening and potential slow structural loss. Such destabilized monomers show a higher tendency to agglomerate or aggregate. The resulting aggregates, depending on the reversibility of the changes might be or consist of aggregation prone regions.

Out of the MFI analysis, sample pictures (microscopic) have been captured as illustrated in Figure 3- 61 (left). Each stress condition caused characteristic particle morphologies:

Temperature stress led to inhomogeneous, but most likely dark grey particles (densely packed) in all sizes. The pH stressed samples showed a large amount of more homogenous but highly translucent particles (more loosely packed) over a wide size range. The reducing conditions led to dark and dense particles over broad size range, but characteristic in structure. The stirring stressed suspension showed heterogeneous particle in a lower size range and based on the captured picture characteristics were hardly achieved. For comparison covalently coupled monomer particles (DSG-particles) are also shown.

On the right of Figure 3- 61 visual appearance is shown for the unstressed (w/o), the reducing stress sample (red) and the pH stress sample (pH). The reduced sample showed a high turbidity as measured by the A320 value. The particles form a homogenous suspension. By storage of the

suspension, a precipitate was observed. The pH stressed sample showed a turbid, blueish appearance. In contrast to the reduced sample, no precipitate was observable after storage.

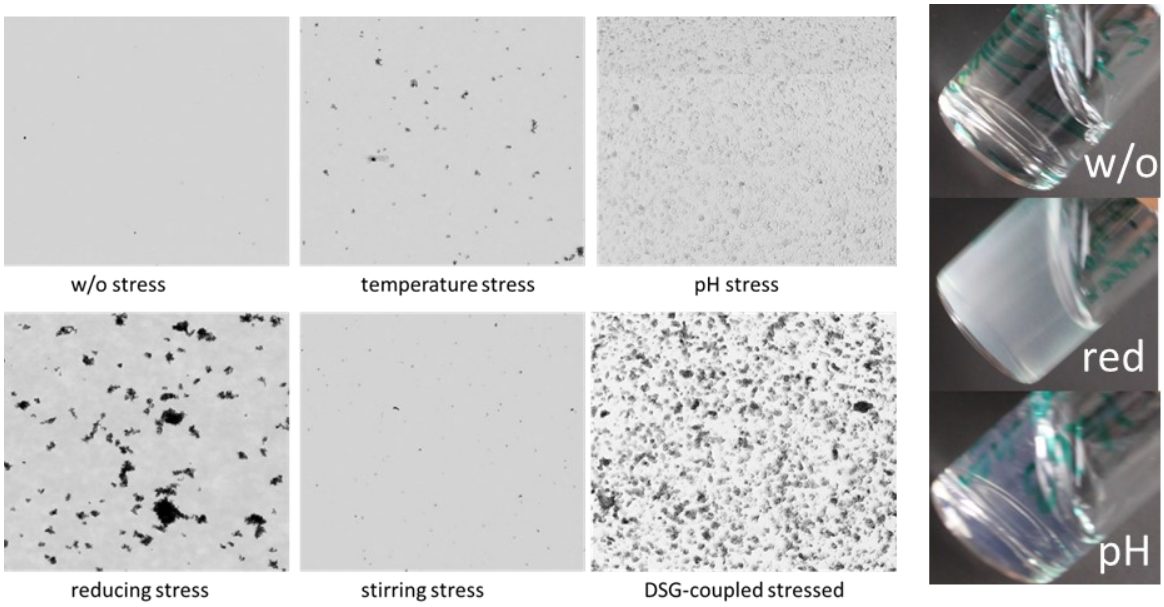

Figure 3- 61: Further protein aggregation studies mAB3: Pictures of the MFI analysis (outtake of flow cell) and visual appearance.
The illustration shows pictures of the different stressed suspensions of mAB3 on the left (w/o = unstressed). On the right, the visual appearance of the unstressed (w/o), the reduced stressed (red) and the pH stressed (pH) suspensions.

The aggregation processes induced by reducing and acidic conditions were further investigated by the Zetasizer Helix. The experiments were performed for 1.5 h, i.e. 0.5 h longer than the seed production procedure.

The results of the reducing experiment are summarized in Figure 3- 62. During the reducing conditions, z-average and PDI increase. The result after incubation of 1 h were similar to the result above. The disulfide band intensity decreased as disulfide bond were reduced. Secondary structure changes occurred within the 1 h incubation time: alpha helices increased from 10 % to 47 %; beta sheets and turns decreased from 47 % to 25 %, respectively from 25 % to 10 %. The tertiary structure marker tyrosine (intensity ratio 857 cm^{-1}/831 cm^{-1}) decreased from 1.2 to 0.3 indicating more buried tyrosine side chains. The results confirmed the process as described above. The reduction of the disulfide bonds caused a structural loss of the molecule and the resulting fragments (tyrosine initially is exposed to hydrophilic environment) aggregate to achieve an energetically more favorable state (tyrosine gets buried in hydrophobic environment).

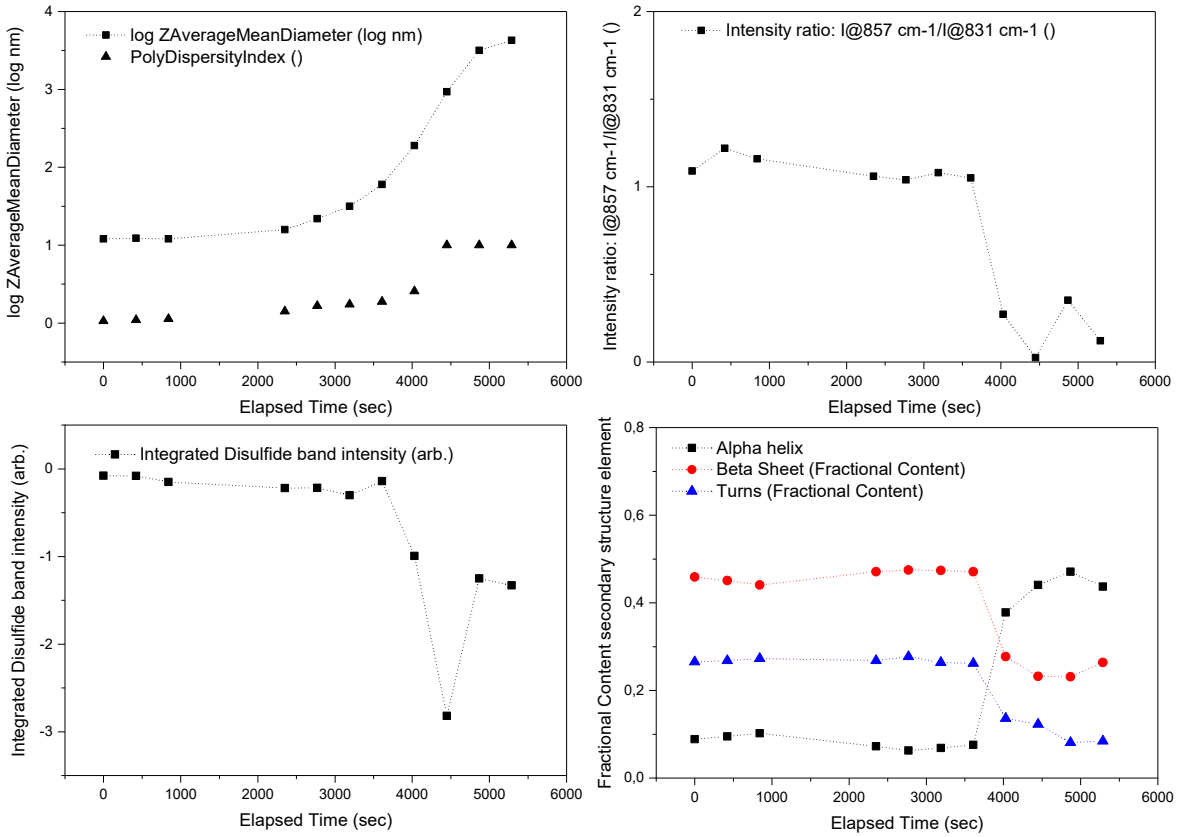

Figure 3- 62: Further protein aggregation studies mAB3: Zetasizer Helix results reducing stress conditions. The mAB3 suspension was analyzed by Zetasizer Helix, first without any reducing agent (first three data points) and subsequently in presence of reducing agent over a time course of 1.5 h. The DLS results (z-average and PDI) are shown in the upper left graph, changes in the disulfide band are shown in the lower left graph, tertiary structure marker tyrosine (intensity ratio 857cm-1/831cm-1) changes are shown in the upper right graph and secondary structure maker changes are shown in the lower right graph.

During the acidic conditions, z-average and PDI increased initially and stayed constant after about 1000 sec (z-average ~ 15 nm, PDI~0,1). The result after incubation of 1 h were similar to the result shown in Table 19. The other markers for disulfide band intensity, secondary structure and tertiary structure did not show significant changes as illustrated in Figure 3- 63. The aggregation due to extreme pH is most likely due to colloidal instability. The protein structure (secondary and also tertiary) did not show significant changes. From the visual characteristics and these results, pH aggregates could be imagined as a transient dynamic net of almost native monomers with crowed positive charges. These charges may also stabilize the net structure and suggest a reversibility of the aggregates.

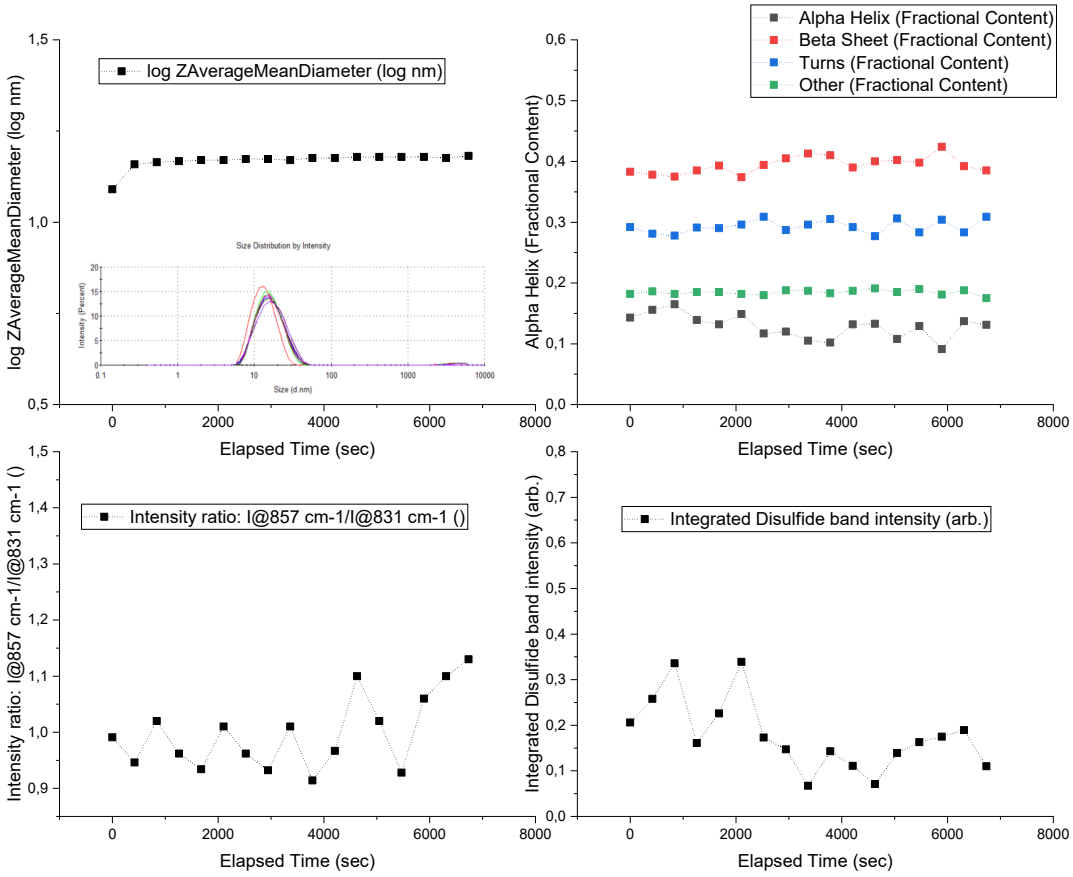

Figure 3- 63: Further protein aggregation studies mAB3: Zetasizer Helix results acidic stress conditions.
The mAB3 suspension was analyzed by Zetasizer Helix, first without any reducing agent (first three data points) and subsequent under extreme acidic conditions (pH~4) over a time course of 1.5 h. The DLS results (z-average and PDI) are shown in the upper left graph, changes in the disulfide band are shown in the lower left graph, tertiary structure marker tyrosine (intensity ratio 857cm-1/831cm-1) changes are shown in the upper right graph and secondary structure maker changes are shown in the lower right graph.

In a further approach the stressed protein suspensions (see Table 19) have been spiked to unstressed suspensions of mAB3 (final 10 vol% stressed suspension). Similar to the long-term stability study (10.1.4) the spiked suspensions have been stored at RT under light exclusion and analyzed by turbidity measurements A320, HP-SEC, DLS, NTA and MFI at the pull points 0 weeks, 4 weeks, 8 weeks and 12 weeks. The results are summarized in Figure 3- 64. In comparison to the unspiked suspension of mAB3 (w/o), in particular the pH-seed approach and the reduced seed approach showed significant changes. The turbidity changes over time were comparable for unstressed, temperature-seed and stirring-seed suspensions. Same applied to the DLS results and SEC results. All particle concentrations detected by NTA and MFI for the spiked were higher than

the unstressed suspension. Temperature-seed and stirring-seed suspensions showed slightly increasing particle concentrations over the 12 weeks.

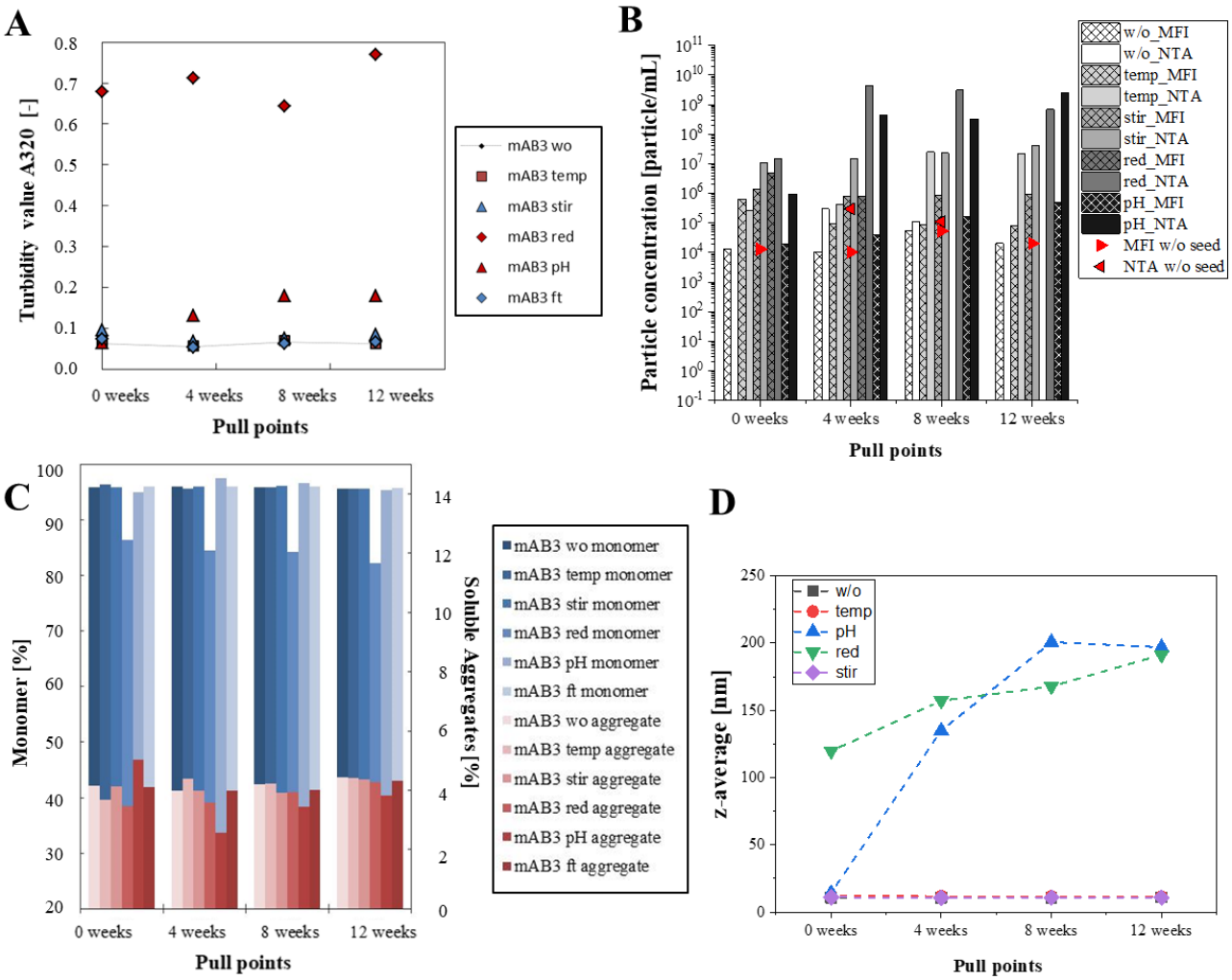

Figure 3- 64: Further protein aggregation studies mAB3: Overview results seeding experiments.
For the investigation of aggregation processes of mAB3 in presence of specifically stressed protein, the stressed protein was spiked to unstressed mAB3 suspensions and stored for 12 weeks at Room temperature. As stress conditions of the spike suspensions high temperature, mechanical stirring, reducing conditions and extreme acidic pH were selected. An analysis of the sample was performed at the initial start (0 weeks), after 4 weeks, after 8 weeks and after 12 weeks. The results of turbidity value A320 measurements (A), particle analysis by NTA and MFI (B), aggregate analysis by HP-SEC (C) and DLS analysis (D) over time.

The reduced seed suspension showed a high turbidity (A320 about 0.7) right after spiking with a continuous increase of 0.1 after 12 weeks. The z-average measurements showed the same tendency with an initial increase to 120 nm and continuous growth up to 190 nm after 12 weeks. The monomer content decreased initially down to 86 % and further over the 12 weeks down to 81 %.

The soluble aggregate content of the reduced seed suspension was below the value of the unstressed suspension at all time points but showed a continuous increase over the time. Considering the particle content, initially in the whole size range (NTA and MFI) showed higher amounts of 10^7 particle/ml. The particle concentration above 2 µm subsequently decreased and were below the MFI detection limit after 8 weeks. The particle concentration between 400 nm and 1 µm increased in the first 4 weeks up to about 10^{10} particle/ml and decreased over the last 8 weeks.

The pH seed suspension, in contrast, did not show an initial increase as the turbidity and the z-average value at the start were in the same range as the unstressed suspension. Both, turbidity and z-average, increased over 8 weeks to a maximal value (A320~0.19; z-average~200 nm) with no further increase over the last 4 weeks. The monomer content showed an initial significant monomer loss (monomer~95%). After 4 weeks incubation, the monomer content increased to 97.5 %, but further decreased slightly over the last 8 weeks. The soluble aggregate content behaved opposite: initial increase to 5 %, after 4 weeks decrease to 2.5 % and slight increase over the last 8 weeks. Considering the particle content, both, NTA and MFI, showed increasing particle concentrations over the whole time points.

PART IV: Summary and Outlook

~

The biopharmaceutical sector is one of most promising and profitable sectors in medical treatment of a multitude of severe diseases. Biological molecules, however, lead to new challenges for the manufacturing companies. This thesis focused on one of the main challenges for therapeutic proteins: protein aggregation and the detection of the resulting particles. Within this thesis, three main tasks have been addressed:

(1) the evaluation of emerging particle detection and characterization techniques
(2) the evaluation of novel technologies for aggregation and unfolding process characterization
(3) the investigation of the aggregation process of current therapeutic proteins (mABs)

11. Evaluation of selected emerging particle detection and characterization techniques for protein particles

For the evaluation of particle detection and characterization techniques for the application on protein samples, the following three techniques have been selected: Nanoparticle tracking analysis (NTA), Tunable resistive pulse (TRPS) and STEP-technology® (space and time-resolved extinction profiles) applied in the LUMiSizer®. All techniques rely on different measurement principles and can be claimed as orthogonal methods. These techniques have been shown to be applicable for polystyrene particle suspensions and showed high agreement for the size and/ or concentration determinations of these particles. In the first step, all techniques have been evaluated in two comparative studies analyzing BSA standard particle suspensions and monoclonal antibody suspensions (11.1 and 11.2). In a second step, a more detailed evaluation of the NTA and the STEP-technology® was performed (11.3 and 11.4).

11.1. Summary and conclusion of case study I: BSA standard particle

In case study I, all three emerging techniques have been evaluated in a comparative study for their suitability to investigate novel protein particle standard suspensions containing chemically cross-linked BSA particle. All tested techniques were at least partially suitable for the detection and/or quantification of these protein-based particles and the results are summarized in Figure 3- 6.

NTA, with the appropriate expertise, can be a great tool for particle detection and also quantification in the submicron range, but depends on optical properties and the operator. It was the only technique that determined the concentration with about 1 x 10^8 particle/ml.
The ***STEP-technology®*** as applied in the LUMiSizer®, showed a broad size range but no direct quantification. It was the only technique that was suitable for the determination of larger particle populations in the micro- and millimeter size range.
The ***TRPS-technology*** showed also in our experiments a great resolution if a measurement was possible. The technique, however, showed only partial suitability for the BSA particle as unspecific interaction of the particles with the membrane and the large size range within the standard suspension led most likely to pore blockage.

Following the results of the BSA suspensions characterization are summarized:

- ***BSA1*** was the most stable and most uniform BSA standard suspension. It showed a total particle concentration of 1 x 10^8 particle/ml, the lowest polydispersity and a main particle population with a size around 200 nm. In addition, larger particle from 450 nm to 3000 nm were detected.
- ***BSA2*** was more polydispers than BSA1 and higher deviations between the orthogonal results were observable. A main particle population with a size between 400 nm and 600 nm and a minor population around 10000 nm was detected.
- ***BSA3*** represented a highly polydispers and heterogeneous sample. A clear analysis of this standard suspension was not possible, and it was highly instable. For this reason, the BSA3 is not suitable as standard suspension.

Study I demonstrated the applicability of the three techniques, at least partially in case of TRPS, in a reliable and reproducible manner for the protein-based BSA standard. In addition, the approach of chemically cross-linked BSA particles was shown to appear as suitable protein-based standard in the nanometer size range. However, ongoing search for stable standards is required as instabilities, as seen for BSA3, are still a great challenge.

11.2. Summary and conclusion of case study II: Therapeutic monoclonal antibodies (mABs)

Therapeutic monoclonal antibody suspensions (mABs) are highly complex samples and challenge the limits of current particle detection techniques. In case study II, all three emerging techniques have been evaluated for their suitability to investigate mAB suspensions containing a large portion of monomers and a small portion of larger protein particles of heterogeneous nature (aggregates) covering a wide size range.

For the evaluation, five mAB suspensions (one unstressed and four stressed) have been prepared by applying four different stress conditions (stirring, temperature, reducing and ionic stress). Additionally, even though the same samples have been analyzed by all techniques the results are not comparable as the analyses have been performed over a longer time period and the samples might have been changed. Following the results of the mAB suspension characterization are summarized:

- ***Unstressed mAB***: None of the techniques detected any subvisible or visible particles in the clear suspension in the size range above 50 nm.
- ***Stirring and temperature stress (mAB2)***: The sample appeared highly turbid, but with no visible particles. Further analysis using STEP-technology® indicated the presence of subvisible particles between 100 nm and 800 nm. The addition of temperature stress at 60 °C to the stirring stress led to the disappearance of visible particles but to higher concentrations of subvisible particles (more turbid). Further investigations of the aggregation mechanisms should be performed.
- ***Reducing stress (mAB3)***: The turbid suspension containing a few visible particles was investigated by NTA and MFI. A total particle concentration of 1 x 10^9 particle/ ml from 50 nm to 100 µm was detected with a main population from 70 nm to 90 nm. The particle in the micrometer range occurred as fiber-like protein particles.
- ***Ionic stress (mAB4)***: The aggregation of a protein sensitive to NaCl was initiated by the addition of NaCl leading to increasing turbidity and the appearance of visible particles. The analysis by TRPS indicated a main particle population around 600 nm up to 2 µm particle.

In conclusion, all tested techniques were suitable to measure at least one but not all of the prepared mAB suspensions. ***NTA*** was able to measure all samples, but for highly polydisperse samples

results are sensitive not only to operator settings, but also to background noise and interferences caused by larger particles. ***TRPS-technology*** unfortunately, was hardly applicable for stressed mAB suspensions due to blockage and protein-pore interactions. The ***STEP-technology®*** was able to measure a wide size range and showed a great resolution over the broadest size range, but no quantification was possible and a low transmission is necessary.

The major challenges that occurred are summarized as follows:

- The detection of the monomers, dimers or low-molecular aggregates up to 50 nm is not possible with any of the tested techniques. In some cases, the monomers can even have a destructive influence, e.g. as a high background noise they cause during NTA measurements.
- At higher protein concentrations the viscosity increases, and the hindered movement of particles appear as a problem, for instance in centrifugation processes.
- Unwished interactions of monomers, but also aggregates, with instrument materials can also influence the results as this was often seen by TRPS measurements.
- Biopharmaceutical samples show low particle concentrations, but also these concentrations have to be detected in a reliable manner to avoid safety risks. This might be, in particular, challenging in ensemble techniques as demonstrated by STEP-technology®. Low concentrations are also a challenge for single particle measurements as higher sample volumes are necessary to obtain reliable and statistically educated result.
- Aggregation processes result in particles within a wide size range from few nanometer to some millimeter. This is still an immense problem if no separation is performed in prior as interferences or mechanical blockage may appear. Furthermore, most principles allow only a small size range.

Addressing the last stated challenge, one potential approach was the combination of NTA and MFI. In this study it was demonstrated as versatile approach in particular for the investigation of the whole subvisible range. The combination indeed is not sufficient to practically close the 1µm gap completely due the imprecise results at technique limits and NTA is most likely disturbed by micrometer range particles.

Study II demonstrated the applicability of the three techniques, at least partially in case of TRPS, in a reliable and reproducible manner for the therapeutic protein samples. The tested techniques

may be suitable, but significant challenges are still present. Ongoing search for suitable techniques to overcome these challenges is required as technical developments might solve some problems.

11.3. Summary and conclusion NTA evaluation

The measurement of particles in suspension is still a great challenge, especially for highly polydisperse, polymodal samples. The NTA technique as used in this study has high potential and new opportunities compared to prior methods. It can provide good and reproducible results in detecting simultaneously size distributions and particle concentrations for mono- and bimodal PS particle suspensions, as long as the sample composition is known. Depending on the particle properties, in particular the refractive index, particles sizes of 20 nm (e.g. PS- or Au-particles) or at least 50 nm (e.g. protein material) can be detected. Nevertheless, highly polydisperse or proteinaceous sample suspensions remain still challenging and the choice of parameter settings (e.g. camera level or detection threshold) can influence the result significantly. Even with the same raw data video the operator can affect the final result significantly in particle size peaks or particle concentrations by setting the DT. This can lead to appearance and disappearance of peaks and "false" results. Based on this knowledge protein samples with a high range of unknown particle sizes and concentrations as well as high monomer contents are challenging to investigate and evaluate. At this point a more automated and supportive system as it was provided in the live monitoring mode would help to get at least more comparable outcomes. In addition, the results show that this mode is a more robust tool as the results were more reproducible and more sensitive for changes in protein samples compared to the general capture mode. In conclusion, we show NTA results highly depending on the operator and this need to be taken into account when results are evaluated and compared. The technique should be applied by an experienced and skilled user. We would also emphasize that the measuring parameters should be presented directly with the NTA results. This would help to better judge the results.

11.4. Summary and conclusions LUMiSizer® evaluation

The STEP-technology® applied in the analytical photocentrifuge LUMiSizer® is a potential technique also for the investigation of biopharmaceutical proteins. However, protein particles are

challenging due to their heterogeneity, low refractive indices and unknown particle densities. LUMiSizer® analysis is a new tool offering a broad range of information for studying biopharmaceuticals, if samples show (1) a turbidity value or transmission A320 value of at least 1 and if (2) sample composition changes and sedimentation information is needed. The particle size distributions are hard to achieve since specific particle properties, like the density of the particle populations might differ extremely and are generally hard to achieve for protein particles and aggregates. In two approaches, we were able to demonstrate the potential and advantages of LUMiSizer® analysis for monoclonal antibody suspensions: In the first approach, we showed the successful application for protein standard particles and confirmed the complementary application to light scattering methods. In the second approach we demonstrated that stressed mAB suspensions are evaluable and that the resulting transmission profiles characterize properties, sedimentation behavior and particle interactions in a unique manner.

11.5. General summary and evaluation of emerging techniques for biologics

From the biopharmaceutical perspective, there is a continuous need for more accurate and orthogonal techniques concerning particle analysis. Protein particle detection and characterization will remain highly challenging as these particle suspensions are highly polydisperse and appear highly variable in their properties within the sample. The techniques of NTA, MFI, TRPS and STEP have been chosen to address still existing challenges in this field by emerging techniques and approaches:

(i) the presence of the detection gap around 1 µm,
(ii) limited size and concentration measurement ranges,
(iii) insufficient resolution of multimodal and polydispers samples,
(iv) the need for orthogonal and quantitative techniques and
(v) the lack of suitable protein-based/protein-like particle and calibration standards.

We addressed these challenges to the four emerging techniques in the two case studies and demonstrated their applicability for a protein-based particle standard as well as various stressed mAB suspensions.

In the first case study, we evaluated the chosen techniques based on BSA standard particle suspensions. These particle suspensions have been analyzed by the manufacturer and in our lab by DLS measurements. All evaluated techniques were able to detect and characterized the BSA particle standards BSA1 and BSA2 in great agreement with the expectations. The obtained particle size distributions of NTA, TRPS and LUMiSizer® appeared in a similar range. Concentrations determinations of these samples have only be achieved by NTA. The LUMiSizer® results showed in each sample larger particles outside of the detection range of the other techniques. At this point we could not prove if these particles have been introduced by the technique or have been present before. In conclusion, we were able to demonstrate that the BSA particle standards BSA1 and BSA2 are promising protein particle standards providing comparable results of the tested orthogonal techniques (v). At the same time the techniques have been evaluated as suitable orthogonal protein-based particle analysis techniques that are in some cases able to close the 1 µm gap with good resolution (i-iv).

In the second case study the evaluated techniques have been used for the investigation of mAB suspensions. One important observation was the dependence of the applicability on the applied stress. The variety of particle and suspension properties due to these variations allows no general statement of the applicability of a technique to mAB suspensions. However, in most cases we were to analyze the samples. The challenge of covering the whole size range of subvisble particles qualitative and quantitative was firstly targeted by combining NTA and MFI. We were able to demonstrate the combination as a versatile approach covering the size range between 50 nm and 100 µm. However, results around the 1 µm detection gap showed high deviations suggesting a further technique to ensure the results in this range. Nevertheless, as the results of NTA are operator-dependent the techniques will remain challenging. On the other hand, MFI is a potential technique for future authority regulations. Most likely MFI appears as highly versatile techniques orthogonal to LO. While MFI is a potential technique for future authority regulations, absolute numbers for concentrations are hardly achievable by NTA. However, relative comparisons with the same settings are highly potential for stability studies. Although a wide size range is covered, it is still not the whole range. Methods that could complete the range are in most cases only qualitative or semi-quantitative. The high deviations around the lower and upper limit confirm the still existing detection gap around 1 µm.

The challenge of closing the detection gap around 1 µm with an orthogonal principle was targeted by the modified RPS principle, TRPS. As already demonstrated in various studies before, TRPS is a great technique for the analysis of particle suspensions with low polydispersity (about the size range one pore can cover) and with low interaction potential with the pore. It is able to close the gap in these cases. Protein samples in general are analyzable as shown by BSA particles. However, stressed antibody solutions are highly challenging due to their high polydispersity and their heterogenic surface/nature. STEP-technology® was evaluated as further technique to close the detection gap around 1 µm and analyzing a wide size range with an orthogonal principle was targeted by the STEP-technology®. The technique works very well if sufficient turbidity was detectable and over a great size range up to visible particles. However, quantification – as one of the most common parameters – cannot be achieved and unstressed antibody solutions cannot be analyzed.

In summary, the four techniques used in the case studies are compared to each other and compared to the primary compendial technique for parenterals, LO, in Table 20. Indeed, all techniques have advantages and drawbacks. Table 20 points out some of the major advantages and disadvantages, in particular for protein applicability. As there is still no single method that can cover all requirements or give alone standing information the combination of complementary methods, as shown by MFI and NTA, is state of the art. For the optimal combination of those methods, the principle as well as the benefits and limits should be intensively considered for the specific sample specifications and properties. Furthermore, new challenges arise with new application/dosage requirements, e.g. HCLFs, high throughput, automation.

Table 20: Final evaluation of emerging techniques and comparison to Light obscuration: Advantages and disadvantages.

	Light Obscuration LO	**Micro Flow Imaging MFI**	**(Nano-) Particle tracking Analysis NTA**	**Tunable Pulse Resistive Sensing TRPS**	**Space and Time resolved Extinction Profile STEP**
Operating Principle	Particle-light interactions (static), particle-by-particle	Microscopy and imaging, particle-by-particle	Particle-light interactions (dyn.), particle-by-particle	Electrozone sensing/ Coulter principle, particle-by-particle	Sedimentation and centrifugation, ensemble
Size Range[1]	1 µm – 600 µm	2 µm – 100 µm	20 nm – 1 µm	50 nm – 10 µm	20 nm - 100 µm
Input/ analysis required information	no	no	measurement and evaluation settings	choose pore size, Set stretch, pressure, voltage	RI and density for PSD, centrifugation protocol
Output/ Provided info:					
Particle concentration	Yes	Yes	Yes	Yes	No
Particle size	Yes	Yes	Yes	Yes	Yes
Size distribution (PSD)	Yes	Yes	Yes	Yes	Yes
Shape	-	Circularity, aspect ratio	-	Yes (duration)	-
Structure	-	Related to contrast	-	-	-
Identity	-	Due to shape/structure particle images	-	-	-
Other	-		scatter intensities and RI	particle charge	sedimentation velocities, suspension stability

[1] limits as mentioned by the manufactures; depending on the material these limits might vary, e.g. NTA detects gold nanoparticle of 10 nm but starts detection of protein particle of 50 nm

	Light Obscuration LO	**Micro Flow Imaging MFI**	**(Nano-) Particle tracking Analysis NTA**	**Tunable Pulse Resistive Sensing TRPS**	**Space and Time resolved Extinction Profile STEP**
Equivalent Particle Diameter	Projected area	Projected area	Hydrodynamic	Volume	Volume
Material Differentiation	no	yes; due to shape and gray scale	no; potential differentiation due to scatter intensity	no; potential differentiation due to charge	no
Detection of translucent particles?	+	++	++	+++	+
Destructive?	no/yes (dilution)	no/yes (dilution)	no	no/yes by voltage	no/yes by crowding
Particle separation required?	no	no	no/yes for highly polydisperse suspensions	no/yes for highly polydisperse suspensions	no
Sample handling and preparation	++	++	++	++	+++
Sample volume (minimal)	2 ml/25 ml (Ph.Eur.)	0.5 -1.0 ml	0.5 -1.0 ml	40 – 120 µl	0.4 - 1.5 ml
Particle concentration	≤ 18 000 counts/ml	≤ 850 000 counts/ml	10^7-10^9 particle/ml	10^5-10^{11} particle/ml	0.00015 Vol % – 90 Vol %
Calibration Yes/No	No	No	No	Yes	No/Yes
Speed/sample	5 min	8 min	12 min	10 min	Depending on sample
High throughput/ autosampler	Yes/no autosampler	Yes/ autosampler	No/no autosampler	Yes/no autosampler	Yes/12 samples simultaneous

	Light Obscuration LO	Micro Flow Imaging MFI	(Nano-) Particle tracking Analysis NTA	Tunable Pulse Resistive Sensing TRPS	Space and Time resolved Extinction Profile STEP
Provided Software:					
Measurement	yes	yes	yes	yes	yes
Data evaluation	yes	yes	yes	yes	yes
Report	yes	yes	yes	yes	yes
Data export:					
Raw data		CSV	CSV, video	CSV,	CSV, PDF
Graph/processed		PDF	PDF, jpeg	rtf, jpeg	CSV, PDF
Particle size distribution					
Accuracy	++	++	++	+++	++
Repeatability	++	+++	++	+++	+++
Resolution	++	++	++	+++	++
Protein applicability					
BSA standard	+++	+++	+++	+++	+++
mAB solution	+++	+++	++	+	+
Portability/ space	++	++	+ (NS500), ++ later versions	+++	++
Advantages and benefit	• Primary pharmacopeial method • Protocol and instrument set • Easy-to-use	• Good, emerging technique orthogonal to LO • Morphological analysis • Small volumes possible • Images, re-analysis possible	• Quantification, size determination and PSD in nanometer range • Determination RI	• High resolution • Wide total size range • Small sample volume • Orthogonal method to light scattering	• Good resolution • Highly polydisperse samples • Suspension stability and storage predictions
Disadvantages and limitations	• Only micrometer size range above 2µm • No detection of translucent particles • Low max. count rate • Larger volume	• Only micrometer size range above 2µm • Image analysis algorithm dependent • Small volumes representative results	• Experienced operator necessary • Result influenced by operator • Narrow concentration range • Scatter intensities	• To cover the whole range pores must be changed • Influence of electrolyte on sample • Blockage of pore and particle-pore interactions	• No quantification • No direct detection • High turbidity necessary

	Light Obscuration LO	**Micro Flow Imaging MFI**	**(Nano-) Particle tracking Analysis NTA**	**Tunable Pulse Resistive Sensing TRPS**	**Space and Time resolved Extinction Profile STEP**
Application	Compendial technique (USP<788>) for micrometer range in parenterals, PSD and quantitation	Micrometer range with the potential of particle classification based on shape and optical contrast, PSD and quantitation	Submicron size range, PSD and quantitation	Submicron and micrometer range, Low polydispersity, low binding, PSD and quantitation	Submicron and micrometer range, stable in centrifugation field, PSD

12. Evaluation of selected novel technologies for the investigation and characterization of protein unfolding and aggregation processes

For the evaluation of novel technologies for the investigation and characterization of protein unfolding and aggregation processes, the following two techniques have been selected: Zetasizer Helix system and the SwitchSENSE®. The techniques rely on different measurement principles; offer several analysis approaches and their potential for application for therapeutic protein samples was evaluated.

12.1. Summary and conclusions Zetasizer Helix evaluation

The ***Zetasizer Helix system*** is an instrument combining dynamic light scattering and Raman spectroscopy.

The three measurement modes (sample series, isothermal incubation, temperature ramp) have been successfully evaluated for selected therapeutic mABs. In a dilution series experiment of mAB2 (concentration range from 10 mg/ml to 211 mg/ml), the combined results of DLS and Raman spectroscopy indicated potential protein-protein interactions, hydration changes and viscosity effects. In a buffer exchange sample series, the buffer influences have been detected in DLS results (shift of z-average) and the tertiary structure markers indicating changes in the hydration shell. No significant secondary structural changes were determined. The performance of isothermal kinetics at 75 °C was realized for mAB1 and mAB2. In result, aggregation was detected by DLS for both mABs. Differences between the mABs were pointed out by structural changes during the aggregation process for mAB2 but not for mAB1. This outcome indicated differences in the aggregation mechanism. The same applies to the thermal ramp experiments. In addition, the obtained melting temperatures and aggregation onset fit to the results of orthogonal methods (DSC, ITF, SwitchSENSE®).

Challenging for Zetasizer Helix analyses and final evaluation appears that the Raman spectra are often noisy, and the spectra analysis would need a specialist to get reliable results in some cases. In conclusion, the Zetasizer Helix is an instrument that is not applicable in a high throughput manner, but it gives valuable information for better understanding the correlation between structural changes and aggregation behavior.

12.2. Summary and conclusions SwitchSENSE® technology evaluation

The ***SwitchSENSE® technology*** is a chip-based analytical platform using a specific DNA-based biosurface system to investigate molecular interactions, such as binding kinetics and affinities or enzymatic activities.

Out of the various applications of the SwitchSENSE® technology, the following applications were evaluated for therapeutic proteins: protein sizing, protein interaction and thermal melting approaches. Protein size determinations for the investigated proteins with molecular weights of 90 to 150 kDa and expected hydrodynamic sizes around 10 nm were only possible in a relative and comparable manner. Absolut size calculations based on the provided database were not suitable. A future enlargement of the database, however, is planned and may enable absolute sizing. The experimental approach to investigate protein-protein self-interactions was not suitable due to unspecific interactions of the monomers with the chip surface. The most promising approach was the usage of the SwitchSENSE® system as orthogonal method for the characterization of the thermal melting behavior. The combination of sizing step and thermal melting step gave information about the refolding potential.

Comparative investigations with DSC and ITF showed good coincidence of unfolding start and melting temperature determinations. The temperature limit of the system with about 80°C is still not sufficient for complete unfolding but improvements have already been applied. The system development and application identification is ongoing and continuous updates are necessary for further potential approaches.

13. Investigation of the aggregation processes of current therapeutic proteins (mABs): Protein aggregation case studies

For these protein aggregation case studies, three monoclonal antibodies (mAB1, mAB2 and mAB3) have been selected and transferred into a specific defined buffer (10 mM sodium phosphate, 10 mM sodium chloride, pH 6.5). Following these model systems have been investigated considering their stability and aggregation behaviour using established and novel techniques and technologies.

Initially a biophysical characterization of the model systems was performed. Colloidal stability parameters A2, B22 and kD indicated mAB3 as least stable; mAB1 and mAB2, indeed occurred with similar colloidal stability. Zetapotential (ZP) determinations showed positive charges for all mABs from + 2mV to + 4 mV. The isoelectric point (IP) based on the apparent ZP showed significant differences to the theoretical values. In particular, for mAB3 the determined IP was with 7.0 close to the pH of the chosen buffer. Secondary structure analysis by Raman spectroscopy resulted in similar structural compositions with a main fraction of beta-sheets and beta-turns. Conformational stability was evaluated by thermal melting (DSC, ITF) and chemical denaturation experiments. Based on the unfolding start, mAB2 was the most stable molecule and mAB3 the least stable. The $C_{1/2}$ values indicated mAB1 as the most stable molecule. Aggregate and particle analyses showed the highest particle amounts and significant monomer loss for mAB3. Long-term stability over 24 weeks confirmed mAB3 as the most instable model system and similar stability for mAB1 and mAB2. All three model systems, however, were stable over time. The biophysical characterization identified already mAB3 as most instable model system with high tendency to aggregate without unfolding (self-association). The model systems mAB1 and mAB2, indeed, showed similar stability but mAB1 indicated a higher aggregation tendency based on particle content and chemical denaturation results.

For a first aggregation study approach, temperature ramp experiments have been performed with mAB1 and mAB2. The aggregation process during a temperature ramp from 25 °C to 95 °C was investigated by ITF-backscattering (Prometheus NT), ITF-RALS (Optim 1000), DSC (VP-DSC), DLS-Raman (Zetasizer Helix) and SwitchSENSE®. Depending on the principles, each method described the unfolding and aggregation process from a different perspective. Summarizing these results, a hypothetical aggregation process/mechanism was described for each mAB. Based on the detected aggregation start temperatures, four phases have been defined: pre-aggregation phase,

first aggregation phase, second aggregation phase and third aggregation phase. In the pre-aggregation phase, both mABs started unfolding and for mAB2 even the first unfolding melting point was reached. The aggregation of mAB1 started earlier than the aggregation of mAB2 compared to the unfolding state and the aggregation in the first aggregation phase occurred slower. Loss of secondary structure was detected, for both mABs, in the second aggregation phase within the second unfolding transition. Consequently, in the third aggregation phase, unstructured and uncontrolled. Concluding, mAB1 and mAB2 follow different aggregation mechanisms over the applied temperature range. The mAB1 aggregation is unfolding-driven over the complete process. It is a slow ongoing process. The mAB2 aggregation start is triggered by reaching a specific unfolding state, but after aggregation started unfolding is not the driving factor. It is a fast process. Further ITF-backscattering measurements varying protein concentrations and heating rates confirmed the statements. The applied techniques and approaches appeared as suitable platform to describe and suggest protein aggregation processes of mAB1 and mAB2.

For a second aggregation study approach, isothermal experiments were performed for all three mAB model systems. The aggregation process during isothermal incubation at various temperatures above 50 °C was investigated by turbidity, DLS, HP-SEC, MFI, LUMiSizer®, ITF-backscattering (Prometheus NT), ITF-RALS (Optim 1000), and DLS-Raman (Zetasizer Helix).

For mAB1 and mAB2, an incubation at 75 °C was initially evaluated over 120 h. Within the first 2 h, back-scattering results were misleading as they indicated faster aggregation for mAB1 and less instability of mAB2. An investigation, however, by the further methods clarified the aggregation process and differences of both mABs. Aggregation of mAB1 occurred from the beginning with slow continuous z-average increase and increase of hydrophobicity indicating slow unfolding (but no loss of secondary structure). Aggregates grow slow by addition of partially unfolded monomers indicated by increasing turbidity and adhering particle during LUMiSizer® experiments. Aggregation of mAB2 occurred from the beginning with faster continuous z-average increase up to 50 min. Afterwards autocorrelation function and Raman spectra collapsed suddenly (structural and aggregation collapse). Aggregates grow fast to large visible particles without clear unfolding of monomers indicated by lower turbidity, first non-adhering particles during LUMiSizer® experiments. As unfolding is ongoing over time these visible particles adhere later (increased hydrophobicity). The differences in the aggregation mechanisms determined by temperature ramps were confirmed by the isothermal approach. The selected temperature of 75 °C

was suitable for the slow unfolding-driven aggregation processes of mAB1. For mAB2, aggregation was detectable at 75°C, but process happened fast. An isothermal aggregation approach at 65 °C over 2 h and 14 h were performed, but no significant aggregation (slight increase z-average) or changes in the Raman spectra was detected. For future investigations, isothermal studies at 70 °C are advisable. For mAB3, a setting with lower temperatures, namely 55 °C, 60 °C and 65°C was chosen. Based on DLS results, the aggregation process at each temperature consisted of three aggregation phases. From the start of the second aggregation phase, the aggregation process depended on the unfolding process indicated by the temperature dependency of the aggregation start phase 2 and the final z-average. In the second phase, secondary structure changes were detected. As aggregation was detected in the first phase without significant structure changes, in this phase self-association seemed possible. Further experiments, e.g. protein concentration variations, are advisable to clarify the process.

For a third aggregation study approach, the impact of further protein stress factors, such as extreme temperature, mechanical stirring, extreme acidic pH, reducing stress, have been investigated for mAB3. In result, the specific aggregation processes led to stress specific aggregates characterized by turbidity, DLS, SEC-MALS, NTA and MFI measurements. Based on the results of this analysis as well as potentially underlying aggregation mechanism and processes, these aggregates showed properties that may further induce aggregation when used as seeds. Characteristics have been monitored by visual appearance and MFI images. In particular, temperature stress aggregates (unfolding processes) and reduced fragments and resulting aggregates (highly instable) were aggregation-prone seeds. For that reason the aggregation process under reducing conditions and under extreme acidic conditions have been investigated in more detail by DLS-Raman to characterize the final aggregates. Reduced aggregates characteristics are of disulphide bonds and structure loss, suggesting irreversible aggregates. Aggregates caused by extreme acidic pH, however, showed no structure loss, suggesting reversible net like (gel-like) aggregates. In a final experiment, the resulting aggregates have been used as potential aggregation seed in an unstressed mAB suspension and the subsequent aggregation process was investigated over 12 weeks. Interestingly, only the pH seed and the reducing seed showed significant influences and induced faster aggregation. All other approaches showed only slight differences and were rather similar to the process in the unstressed sample. The approach inducing aggregation process by seeding of stressed suspensions is consequently a good approach to shorten the aggregation lag phase. It helps

to understand mechanisms and forces, but may also show no effect, if the spiked aggregate is not prone enough to influence model system stability.

In summary, the results of these case studies describe the stability and aggregation processes of the three monoclonal antibodies. Depending on different stress factors (temperature, pH, reducing conditions, etc.) and different approaches (temperature ramp, isothermal incubation and extreme conditions), molecule specific aggregation mechanisms were postulated. The application of the evaluated technologies in the case studies outline their suitability for practical stability studies.

14. Zusammenfassung

Der Einsatz von Biopharmazeutika ist ein vielversprechender Ansatz für die Behandlung einer Vielzahl von Krankheiten. Diese biologischen Moleküle, bspw. therapeutische Antikörper, führen allerdings zu neuen Herausforderungen, denen sich die Pharmaindustrie stellen muss. Eine Herausforderung von therapeutischen Proteinen sind bspw. Aggregationsprozesse und folglich die Detektion der resultierenden Proteinpartikel mit geeigneten Methoden. Die Ziele dieser Arbeit waren daher die Evaluierung neuaufkommender Techniken für die Partikeldetektion und -charakterisierung, die Evaluierung neuer Technologien zur Untersuchung von Proteinentfaltungs- und Aggregationsprozessen und die Untersuchung des Aggregationsverhalten von drei therapeutischen Modellproteinen (monoklonale Antikörper).

Für die Evaluierung neuaufkommender Techniken für die Partikeldetektion wurden drei Technologien untersucht: Nanoparticle Tracking Analysis (NTA), Tunable Resistive Pulse Sensing angewendet in dem Gerät qNano (TRPS) und die STEP-technology® angewendet in dem Gerät LUMiSizer®. Die initiale Vergleichbarkeit der Technologien und der Analyseergebnisse wurde zunächst gezeigt mit Hilfe von Latexpartikel Standard Suspensionen. Die anschließende Analyse von drei BSA (bovine serum albumin) Proteinpartikel Standard Suspensionen (mit nominalen Partikelgröße BSA1~150 nm; BSA2~500 nm und BSA3~750 nm) zeigte, vor allem für die heterogeneren Suspensionen BSA2 und BSA3 mit höherer Polydispersität, schon erste Herausforderungen für die Techniken. Während der TRPS-Analyse (Coulter Counter Prinzip) traten die Blockade der Pore sowie eine Proteinschicht auf der Membran auf. Diese Probleme wurden während der Analyse von gestressten therapeutischen Antikörperproben bestätigt und das TRPS-Gerät wurde für die Anwendung für Proteinproben als ungeeignet bewertet. Für NTA und den LUMiSizer® konnte in einer detaillierten Evaluierung hingegen die Anwendbarkeit demonstriert werden. Das NTA, eine Lichtstreu-basierte Methode, bietet dabei eine quantitative Methode zur Bestimmung der Partikelgrößenverteilung im nanometer-Größenbereich (150 nm bis ca. 1000 nm). Die Herausforderung bildet dabei die Einstellung geeigneter Messparameter (z.B. Detection Threshold). Der LUMiSizer®, eine Photozentrifuge, ist hingegen nicht für Konzentrationsbestimmungen geeignet, ermöglicht allerdings eine non-destruktive Analyse der Partikelgrößenverteilung über den nanometer und mikrometer Größenbereich. Die Herausforderung der Methode ist eine ausreichende Trübung der Probe, um die Partikelbewegung detektieren zu können.

Zur Untersuchung von Proteinentfaltungs- und Aggregationsprozessen wurden zwei Technologien evaluiert: der Zetasizer Helix, eine Kombination aus Dynamischer Lichtstreuung und Raman Spektroskopie und die SwitchSENSE Technologie, eine chip-basierter Biosensorplattform. Der Zetasizer Helix ermöglicht die simultane Untersuchung von Partikelbildung (kolloidaler Stabilität) und Proteinstrukturänderungen (konformative Stabilität). Es konnte in dieser Arbeit gezeigt werden, dass dieser Ansatz für Proteinaggregationsstudien gut geeignet ist. Die SwitchSENSE Technologie bietet ein breites Einsatzgebiet. In dieser Arbeit konnte eine orthogonale Methode für die Untersuchung des Entfaltungsprozesses von mABs evaluiert werden. Für weitere Anwendungen zur Untersuchung von Proteinaggregation konnten keine neuen Vorteile durch die Verwendung der SwitchSENSE Technologie aufgezeigt werden.

Im dritten Abschnitt der Arbeit wurden Aggregationsprozesse der Modellantikörper mAB1, mAB2 und mAB3 untersucht. Die Proteinsuspensionen wurden zunächst biophysikalisch untersucht, um die kolliodale und konformative Stabilität zu beschreiben. Während mAB1 und mAB2 vergleichbar stabil waren, zeigte mAB3 eine signifikant geringere Stabilität. Anschließend wurden die Aggregationsprozesse unter verschiedenen Stresskonditionen (u.a. Temperaturrampen, isothermer Stress oder extrem saurer pH-Wert) untersucht. Der Aggregationsprozess von mAB1 ist gekennzeichnet durch einen langsamen Verlauf, als rate-limiting Schritt kann der Entfaltungsschritt angenommen werden und der gesamte Prozess scheint entfaltungsgetrieben. Der Aggregationsprozess von mAB2 ist gekennzeichnet durch einen schnellen Verlauf, als rate-limiting Schritt kann die Formation eines irreversiblen Nukleus (Nukleationskontrolliert) angenommen werden und der Einfluss der Entfaltung scheint nach dem Aggregationsstart reduziert. Der Aggregationsprozess von mAB3 scheint hingegen gekennzeichnet durch Selbstassoziation der Monomere, einen schnellen Verlauf und als rate-limiting Schritt kann die Monomeraddition angenommen werden.

Zusammenfassend konnten fünf neue Technologien evaluiert und in Aggregationsstudien implementiert werden, um die Aggregationsprozesse/-charakteristika von drei Modellantikörpern zu beschreiben. Die Beschreibung und das Verständnis von Aggregationsprozessen unterstützen die Entwicklung einer stabilen Formulierung von therapeutischen Proteinen und bildet daher einen wertvollen Beitrag für die Entwicklung solcher Biopharmazeutika.

PART V: References

~

<776>, U.S.P. (2014). "Opticle Microscopy." USP29-NF24(30(6)).

<787>, U.S.P. (2014). "SUBVISIBLE PARTICULATE MATTER IN THERAPEUTIC PROTEIN INJECTIONS." National Formulary USP 38 NF 33(39 (2)).

<788>, U.S.P. (2014). "PARTICULATE MATTER IN INJECTIONS." National Formulary USP 38 NF 33(37 (6)).

<790>, U.S.P. (2015). "Visible Particulates in Injections." National Formulary.

<1787>, U.S.P. (2015). "Subvisible Particulate Matter in Therapeutic Protein Injections." National Formulary.

Agency, E. M. (2016). "Guideline on development, production, characterisation and specification for monoclonal antibodies and related products." (EMA/CHMP/BWP/532517/2008).

Ahmadi, M., C. J. Bryson, E. A. Cloake, K. Welch, V. Filipe, S. Romeijn, A. Hawe, W. Jiskoot, M. P. Baker and M. H. Fogg (2015). "Small amounts of sub-visible aggregates enhance the immunogenic potential of monoclonal antibody therapeutics." Pharm Res 32(4): 1383-1394.

Albrechtsson, U., G. A. Hansson and T. Olin (1977). "Vascular occlusion with a ferromagnetic particle suspension. An experimental investigation in rabbits." Acta Radiol Diagn (Stockh) 18(3): 279-291.

Alford, J. R., B. S. Kendrick, J. F. Carpenter and T. W. Randolph (2008). "High concentration formulations of recombinant human interleukin-1 receptor antagonist: II. Aggregation kinetics." J Pharm Sci 97(8): 3005-3021.

Alford, J. R., B. S. Kendrick, J. F. Carpenter and T. W. Randolph (2008). "Measurement of the second osmotic virial coefficient for protein solutions exhibiting monomer-dimer equilibrium." Anal Biochem 377(2): 128-133.

Alford, J. R., S. C. Kwok, J. N. Roberts, D. S. Wuttke, B. S. Kendrick, J. F. Carpenter and T. W. Randolph (2008). "High concentration formulations of recombinant human interleukin-1 receptor antagonist: I. Physical characterization." J Pharm Sci 97(8): 3035-3050.

Amin, S., S. Blake, S. M. Kenyon, R. C. Kennel and E. N. Lewis (2014). "A novel combination of DLS-optical microrheology and low frequency Raman spectroscopy to reveal underlying biopolymer self-assembly and gelation mechanisms." The Journal of Chemical Physics 141(23): 234201.

Anderson, W., D. Kozak, V. A. Coleman, A. K. Jamting and M. Trau (2013). "A comparative study of submicron particle sizing platforms: accuracy, precision and resolution analysis of polydisperse particle size distributions." J Colloid Interface Sci 405: 322-330.

Andrews, J. M. and C. J. Roberts (2007). "A Lumry-Eyring nucleated polymerization model of protein aggregation kinetics: 1. Aggregation with pre-equilibrated unfolding." J Phys Chem B 111(27): 7897-7913.

Balcão, V. M. and M. M. Vila (2015). "Structural and functional stabilization of protein entities: state-of-the-art." Advanced drug delivery reviews 93: 25-41.

Bansal, R., S. Gupta and A. S. Rathore (2019). "Analytical Platform for Monitoring Aggregation of Monoclonal Antibody Therapeutics." Pharmaceutical Research 36(11).

Bargieł, M., R. A. Ford and E. M. Tory (2005). "Simulation of sedimentation of polydisperse suspensions: A particle-based approach." AIChE Journal 51(9): 2457-2468.

Barnett, G. V., M. Drenski, V. Razinkov, W. F. Reed and C. J. Roberts (2016). "Identifying protein aggregation mechanisms and quantifying aggregation rates from combined monomer depletion and continuous scattering." Anal Biochem 511: 80-91.

Barnett, G. V., W. Qi, S. Amin, E. N. Lewis, V. I. Razinkov, B. A. Kerwin, Y. Liu and C. J. Roberts (2015). "Structural Changes and Aggregation Mechanisms for Anti-Streptavidin IgG1 at Elevated Concentration." J Phys Chem B 119(49): 15150-15163.

Beekman, A., D. Shan, A. Ali, W. Dai, S. Ward-Smith and M. Goldenberg (2005). "Micrometer-scale particle sizing by laser diffraction: critical impact of the imaginary component of refractive index." Pharm Res 22(4): 518-522.

Bell, N. C., C. Minelli, J. Tompkins, M. M. Stevens and A. G. Shard (2012). "Emerging techniques for submicrometer particle sizing applied to Stober silica." Langmuir 28(29): 10860-10872.

Bernard, S. L., T. Obermiller, N. L. Polissar, J. M. Mendenhall, J. Butler and S. Lakshminarayan (1993). "Fifteen micrometer microspheres reflux up the pulmonary veins during pulmonary artery occlusion." Microvasc Res 45(3): 262-268.

Blundell, E. L., R. Vogel and M. Platt (2016). "Particle-by-Particle Charge Analysis of DNA-Modified Nanoparticles Using Tunable Resistive Pulse Sensing." Langmuir 32(4): 1082-1090.

Blundell, E. L. C. J., L. J. Mayne, E. R. Billinge and M. Platt (2015). "Emergence of tunable resistive pulse sensing as a biosensor." Analytical Methods 7(17): 7055-7066.

Bogdanovic, J., J. Colon, C. Baker and Q. Huo (2010). "A label-free nanoparticle aggregation assay for protein complex/aggregate detection and study." Analytical Biochemistry 405(1): 96-102.

Boing, A. N., E. van der Pol, A. E. Grootemaat, F. A. Coumans, A. Sturk and R. Nieuwland (2014). "Single-step isolation of extracellular vesicles by size-exclusion chromatography." J Extracell Vesicles 3.

Boyd, R. D., S. K. Pichaimuthu and A. Cuenat (2011). "New approach to inter-technique comparisons for nanoparticle size measurements; using atomic force microscopy, nanoparticle tracking analysis and dynamic light scattering." Colloids and Surfaces A: Physicochemical and Engineering Aspects 387(1): 35-42.

Bracewell, D. G. and C. M. Smales (2013). "The challenges of product- and process-related impurities to an evolving biopharmaceutical industry." Bioanalysis 5(2): 123-126.

Brinks, V., D. Weinbuch, M. Baker, Y. Dean, P. Stas, S. Kostense, B. Rup and W. Jiskoot (2013). "Preclinical models used for immunogenicity prediction of therapeutic proteins." Pharm Res 30(7): 1719-1728.

Brummitt, R. K., D. P. Nesta, L. Chang, A. M. Kroetsch and C. J. Roberts (2011). "Nonnative aggregation of an IgG1 antibody in acidic conditions, part 2: nucleation and growth kinetics with competing growth mechanisms." J Pharm Sci 100(6): 2104-2119.

Brummitt, R. K., D. P. Nesta, L. Chang, A. M. Kroetsch and C. J. Roberts (2011). "Nonnative aggregation of an IgG1 antibody in acidic conditions, part 2: Nucleation and growth kinetics with competing growth mechanisms." Journal of Pharmaceutical Sciences 100(6): 2104-2119.

Carpenter, J. F., T. W. Randolph, W. Jiskoot, D. J. A. Crommelin, C. R. Middaugh, G. Winter, Y.-X. Fan, S. Kirshner, D. Verthelyi, S. Kozlowski, K. A. Clouse, P. G. Swann, A. Rosenberg and B. Cherney (2009). "Overlooking subvisible particles in therapeutic protein products: Gaps that may compromise product quality." Journal of Pharmaceutical Sciences 98(4): 1201-1205.

Casadevall, A., E. Dadachova and L.-a. Pirofski (2004). "Passive antibody therapy for infectious diseases." Nat Rev Micro 2(9): 695-703.

Cavagnaro, J. A. (2013). Preclinical Safety Evaluation of Biopharmaceuticals: A Science-Based Approach to Facilitating Clinical Trials, Wiley.

Cohen, S. I., M. Vendruscolo, C. M. Dobson and T. P. Knowles (2012). "From macroscopic measurements to microscopic mechanisms of protein aggregation." Journal of molecular biology 421(2): 160-171.

Corvari, V., L. O. Narhi, T. M. Spitznagel, N. Afonina, S. Cao, P. Cash, I. Cecchini, M. R. DeFelippis, P. Garidel, A. Herre, A. V. Koulov, T. Lubiniecki, H. C. Mahler, P. Mangiagalli, D. Nesta, B. Perez-Ramirez, A. Polozova, M. Rossi, R. Schmidt, R. Simler, S. Singh, A. Weiskopf and K. Wuchner (2015). "Subvisible (2-100 mum) particle analysis during biotherapeutic drug product development: Part 2, experience with the application of subvisible particle analysis." Biologicals 43(6): 457-473.

Cromwell, M. E., E. Hilario and F. Jacobson (2006). "Protein aggregation and bioprocessing." AAPS J 8(3): E572-579.

Dathe, M., K. Gast, D. Zirwer, H. Welfle and B. Mehlis (1990). "Insulin aggregation in solution." International Journal of Peptide and Protein Research 36(4): 344-349.

Davies, D. R. and H. Metzger (1983). "Structural Basis of Antibody Function." Annual Review of Immunology 1(1): 87-115.

De Jong, W. H., W. I. Hagens, P. Krystek, M. C. Burger, A. J. Sips and R. E. Geertsma (2008). "Particle size-dependent organ distribution of gold nanoparticles after intravenous administration." Biomaterials 29(12): 1912-1919.

De Young, L. R., A. L. Fink and K. A. Dill (1993). "Aggregation of globular proteins." Accounts of chemical research 26: 614-614.

Demeule, B., S. Messick, S. J. Shire and J. Liu (2010). "Characterization of particles in protein solutions: reaching the limits of current technologies." AAPS J 12(4): 708-715.

den Engelsman, J., F. Kebbel and P. Garidel (2012). Laser Light Scattering-Based Techniques Used for the Characterization of Protein Therapeutics. Analysis of Aggregates and Particles in Protein Pharmaceuticals, John Wiley & Sons, Inc.: 37-60.

Dragovic, R. A., C. Gardiner, A. S. Brooks, D. S. Tannetta, D. J. Ferguson, P. Hole, B. Carr, C. W. Redman, A. L. Harris, P. J. Dobson, P. Harrison and I. L. Sargent (2011). "Sizing and phenotyping of cellular vesicles using Nanoparticle Tracking Analysis." Nanomedicine 7(6): 780-788.

Ecker, D. M., S. D. Jones and H. L. Levine (2015). "The therapeutic monoclonal antibody market." MAbs 7(1): 9-14.

Ellis, R. J. and A. P. Minton (2006). "Protein aggregation in crowded environments." Biol Chem 387(5): 485-497.

Filipe, V., A. Hawe and W. Jiskoot (2010). "Critical evaluation of Nanoparticle Tracking Analysis (NTA) by NanoSight for the measurement of nanoparticles and protein aggregates." Pharm Res 27(5): 796-810.

Filipe, V., W. Jiskoot, A. H. Basmeleh, A. Halim, H. Schellekens and V. Brinks (2012). "Immunogenicity of different stressed IgG monoclonal antibody formulations in immune tolerant transgenic mice." MAbs 4(6): 740-752.

Fischer, H., I. Polikarpov and A. F. Craievich (2004). "Average protein density is a molecular-weight-dependent function." Protein Sci 13(10): 2825-2828.

Fletcher, G. C. (1976). "Dynamic light scattering from collagen solutions. I. Translational diffusion coefficient and aggregation effects." Biopolymers 15(11): 2201-2217.

Folzer, E., T. A. Khan, R. Schmidt, C. Finkler, J. Huwyler, H. C. Mahler and A. V. Koulov (2015). "Determination of the Density of Protein Particles Using a Suspended Microchannel Resonator." J Pharm Sci 104(12): 4034-4040.

Fradkin, A. H., J. F. Carpenter and T. W. Randolph (2009). "Immunogenicity of aggregates of recombinant human growth hormone in mouse models." J Pharm Sci 98(9): 3247-3264.

Freire, E., A. Schön, B. M. Hutchins and R. K. Brown (2013). "Chemical denaturation as a tool in the formulation optimization of biologics." Drug discovery today 18(19-20): 1007-1013.

Freitag, A. J., M. Shomali, S. Michalakis, M. Biel, M. Siedler, Z. Kaymakcalan, J. F. Carpenter, T. W. Randolph, G. Winter and J. Engert (2015). "Investigation of the immunogenicity of different types of aggregates of a murine monoclonal antibody in mice." Pharm Res 32(2): 430-444.

Frieden, C. (2007). "Protein aggregation processes: In search of the mechanism." Protein Sci 16(11): 2334-2344.

Gardiner, C., M. Shaw, P. Hole, J. Smith, D. Tannetta, C. W. Redman and I. L. Sargent (2014). "Measurement of refractive index by nanoparticle tracking analysis reveals heterogeneity in extracellular vesicles." J Extracell Vesicles 3: 25361.

Garidel, P., A. Blume and M. Wagner (2015). "Prediction of colloidal stability of high concentration protein formulations." Pharm Dev Technol 20(3): 367-374.

Garidel, P. and F. Kebbel (2010). Protein therapeutics and aggregates characterized by photon correlation spectroscopy.

Garidel P, Kuhn AB, Schäfer LV, Karow-Zwick AR, Blech M. (2017). High-concentration protein formulations: How high is high? Eur J Pharm Biopharm. 2017 Oct;119:353-360. doi: 10.1016/j.ejpb.2017.06.029. Epub 2017 Jul 6. PMID: 28690199.

Gerhardt, A., K. Bonam, J. S. Bee, J. F. Carpenter and T. W. Randolph (2013). "Ionic strength affects tertiary structure and aggregation propensity of a monoclonal antibody adsorbed to silicone oil-water interfaces." J Pharm Sci 102(2): 429-440.

GIReseach (2013).

GmbH, L. U. M. (2016). "Literature database." https://www.lum-gmbh.com/Literature_Database.html.

Gross, J., S. Sayle, A. R. Karow, U. Bakowsky and P. Garidel (2016). "Nanoparticle Tracking Analysis of Particle Size and Concentration Detection in Suspensions of Polymer and Protein Samples: Influence of Experimental and Data Evaluation Parameters." Eur J Pharm Biopharm.

Gruia, F., A. Parupudi and A. Polozova (2015). "Practical Considerations for Detection and Characterization of Sub-Micron Particles in Protein Solutions by Nanoparticle Tracking Analysis." PDA Journal of Pharmaceutical Science and Technology 69(3): 427-439.

Hall, D. and A. P. Minton (2003). "Macromolecular crowding: qualitative and semiquantitative successes, quantitative challenges." Biochim Biophys Acta 1649(2): 127-139.

Hamrang, Z., N. J. Rattray and A. Pluen (2013). "Proteins behaving badly: emerging technologies in profiling biopharmaceutical aggregation." Trends Biotechnol 31(8): 448-458.

Haskell, R. J. (1998). "Characterization of submicron systems via optical methods." J Pharm Sci 87(2): 125-129.

Hermeling, S., D. J. Crommelin, H. Schellekens and W. Jiskoot (2004). "Structure-immunogenicity relationships of therapeutic proteins." Pharm Res 21(6): 897-903.

Hirn, S., M. Semmler-Behnke, C. Schleh, A. Wenk, J. Lipka, M. Schaffler, S. Takenaka, W. Moller, G. Schmid, U. Simon and W. G. Kreyling (2011). "Particle size-dependent and surface charge-dependent biodistribution of gold nanoparticles after intravenous administration." Eur J Pharm Biopharm 77(3): 407-416.

http://www.proteinsimple.com/mfi_overview.html, P. S. (June 2016).

Hu, Z. and D. C. Ripple (2014). "The Use of Index-Matched Beads in Optical Particle Counters." J Res Natl Inst Stand Technol 119: 674-682.

Huang, C.-T., D. Sharma, P. Oma and R. Krishnamurthy (2009). "Quantitation of protein particles in parenteral solutions using micro-flow imaging." Journal of Pharmaceutical Sciences 98(9): 3058-3071.

Israelachvili, J. and H. Wennerstrom (1996). "Role of hydration and water structure in biological and colloidal interactions." Nature 379(6562): 219-225.

IUPAC (2006). "Compendium of Chemical Terminology." Blackwelll Scientific Publications, Oxford.

Izon (2016). "Homepage iZon." http://www.izon.com/products/qnano/.

Jaenicke, R. (1991). "Protein stability and molecular adaptation to extreme conditons." European Journal of Biochemistry 202(3): 715-728.

Jin, H., D. A. Heller, R. Sharma and M. S. Strano (2009). "Size-dependent cellular uptake and expulsion of single-walled carbon nanotubes: single particle tracking and a generic uptake model for nanoparticles." ACS Nano 3(1): 149-158.

Jiskoot, W., G. Kijanka, T. W. Randolph, J. F. Carpenter, A. V. Koulov, H. C. Mahler, M. K. Joubert, V. Jawa and L. O. Narhi (2016). "Mouse Models for Assessing Protein Immunogenicity: Lessons and Challenges." J Pharm Sci.

Jiskoot, W., T. W. Randolph, D. B. Volkin, C. R. Middaugh, C. Schoneich, G. Winter, W. Friess, D. J. Crommelin and J. F. Carpenter (2012). "Protein instability and immunogenicity: roadblocks to clinical application of injectable protein delivery systems for sustained release." J Pharm Sci 101(3): 946-954.

Johnson, R. and W. Jiskoot (2012). "Models for evaluation of relative immunogenic potential of protein particles in biopharmaceutical protein formulations." J Pharm Sci 101(10): 3586-3592.

Joubert, M. K., M. Hokom, C. Eakin, L. Zhou, M. Deshpande, M. P. Baker, T. J. Goletz, B. A. Kerwin, N. Chirmule, L. O. Narhi and V. Jawa (2012). "Highly aggregated antibody therapeutics can enhance the in vitro innate and late-stage T-cell immune responses." J Biol Chem 287(30): 25266-25279.

Kádár, R., I. Naue and M. Wilhelm (2014). Simultaneous in-situ analysis of instabilities and first normal stress difference during polymer melt extrusion flows.

Kaiser, W. and U. Rant (2010). "Conformations of End-Tethered DNA Molecules on Gold Surfaces: Influences of Applied Electric Potential, Electrolyte Screening, and Temperature." Journal of the American Chemical Society 132(23): 7935-7945.

Kalonia, C., V. Toprani, R. Toth, N. Wahome, I. Gabel, C. R. Middaugh and D. B. Volkin (2016). "Effects of Protein Conformation, Apparent Solubility, and Protein-Protein Interactions on the Rates and Mechanisms of Aggregation for an IgG1Monoclonal Antibody." J Phys Chem B 120(29): 7062-7075.

Karow, A. R., J. Gotzl and P. Garidel (2015). "Resolving power of dynamic light scattering for protein and polystyrene nanoparticles." Pharm Dev Technol 20(1): 84-89.

Kathe, N., B. Henriksen and H. Chauhan (2014). "Physicochemical characterization techniques for solid lipid nanoparticles: principles and limitations." Drug Dev Ind Pharm 40(12): 1565-1575.

Kim, Y. S., T. W. Randolph, M. B. Seefeldt and J. F. Carpenter (2006). "High-pressure studies on protein aggregates and amyloid fibrils." Methods Enzymol 413: 237-253.

Kim, Y. S., T. W. Randolph, F. J. Stevens and J. F. Carpenter (2002). "Kinetics and energetics of assembly, nucleation, and growth of aggregates and fibrils for an amyloidogenic protein. Insights into transition states from pressure, temperature, and co-solute studies." J Biol Chem 277(30): 27240-27246.

Koide, H., T. Asai, K. Hatanaka, T. Urakami, T. Ishii, E. Kenjo, M. Nishihara, M. Yokoyama, T. Ishida, H. Kiwada and N. Oku (2008). "Particle size-dependent triggering of accelerated blood clearance phenomenon." Int J Pharm 362(1-2): 197-200.

Köpf, E. and W. Frieß (2016). "Proteinformulierung: Vom Molekül zum Medikament Protein pharmaceuticals: challenges and approaches." PHARMAKON 4(2): 125-133.

Kozak, D., W. Anderson, R. Vogel, S. Chen, F. Antaw and M. Trau (2012). "Simultaneous size and zeta-potential measurements of individual nanoparticles in dispersion using size-tunable pore sensors." ACS Nano 6(8): 6990-6997.

Kozak, D., W. Anderson, R. Vogel and M. Trau (2011). "Advances in Resistive Pulse Sensors: Devices bridging the void between molecular and microscopic detection." Nano Today 6(5): 531-545.

Kramberger, P., M. Ciringer, A. Strancar and M. Peterka (2012). "Evaluation of nanoparticle tracking analysis for total virus particle determination." Virol J 9: 265.

Kubo, S., A. Diaz, Y. Tang, T. S. Mayer, I. C. Khoo and T. E. Mallouk (2007). "Tunability of the Refractive Index of Gold Nanoparticle Dispersions." Nano Letters 7(11): 3418-3423.

Kueltzo, L. A., W. Wang, T. W. Randolph and J. F. Carpenter (2008). "Effects of solution conditions, processing parameters, and container materials on aggregation of a monoclonal antibody during freeze-thawing." J Pharm Sci 97(5): 1801-1812.

Lakowicz, J. R. (2006). "Principles of fluorescence spectroscopy. 3rd ed. 2006." New York: Springer.

Langer, A., P. A. Hampel, W. Kaiser, J. Knezevic, T. Welte, V. Villa, M. Maruyama, M. Svejda, S. Jähner, F. Fischer, R. Strasser and U. Rant (2013). "Protein analysis by time-resolved measurements with an electro-switchable DNA chip." Nature Communications 4: 2099.

Langer, A., P. A. Hampel, W. Kaiser, J. Knezevic, T. Welte, V. Villa, M. Maruyama, M. Svejda, S. Jähner, F. Fischer, R. Strasser and U. Rant (2013). "Protein analysis by time-resolved measurements with an electro-switchable DNA chip." Nature Communications 4(1): 2099.

Langer, A., W. Kaiser, M. Svejda, P. Schwertler and U. Rant (2014). "Molecular dynamics of DNA-protein conjugates on electrified surfaces: solutions to the drift-diffusion equation." J Phys Chem B 118(2): 597-607.

Langer, A., W. Kaiser, M. Svejda, P. Schwertler and U. Rant (2014). "Molecular Dynamics of DNA–Protein Conjugates on Electrified Surfaces: Solutions to the Drift-Diffusion Equation." The Journal of Physical Chemistry B 118(2): 597-607.

Langer, A., M. Schräml, R. Strasser, H. Daub, T. Myers, D. Heindl and U. Rant (2015). "Polymerase/DNA interactions and enzymatic activity: multi-parameter analysis with electro-switchable biosurfaces." Scientific Reports 5(1): 12066.

Langille, S. E. (2013). "Particulate matter in injectable drug products." PDA J Pharm Sci Technol 67(3): 186-200.

Le Brun, V., W. Friess, S. Bassarab, S. Muhlau and P. Garidel (2010). "A critical evaluation of self-interaction chromatography as a predictive tool for the assessment of protein-protein interactions in protein formulation development: a case study of a therapeutic monoclonal antibody." Eur J Pharm Biopharm 75(1): 16-25.

Lewis, E., W. Qi, L. Kidder, S. Amin, S. Kenyon and S. Blake (2014). "Combined Dynamic Light Scattering and Raman Spectroscopy Approach for Characterizing the Aggregation of Therapeutic Proteins." Molecules 19(12): 20888.

Li, G. G., S. Cao, N. Jiao and Z. Q. Wen (2014). "Classification of glass particles in parenteral product vials by visual, microscopic, and spectroscopic methods." PDA J Pharm Sci Technol 68(4): 362-372.

Li, Y., B. A. Ogunnaike and C. J. Roberts (2010). "Multi-variate approach to global protein aggregation behavior and kinetics: effects of pH, NaCl, and temperature for alpha-chymotrypsinogen A." J Pharm Sci 99(2): 645-662.

Li, Y. and C. J. Roberts (2009). "Lumry− Eyring nucleated-polymerization model of protein aggregation kinetics. 2. Competing growth via condensation and chain polymerization." The Journal of Physical Chemistry B 113(19): 7020-7032.

Li, Y., W. F. Weiss and C. J. Roberts (2009). "Characterization of high-molecular-weight nonnative aggregates and aggregation kinetics by size exclusion chromatography with inline multi-angle laser light scattering." Journal of pharmaceutical sciences 98(11): 3997-4016.

Ling, T. Y., J. Wang and D. Y. H. Pui (2006). "Comparison of the aerosolization and nanoparticle tracking (Nanosight LM10) techniques for size and concentration measurements of colloidal suspensions and its application in determining retention of nanoparticles in liquids." International Aerosol Conference, Sept 10–15th, St. Paul, Minnesota USA, 2006.

Ltd, P. W. (2014). "Top 50 pharmaceutical products by global sales." http://www.pmlive.com/top_pharma_list/Top_50_pharmaceutical_products_by_global_sales.

Lux, G., A. Langer, M. Pschenitza, X. Karsunke, R. Strasser, R. Niessner, D. Knopp and U. Rant (2015). "Detection of the Carcinogenic Water Pollutant Benzo[a]pyrene with an Electro-Switchable Biosurface." Analytical Chemistry 87(8): 4538-4545.

Makowski, L., S. A. Berkowitz and D. J. Houde (2015). Scattering Techniques for the Characterization of Biopharmaceuticals. Biophysical Characterization of Proteins in Developing Biopharmaceuticals: 171-209.

Male, D. K., J. Brostoff and I. M. Roitt (2013). Immunology,With STUDENT CONSULT Online Access,8: Immunology, Elsevier/Saunders.

Malvern (2016)."Application of Dynamic Light Scattering (DLS) to Protein Therapeutic Formulations: Principles, Measurements and Analysis - 3. DLS Deconvolution Algorithms." white paper.

Malvern Instruments GmbH, w. m. c. d. p. t. n.-t.-a. (June 2016).

Manning, M. C., D. K. Chou, B. M. Murphy, R. W. Payne and D. S. Katayama (2010). "Stability of protein pharmaceuticals: an update." Pharmaceutical research 27(4): 544-575.

Manning, M. C., K. Patel and R. T. Borchardt (1989). "Stability of Protein Pharmaceuticals." Pharmaceutical Research 6(11): 903-918.

Meisl, G., J. B. Kirkegaard, P. Arosio, T. C. Michaels, M. Vendruscolo, C. M. Dobson, S. Linse and T. P. Knowles (2016). "Molecular mechanisms of protein aggregation from global fitting of kinetic models." Nat Protoc 11(2): 252-272.

Michl, D. and A. Heinemann (2009). "Medizinische Biotechnologie in Deutschland 2009:

Wirtschaftsdaten von Biopharmazeutika und Therapiefortschritt durch Antikörper." Boston Consulting Group Report.

Morea, V., A. M. Lesk and A. Tramontano (2000). "Antibody modeling: implications for engineering and design." Methods 20(3): 267-279.

Morris, A. M., M. A. Watzky, J. N. Agar and R. G. Finke (2008). "Fitting Neurological Protein Aggregation Kinetic Data via a 2-Step, Minimal/"Ockham's Razor" Model: The Finke− Watzky Mechanism of Nucleation Followed by Autocatalytic Surface Growth." Biochemistry 47(8): 2413-2427.

Morris, A. M., M. A. Watzky and R. G. Finke (2009). "Protein aggregation kinetics, mechanism, and curve-fitting: a review of the literature." Biochim Biophys Acta 1794(3): 375-397.

Morris, A. M., M. A. Watzky and R. G. Finke (2009). "Protein aggregation kinetics, mechanism, and curve-fitting: A review of the literature." Biochimica et Biophysica Acta (BBA) - Proteins and Proteomics 1794(3): 375-397.

Moussa, E. M., J. P. Panchal, B. S. Moorthy, J. S. Blum, M. K. Joubert, L. O. Narhi and E. M. Topp (2016). "Immunogenicity of Therapeutic Protein Aggregates." J Pharm Sci 105(2): 417-430.

Murphy, K. and C. Weaver (2016). Janeway's immunobiology, Garland Science.

Nicoud, L., P. Arosio, M. Sozo, A. Yates, E. Norrant and M. Morbidelli (2014). "Kinetic analysis of the multistep aggregation mechanism of monoclonal antibodies." J Phys Chem B 118(36): 10595-10606.

Nicoud, L., J. Jagielski, D. Pfister, S. Lazzari, J. Massant, M. Lattuada and M. Morbidelli (2016). "Kinetics of Monoclonal Antibody Aggregation from Dilute toward Concentrated Conditions." J Phys Chem B 120(13): 3267-3280.

Nicoud, L., M. Lattuada, S. Lazzari and M. Morbidelli (2015). "Viscosity scaling in concentrated dispersions and its impact on colloidal aggregation." Phys Chem Chem Phys 17(37): 24392-24402.

Nicoud, L., M. Owczarz, P. Arosio and M. Morbidelli (2015). "A multiscale view of therapeutic protein aggregation: a colloid science perspective." Biotechnol J 10(3): 367-378.

Oliva, A., M. Llabres and J. B. Farina (2015). "Fitting bevacizumab aggregation kinetic data with the Finke-Watzky two-step model: Effect of thermal and mechanical stress." Eur J Pharm Sci 77: 170-179.

Patel, A. R., D. Lau and J. Liu (2012). "Quantification and characterization of micrometer and submicrometer subvisible particles in protein therapeutics by use of a suspended microchannel resonator." Anal Chem 84(15): 6833-6840.

Patois, E., M. A. H. Capelle, C. Palais, R. Gurny and T. Arvinte (2012). "Evaluation of nanoparticle tracking analysis (NTA) in the characterization of therapeutic antibodies and seasonal influenza vaccines: Pros and cons." Journal of Drug Delivery Science and Technology 22(5): 427-433.

Pedersen, J. S. and M. Persson (2014). "Unmasking translucent protein particles by improved micro-flow imaging algorithms." J Pharm Sci 103(1): 107-114.

Philo, J. S. and T. Arakawa (2009). "Mechanisms of protein aggregation." Curr Pharm Biotechnol 10(4): 348-351.

Pindrus, M., S. J. Shire, R. F. Kelley, B. Demeule, R. Wong, Y. Xu and S. Yadav (2015). "Solubility Challenges in High Concentration Monoclonal Antibody Formulations: Relationship with Amino Acid Sequence and Intermolecular Interactions." Mol Pharm 12(11): 3896-3907.

Rant, U. (2012). "Sensing with electro-switchable biosurfaces." Bioanalytical Reviews 4(2): 97-114.

Ripple, D. C. and M. N. Dimitrova (2012). "Protein particles: what we know and what we do not know." J Pharm Sci 101(10): 3568-3579.

Ripple, D. C. and M. N. Dimitrova (2012). "Protein Particles: What We Know and What We Don´t Know." Journal of Pharmaceutical Sciences 101(10): pp. 3568 - 3579.

Ripple, D. C., C. B. Montgomery and Z. Hu (2015). "An Interlaboratory Comparison of Sizing and Counting of Subvisible Particles Mimicking Protein Aggregates." Journal of Pharmaceutical Sciences 104(2): 666-677.

Ripple, D. C., J. R. Wayment and M. J. Carrier (2012). "Standards for Optical Detection of Protein Particles." Amer. Pharm. Rev. 14: 90-96.

Roberts, C. J. (2003). "Kinetics of irreversible protein aggregation: analysis of extended Lumry− Eyring models and implications for predicting protein shelf life." The Journal of Physical Chemistry B 107(5): 1194-1207.

Roberts, C. J. (2007). "Non-native protein aggregation kinetics." Biotechnol Bioeng 98(5): 927-938.

Roberts, C. J. (2014). "Therapeutic protein aggregation: mechanisms, design, and control." Trends Biotechnol 32(7): 372-380.

Roberts, G. S., D. Kozak, W. Anderson, M. F. Broom, R. Vogel and M. Trau (2010). "Tunable nano/micropores for particle detection and discrimination: scanning ion occlusion spectroscopy." Small 6(23): 2653-2658.

Roberts, G. S., S. Yu, Q. Zeng, L. C. Chan, W. Anderson, A. H. Colby, M. W. Grinstaff, S. Reid and R. Vogel (2012). "Tunable pores for measuring concentrations of synthetic and biological nanoparticle dispersions." Biosens Bioelectron 31(1): 17-25.

Rong, Y., T. Zhou, W. Cheng, J. Guo, X. Cui, Y. Liu and W. Chen (2013). "Particle-size-dependent cytokine responses and cell damage induced by silica particles and macrophages-derived mediators in endothelial cell." Environ Toxicol Pharmacol 36(3): 921-928.

Rowe, A. J. (2001). "Probing hydration and the stability of protein solutions — a colloid science approach." Biophysical Chemistry 93(2–3): 93-101.

Sanchez-Ruiz, J. M. (2010). "Protein kinetic stability." Biophys Chem 148(1-3): 1-15.

Sanchis, J., C. Bosch-Orea, M. Farre and D. Barcelo (2015). "Nanoparticle tracking analysis characterisation and parts-per-quadrillion determination of fullerenes in river samples from Barcelona catchment area." Anal Bioanal Chem 407(15): 4261-4275.

Sancho, J. (2013). "The stability of 2-state, 3-state and more-state proteins from simple spectroscopic techniques... plus the structure of the equilibrium intermediates at the same time." Archives of Biochemistry and Biophysics 531(1–2): 4-13.

Schaz, S. H. (2015). "Flow Cytometry for Automated Particle Detection in Formulation Development." Master Thesis Biberach University of Applied Science.

Shanley, A. (2019). "Getting a Handle on Biopharma's Most Critical Quality Attributes and Quality Control." BioPharm International 32 (5).

Sharma, D. K., D. King and C. Merchant (2011). "Reference material development for calibration and verification of image-based particle analyzers." Int J Pharm 416(1): 293-295.

Sharma, D. K., D. King, P. Oma and C. Merchant (2010). "Micro-flow imaging: flow microscopy applied to sub-visible particulate analysis in protein formulations." AAPS J 12(3): 455-464.

Sharma, D. K., P. Oma, M. J. Pollo and M. Sukumar (2010). "Quantification and characterization of subvisible proteinaceous particles in opalescent mAb formulations using micro-flow imaging." J Pharm Sci 99(6): 2628-2642.

Shekunov, B. Y., P. Chattopadhyay, H. H. Tong and A. H. Chow (2007). "Particle size analysis in pharmaceutics: principles, methods and applications." Pharm Res 24(2): 203-227.

Shire, S. J., Z. Shahrokh and J. Liu (2004). "Challenges in the development of high protein concentration formulations." Journal of pharmaceutical sciences 93(6): 1390-1402.

Shomali, M., A. Freitag, J. Engert, M. Siedler, Z. Kaymakcalan, G. Winter, J. F. Carpenter and T. W. Randolph (2014). "Antibody responses in mice to particles formed from adsorption of a murine monoclonal antibody onto glass microparticles." J Pharm Sci 103(1): 78-89.

Shomali, M., S. Tanriverdi, A. J. Freitag, J. Engert, G. Winter, M. Siedler, Z. Kaymakcalan, J. F. Carpenter and T. W. Randolph (2015). "Dose levels in particulate-containing formulations impact anti-drug antibody responses to murine monoclonal antibody in mice." J Pharm Sci 104(5): 1610-1621.

Singla, A., R. Bansal, V. Joshi and A. S. Rathore (2016). "Aggregation Kinetics for IgG1-Based Monoclonal Antibody Therapeutics." AAPS J 18(3): 689-702.

Slutter, B. and W. Jiskoot (2016). "Sizing the optimal dimensions of a vaccine delivery system: a particulate matter." Expert Opin Drug Deliv 13(2): 167-170.

Sowerby, S. J., M. F. Broom and G. B. Petersen (2007). "Dynamically resizable nanometre-scale apertures for molecular sensing." Sensors and Actuators B: Chemical 123(1): 325-330.

Sugimoto, K., J. Shiraishi, F. Moriyasu, S. Ichimura, R. Metoki and K. Doi (2010). "Analysis of intrahepatic vascular morphological changes of chronic liver disease for assessment of liver fibrosis stages by micro-flow imaging with contrast-enhanced ultrasound: preliminary experience." Eur Radiol 20(11): 2749-2757.

Syvitski, J. P. M. (1991). "Principles, Methods and Application of Particle Size Analysis." Cambridge University Press(ISBN: 978-0-521-36472-0).

ThermoFisher (2016). "https://www.thermofisher.com/de/de/home/life-science/antibodies/antibodies-learning-center/antibodies-resource-library/antibody-methods/antibody-fragmentation.html."

van der Pol, E., F. A. Coumans, A. E. Grootemaat, C. Gardiner, I. L. Sargent, P. Harrison, A. Sturk, T. G. van Leeuwen and R. Nieuwland (2014). "Particle size distribution of exosomes and microvesicles determined by transmission electron microscopy, flow cytometry, nanoparticle tracking analysis, and resistive pulse sensing." J Thromb Haemost 12(7): 1182-1192.

Van Der Pol, E., F. A. W. Coumans, A. Sturk, R. Nieuwland and T. G. Van Leeuwen (2014). "Refractive index determination of nanoparticles in suspension using nanoparticle tracking analysis." Nano Letters 14(11): 6195-6201.

van der Pol, E., A. G. Hoekstra, A. Sturk, C. Otto, T. G. van Leeuwen and R. Nieuwland (2010). "Optical and non-optical methods for detection and characterization of microparticles and exosomes." J Thromb Haemost 8(12): 2596-2607.

van Oss, C. J. (2003). "Long-range and short-range mechanisms of hydrophobic attraction and hydrophilic repulsion in specific and aspecific interactions." Journal of Molecular Recognition 16(4): 177-190.

Varenne, F., A. Makky, M. Gaucher-Delmas, F. Violleau and C. Vauthier (2016). "Multimodal Dispersion of Nanoparticles: A Comprehensive Evaluation of Size Distribution with 9 Size Measurement Methods." Pharm Res 33(5): 1220-1234.

Vasudev, R., S. Mathew and N. Afonina (2015). "Characterization of submicron (0.1-1 mum) particles in therapeutic proteins by nanoparticle tracking analysis." J Pharm Sci 104(5): 1622-1631.

Verwey, E. and J. T. G. Overbeek (1946). "Long distance forces acting between colloidal particles." Transactions of the Faraday Society 42: B117-B123.

vfa (2016). "BCG - Medizinische Biotechnologie in Deutschland 2016- Biopharmaceutical pipeline." (192463): 13.

vfa (2016). "BCG - Medizinische Biotechnologie in Deutschland 2016- Sales Germany." (30795): 8.

Vogel, R., G. Willmott, D. Kozak, G. S. Roberts, W. Anderson, L. Groenewegen, B. Glossop, A. Barnett, A. Turner and M. Trau (2011). "Quantitative sizing of nano/microparticles with a tunable elastomeric pore sensor." Anal Chem 83(9): 3499-3506.

Wagner, M., K. Reiche, A. Blume and P. Garidel (2013). "Viscosity measurements of antibody solutions by photon correlation spectroscopy: an indirect approach - limitations and applicability for high-concentration liquid protein solutions." Pharm Dev Technol 18(4): 963-970.

Walsh, G. (2013). Biopharmaceuticals: Biochemistry and Biotechnology, Wiley.

Walsh, G. (2014). "Biopharmaceutical benchmarks 2014." Nat Biotechnol 32(10): 992-1000.

Walter, J., K. Lohr, E. Karabudak, W. Reis, J. Mikhael, W. Peukert, W. Wohlleben and H. Colfen (2014). "Multidimensional analysis of nanoparticles with highly disperse properties using multiwavelength analytical ultracentrifugation." ACS Nano 8(9): 8871-8886.

Walter, J. and W. Peukert (2016). "Dynamic range multiwavelength particle characterization using analytical ultracentrifugation." Nanoscale 8(14): 7484-7495.

Walter, J., T. Thajudeen, S. Suss, D. Segets and W. Peukert (2015). "New possibilities of accurate particle characterisation by applying direct boundary models to analytical centrifugation." Nanoscale 7(15): 6574-6587.

Wang, W. (1999). "Instability, stabilization, and formulation of liquid protein pharmaceuticals." International Journal of Pharmaceutics 185(2): 129-188.

Wang, W., S. Nema and D. Teagarden (2010). "Protein aggregation--pathways and influencing factors." Int J Pharm 390(2): 89-99.

Wang, W. and C. J. Roberts (2010). Aggregation of therapeutic proteins, John Wiley & Sons.

Wang, W., S. Singh, D. L. Zeng, K. King and S. Nema (2007). "Antibody structure, instability, and formulation." J Pharm Sci 96(1): 1-26.

Wang, X., X. Li, A. Ito, Y. Sogo and T. Ohno (2013). "Particle-size-dependent toxicity and immunogenic activity of mesoporous silica-based adjuvants for tumor immunotherapy." Acta Biomater 9(7): 7480-7489.

Weatherall, E. and G. R. Willmott (2015). "Applications of tunable resistive pulse sensing." Analyst 140(10): 3318-3334.

Weinbuch, D., J. K. Cheung, J. Ketelaars, V. Filipe, A. Hawe, J. den Engelsman and W. Jiskoot (2015). "Nanoparticulate Impurities in Pharmaceutical-Grade Sugars and their Interference with Light Scattering-Based Analysis of Protein Formulations." Pharm Res 32(7): 2419-2427.

Weinbuch, D., S. Zolls, M. Wiggenhorn, W. Friess, G. Winter, W. Jiskoot and A. Hawe (2013). "Micro-flow imaging and resonant mass measurement (Archimedes)--complementary methods to quantitatively differentiate protein particles and silicone oil droplets." J Pharm Sci 102(7): 2152-2165.

Wen, Z. Q. (2007). "Raman spectroscopy of protein pharmaceuticals." Journal of pharmaceutical sciences 96(11): 2861-2878.

Westermaier, Y., M. Veurink, T. Riis-Johannessen, S. Guinchard, R. Gurny and L. Scapozza (2013). "Identification of aggregation breakers for bevacizumab (Avastin®) self-association through similarity searching and interaction studies." European Journal of Pharmaceutics and Biopharmaceutics 85(3, Part A): 773-780.

Willmott, G. R. and P. W. Moore (2008). "Reversible mechanical actuation of elastomeric nanopores." Nanotechnology 19(47): 475504.

Willmott, G. R., R. Vogel, S. S. Yu, L. G. Groenewegen, G. S. Roberts, D. Kozak, W. Anderson and M. Trau (2010). "Use of tunable nanopore blockade rates to investigate colloidal dispersions." J Phys Condens Matter 22(45): 454116.

Wilson, G. A. and M. C. Manning (2013). "Flow imaging: moving toward best practices for subvisible particle quantitation in protein products." J Pharm Sci 102(3): 1133-1134.

Wright, M. (2012). "Nanoparticle tracking analysis for the multiparameter characterization and counting of nanoparticle suspensions." Methods Mol Biol 906: 511-524.

Wu, L., T. Martin, Y. Li, L. Yang, M. Halpenny, A. Giulivi and D. S. Allan (2012). "Cell aggregation in thawed haematopoietic stem cell products visualised using micro-flow imaging." Transfus Med 22(3): 218-220.

Yang, H., G. J. Liu, M. D. Lu, H. X. Xu and X. Y. Xie (2013). "Evaluation of the vascular architecture of focal liver lesions using micro flow imaging." J Ultrasound Med 32(7): 1157-1171.

Zheng, S., Y. Y. Bai, Y. Changyi, X. Gao, W. Zhang, Y. Wang, L. Zhou, S. Ju and C. Li (2014). "Multimodal nanoprobes evaluating physiological pore size of brain vasculatures in ischemic stroke models." Adv Healthc Mater 3(11): 1909-1918.

Zhou, C., A. B. Krueger, J. G. Barnard, W. Qi and J. F. Carpenter (2015). "Characterization of Nanoparticle Tracking Analysis for Quantification and Sizing of Submicron Particles of Therapeutic Proteins." Journal of Pharmaceutical Sciences 104(8): 2441-2450.

Zhou, C., W. Qi, E. Neil Lewis and J. F. Carpenter (2015). "Concomitant Raman spectroscopy and dynamic light scattering for characterization of therapeutic proteins at high concentrations." Analytical Biochemistry 472 (Supplement C): 7-20.

Zhou, C., W. Qi, E. Neil Lewis and J. F. Carpenter (2015). "Concomitant Raman spectroscopy and dynamic light scattering for characterization of therapeutic proteins at high concentrations." Analytical Biochemistry 472: 7-20.

Zolls, S., M. Gregoritza, R. Tantipolphan, M. Wiggenhorn, G. Winter, W. Friess and A. Hawe (2013). "How subvisible particles become invisible-relevance of the refractive index for protein particle analysis." J Pharm Sci 102(5): 1434-1446.

Zouali, M. (2001). Natural Antibodies. eLS, John Wiley & Sons, Ltd.

Appendix

~